UNIVERSITÀ DEGLI STUDI DI MILANO

Scuola di Dottorato in Fisica, Astrofisica e Fisica Applicata

Dipartimento di Fisica

Corso di Dottorato in Fisica, Astrofisica e Fisica Applicata

Ciclo XXV

Searching for physics beyond the Standard Model in ATLAS with the third generation quarks

Settore Scientifico Disciplinare FIS/01 e FIS/04

Supervisore: Professor Attilio ANDREAZZA

Coordinatore: Professor Marco BERSANELLI

Tesi di Dottorato di:

Andrea Favareto

Anno Accademico 2011/2012

Commission of the final examination:

External Referee:
Professor Edoardo GORINI

External Member:
Professor Tommaso TABARELLI DE FATIS

External Member:
Professor Daniel FOURNIER

Internal Member:
Professoressa Laura PERINI

Final examination:

Date 18/02/2012

Università degli Studi di Milano, Dipartimento di Fisica, Milano, Italy

PACS:

29.40.Gx

14.65.Ha

14.80.Ly

Introduction

The Large Hadron Collider (LHC) is a particle physics accelerator built at CERN. It collides head-on bunches of protons or heavy ions. The analysis of these collisions resulted in the discovery of a particle candidate for the Standard Model (SM) Higgs boson and will allow to explore new physics phenomena beyond the SM.

The ATLAS experiment is a general purpose experiment that records collision events produced by the LHC. The ATLAS detector consists of inner tracking devices surrounded by a superconducting solenoid, electromagnetic and hadronic calorimeters and a muon spectrometer with a toroidal magnetic field.

The ATLAS Inner Detector is designed to precisely reconstruct the trajectory of charged particles (*tracking*) at LHC luminosities with a hermetic detector covering 5 units in pseudorapidity. It features a large silicon tracker subdivided into a pixel and a strip system for precise tracking and primary/secondary vertex reconstruction in order to provide excellent b-tagging[1] capabilities. A Transition Radiation Tracker improves the momentum reconstruction and provides electron identification information.

This thesis follows the evolution of my involvement in the 2010-2012 ATLAS data-taking, starting with a performance measurement of the Inner Detector, followed by the measurement of an interesting Standard Model process on early data in which tracking and b-tagging play a fundamental role. Finally a search for new physics on the high integrated luminosity sample is presented.

Reconstruction of tracks and measurement of their parameters is mandatory for most physics applications. In particular, the impact parameters[2] and momentum of charged particles have to be measured with high precision. The excellent perfor-

[1] process of identifying jets originating from b-quark fragmentation

[2] the distance of closest approach of the track to the collision point

mance of the Inner Detector provides the impact parameter resolution needed for b-tagging. This has applications in many physics analyses. It greatly helps in the Standard Model measurements (e.g. $\sigma_{b\bar{b}}$, top physics, etc.), in the searches for the Higgs boson and for physics beyond the Standard Model.

The identification of b-jets exploits the high mass and relatively long lifetime of b-hadrons. They can fly a few millimeters before decaying. For example, jets containing b-hadrons can therefore be tagged by measuring the impact parameters of the tracks of the b-hadron decay products.

This PhD thesis includes a detailed measurement of the tracks impact parameter resolution as a function on the pseudorapidity η, the transverse momentum p_T and the number of points on the track measured by the silicon detectors. The transverse impact parameter resolution is measured to be ~ 10 μm for high p_T tracks ($p_T > 20$ GeV) in a central η region. I personally took care of the whole measurement. This activity gave me the possibility to be closely involved in the joint tracking and b-tagging working groups, having also the pleasure of participate actively in conferences and workshops with talks and posters [1, 2, 3].

Two measurements are presented, that profit of this excellent resolution and the related b-tagging performance.

The first is the measurement of the charge asymmetry in the production of top quark pairs in the semileptonic decay channel. Top quark charge asymmetry can only occur in asymmetric initial states in top quark pair production, so the main contribution comes from $q\bar{q}$ production mechanism. It consists in the fact that the top quark is preferably emitted in the direction of the incoming quark and not in the one of the incoming antiquark. This feature originates a difference in top and antitop quark rapidity distributions. The observable chosen to measure the top quark charge asymmetry is:

$$A_C = \frac{N(\Delta|y| > 0) - N(\Delta|y| < 0)}{N(\Delta|y| > 0) + N(\Delta|y| < 0)} \tag{1}$$

The asymmetry foreseen at the LHC according to the Standard Model is small. Some Beyond the Standard Model theories predict, at the opposite, a sizable asymmetry. As a consequence, this measurement can provide a window on new physics. Furthermore the CDF Collaboration measurement, performed at the Tevatron collider at Fermilab, has shown a deviation larger than 3σ from the Standard Model prediction in the large $t\bar{t}$ invariant mass region. Within this measurement I was

mainly involved in the definition of the discriminant variables and in the selection cuts optimization. Furthermore I contributed significantly in the identification of which observables are more sensitive to new physics and their dependence with respect to top quark pair kinematic variables, since different Beyond the Standard Model theories predict different dependencies and different relations between variables. I also presented this analysis in a national conference, the "XCV Congresso Nazionale della Societá Italiana di Fisica".

A dataset corresponding to an integrated luminosity of 1.04 fb^{-1}, obtained at a centre-of-mass energy of $\sqrt{s} = 7$ TeV is used. After performing a selection of events with one isolated lepton, at least four jets (at least one of them tagged as b-jet) and missing transverse energy, a kinematic fit is performed to reconstruct the $t\bar{t}$ event topology. The charge asymmetry is determined using the differential distribution of the reconstructed observable $|y_t| - |y_{\bar{t}}|$, where y_t and $y_{\bar{t}}$ denote the top and antitop quark rapidities, respectively. An unfolding procedure is applied to correct for detector acceptance and resolution effects and to obtain the corresponding distribution at parton level. The total charge asymmetry after unfolding is measured to be

$$A_C^{unf} = -0.019 \pm 0.028(\text{stat.}) \pm 0.024(\text{syst.}) \tag{2}$$

in agreement with the Standard Model prediction of $A_C = (0.60 \pm 0.03)\%$. In addition, a simultaneous unfolding in $|y_t| - |y_{\bar{t}}|$ and the invariant $t\bar{t}$ mass, $M_{t\bar{t}}$, was performed.

Finally, the results of a search for direct pair production of supersymmetric partners of the top quark in 4.7 fb^{-1} and 13.0 fb^{-1} of integrated luminosity from proton-proton collisions respectively collected at 7 TeV in 2011 and 8 TeV in 2012 are reported. Scalar top quarks decaying into a b-quark and a superymmetric chargino are searched for in events with two leptons in the final state. This events have a final state topology similar to that of $t\bar{t}$ events and this analysis builds up on the experience that I gained with the $t\bar{t}$ charge asymmetry measurement. No excess above the Standard Model expectation is observed. A scalar top with mass between 150 and 450 GeV is excluded at 95% CL for a chargino approximately degenerate with the scalar top and a massless ligthest neutralino. I heavily contributed in the 4.7 fb^{-1} 7 TeV part of the analysis, with particular emphasis on the identification of the discriminant variables, on the selection cuts optimization,

and on the background and systematics estimate. Furthermore I helped in the background estimate and in the upgrade of the analysis with the 13.0 fb^{-1} 8 TeV data. Thanks to this work I have been invited to give a combined ATLAS and CMS talk with the title "Third Generation SUSY Searches at the LHC" at the "2013 Recontres de Moriond" conference.

Contents

Chapter 1

The ATLAS experiment

1.1 The Large Hadron Collider (LHC)

In the early '90, the scientific community started to design an high energy physics collider able to deliver a center of mass energy one order of magnitude greater than the other already existing colliders (LEP and Tevatron). The main objective of this new machine would have been the investigation of the nature of electroweak symmetry breaking and the search for physics beyond Standard Model at TeV scale: this includes the search for the Higgs boson and for particles predicted by Supersymmetric models (SUSY).

The result of this design challenge is the Large Hadron Collider (LHC) [4]: a hadronic (proton-proton and lead ions) collider built inside the tunnel that housed LEP (Large Electron-Positron collider) near the city of Geneve in Switzerland.

1.1.1 The choice of a hadron collider

The main motivation to use a hadronic collider instead of electron-positron one is the large energy loss due to synchrotron radiation in e^+e^- colliders. In fact, charged particles moving along a curve trajectory loose energy following the relation:

$$\frac{dE}{dt} \propto \frac{E^4}{m^4 R} \tag{1.1}$$

where E and m are particle's energy and mass, while R is the trajectory's radius

of curvature. This implies that at fixed energy and collider dimensions (radius), electrons loose $(m_p/m_e)^4 \sim 10^{12}$ times more energy than a proton beam with the same characteristics. The use of electrons would have been possible only in a synchrotron with a much larger radius or in a linear accelerator, options much more costly than the one adopted.

An hadron collider brings some problems that are absent in leptonic colliders due to the proton's composite structure. Proton-proton collisions can be of two different types: *soft collisions* or *hard collisions*[1].

Soft collisions are distant collisions, with protons interacting as a whole object. These interactions have a small transferred momentum and the interaction's products have a small transverse momentum ($\langle p_T \rangle \simeq 500$ MeV).

In *hard collisions* protons interact revealing their inner structure: the collision is studied in terms of QCD processes between different partons. In this type of interaction, the transferred momentum is large and there is a chance to generate new particles. Furthermore, in hadron colliders the partonic center of mass energy is unknown, making kinematic calculation more difficult.

Another problem comes from the fact that the cross section for *hard collisions*, which are important for the discovery of new physics, is much smaller than the one for *soft collisions*: this creates the need for an high luminosity operating collider: the rate R of the proton-proton interactions inside the LHC machine is given by the product of the proton-proton cross section σ and the luminosity: $R = \sigma \times \mathcal{L}$.

Currently in the LHC (2012), as shown in figure 1.1, at every bunch crossing[2] there are up to about 30 soft collisions that will sum themselves to each interaction with large transverse momentum. This soft-collision background is usually called *pile-up*.

1.1.2 Experiments at the LHC

The LHC is located about 100 m underground in a large ring tunnel of about 27 km circumference. It is partly in France and partly in Switzerland, between the

[1] Most of the proton-proton interactions are just glancing blows. In most of these collisions the protons aren't even smashed up; or they are broken into very few particles. A generic mixture of soft and hard collisions is called *minimum-bias* event.

[2] at the LHC bunches of about 10^{11} protons can be brought to collision at a bunch crossing rate (BCR) of ≈ 40 MHz within one of the various detectors, at nominal conditions.

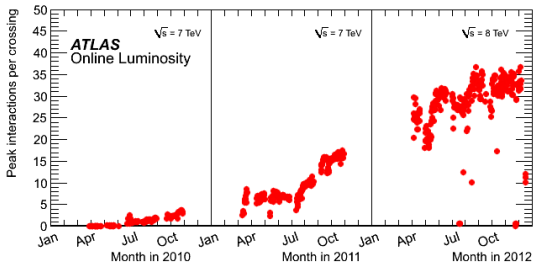

Figure 1.1: Number of events per bunch crossing versus day during the proton-proton runs of 2010,2011 and 2012. The mean value of the number of events in each bunch crossing has been calculated within periods corresponding to about two minutes of data-taking (*luminosity block*), then the maximum value during stable beam periods is taken [5]

Jura mountains and the airport of Geneva.

At four points of the ring the two LHC vacuum beam pipes intersect. Here, the charged particles of the two beams traveling in opposite directions collide. In such collisions lots of new particles are produced, which fly from the collision point into all directions. By measuring these particles with a large detector, that is arranged around the interaction point, it can be concluded how matter behaves at the highest energies or the smallest dimensions. Figure 1.2 shows a schematic view of the LHC and its four experiments ALICE (A Lhc Ion Collider Experiment) [6], ATLAS (A Toroidal Lhc ApparatuS) [7], CMS (Compact Muon Solenoid) [8] and LHCb (LHC beauty experiment) [9]. The first two are multi-purpose experiments, designed to study high transverse momentum events for the search of the Higgs boson and phenomena beyond the Standard Model. LHCb has instead been designed especially to study b-physics, while ALICE was built to analyze mainly heavy ion collisions, to study the formation of a quark-gluon plasma.

1.1.3 CERN accelerator chain

Before being injected into the LHC, the particles are accelerated step by step up to the injection energy of 450 GeV, by a series of accelerators. For protons, the first system is the linear accelerator (LINAC2), which generates them at an energy of 50 MeV. The protons then go through the Proton Synchrotron Booster

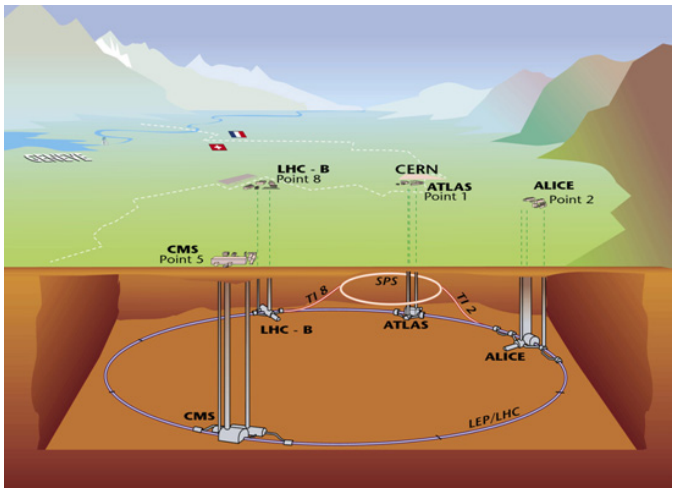

Figure 1.2: Schematic view of the LHC-accelerator and its four experiments

(PSB) and are accelerated to 1.4 GeV. After that they are injected into the Proton Synchrotron (PS), where they are accelerated to 26 GeV. Finally, the Super Proton Synchrotron (SPS) is used to further increase their energy to 450 GeV. For lead ions the production is different. They are first accelerated by the linear accelerator (LINAC3). The ions are then further accelerated by the PS and SPS before being injected into the LHC ring. The whole accelerator chain is shown in figure 1.3.

1.1.4 LHC parameters and operation

1.1.4.1 LHC parameters

The LHC design value for instantaneous luminosity in proton-proton collisions at center of mass energy $\sqrt{s} = 14$ TeV is $\mathcal{L} = 10^{34}$ cm^{-2}s^{-1}. With this configuration there are an average of about 23 inelastic scatterings per bunch crossing, in which nearly 1000 new particles are produced. The current working parameters are an average of 30 inelastic scatterings per bunch crossing in proton-proton collisions at a center of mass energy of $\sqrt{s} = 8$ TeV. A bunch spacing of 50 ns is used and a peak instantaneous luminosity of 8×10^{33} cm^{-2}s^{-1} has been reached. As defined in equation 1.2, the instantaneous luminosity $\mathcal{L}$ is the product of the numbers of particles n_1, n_2 in both crossing bunches and the frequency f of bunch crossings,

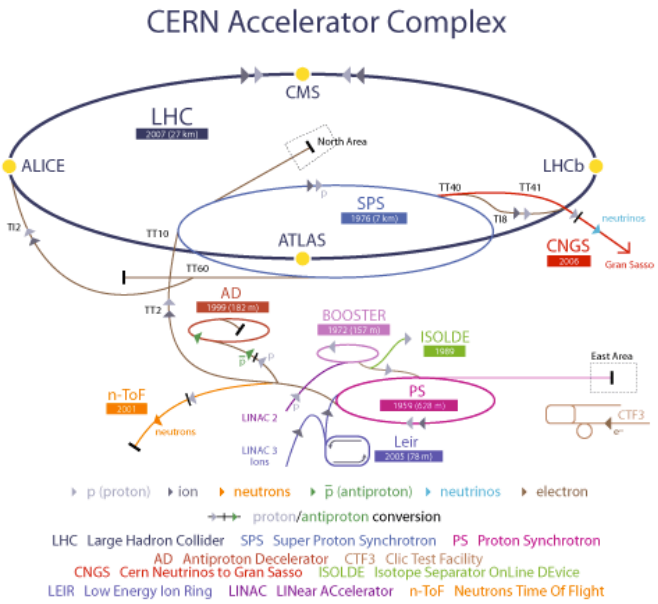

Figure 1.3: Scheme of the accelerator chain up to LHC

divided by the cross sectional area $A = 4\pi\sigma_x\sigma_y$ of a bunch:

$$\mathcal{L} = f\frac{n_1 n_2}{4\pi\sigma_x\sigma_y} \tag{1.2}$$

The LHC bunches nominally contain $\sim 10^{11}$ protons each, and the nominal bunch separation is 25 ns.

The charged particles get the energy by radio frequency radiation from superconducting cavities operating at a temperature of 4.5 K (-268.65 °C) and at a frequency of 400 MHz. For each beam there are eight cavities, each delivering an accelerating field of 5 MV/m. To keep the particles circulating around the ring and inside the beam pipe (vacuum pressure of 10^{-13} atm), a magnetic field of 8.3 T is needed: this value corresponds to proton-proton collisions at $\sqrt{s} = 14$ TeV. This field is generated by superconducting dipole electromagnets operating at a current of 11.7 kA and at a temperature of 1.9 K (-271.3 °C).

Superfluid helium acts as cooling fluid. It has a very high thermal conductivity, which is intended to stabilize the large superconducting system. Figure 1.4 shows the cross section of a LHC dipole. In total, there are 1232 dipoles of 15 m length

and 35 t weight in the LHC ring cooled by 120 t of helium.

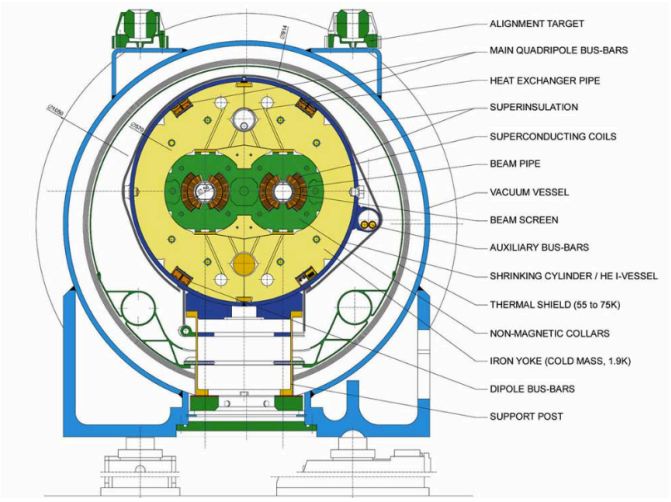

Figure 1.4: Cross section of the vacuum pipes inside a dipole magnet

Without further magnetic fields the charged particles repelling each other would deviate from the ideal trajectory, diverge in the plane transverse to the beam and be absorbed by the beam pipe vacuum vessel. To keep the particles densely together, many other focusing magnets, including 392 quadrupoles, are used. Such magnets are also used around the interaction points, in order to squeeze the particle bunches as much as possible to increase the probability of a collision. Due to the radio frequency acceleration scheme, the protons circulating inside one beam pipe ring are divided into bunches of about 10^{11} particles. The design number of bunches is 2808. These bunches circumnavigate the ring at nearly the speed of light (v/c = 0.999 999 991). Thus, they traverse the entire ring about 10^4 times per second. The bunches follow each other at separation of about 7.5 m in length or 25 ns in time. This corresponds to a collision rate of $\approx$ 40 MHz at the interaction points.

1.1.4.2 LHC operation

The LHC started its operations on 10th September 2008, with the first beams circulating into the rings, in both directions, without collisions. After a commissioning phase, first collisions were expected few days later. Unfortunately, on 19th September of the same year a major accident happened, due to a defective electrical

connection between two magnets. In the accident 53 magnets were damaged. This caused a long stop of the machine, to repair the damaged magnets, to check the electrical connections and to improve the safety systems. During Fall 2009, after more than one year stop, the operations started again, with the first proton-proton collisions at a centre of mass energy of 900 GeV recorded by the four experiments on 23rd November 2009. After a 900 GeV collisions data taking, the centre of mass energy was further increased to 2.36 TeV, beating the Tevatron's previous record of 0.98 TeV per beam and giving therefore collisions at the highest energy ever reached before. After some months, the first proton-proton collisions at $\sqrt{s} = 7$ TeV were registered, on 30th March 2010, starting a new running period that went on until the beginning of November, when the LHC provided the first heavy ion collisions. After the lead ions collisions period and a technical stop during the winter, proton-proton collisions have started again on 13th March 2011. During the commissioning phase, the number of colliding bunches has been progressively increased to reach the design value, even if this has never been reached for physics. At the end of 2010 the maximum number of colliding bunches has been 348, a maximum number of 1092 has been then reached in June 2011. At the end of 2011 proton-proton run the number of colliding bunches is about 1300, as shown in figure 1.5: the bunch separation of 50 ns has been reached. Only in 2015 the nominal value of 25 ns will be reached.

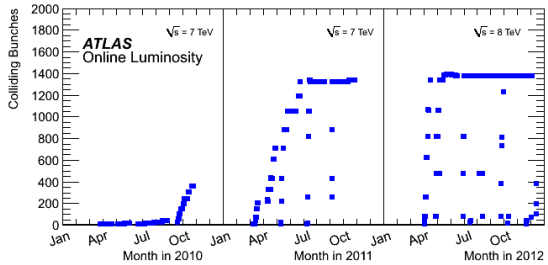

Figure 1.5: The number of colliding bunches in ATLAS versus time during the proton-proton runs of 2010,2011 and 2012 [5]

The maximum instantaneous luminosity that has been reached in 2010 is slightly higher than 2×10^{32} cm^{-2}s^{-1}, while during 2011 run a peak of 3.65×10^{33} cm^{-2}s^{-1} has been achieved. In 2010 and 2011 HI running collisions at 2.76 TeV per nucleon took place, reaching a peak instantaneous luminosity of 30×10^{24} cm^{-2}s^{-1}.

The delivered integrated luminosity for 2010 and 2011 heavy ions (HI) run is shown in figure 1.6. At the end of the 2010 proton-proton running period, ATLAS accumulated 45 pb^{-1} of integrated luminosity, of the 48.9 pb^{-1} delivered by the LHC. Data-taking has re-started in March 2011 and at the end of the 2011 proton-proton run 5.2 fb^{-1} were accumulated. The LHC provides proton-proton collisions at a center of mass energy of 8 TeV, having accumulated about 22 fb^{-1}. Also the delivered integrated luminosity for 2010, 2011 and 2012 proton-proton run is shown in figure 1.6. The 8 TeV data taking will end in 2012, when the LHC will undergo a maintenance stop in order to reach the design center of mass energy of 14 TeV in 2014.

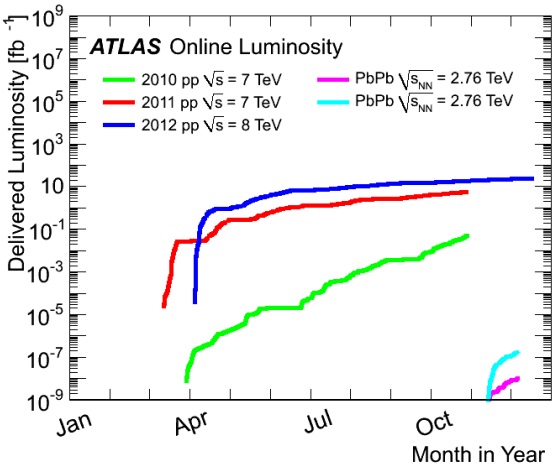

Figure 1.6: Cumulative luminosity versus day delivered to ATLAS during stable beams and for proton-proton and Pb-Pb collisions. This is shown for 2010 (green for proton-proton, magenta for Pb-Pb), 2011 (red for proton-proton, turquoise for Pb-Pb) and 2012 (blue) running. The online luminosity is shown [5]

In the next section, we present the LHC experiment ATLAS in detail, where such particle collision events are detected and analyzed.

1.2 Detectors and optimal performance requirements

The very high luminosity of the LHC is needed to pursue most of physics processes of interest, since the cross sections of these processes are very low compared to the

QCD jets production (see figure 1.7). High luminosity regime introduces however some difficulties as well. One of them is the presence of pile-up, that is the superposition of high cross section inelastic events over the candidates for new physics. Another difficulty due to the nature of proton-proton collisions is that the QCD processes will dominate over the processes physicists are most interested in. This imposes strong demands on the capability of the detectors to identify experimental signatures characteristic of the interesting processes.

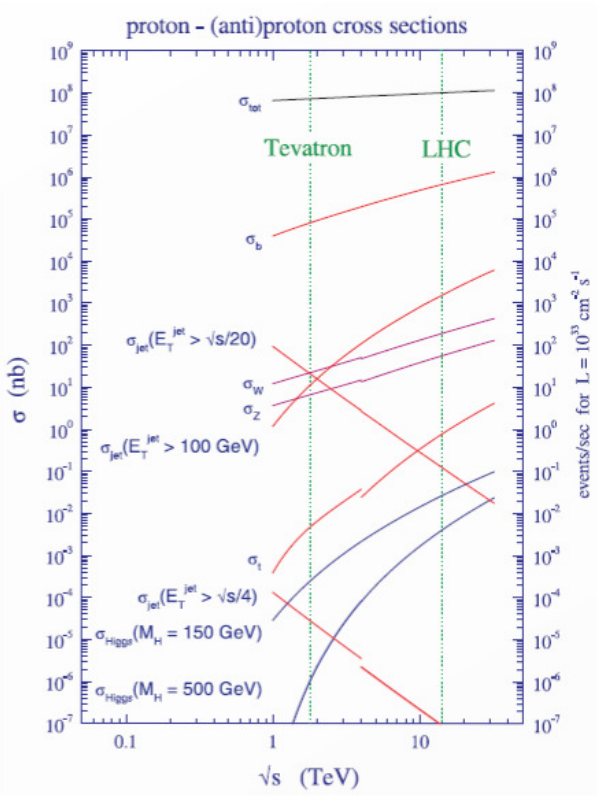

Figure 1.7: Standard Model production cross sections for Tevatron and LHC

The physics program therefore translates into requirements the ATLAS detector have to face:

- *Response Speed*: the large number of overlapping events requires the use of quick electronics in order to have a good time resolution and minimize the pile-up effect. In fact the best situation is to collect the data only belonging to a single bunch crossing (BC). If the electronics isn't quick enough it becomes necessary to integrate the sub-detectors' response over more than one BCs.

- *Granularity*: the presence of pile-up implies a large number of particles. Using a detector with high granularity and good spatial resolution is essential to separate the individual contributions of each particle.

- *Radiation Resistance*: the radiation flux is dependent on the distance from the interaction point. Inner detectors will receive a large dose of radiation (of the order of 10^{14} had cm^{-2} per year). Detectors are designed to resist a large dose of radiation and keep performance constant over the longest time possible.

- *Trigger*: in order to be able to acquire all information about interesting events, we need an efficient trigger system with the rejection factor needed to go from the 40MHz interaction rate at high luminosity to 200Hz data writing rate.

- *Geometric Coverage*: the detector should cover the largest possible part of the solid angle in order to produce an accurate reconstruction of the collision event.

- *Particle identification*: a critical requirement is the ability to discriminate between different types of particles: this quality determines the characteristics of sub-detectors.

- *Data acquisition*: every detector should be able to correctly record the large quantity of data coming from the high-luminosity data taking

1.3 The ATLAS experiment

The ATLAS Experiment is positioned in a cavern at a depth of 100 m. With its height of 25 m and its length of 44 m it is one of the biggest detectors ever built. It weights about 7000 tons and it has a cylindric symmetry. After the cavern was

completed, the construction started in 2003 and it went on until July 2007, with the insertion of the innermost detector and the lowering of the last end-cap toroidal magnet. Since 2009 it has been recording cosmic-ray events and, since November 2009, proton-proton collision events at rates of up to 400 Hz.

1.3.1 Physics at the ATLAS experiment

ATLAS is a general purpose detector with different objectives in both Standard Model and Beyond Standard Model physics searches.

1.3.1.1 Standard Model

Standard Model (SM) precision measurements are the first step on ATLAS physics roadmap. These studies have different motivations: in the first place they were used to understand the detector response to known processes. In second place a lot of the Standard Model events are seen as background in new physics channels: for this reason it's very important to have an extremely precise measurement of the known processes. Finally these measurements work not only as SM consistence tests, but also as indirect search for new physics.

- *QCD*: several studies have been done in the QCD field, measuring jets spectra, their production cross sections and multiplicity [10, 11, 12, 13]. Furthermore, the production cross sections of SM vector bosons (W and Z) bosons in association with QCD jets have been measured as a function of the number of jets [14, 15, 16]. The production cross sections of W and Z bosons in association with a jet originated from a b-quark have been measured as well [17, 18].

- *Electroweak processes*: a very important group of measurement is the study of electroweak production of SM vector bosons. Many studies have been done using 2010 and 2011 data and they show a good agreement with the SM predictions. In particular some studies have been done to measure gauge bosons couplings ($Z\gamma$, $W\gamma$, WW, ZW and ZZ) in different final states [19, 20, 21, 22]. In addition, the kinematics of events with a W or a Z bosons has been explored [23, 24] and the charge asymmetry in W boson production has been measured [25]. These measurements have been used to constrain

the PDF uncertainty [26]. It will be possible to improve the measurements of quantities known with scarce precision like proton's partonic distribution function (PDF): the angular distribution of leptons coming from W and Z decays depends on these PDFs and can be used to determine them.

- *Top quark physics*: there are a lot of open questions on the top quark physics. The top quark mass is about 35 times bigger than the mass of the second heaviest quark (bottom) and is near to the electroweak symmetry break energy scale: hence posing questions about this quark having a particular role in the symmetry breaking or about the Higgs boson coupling. In the top physics sector, many studies have been done to measure production cross sections[3] and main properties, e.g production and decay vertices properties (giving access to a direct measurement of V_{tb}), mass measurement, spin correlation between quarks in $t\bar{t}$ pairs, search for non standard model predicted decays (e.g. $t \to H + b$ or $t \to Z/\gamma + q$), $t\bar{t}$ resonances, which are not discussed in this thesis, but some of them documented in [27, 28, 29, 30, 31], and charge asymmetry measurement in $t\bar{t}$ pair production [32] that will be described in details in chapter 3.

- *other SM measurements*: finally there are many other studies performing SM measurements such as B-physics, minimum-bias, etc.

1.3.1.2 Higgs Boson

The investigation of the dynamics responsible for electroweak symmetry breaking is one of the prime tasks of ATLAS. Within the SM, the Higgs mechanism is invoked to break the electroweak symmetry. A doublet of complex scalar fields is introduced, of which a single neutral scalar physical particle, the Higgs boson, remains after the symmetry breaking.

The direct search at the LEP collider has led to a lower bound on its mass of 114.4 GeV [33]. Recently, the experiments at the Tevatron have excluded at 95% C.L. a SM Higgs with a mass in two mass ranges: $156 < \mathrm{m_H} < 177$ GeV and $100 < \mathrm{m_H} < 108$ GeV [34]. The LHC experiments have the capability to extend

[3] there is a theoretical uncertainty of about 10% NLO computed cross sections for these processes

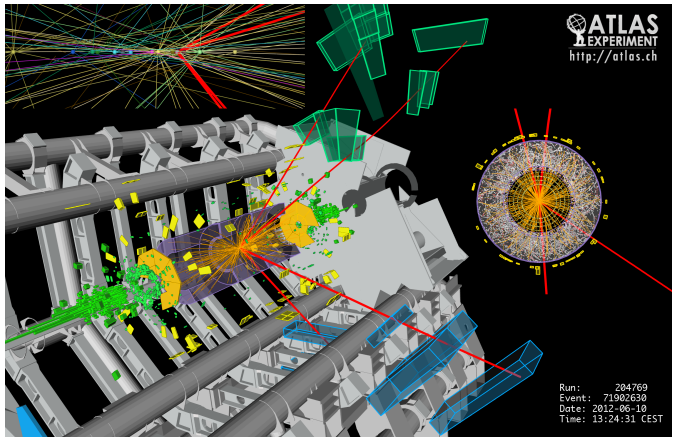

Figure 1.8: Spectacular ATLAS event display of H $\rightarrow 4\mu$ candidate with $m_{4\mu} = 125.1$ GeV

the reach for a standard Higgs up to about 1 TeV. If the Higgs boson is found its mass and couplings will be determined.

The 4th July 2012, at a seminar held at CERN, the ATLAS and CMS experiments presented their latest preliminary results in the search for the long sought Higgs particle. Both experiments observe a new particle with a significant excess (5-6σ) in the mass region around 125-126 GeV [35, 36].

The results presented are based on data collected in 2011 and 2012, with the 2012 data still under analysis. A more complete picture of this observations will emerge later in 2012 after the LHC provides the experiments with more data.

In particular, focusing my attention on the ATLAS experiment, Standard Model Higgs searches have been performed over the mass region 110-600 GeV in many different channels (see figure 1.9). $\sim 10.7\text{fb}^{-1}$ recorded at $\sqrt{s}$ =7 and 8 TeV have been used for H $\rightarrow \gamma\gamma$, H $\rightarrow ZZ \rightarrow 4l$, and H $\rightarrow WW$ channels and the 2011 data ($\sqrt{s}$ =7 TeV, $\sim 4.9\text{fb}^{-1}$) for the other channels. Exclusion limits at 95% C.L. have been placed in the full region up to 557 GeV except $122.7 < m_H < 129$ GeV (see figure 1.10 right). An excess of events has been observed at $m_H \sim 126$ GeV with local significance of 6σ (see figure 1.10 left).

The next step will be to determine the precise nature of the particle and its significance for our understanding of the universe. Are its properties as expected for the long-sought Higgs boson, the final missing ingredient in the Standard Model

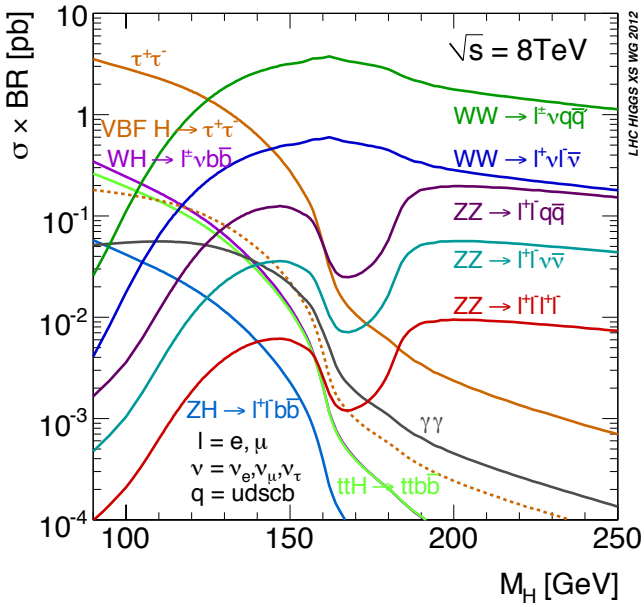

Figure 1.9: The SM Higgs boson production cross section times branching ratio at $sqrts = 8$ TeV. Both inclusive (solid line) and VBF (Vector Boson Fusion, dashed line) $H \to \tau\tau$ are shown

of particle physics? Or is it something more exotic[4]?

1.3.1.3 Supersymmetry

Many studies are dedicated to the search of Supersymmetry (SUSY), which is one of the theoretically favored candidates for physics beyond the SM. Models of supersymmetry involve new, highly massive particles. Some of them, as squarks and gluinos, usually decay into high-energy quarks and stable heavy particles that are very unlikely to interact with ordinary matter. Supersymmetric events are expected to be characterized by several high-momentum jets and missing transverse energy. The ATLAS collaboration has searched for SUSY events in different channels (jets+E_T^{miss}, lepton(s)+E_T^{miss} and b-jets+E_T^{miss}) and, up to now, found

[4]A more exotic version of the Higgs particle could be a bridge to understand the 96% of the universe that remains obscure.

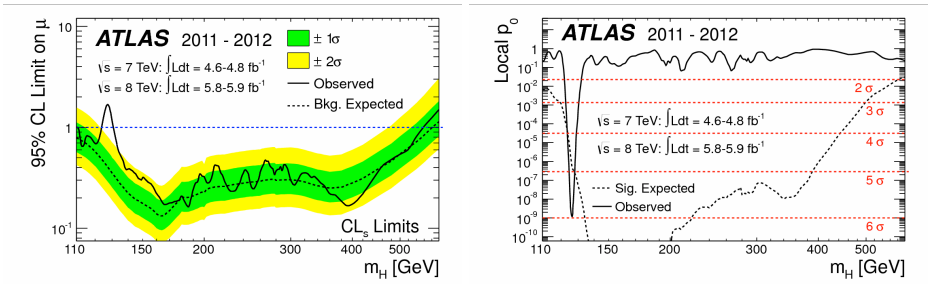

(a) (b)

Figure 1.10: Combined search results: (a) The observed (solid) 95% CL upper limit on the signal strength as a function of m_H and the expectation (dashed) under the background-only hypothesis. The dark and light shaded bands show the plus/minus one sigma and plus/minus two sigma uncertainties on the background-only expectation. (b) The observed (solid) local p_0 as a function of m_H and the expectation (dashed) for a SM Higgs boson signal hypothesis ($\mu = 1$) at the given mass

no evidence of new physics [37, 38, 39]. Lower limits on squarks of the first two generations, and gluino masses up to 1 TeV have been set, with 95% C.L.

1.3.1.4 Other Beyond the Standard Model (BSM) theories

BSM theories, different from Supersymmetry, are studied as well. These theories have been conceived to solve some open issues of the SM, such as the stability of electroweak symmetry breaking scale with respect to radiative corrections, the dark matter nature, neutrino masses, the large number of the SM free parameters, etc. Furthermore, some of them can explain inconsistencies between the SM predictions and the Tevatron data. This is the case of the top quark charge asymmetry measurement, see details in chapter 3.

All searches so far have given results in agreement with SM predictions.

1.3.1.5 Heavy ion physics

The data taking with Pb-Pb collisions will give the possibility to discover new phenomena. The ALICE experiment is dedicated to HI physics, but also the other

experiments have a HI program, even though they have not been designed for this purpose. In particular, thanks to the good performance of the calorimeter system, the ATLAS experiment has observed the "jetquenching" already with few μb^{-1} of data [40]. This new phenomena is characterized by large di-jet asymmetries, not observed in proton-proton collisions and it may point to an interpretation in terms of strong parton energy loss in a hot, dense medium.

1.4 General overview of the ATLAS detector

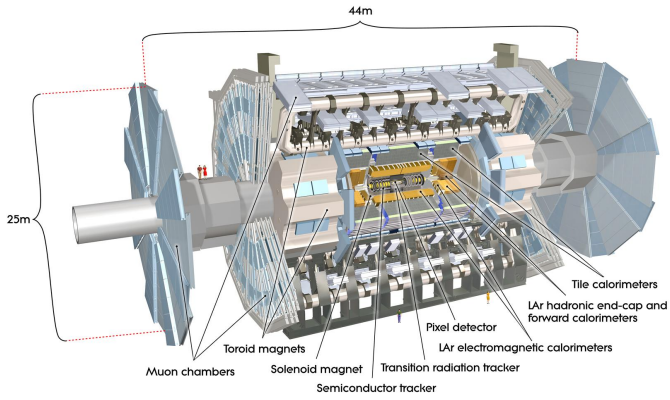

Figure 1.11: Detailed view of the ATLAS detector and its sub-detectors [7]

The ATLAS detector has been designed with a cylindrical symmetry whose longitudinal axis coincides with the beams direction. The general layout of the detector is shown in figure 1.11. The aim pursued during the design phase, as can be seen from the figure itself, was to ensure maximum coverage of the solid angle around the interaction point.

In a LHC collision event many particles are produced. Some types of particles can be directly detected. But since particles differ in their properties and interactions, ATLAS, like the most of the detectors associated with modern colliders, is composed by sub-detectors, each designed and optimized for a specific task within the overall framework: the Inner Detector, the electromagnetic and hadronic calorimeters, and the muon spectrometers, that is the outermost detector. The spatial arrangement of the sub-detectors and an event cross section is

sketched in figure 1.12

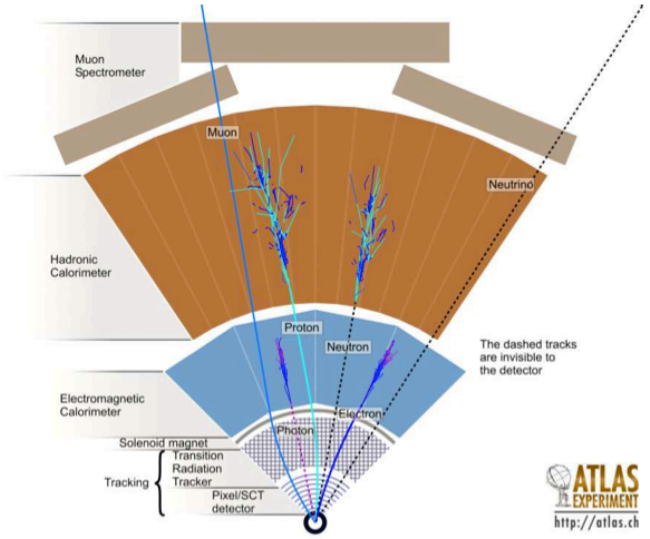

Figure 1.12: Schematical view of the specialized particle detectors of ATLAS and sketch of an event cross section. Not drawn: the toroid magnets between the hadronic calorimeter and the muon spectrometer

1.4.1 ATLAS coordinate system

The ATLAS coordinate system is a right-handed coordinate frame with the x-axis pointing towards the centre of the LHC ring and the z-axis being directed along the beam pipe, while the y-axis points upwards. In this context, the pseudorapidity can be introduced as

$$\eta = -\ln \tan \frac{\theta}{2} \tag{1.3}$$

with θ being the polar angle with respect to the positive y-axis. For massive objects such as jets, the rapidity is used, given by

$$y = \frac{1}{2} \ln \left(\frac{E + p_z}{E - p_z} \right) \tag{1.4}$$

The rapidity (pseudorapidity) is much preferred instead of the polar angle θ because the collisions are boosted relative to each other along the z-axis. This

quantity is additive. A Lorentz boost β' along the z-axis is equivalent to a boost with rapidity $y' = \text{arctanh}(\beta')$, and results in $y \to y + y'$. This means that differences in rapidity are invariant, and as a consequence, the shape of the high energy particle multiplicity spectrum dN/dy is also invariant under a boost along the z-axis.

The transverse momentum p_T of a particle in the detector is defined as the momentum perpendicular to the z-axis:

$$p_T = \sqrt{p_x^2 + p_y^2} \tag{1.5}$$

Furthermore, the azimuthal angle ϕ is defined around the beam axis.

1.4.2 Short list of ATLAS sub-detectors

The ATLAS detector is composed by three blocks of sub-detectors:

- *Inner Detector*: the inner tracking system is the sub-detector closest to the beam-pipe. It provides great tracking efficiency for all charged particles, making possible momentum measurements and reconstruction of primary interaction and particle decay vertexes. This system is composed by different detectors: silicon pixel and microstrip (in the inner part of the volume) along with straw tubes sensible to the transition radiation. The detector has a cylindrical shape of about 1.15 m radius and 6.2 m length: these dimensions cover a $|\eta| < 2.5$ pseudorapidity region.

  In order to measure particle's momentum through track curvature, the whole inner detector is immersed in a 2 T solenoidal magnetic field.

- *Calorimeters*: the function of the calorimetric system is to measure energy and position of electrons, photons and hadronic jets coming from the interaction. In order to do this the entering point of a particle and the following shower are measured. The high luminosity conditions and interesting physics events signatures need calorimeters with extremely good performances in terms of granularity, response time and energy resolution. The calorimetric system is composed by two sections: an electromagnetic calorimeter and a hadronic calorimeter. The electromagnetic calorimeter is a sampling calorimeter that uses liquid argon (LAr) as sensible material [41]: it

is divided into two sections, barrel+end-cap calorimeter for region of $|\eta| < 3.2$ and a forward calorimeter covering $3.2 < |\eta| < 4.9$. The hadronic calorimeter is a Iron-Scintillator sampling calorimeter composed by a central cylinder and two side extensions: the hadronic calorimeter's end-caps use the same LAr technology on which is based the electromagnetic calorimeter [42].

- *Muon Spectrometer*: the muon spectrometer is located in the outer part of the ATLAS detector, all around the calorimeters. This detector is immersed in a toroidal magnetic field and is composed by separated layers of wired chambers: in the central ($|\eta| < 1$) region there are three cylindric layers at 5, 7.5 and 10 m of radius, while in the end-cap region ($1 < |\eta| < 2.7$) there are four discs of chambers at 7, 10.8, 14 and 21.5 m from the interaction point.

Detector component	**Required resolution**	**η coverage**	
		Measurement	Trigger
Tracking	$\sigma_{p_T}/p_T = 0.05\%\ p_T \oplus 1\%$	± 2.5	
EM calorimetry	$\sigma_E/E = 10\%/\sqrt{E} \oplus 0.7\%$	± 3.2	± 2.5
Hadronic calorimetry (jets)			
barrel and end-cap	$\sigma_E/E = 50\%/\sqrt{E} \oplus 3\%$	± 3.2	± 3.2
forward	$\sigma_E/E = 100\%/\sqrt{E} \oplus 10\%$	$3.1 < \|\eta\| < 4.9$	$3.1 < \|\eta\| < 4.9$
Muon spectrometer	σ_{p_T}/p_T=10% at p_T = 1 TeV	± 2.7	± 2.4

Table 1.1: General performance goals of the ATLAS detector. Note that, for high-p_T muons, the muon spectrometer performance is independent of the inner-detector system. The units for E and p_T are in GeV

1.4.3 The magnet system

The ATLAS detector makes use of two different magnetic fields: a solenoidal field for the inner tracker detector and a toroidal field for the muon spectrometer. These magnetic fields are generated through an inner solenoid and eight external superconducting toroidal magnets.

- *Solenoid*: the inner solenoid is made up from a coil of superconducting material 5.8 m long, with inner and outer radius of 1.23 and 1.38 m. It is placed between the inner detector and the electromagnetic calorimeter. In order

to minimize the weight of this structure in terms of radiation length (X_0), the winding coil is placed inside the calorimeter's cryostat making a total of $0.83X_0$. This magnet creates a 2 T magnetic field.

- *External Toroids*: the external toroidal magnetic field is generated by a set of eight superconducting coils put into hollow 25.3 m long toroids placed along the beam direction. Every toroid has a separate cryogenic system, while in the end-caps the coils have common cryostat.

1.5 Inner Detector

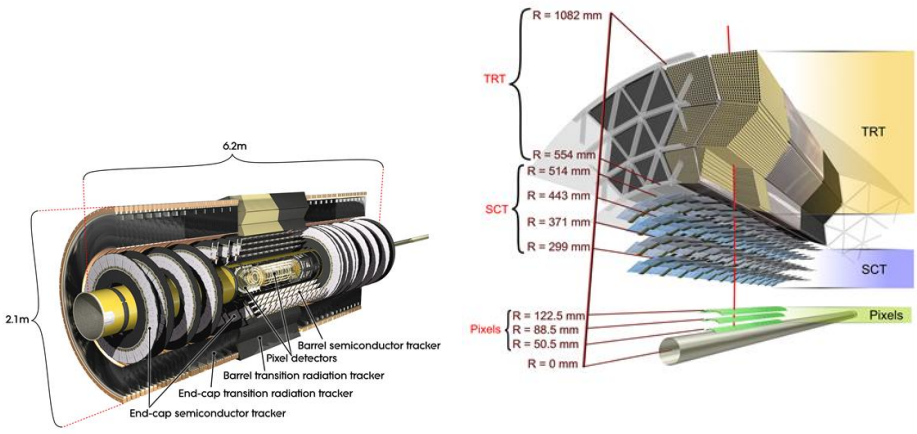

(a) (b)

Figure 1.13: Schematic views of the ATLAS Inner Detector [7]

The Inner Detector is the innermost system of the ATLAS detector. Its schematic view is shown in Figure 1.13. It is composed by three sub-detectors: two silicon detectors, the *Pixel Detector* and the *Semi-Conductor Tracker* (SCT), and the *Transition Radiation Tracker* (TRT). It is immersed in an axial magnetic field of 2 T and its overall dimensions are 2.1 m in diameter and 6.2 m in length and covers a pseudorapidity region of $|\eta| < 2.5$.

The Inner Detector measures tracks from the passage of the charged particles. So it measures charged particles position and, being immersed in a magnetic field,

also their p_T and charge.

A summary of their main characteristics is also reported in table 1.2.

Item		Radial extension (mm)	Length (mm)
Overall ID envelope		$0 < R < 1150$	$0 < \|z\| < 3512$
Beam-pipe		$29 < R < 36$	
Pixel	Overall envelope	$45.5 < R < 242$	$0 < \|z\| < 3092$
3 cylindrical layers	Sensitive barrel	$50.5 < R < 122.5$	$0 < \|z\| < 400.5$
2×3 disks	Sensitive end-cap	$88.8 < R < 149.6$	$495 < \|z\| < 650$
SCT	Overall envelope	$255 < R < 549$ (barrel)	$0 < \|z\| < 805$
		$251 < R < 610$ (end-cap)	$810 < \|z\| < 2797$
4 cylindrical layers	Sensitive barrel	$299 < R < 514$	$0 < \|z\| < 749$
2×9 disks	Sensitive end-cap	$275 < R < 560$	$839 < \|z\| < 2735$
TRT	Overall envelope	$554 < R < 1082$ (barrel)	$0 < \|z\| < 780$
		$617 < R < 1106$ (end-cap)	$827 < \|z\| < 2744$
73 straw planes	Sensitive barrel	$563 < R < 1066$	$0 < \|z\| < 712$
160 straw planes	Sensitive end-cap	$644 < R < 1004$	$848 < \|z\| < 2710$

Table 1.2: Summary of the main characteristics of the three ATLAS Inner Detector sub-detectors [7]

1.5.1 Pixel Detector

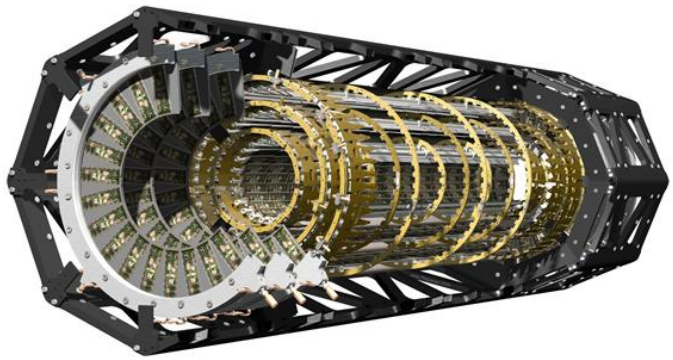

Figure 1.14: The ATLAS Pixel Detector [7]

The ATLAS Pixel Detector (figure 1.14) is the nearest system to the collision

point and it is built directly onto the beryllium beam pipe in order to provide the best possible primary and secondary vertex resolution. It was designed to operate in the high particle multiplicity of LHC, maintaining high efficiency and an excellent position resolution in the $r - \phi$ plane of < 15 μm, as well as a time resolution of less than the 25 ns collision rate of the LHC. After 3 years of operation, at the time of writing, the detector performance is excellent with a hit detection efficiency of $\sim 96\%$.

Built as a three-hit system for pseudorapidity $|\eta| < 2.5$, it consists of three cylindrical barrel layers with 1456 modules and two end-caps with three disks each having a total of 288 modules. The total number of readout channels is approximately 80×10^6. The barrel layers have radii of 50.5 mm (b-layer), 88.5 mm (layer-1) and 122.5 mm (layer-2) and are 800 mm long.

Operation at the LHC imposed a requirement for a radiation tolerance up to 500 kGy for a fluence of 10^{15} 1 MeV n_{eq}/cm^2 and the adoption of an evaporative C_3F_8-based cooling integrated in the modules supports to keep a low leakage current and remove the heat generated by the electronics.

The detector is operated at a coolant temperature of -20°C (corresponding in average to -13°C on detector) since Summer 2009; the cooling system is able to operate down to a coolant temperature of -30°C and this temperature setting will be exploited only later in the detector life when the radiation damage effects will be more important.

A pixel module consists of a 250 μm thick sensor with n^+ pixels implanted on the n-doped bulk with a p^+ backplane on the opposite side, 16 Front-End chips bump-bonded to this sensor and a module controller chip (MCC). Each module has an active area of 16.4×60.8 mm^2 consisting of 47232 (328×144) pixels. The typical pixel size is 50×400 μm^2. To enable full coverage in the regions between front-end chips, approximately 10% of the sensor pixels have a size of 600×50 μm^2 (long pixels). The 16 chips read out in total 46080 channels, but all 47232 pixels are readout, as pixels in the inter-chip regions are ganged to be read out. In order to fully deplete the semi-conductor a bias voltage 150 to 600 V can be applied.

The Pixel Detector has been participating to the ATLAS data taking periods with an efficiency of 99.5% or better, where the small percentage below 100% is mainly due to the switch on time once the "stable beams" condition is declared. The percentage of active modules in data taking in 2011 is 95.9%. In total the number of

disabled modules is 72 out of the total 1744 modules. In addition there are 47 non working front-end chips distributed in the detector. The current understanding of the failures brings to the conclusion that the detector is sensitive to the temperature oscillations during cooling failures or maintenance. For these reasons the cooling is kept always operational and solutions are being investigated to moderate the temperature gradients in the event of cooling failures. The percentage of failures increased from 2.1% to the current 4.1% level during the past ~ 4 years.

During these three years of continuous operations the detector has been regularly calibrated to provide the best possible performance. The calibration stability is quite high and that allows to have long period of intense data taking without the need of corrections. At present time the threshold is set to the value of 3500 e^- with a dispersion of $\sim$ 40 e^- and a fraction of masked pixels around 0.1%. The noise has been measured to be approximately 170 e^- for most pixels, being slightly higher ($\sim$300 e^-) for long and ganged pixels. The noise occupancy as low as 10^{-9} hits per pixel per event allows the reconstruction of very clearly defined clusters without worrying about noise effects. There are nearly 500 reconstructed hits/event in the b-layer and despite the very high pile-up level, the Pixel Detector occupancy[5] is still small.

When a charge deposited in the sensor is above the discriminator threshold, the front-end electronics stores the Time-over-Threshold (ToT) quantity, i.e. the time during which the pre-amplifier output is above threshold. By design the ToT has a nearly linear dependence on the amplitude of the pre-amplifier output and therefore on the charge released in the sensor. The ToT response is calibrated and tuned, via charge injections, to have a homogeneous response for a signal of 20 ke^-, corresponding to the most probable value for the charge deposited by one m.i.p. in the silicon sensor. A ToT target value of 30, in bunch crossing (BC) units (1 BC = 25 ns), is used.

The measurement of the deposited charge, obtained with the calibration of the ToT, allows several improvements for the detector performance, like the position resolution where the improvement is obtained by weighting properly the pixel hit in cluster position reconstruction with a charge sharing algorithm. It is also worth mentioning that the hit-to-track association efficiency is at the level of 99% for

[5]The Pixel Detector occupancy is defined as the fraction of detector channels with a hit in a local area

nearly all detector parts with a lower efficiency for one of the end-cap disks due to few defects on individual modules.

Another important application of the ToT information is the determination of the specific energy loss dE/dx with a resolution of 12%.

The Pixel Detector operates in a solenoidal field of 2 T, therefore the Lorentz angle needs to be determined with good accuracy, by measuring the mean cluster size as a function of the track incident angle. The measured value of $\theta_L = (211.3 \pm 1.6)$ mrad is close to the expected value of 225 mrad (see further details in section 2.3.8).

In addition it is possible to use the Pixel Detector to measure the behavior of the Lorentz angle with the temperature, i.e. the temperature dependence of the electron mobility. The measured value of (-0.78 ± 0.18) mrad/K is in agreement with the theoretical expectation of -0.74 mrad/K. Furthermore, the excellent performance of the Pixel Detector leads to accurate measurements of tracks' parameters.

Using the secondary vertices map for hadronic interactions it is possible to build a nice "hadro-graphy" of the entire detector with a very accurate material mapping. For example, this has applications in λ_l measurements and in positioning of non-sensitive material (beam pipe, support structures).

1.5.2 Semi-Conductor Tracker (SCT)

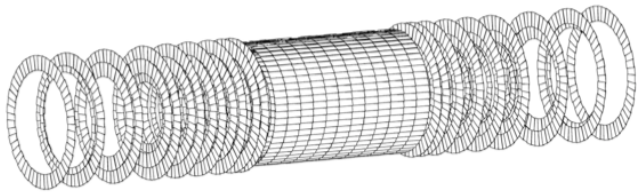

Figure 1.15: Geometrical layout of the SCT [7]

The SCT is the second element of the tracking system, going from the beam pipe outwards. It is composed by four cylinders in the barrel region covering the pseudorapidity range $|\eta| < 1.1 - 1.4$, with radii between 299 mm and 514 mm and a full length of 1492 mm. Each of the two end-caps consists of 9 disks (figure 1.15) covering pseudorapidity range $1.1 - 1.4 < |\eta| < 2.5$ and radii extending to 56

cm. It provides typically eight strip measurements (four space-points) for particles originating in the beam-interaction region.

The SCT comprises 61 m^2 of silicon sensors with 6.3 million readout channels. It operates in a near zero humidity nitrogen environment and is cooled nominally to -7°C by a C_3F_8 evaporative cooling system, to suppress reverse annealing arising from radiation damage.

The silicon sensors are all 285 μm thick single-sided p-on-n devices, with 768 AC-coupled micro-strips. There are 8448 identical rectangular shaped barrel sensors with size 64.0×63.6 mm and 80 μm strip pitch. The end cap disks use wedge shaped sensors of five slightly different sizes to accommodate the more complex geometry. There are 6944 wedge sensors in total, with strip pitch ranging from 56.9 to 90.4 μm.

The basic granularity is the silicon module. There are 2112 identical rectangular shaped modules used to construct the barrel cylinders, and 1976 wedge shaped modules of three different sizes used to construct the end-cap disks. Modules consist of two pairs of back-to-back sensors, glued to a thermally conductive substrate for mechanical and thermal stability. Pairs on opposite sides are rotated by 40 mrad to form a stereo angle in order to enable a resolution measurement in the direction parallel to the strips. The sensor micro-strips are wire bonded across to form effectively 12 cm long strips.

More than 99% of the SCT strips have remained fully functional and available for tracking throughout all data taking periods. The number of disabled strips (typically due to high noise or un-bonded channels) and non-functioning chips is negligible and the largest contribution is due to disabled modules (total fraction: 0.73%). Half of the disabled modules are due to one cooling loop permanently disabled as a result of an inaccessible leak in that loop. Fortunately this affects one quadrant of one of the outermost end-cap disks, and has negligible impact on tracking performance. The remaining modules are predominantly due to on-detector connection issues.

The intrinsic accuracies of the SCT are 17 μm in the azimuthal direction and 580 μm along the beam direction, while the intrinsic hit efficiency is determined by counting the number of recorded hits on high p_T tracks (> 1 GeV/c) through the SCT by the number of possible hits, after ignoring known disabled strips. The nominal design requirement was for hit efficiency to be $> 99\%$. The barrels have

a mean hit efficiency of 99.9% over all layers. Similarly, the hit efficiencies for the SCT end-caps are measured to be 99.8%.

1.5.3 Transition Radiation Tracker (TRT)

The TRT is the outermost system of the Inner Detector. Its sensitive volume covers radial distances from 563 mm to 1066 mm. It consists of drift tubes with a 4 mm diameter that are made from Wound Kapton (straw tubes) and reinforced with thin carbon fibers. In the centre of each tube there is a gold-plated tungsten wire of 31 μm diameter. With the wall kept at a voltage of -1.5 kV and the wire at ground potential, each tube acts as a small proportional counter. The tubes are filled with a gas mixture of 70% Xe, 27% CO_2, and 3% O_2.

The TRT barrel region contains 52544 straw tubes of 1.5 m length, parallel to the beam axis, arranged in three cylindrical layers and 32 ϕ sectors. They cover a radius from 0.5 m to 1.1 m and a pseudorapidity range of $|\eta| < 1$. The central wires are electrically split and read out at both ends of the straw. The end-caps contain radial 0.4 m long straws that are arranged perpendicular to the beam axis. Each side consists of 122880 straws, covering the geometrical range 0.8 m$< |z| <$ 2.7 m and $1 < |\eta| < 2$. The end-cap straws are read out at their outer end.

When a charged particle traverses the TRT, it ionizes the gas inside the straws. The resulting free electrons drift towards the wire where they are amplified and read out. The front-end electronics sample the incoming signal in 24 time bins of 3.12 ns and compare it against a threshold corresponding to 300 eV, resulting in a 24-bit pattern that gets buffered in a digital pipeline and then passed on to the central ATLAS data acquisition.

The spaces between the straws are filled with polymer fibers (barrel) and foils (end-caps) to create transition radiation, which may be emitted by highly relativistic charged particles as they traverse a material boundary. This effect depends on the relativistic factor $\gamma = E/m$ and is strongest for electrons. Typical photon energies are 5-30 keV. These soft X-rays can be absorbed by Xe atoms, depositing additional energy in the gas and leading to significantly higher readout signals. Such signals are detected by comparing them against an additional high threshold of 6 keV that is sampled in three 25 ns time bins alongside the pattern described before.

This design makes the TRT complementary to the silicon-based tracking devices: the single-point resolution of 120 μm is larger than that of the silicon trackers, but this is compensated by the large number of hits per track (typically more than 30) and the long lever arm.

The TRT readout data merely contains time information, which needs to be calibrated to be useful for tracking. The first step is the T_0 calibration, defining the offset between the start of the readout and the arrival of particles. It accounts for the time of flight, the signal propagation, and clock offsets. Its results are subject to small daily variations on the level of 100 ps, which are mainly caused by a drift of the central ATLAS clock.

The $R(t)$ calibration relates the measured drift time with a particle's distance of closest approach to the readout wire. It depends on the properties of the active gas (mixture, pressure, temperature), the voltage that is applied to the tube, and the magnetic field. The $R(t)$ relation is modeled by a third-order polynomial. The resulting coefficients turn out to be very stable on the time scale of months. This is due to the TRT's "Gas Gain Stabilization System", which automatically adjusts the applied voltages to compensate for small variations of the other gas parameters, and also a precise monitoring of the composition of the gas mixture.

A key ingredient for maximum tracking performance is the alignment of all detector elements. Such effects are cured by a track-based wire-by-wire alignment. Using the alignment data of autumn 2010, residual widths of 118 μm and 132 μm can be achieved for the barrel and end-cap regions respectively, applying a cut of $p_T > 15$ GeV. Providing an average of 30 such position measurements, the TRT contributes significantly to the tracking performance of the Inner Detector as a whole, particularly at high p_T.

The fact that the emission of transition radiation is much more likely for an electron than for a pion of the same momentum can be used to discriminate these particle types. The probability of getting a high-threshold as a function of a particle's relativistic γ factor is low for pions over a large momentum range (and almost entirely due to Landau fluctuations), but it rises quickly for electrons with momenta of only few GeV. This allows electron-hadron discrimination up to energies of 150 GeV.

Another source of information for the particle identification is the time over threshold (ToT), i. e. the number of time bins for which a readout signal exceeds

the (low) threshold. This quantity depends on the particle's specific energy loss dE/dx, which in turn depends on the relativistic velocity β according to the Bethe-Bloch law.

1.5.4 Inner Detector performance

1.5.4.1 Track reconstruction

Reconstruction of tracks and measurement of their parameters is mandatory for most physics analyses. In particular, the impact parameters and momentum of charged particles have to be measured with high precision. Tracks are reconstructed within the full ID acceptance range ($|\eta| < 2.5$) using a χ^2 fitter. The pattern recognition [43] works primarily inside-out, associating first the silicon hits and then extrapolating to the TRT to include its measurements. Though there is also an outside-in tracking, which uses the TRT track segments seeds plus and inward extension in order to efficiently reconstruct tracks with secondary interactions. The pattern recognition selects first very loose track candidates and then a stringent ambiguity processor selects good track candidates (figure 1.16). Only those satisfying a minimum number of silicon hits and a cut in the transverse and longitudinal impact parameter with respect to the beam spot are kept. The tracking has been performed down to p_T as low as 100 MeV [44] with efficiency shown in figure 1.17.

Heavy ion conditions give also the opportunity to study tracking under high occupancy conditions, comparable to the ones expected in future high luminosity LHC upgrades. Under these conditions tighter requirement need to be applied [45].

1.5.4.2 Vertex reconstruction

Measured tracks are used to reconstruct the interaction point and secondary vertices from particle decays and interactions with detector material. Excellent performance of the vertex reconstruction is mandatory for many applications like b-tagging or the identification and rejection of pile-up, where many proton-proton collisions occur in the same beam crossing. This is especially relevant at the high peak luminosity of 3.65×10^{33} cm^{-2}s^{-1} reached in 2011 which corresponded on average to 17 interactions per crossing.

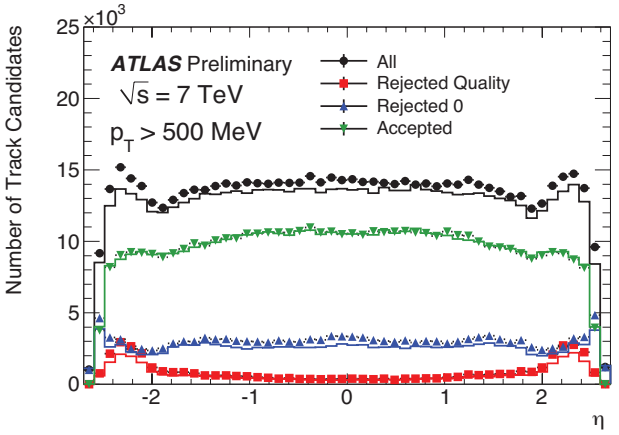

Figure 1.16: $p_T > 500$ MeV. Number of track candidates as a function of η and at different stages of the track finding: entering the ambiguity solver (black), rejected because they are assigned a track score of zero (blue), rejected because of quality cuts (red) and accepted as resolved tracks (green) in the different stages inside the ambiguity solver in data and simulation. The number of track candidates in data are shown as markers and the simulation as histograms [43]

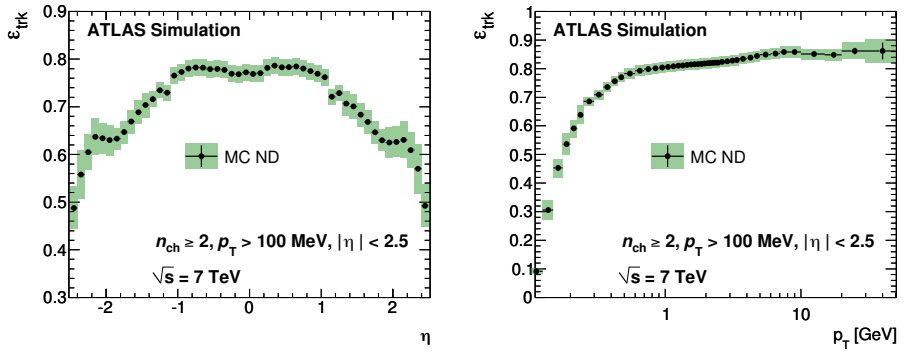

(a) (b)

Figure 1.17: Track reconstruction efficiency as a function of η (left) and of p_T (right) extracted from non-diffractive MC [44]

The ATLAS vertex reconstruction works using an iterative algorithm [46]: first a vertex finder is executed where tracks are associated to a primary vertex and in the second stage the vertex is fitted (with a χ^2 technique). The vertex fitter include a beam-spot constraint, which is routinely online and offline computed. It is approximatively 15 μm in the transverse plane, and 5.7 mm in the longitudinal plane as shown in figure 1.18. The primary vertex resolution is extracted using a data driven method (mainly split vertex technique [46]). It is about 23 μm on the transverse plain and about 40 μm on the longitudinal plane for vertices with 70 tracks. It depends on the number of tracks as well as on the $\sqrt{\sum_{\text{trk}} p_T^2}$. The vertex reconstruction efficiency is sample dependent in fact nearby vertices can shadow a clean reconstruction. The expected vertex reconstruction efficiency is $\sim 95\%$ for non-diffractive events.

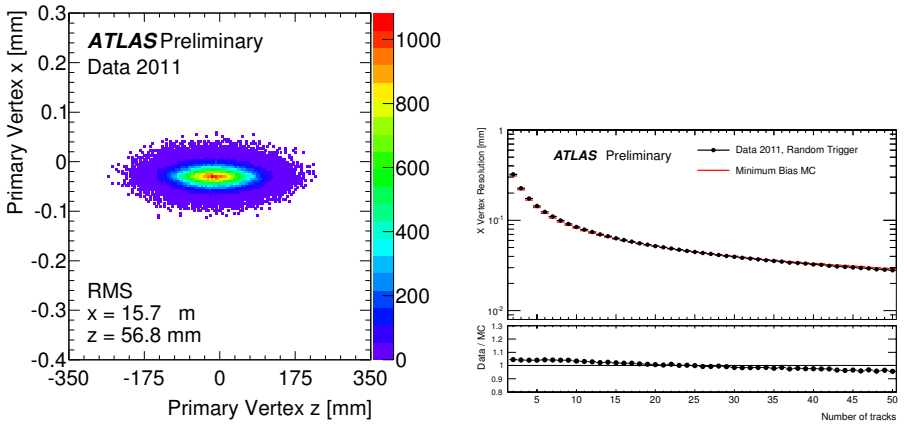

(a) (b)

Figure 1.18: Two dimensional distribution of reconstructed primary vertices in the (x, z) plane (left), and the estimated vertex resolution σ_X as a function of tracks per vertex (right) [47]

An excellent vertex resolution has been achieved also for secondary vertices: from MC studies, for a hadronic interaction, the vertex resolution has been estimated to be 200-300 μm (in both R and z) for reconstructed vertices with radii $\leq$ 100 mm and $\sim$ 1 mm at larger radii [48]. Simulations have been used also to study higher pile-up scenarios.

1.5.4.3 Material studies

The precise knowledge of the material budget within the tracking volume is mandatory for an accurate track reconstruction and a precise determination of the track parameters. Mapping of the amount of passive material in the tracking volume is mainly performed using photon conversions and hadronic interactions [48, 49] (figure 1.19). The comparison between real data and simulation of the spatial distribution of the reconstructed secondary vertices (either with photon conversions or hadronic interactions) helps to improve the description of material in the detector geometry. In the same sense, the rate of photon conversions inside the tracker volume compared with the beryllium beam pipe (very well known object) helps to assess the amount of material inside the real detector. The material uncertainty in simulation is constrained summing photon conversions and hadronic interactions with other different techniques (e.g. study of K^0 and other mass signals, study of multiple scattering resolution term, etc.). The estimated uncertainty is better than $\sim 5\%$ in the central region and at the level of $\sim 10\%$ in the end-caps.

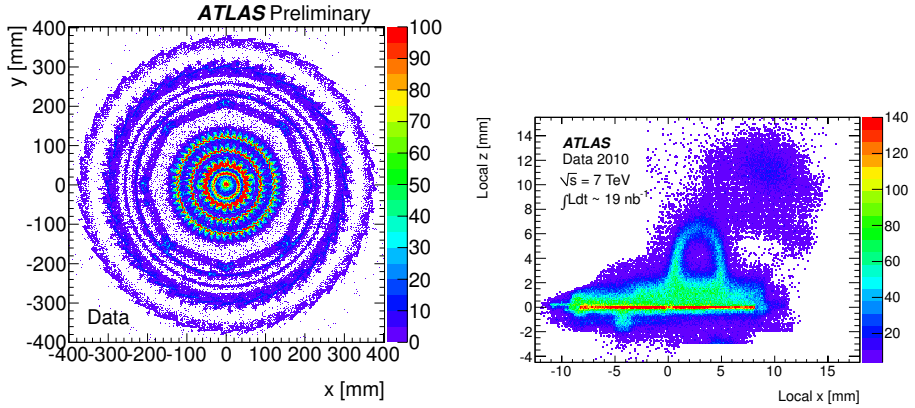

(a) (b)

Figure 1.19: Distribution of the reconstructed photon conversions for data events as a function of the transverse positions (x, y) (left), and of the reconstructed hadronic interactions for data events in the local coordinate system for the first pixel detector layer (right) [48, 49]

1.5.4.4 Inner Detector alignment

The limited knowledge of the relative position of detector pieces should not lead to a significant degradation of the track parameter measurement/resolution beyond the intrinsic tracker resolution, nor introduce biases. Thus the goal of the alignment is to provide an accurate description of the geometry of the detector: the location and orientation of every tracking element. A very high accuracy is needed for precision physics measurements, e.g. a 15 MeV precision in W mass requires a $\sim 1\mu$m alignment [7].

The ID has been aligned using a track based method [50]. It consists in a χ^2 minimization of the track-hit residuals. The alignment procedure has been executed at 3 different levels in accordance with the assembly of the ID structures, i.e. with increasing number of aligned substructures proceeding from large structures to module level with increasing granularity of structures and degrees of freedom. The level 1 corresponds to the large barrel and end-cap structures of the Pixel, SCT and TRT (just 7 structures to align) . The level 2 deals with the barrel layers and end-cap disks of the Pixel and SCT (31 structures) and the barrel modules and end-cap wheels of the TRT (176 structures). Finally, the level 3 aligns each pixel and SCT modules (5,832) and TRT straw tubes (350k). In total, one has to deal with more than 700k degrees of freedom. The alignment is monitored on a run by run basis. There are two dedicated data streams selected by the high level trigger: a collection of high p_T and isolated collision tracks and cosmic-ray tracks triggered during the empty LHC bunches [51]. With a run-by-run alignment one can test the detector stability (figure 1.20 left). Large movements of the detector are due to changes in operational conditions (typical size < 10 μm) after hardware incidents. In between these periods little (< 1 μm) movement is observed indicating that the detector is generally very stable. In order to derive the alignment constants over many data taking periods an offline alignment is run. The alignment software allows to set constraints from the beam spot, assembly survey data [52], momentum of the muons from the Muon Spectrometer and E/p from electrons.

A very detailed alignment validation program is executed, which comprises a detailed check of many alignment specific distributions (as the residuals of all components) and checks for track parameters and their errors. The resonance invariant masses (light as K^0_s and heavy as Z) are scrutinized against all the track

parameters in order to detect and correct possible biases (figure 1.20 right).

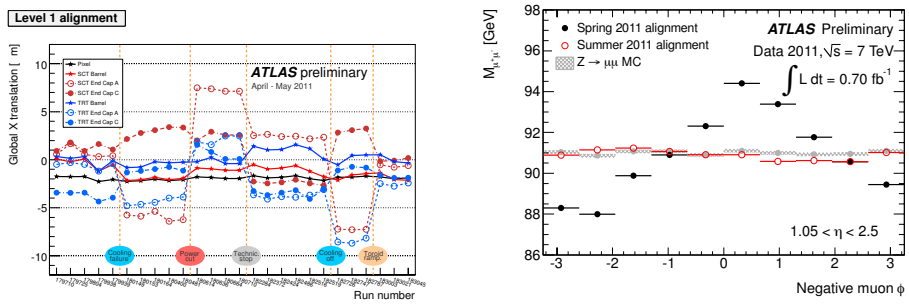

(a) (b)

Figure 1.20: Subsystem level, "Level One", alignment corrections performed on a run by run basis starting from a common set alignment constants (left), and mean Z invariant mass versus ϕ for negative muons (right) [47]

1.6 Calorimeters

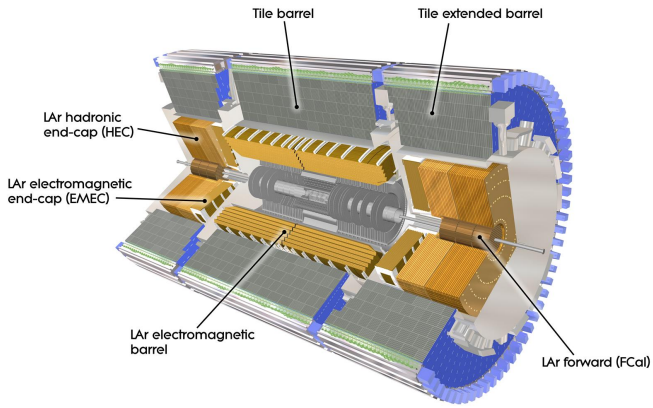

Figure 1.21: Schematic view of the ATLAS Calorimetric system [7]

The calorimeter system includes both the Electromagnetic (EM) Calorimeter and the Hadronic (Had) Calorimeter. The first is dedicated to the measurement of

electrons and photons, the latter to the measurement of hadrons. These calorimeters cover the range $|\eta| < 4.9$, using different techniques suited to the widely varying requirements of the physics processes of interest and of the radiation environment over this large η-range. A schematic view of the calorimeter system is shown in figure 1.21.

The main purpose of the calorimeters is to measure the energy of the particles and their position. One of the most important requirements for calorimeters is to provide good containment for electromagnetic and hadronic showers: the number of jets reaching the muon system (punch-through) has to be limited in order to have a good muon identification. Therefore, calorimeter depth is an important consideration. The total thickness of the EM calorimeter is more than 22 radiation lengths (X_0) in the barrel and more than 24 X_0 in the end-caps. It contains electrons and photons showers up to $\sim$ 1 TeV and it also absorbs almost 2/3 of a typical hadronic shower. The approximate 9.7 (10) interaction lengths λ of active calorimeter (EM + Had) in the barrel (end-caps) are adequate to provide good resolution for high-energy jets. The total thickness, including 1.3 λ from the outer support, is 11 λ at $\eta = 0$ and has been shown both by measurements and simulations to be sufficient to reduce punch-through well below the irreducible level of prompt or decay muons.

The ATLAS calorimetry is non-compensating, meaning that a hadron will deposit a smaller fraction of its energy in the active portion of the calorimeter, on average, than an electron or photon will. The difference must be taken into account by an additional correction applied to hadronic objects. There are several ways to select hadronic objects and correct their energy.

Some details on the different calorimeter regions are given below, and its nominal performance goals are summarized in table 1.3

1.6.1 EM Calorimeter

The EM calorimeter is a lead liquid Argon (LAr) detector. To ensure the maximum azimuthal coverage the EM Calorimeter was designed with an accordion geometry, as shown in figure 1.22: the readout electrodes and the lead absorbers are laid out radially and folded so that particles can not cross the calorimeter without being detected. It is divided into one barrel part ($|\eta| < 1.475$) and two end-caps

Detector component	Required resolution (σ_E/E)	η coverage
EM calorimeter	$10\%\sqrt{E} \oplus 0.7\%$	± 3.2 (± 2.5 for the trigger)
Had calorimeter		
barrel and end-cap	$50\%\sqrt{E} \oplus 3\%$	± 3.2
forward	$100\%\sqrt{E} \oplus 3.1\%$	± 4.9

Table 1.3: Nominal calorimeters' performance goals and coverage for the ATLAS detector [7]

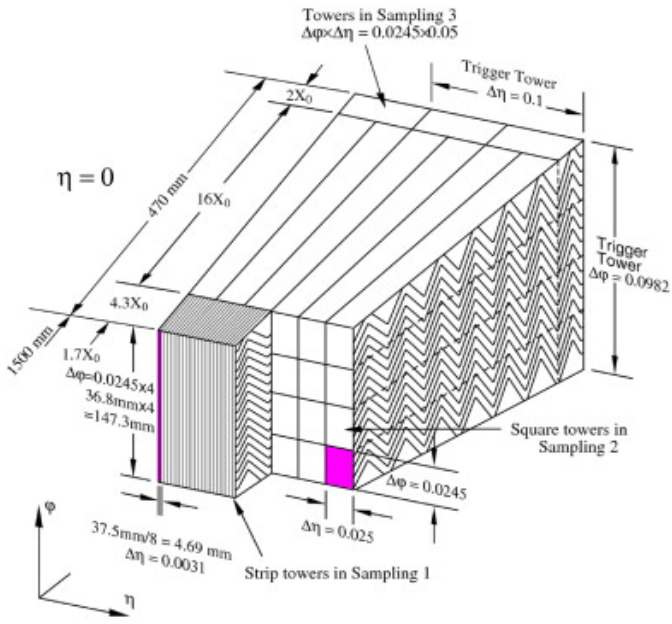

Figure 1.22: Schematic view of the accordion geometry [7]

($1.375 < |\eta| < 3.2$), each one with its own cryostat. The position of the central solenoid in front of the EM calorimeter demands optimization of the material in order to achieve the desired calorimeter performance. As a consequence, the central solenoid and the LAr calorimeter share a common vacuum vessel, thereby eliminating two vacuum walls. The barrel calorimeter consists of two identical half-barrels, separated by a small gap (4 mm) at $z = 0$. Each end-cap calorimeter is mechanically divided into two coaxial wheels: an inner wheel covering the region $1.375 < |\eta| < 2.5$, and an outer wheel covering the region $2.5 < |\eta| < 3.2$.

Over the region devoted to precision physics ($|\eta| < 2.5$), the EM calorimeter is segmented into three longitudinal sections: strips, middle and back. While most of the energy of electrons and photons is collected in the middle, the fine granularity of the strips is necessary to improve the $\gamma - \pi^0$ discrimination and the back measures the tails of highly energetic electromagnetic showers, and helps to distinguish electromagnetic and hadronic deposits. For the end-cap inner wheel, the calorimeter is segmented in two longitudinal sections and has a coarser lateral granularity than for the rest of the acceptance.

Because most of the central calorimetry sits behind the cryostat, the solenoid, and the 1-4 radiation-lengths thick Inner Detector, EM showers begin to develop well before they are measured in the calorimeter. In order to measure and correct for these losses, up to $|\eta| = 1.8$ there is an additional pre-sampler layer in front of the sampling portion (i.e. accordion) of the calorimetry. The pre-sampler is 11 mm (5 mm) thick in the barrel (end-cap) and includes fine segmentation in η. Unlike the rest of the calorimetry, the pre-sampler has no absorber layer. In practice, it behaves almost like a single-layer LAr tracker.

The transition region between the barrel and the end-cap EM calorimeters, $1.37 < |\eta| < 1.52$, is expected to have poorer performance because of the higher amount of passive material in front of the calorimeter, this region is often referred as crack region.

The LAr electronic calibration is done using pulse height samples, while the tiles signal is monitored in different ways. Cesium sources, which can scan across the detector, have been installed to check its response (the ratio of the reconstructed signal to the "true" signal). Charge can be injected into a single cell to test and calibrate the read-out electronics and finally lasers can provide light to test the optical connections and photomultiplier tubes response.

1.6.2 Had Calorimeter

The Had Calorimeter is realized with a variety of techniques depending on the region: central, end-cap and forward. In the central region there is the Tile Calorimeter (Tile), which is placed directly outside the EM Calorimeter envelope.

The Tile is a sampling calorimeter which uses steel as absorber and scintillating tiles as active material. It is divided into a barrel ($|\eta| < 1.0$) and two extended barrels ($0.8 < |\eta| < 1.7$). Radially, the Tile goes from an inner radius of 2.28 m to an outer radius of 4.25 m. It is longitudinally segmented in three layers approximately 1.5, 4.1 and 1.8 interaction lengths thick for the barrel and 1.5, 2.6, and 3.3 interaction lengths for the extended barrel.

The Hadronic End-cap Calorimeter (HEC) consists of two independent wheels per end-cap, located directly behind the end-cap EM calorimeter and sharing the same LAr cryostats. It covers the region $1.5 < |\eta| < 3.1$, overlapping both with the Tiles and the Forward Calorimeter. The HEC uses the LAr technology. Each wheel is divided into two longitudinal segments, for a total of four layers per end-cap. The wheels closest to the interaction point are built from 25 mm parallel copper plates, while those further away use 50 mm copper plates. The outer radius of the copper plates is 2.03 m, while the inner radius is 0.475 m (except in the overlap region with the forward calorimeter where this radius becomes 0.372 m). The copper plates are interleaved with 8.5 mm LAr gaps, providing the active medium for this sampling calorimeter.

1.6.3 Forward Calorimeter

The Forward Calorimeter (FCal) covers the $3.1 < |\eta| < 4.9$ region and is another LAr based detector. It is integrated into the end-cap cryostats, it is approximately 10 interaction lengths deep and consists of three 45 cm thick independent modules in each end-cap: the absorber of the first module is copper, which is optimized for electromagnetic measurements, while for other two is tungsten, which is used to measure predominantly the energy of hadronic interactions.

The region where the FCal is set is very close to the beam pipe, so the expected radiation dose is very high. Therefore the electrode structure is different from the accordion geometry, consisting in a structure of concentric rods and tubes parallel to the beam axis. The LAr in the gap between the rod and the tube is the sensitive

medium.

1.7 Muon Spectrometer

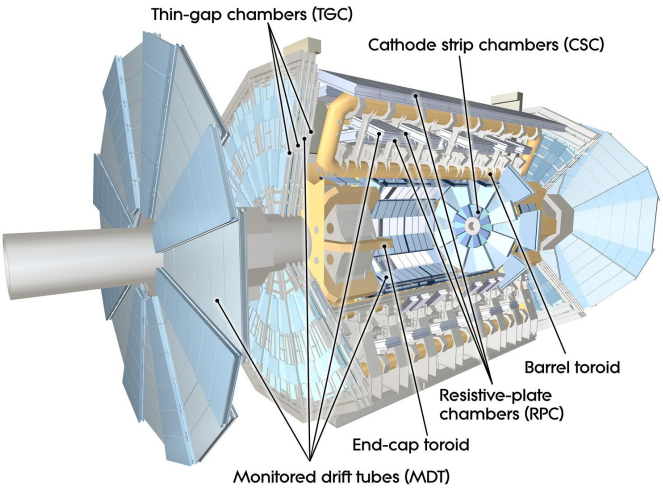

Figure 1.23: Schematic view of the ATLAS Muon Spectrometer [7]

The layout of the Muon Spectrometer is shown in figure 1.23. The muon system has two different functions: it is needed for high precision tracking of muons and also for triggering on them. Muons frequently indicate an interesting event, and, therefore, a muon-based trigger is useful for selecting some new physics signals. On the other hand, in order to precisely measure the decays of new particles, it is necessary to make accurate measurements of each muon's momentum. The momentum measurement is based on the magnetic deflection of muon tracks. Such a large volume magnetic field, which is necessary to bend the particle trajectories, is provided by the large barrel toroid in the region $|\eta| < 1.4$, by two smaller end-cap magnets in the $1.6 < |\eta| < 2.7$ region and by a combination of the two in the transition region ($1.4 < |\eta| < 1.6$). This magnet configuration provides a field which is mostly orthogonal to the muon trajectories, while minimizing the degradation of the resolution due to multiple scattering.

Because the toroidal magnet system of the Muon Spectrometer is completely independent of the solenoid in the Inner Detector, ATLAS is able to acquire two

independent measurements of a muons momentum. The measurement is performed over most of the η-range by the Monitored Drift Tubes (MDT). At large pseudorapidities and close to the interaction point, Cathode Strip Chambers (CSC) with higher granularity are used: they have been designed to withstand the demanding rate and background conditions. The stringent requirements on the relative alignment of the muon chamber layers are obtained by the combination of precision mechanical-assembly techniques and optical alignment systems both within and between muon chambers.

Concerning the triggering function of the muon system, it covers the pseudorapidity range $|\eta| < 2.4$. Resistive Plate Chambers (RPC) are used in the barrel and Thin Gap Chambers (TGC) in the end-cap regions. The trigger chambers for the Muon Spectrometer serve a three-fold purpose: to provide the bunch-crossing identification, to provide a well-defined transverse momentum thresholds and to measure the muon coordinate in the direction orthogonal to that determined by the precision-tracking chambers. The barrel chambers are positioned on three cylinders concentric with the beam axis, at radii of about 5, 7.5, and 10 m. They cover the pseudorapidity range $|\eta| < 1$. The end-cap chambers cover the range $1 < |\eta| < 2.4$ and are arranged in four disks at distances of 7, 10, 14, and 21-23 m from the interaction point, concentric with the beam axis.

The reconstruction efficiency and resolution of the Muon Spectrometer were measured using cosmic ray events in 2008 and 2009 [53]. The reconstruction efficiency, integrated over the detector acceptance, is $\sim 94\%$. At $|\eta| = 0$ there is a gap in the detector for cable routing. If the region of the detector near this crack is excluded, the reconstruction efficiency is increased to 97%. The transverse momentum resolution was determined from this data to be

$$\frac{\sigma_{p_T}}{p_T} = \frac{0.29 \text{ GeV}}{p_T} \oplus 0.043 \oplus 4.1 \times 10^{-4} \text{ GeV}^{-1} \times p_T \tag{1.6}$$

for transverse momentum (p_T) between 5 and 400 GeV.

1.8 Forward detectors

One measurement which is very important for almost every physics analysis is the luminosity measurement [54]. As it is a fundamental quantity, three different

detectors help in its determination. At ±17 m from the interaction region there is the LUminosity measurement using Cerenkov Integrating Detector (LUCID). It detects inelastic proton-proton scattering in the forward direction and it is the main online relative-luminosity monitor for ATLAS.

It is also used, before collisions are delivered by the LHC, to check the beam losses. For the beam monitoring, also another detector has been inserted: the Beam condition Monitor (BCM).

The other detector used for luminosity measurement is called Absolute Luminosity For ATLAS (ALFA). It is located at ±240 m from the interaction point. It consists of scintillating fibre trackers located inside Roman pots which are designed to approach as close as 1 mm from the beam.

The last detector is Zero-Degree Calorimeter (ZDC). It is located at ±140 m from the interaction point, just beyond the point where the common straight-section vacuum-pipe divides back into two independent beam-pipes. The ZDC modules consist of layers of alternating quartz rods and tungsten plates which measure neutral particles at pseudorapidities $|\eta| \geq 8.2$.

1.9 Trigger, readout, data acquisition and control systems

The Trigger and Data Acquisition (collectively TDAQ) systems, the timing and trigger-control logic, and the Detector Control System (DCS) are partitioned into sub-systems, typically associated with sub-detectors, which have the same logical components and building blocks.

The design luminosity of 10^{34} cm^{-2}s^{-1}, in combination with the bunch crossing rate of 40 MHz and the amount of protons contained in each single bunch, leads to a proton-proton collision rate in the GHz regime. This corresponds to an extremely high theoretical raw data rate of about 1.5 PBs^{-1}. Being able to store only a fraction of this amount of data on storage media ($\sim 300 - 500$ MBs^{-1}) and only a small fraction of these collisions being useful for analysis, the ATLAS trigger system [55] has been designed to reduce the initial data rate by several orders of magnitude. Figure 1.7 shows the total rates of several physics processes in comparison to the total interaction rate. As an example, the frequency of the Standard Model $t\bar{t}$

production at $\sqrt{s} = 7$ TeV is of the order of 0.16 Hz, constituting only a small fraction of the total amount of the raw data rate, making the selection of this and other physics processes a crucial task.

In order to achieve such a reduction and to select only relevant physics events/processes, ATLAS uses a three-level trigger system for real-time event selection (with the last two levels being referred to as high-level trigger), while each trigger level refines the decisions of its predecessor applying, where necessary, additional selection criteria. The three levels of the trigger system are : L1, L2, and the Event Filter (EF). The first level uses a limited amount of the total detector information to make a decision in less than 2.5 μs, reducing the rate to about 75 kHz. The two higher levels access more detector information for a final rate of up to 200 Hz with an event size of approximately 1.3 Mbyte.

1.9.1 Trigger system

The L1 trigger searches for high transverse-momentum muons, electrons, photons, jets, and τ-leptons decaying into hadrons, as well as large missing and total transverse energy. Its selection is based on information from a subset of detectors. High transverse-momentum muons are identified using trigger chambers in the barrel and end-cap regions of the spectrometer. Calorimeter selections are based on reduced-granularity information from all the calorimeters. Results from the L1 muon and calorimeter triggers are processed by the central trigger processor, which implements a trigger menu made up of combinations of trigger selections. Pre-scaling of trigger menu items is also available, allowing optimal use of the bandwidth as luminosity and background conditions change. Events passing the L1 trigger selection are transferred to the next stages of the detector-specific electronics and subsequently to the data acquisition via point-to-point links. In each event, the L1 trigger also defines one or more Regions-of-Interest (RoI), i.e. the geographical coordinates in η and ϕ, of those regions within the detector where its selection process has identified interesting features. The RoI data include information on the type of feature identified and the criteria passed, e.g. a threshold. This information is subsequently used by the high-level trigger.

The L2 selection is seeded by the RoI information provided by the L1 trigger over a dedicated data path. L2 selections use, at full granularity and precision, all

the available detector data within the RoI's (approximately 2% of the total event data). The L2 menus are designed to reduce the trigger rate to approximately 3.5 kHz, with an event processing time of about 40 ms, averaged over all events.

The final stage of the event selection is carried out by the Event Filter, which reduces the event rate to roughly 400 Hz. Its selections are implemented using offline analysis procedures within an average event processing time of the order of four seconds.

1.9.2 Readout architecture and data acquisition

The Readout Drivers (ROD's) are detector-specific functional elements of the front-end systems, which achieve a higher level of data concentration and multiplexing by gathering information from several front-end data streams. Although each sub-detector uses specific front-end electronics and ROD's, these components are built from standardized blocks and are subject to common requirements. The front-end electronics sub-system includes different functional components:

- the front-end analogue or analogue-to-digital processing
- the L1 buffer in which the (analogue or digital) information is retained for a time long enough to accommodate the L1 trigger latency
- the derandomising buffer in which the data corresponding to a L1 trigger accept are stored before being sent to the following level. This element is necessary to accommodate the maximum instantaneous L1 rate without introducing significant deadtime (maximum 1%)
- the dedicated links or buses which are used to transmit the front-end data stream to the next stage

After an event is accepted by the L1 trigger, the data from the pipe-lines are transferred off the detector to the RODs. Digitized signals are formatted as raw data prior to being transferred to the DAQ system. The RODs follow some general ATLAS rules, including the definition of the data format of the event, the error detection/recovery mechanisms to be implemented, and the physical interface for the data transmission to the DAQ system. The first stage of the DAQ, the readout system, receives and temporarily stores the data in local buffers. It is subsequently

solicited by the L2 trigger for the event data associated to RoIs. Those events selected by the L2 trigger are then transferred to the event-building system and subsequently to the Event Filter for final selection. Events selected by the Event Filter are moved to permanent storage at the CERN computer centre. In addition to the movement of data, the data acquisition also provides for the configuration, control and monitoring of the hardware and software components which together provide the data-taking functionality.

The Detector Control System (DCS) permits the coherent and safe operation of the ATLAS detector hardware, and serves as a homogeneous interface to all sub-detectors and to the technical infrastructure of the experiment. It controls, continuously monitors and archives the operational parameters, signals any abnormal behavior to the operator, and allows automatic or manual corrective actions to be taken. Typical examples are high and low-voltage systems for detector and electronics, gas and cooling systems, magnetic field, temperatures, and humidity. The DCS also enables bi-directional communication with the data acquisition system in order to synchronize the state of the detector with data-taking. It also handles the communication between the sub-detectors and other systems which are controlled independently, such as the LHC accelerator, the CERN technical services, the ATLAS magnets, and the detector safety system.

Furthermore, in order to ensure that only data taken under well defined and stable conditions is taken into account for physics analyses, dedicated online and offline monitoring systems ensure data integrity and quality. The online data quality monitoring accesses real-time detector status information and makes use of events from the Express trigger stream to provide several low-level quantities and distributions. This allows for a quick response to problems with the LHC beam conditions or the detector that may arise during operation.

The data quality offline monitoring uses a first reconstruction performed in order to identify and record problems in the detector hardware and the data acquisition and processing. All relevant information from the individual detector systems and reconstructed event quantities are combined into a small set of key numbers and distributions to allow for both automatic and manual monitoring.

Information from the online and offline data quality monitoring as well as feedback from the individual shift crews is combined into a database containing LHC beam conditions, detector status and data flow information which can be used to

create lists of runs usable for analyses (*GoodRunsLists*), containing a set of data taking run and luminosity block[6] (LB) information.

1.10 Event reconstruction

Position, energy and all information about the particles that cross the ATLAS detector are reconstructed with a software called *ATHENA*, starting from the signals coming from the detector.

The reconstruction takes place in three phases. In the first phase takes place the initialization of the reconstruction program, loading information concerning the detector's geometry and the magnetic field map.

In the second phase, the signals coming from each sub-detector are reconstructed separately, as explained below.

- In the Inner Detector, the signals coming from pixel and microstrip detectors are combined to determine the three-dimensional coordinates of the particle's trajectory points.

- In the TRT detector, particle's point coordinates come from the measurements of energy deposit position and charge drift time. The reconstruction software attempts to identify the tracks, i.e. helical trajectories compatible with the measured points on the different detector's planes, and reconstruct their parameters.

- In the calorimeters, the cells providing a sufficiently high signal form *seeds*, around which the reconstruction software builds groups of adjacent cells (clusters) that become candidates to be identified as electrons, photons, τ jets and hadronic jets.

- In the muon spectrometer, particle's point coordinates are measured and combined into tracks in similar way as in the inner detector.

Finally the informations of the various sub-detectors are combined together. The following section describes the methods to identify and reconstruct electrons,

[6]The luminosity blocks are defined as periods corresponding to about two minutes of data-taking

jets and missing transverse energy which are used in the analyses described in this thesis.

1.10.1 Electrons

The electron reconstruction and identification algorithms are designed to achieve both a large background rejection and a high and uniform efficiency for isolated electrons over the full acceptance of the detector and with transverse energies above 10 GeV. These electrons need to be separated from hadrons in QCD jets and from secondary electrons originating mostly from photon conversions in the tracker material. The electron reconstruction begins with the creation of a preliminary set of clusters in the EM Calorimeter, using a sliding window algorithm [56]. These seed clusters have a fixed size, 3×5 cells in $\eta \times \phi$, and they must have an energy of at least 2.5 GeV.

For each reconstructed cluster, the reconstruction algorithm tries to find a matching track, within a $\Delta\eta \times \Delta\phi$ range, with respect to the cluster barycenter in the middle calorimeter layer. The cluster energy is determined by computing and summing four different contributions: the energy deposited in the calorimeter inside the cluster, the one deposited in the material in front of the EM calorimeter, the one deposited outside the cluster (lateral leakage) and finally the energy deposited beyond the EM calorimeter (longitudinal leakage). The corrections applied to the measured cluster energy are based on precise Monte Carlo simulations validated by comprehensive measurements with 900 GeV data [57].

The four terms are parametrized as a function of the cluster measured signals in the pre-sampler (where present) and in the three accordion longitudinal layers. The parameters are computed at each pseudorapidity value corresponding to the centre of a middle cell and stored in a database [58].

The baseline ATLAS electron identification algorithm relies on variables which deliver good separation between isolated electrons and fake signatures from QCD jets. These variables include information from the calorimeter, the tracker and the matching between tracker and calorimeter. Three reference set of cuts have been defined for electrons (loose, medium, tight):

- *Loose*: this set of cuts performs a simple electron identification based only on limited information from the calorimeters. Cuts are applied on the hadronic

leakage and on shower-shape variables, derived from the middle layer of the EM calorimeter only. This set of cuts provides excellent identification efficiency, but poor background rejection.

- *Medium*: this set of cuts improves the background rejection quality, by adding cuts on the energy deposits in strips in the first layer of the EM calorimeter and on the tracking variables. Strip-based cuts are adequate for e - π^0 separation. The tracking variables include the number of hits in the pixels, the number of silicon hits (pixels plus SCT) and the transverse impact parameter. The medium cuts increase the jet rejection by a factor of 6 with respect to the loose cuts, while reducing the identification efficiency by $\sim 4\%$.

- *Tight*: this set of cuts makes use of all the particle identification tools currently available for the electrons. In addition to the criteria used in the medium identification, cuts are applied on the number of hits in the first pixel layer (to reject electrons from conversions), on the number of hits in the TRT, on the ratio of high-threshold hits to the number of hits in the TRT (to reject the dominant background from charged hadrons), on the difference between the cluster and the extrapolated track positions in η and ϕ, and finally on the ratio of the cluster energy to the track momentum ratio. The jet rejection is $\sim 10^5$, while the identification efficiency is $\sim 70\%$.

Since the beginning of the data-taking many studies have been done on the electron identification performance. The agreement of the Monte Carlo with the data is found to be good. At the beginning of data taking electron reconstruction performance was studied using electrons from J/Ψ meson decay. The invariant mass of this meson was reconstructed despite the challenges introduced by the low p_T of the electrons, for which ATLAS is not optimized.

Then the electrons from the Z boson decay have been studied and used for calibrations. Figure 1.24 shows the J/Ψ and the Z invariant masses.

1.10.2 Muons

Muon reconstruction is based on the information from Muon Spectrometer, Inner Detector and calorimeters. Different kinds of muon candidates are built, depending on how the detector information is used in reconstruction.

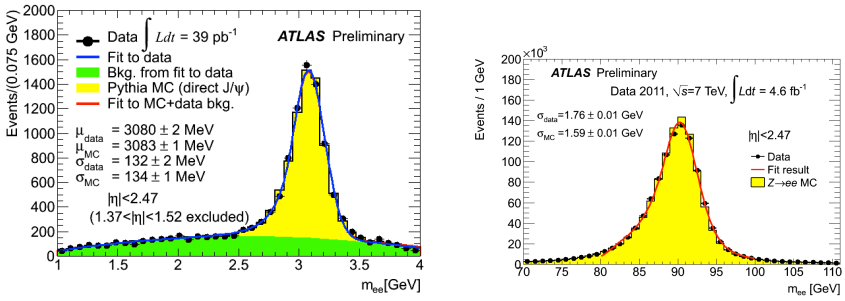

(a) (b)

Figure 1.24: Invariant mass of J/Ψ meson (left) [59], measured with an integrated luminosity of 39 pb^{-1}; Invariant Z mass for electron pairs (right) with an integrated luminosity of 4.6 fb^{-}1 [59]

- *Stand-alone*: the hits from Muon Spectrometer are combined into segments to form a track. The muon momentum is measured using this track and then it is corrected for the parametrized muon energy loss in the calorimeter, to obtain its momentum at the interaction point. The track is extrapolated back to the beam axis to obtain the muon η and ϕ coordinates and its impact parameter with respect to the interaction point.

- *Combined*: stand-alone muons are combined with an Inner Detector track. The muon parameters are derived from a combined track fit to the hits in the two sub-detectors.

- *Segment tagged*: an Inner Detector track is used as a seed. The reconstruction algorithms then search for track segments in the precision muon chambers that can be associated to the Inner Detector track extrapolated to the Muon Spectrometer.

- *Calorimeter tagged*: They are built starting from an Inner Detector track. The track is identified as a muon if energy depositions compatible with the minimum ionizing particle hypothesis can be associated to it.

In the early data analysis ATLAS uses two different chains to evaluate the muon performance in detail, *STACO* [60] and *MuId* [61]. These chains correspond to

different sets of algorithms that build the classes of candidates listed above. Both muon combination algorithms create combined tracks out of pairs of Muon-only and Inner-Detector-only tracks. To do this, a χ^2 match is used and corrections are made for energy losses in the calorimeter, however the two algorithms handle the combined track in a slightly different way. STACO does a statistical combination of the track vectors to obtain the combined track vector, while MuId refits the combined track, starting from the Inner Detector track and then adding Muon Spectrometer measures.

The two algorithm have shown very similar performances and can be both used for the analysis. The muon reconstruction performance was studied first of all in minimum bias events, just comparing basic reconstruction quantities with the Monte Carlo simulation [62], and later on using muons coming from J/Ψ and Z decays. Detector efficiencies, hit multiplicities, muon isolation, and residual distributions of reconstructed muon tracks were measured and found to be well reproduced by the Monte Carlo simulation. The capability of the ATLAS detector to reconstruct muons on a wide p_T range is illustrated in figure 1.25, where the di-muon spectrum is shown. Resonances down to J/Ψ and up to Z are evident.

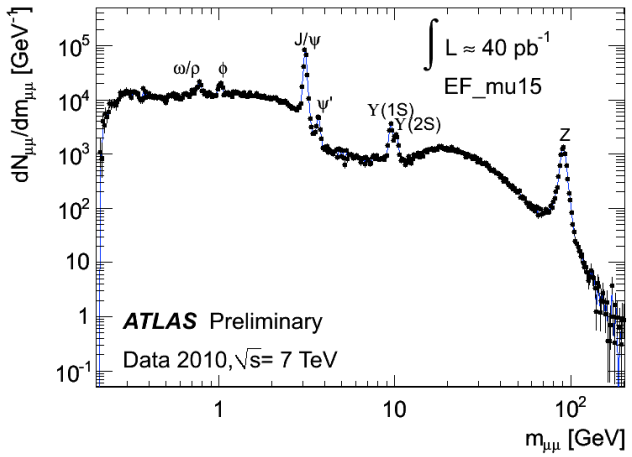

Figure 1.25: Di-muon invariant mass spectrum for data, from combined opposite sign muons. Peaks corresponding to various resonances are evident [63]

1.10.3 Jets

Hadronic particles in ATLAS deposit their energies mainly in the calorimeter system. In an attempt to resolve particles coming from the hard scatter, these energy deposits may be grouped into objects called jets.

As described in section 1.6, the ATLAS calorimeters have a high granularity (about 187000 cells independently read-out) and a high particle stopping power over the whole detector acceptance ($|\eta| < 4.9$). This calorimeter features allow a high quality jet reconstruction in the challenging environment of the proton-proton collisions at the LHC.

Cells provide energy information. They are primarily set at the so-called "electromagnetic scale", as it has been determined by electron test beams and simulations. This energy scale accounts correctly for the energy of electrons and photons, but it underestimates hadron energy, because the ATLAS calorimeters are not compensating. As a consequence electromagnetic showers generate larger signal than hadrons depositing the same energy and therefore a specific correction for the hadronic signals is needed.

It's not very convenient to use the individual cell signals, because they can be negative, due to noise effects, and because it is difficult to determine the source of the signal without signals from neighbors. The cells have thus to be collected into larger objects. The jets used for the analyses presented in this thesis have been built from topological clusters (*topoclusters*). Topoclusters are basically an attempt to reconstruct three-dimensional energy deposits from the showers developing for each particle entering the calorimeter. The clustering starts with seed cells with a signal-to-noise ratio $\Gamma = E_{\text{cell}}/\sigma_{\text{noise, cell}}$ above 4. Then topological clusters are built by iteratively adding neighboring cells with $|\Gamma| > 2$. Finally, a ring of guard cells, with signal significances above a basic threshold $|\Gamma| > P = 0$, is added to the cluster. A schematic representation of a topocluster is shown in figure 1.26. After the initial clusters are formed, they are analyzed for local signal maximums by a splitting algorithm. If more than one maximum is found, the cluster is split.

The mapping from partons to jets is a complex problem and it depends strongly on the used jet algorithm. Many solutions have been used or proposed for defining jets. An important common feature is that, in ATLAS reconstruction software frame-work ATHENA, the same jet finder code can be run on objects like topoclus-

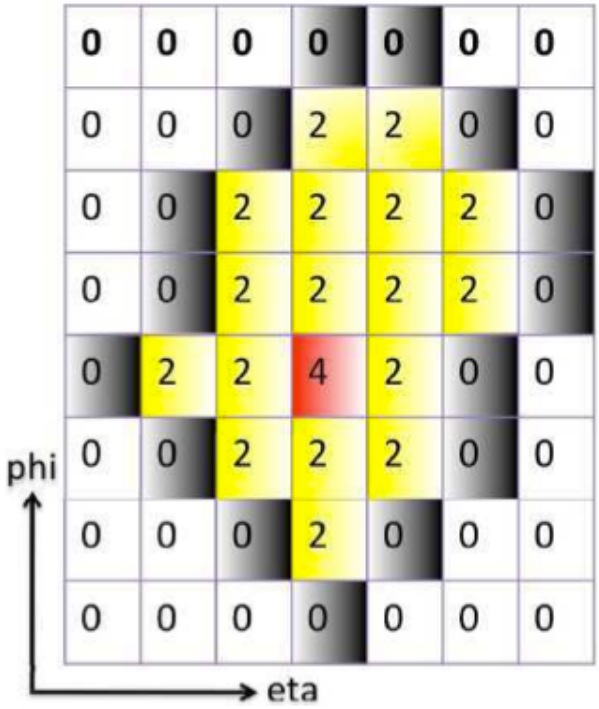

Figure 1.26: Topocluster schematic representation

ters, reconstructed tracks, and generated particles and partons. The algorithm adopted by the ATLAS collaboration as default is the anti-k_t [64]. This belongs to the category of Cluster Algorithms which are based upon pair-wise clustering of the initial constituents. The algorithms define a distance measure between objects and also some condition upon which clustering should be terminated. For each measured object i with an associated four-momentum, the quantities d_{ij} and d_{iB} are defined and evaluated as follows:

$$d_{ij} = min\left(p_{Ti}^{2p}, p_{Tj}^{2p}\right)\frac{\Delta R_{ij}^2}{R^2} \tag{1.7}$$

$$d_{iB} = p_{Ti}^{2p} \tag{1.8}$$

where $\Delta R_{ij}^2 = (y_i - y_j)^2 + (\phi_i - \phi_j)^2$, y_i is the rapidity of object i and p_{Ti} is the i object transverse momentum.

In the sense defined by the algorithm, the d_{ij} is the distance between two objects, and d_{iB} is the distance between the object and the beam. These distance definitions are common between different algorithms which differ from the value of the p parameter: for the anti-k_t algorithm, $p = -1$.

The variable R is a parameter of the algorithm setting the resolution at which jets are resolved from each other with respect to the beam, for my analysis I have used $R = 0.4$.

This means that in the vicinity $\Delta R < R$ of a hard object, all softer objects will be merged with the harder object in order of their closeness in ΔR. If two comparably hard objects are within $R < \Delta R < 2R$ of each other, energy will be shared between them depending upon their relative p_T and distance. For hard objects within $\Delta R < R$ of each other, a single jet will be formed containing both hard objects and the soft objects within their vicinity.

The algorithm proceeds by compiling a list of all the distances d. If the smallest entry is a d_{ij}, objects i and j are combined and the list is remade. If the smallest entry is a d_{iB}, this object is considered a complete jet and is removed from the list. The distances are recalculated and the procedure repeated until no entities are left. This algorithm jet shape is unaffected from soft radiation, and the results are independent from the merging order.

The ATLAS calorimeters are not compensating, so the energy of hadronic particles is underestimated. In order to reconstruct the energy of the jets, a calibration

procedure is needed. ATLAS has developed several calibration schemes with different levels of complexity.

- *Simple p_T and η-dependent calibration scheme (EMJES calibration)*: the goal of the Jet Energy Scale calibration, here called EMJES because it is applied on top of the EM scale, is to correct the energy and momentum of jets measured in the calorimeter, using as reference the kinematics of the corresponding Monte Carlo Truth jets. The jet energy scale calibration is derived as a global function depending on p_T and η. Systematics are due to dead material and to uncertainties on calorimeters energy scale calculated from test beams, on simulation of the hadron showers in calorimeters and on Monte Carlo event generator description of fragmentation and underlaying event.

- *Global cell energy density weighting calibration scheme (GCW calibration)*: electromagnetic deposits in calorimeters are characterized by their compactness and relatively high energy density. The hadronic component produced by the hadrons has a broader energy deposit. The energy density is therefore sensitive to the type of energy deposit: electromagnetic or hadronic. The GCW calibration method exploit this sensitivity to assign to each cell a correction weight based on its energy density. The reconstructed jet energy is then defined as:
$$E_{\text{recoJets}} = \sum_{i=\text{cells}} w_i(\rho) \cdot E_i \tag{1.9}$$
The weights w_i are obtained minimizing the difference between E_{recoJets} and the reference jet energy.

- *Local Hadron Calibration (LCW calibration)*: the input for this calibration procedure are topological clusters. The clustering of the energy deposit in calorimeters allows to make a relatively good matching between clusters and stable particles in jets. Each cluster can be classified as mainly electromagnetic, hadronic or unknown, according to its shape (classification based on the predicted shape obtained in simulation). Clusters classified as hadronic receive the appropriate calibration weight, to bring back the measured energy to the "true" energy deposit in calorimeter. Jets are then built from the calibrated clusters (while in the global calibration, jets were built from the uncalibrated clusters). There is still a difference between the calibrated

energy and the reference jet energy due in particular to the fact that some particles composing the reference jet might be bent out of the acceptance of the reconstructed jet, or leave an energy which is too low to be included in a cluster. For this reason, additional corrections are requested in order to calibrate the reconstructed jet to the reference jet energy. With respect to the global calibration, where all detector effects are factorized in a unique weighting function, the local calibration proceeds step-by-step, correcting in a separated way the different detector effects (first, the non-compensation, and then the out of cone and the energy loss in dead material).

1.10.3.1 b-tagging performance

The process of identifying jets originating from b-quark fragmentation (b-jets) is called b-tagging. This has applications in many physics analyses, for example it greatly helps in the Standard Model measurements (e.g. $\sigma_{b\bar{b}}$, top physics, etc.), in the searches for the Higgs boson and for physics beyond the Standard Model.

The identification of b-jets exploits the high mass and relatively long lifetime of b-hadrons. They can fly a few millimeters before decaying. Jets containing b-hadrons can therefore be tagged either inclusively by measuring the impact parameters of the tracks (i.e. the distance of closest approach of the track to the collision point) of the b-hadron decay products, or by explicitly reconstructing a displaced vertex in jet. Furthermore the semi-leptonic decays of b-hadrons can also be used by tagging the lepton in the jet.

The first physics measurements published by the ATLAS Collaboration [11, 17, 65] used a set of basic algorithm termed as “early data taggers", which were commissioned shortly after the beginning of data taking [66]. More advanced taggers, with improved light-jet rejection capability have been recently calibrated [67] and already heavily used in ATLAS physics measurements.

For early 2010 data two simple b-tagging algorithms were commissioned: JetProb [68] and SV0 [69]. JetProb is an impact parameter based tagger using both the transverse and longitudinal impact parameters of tracks with respect to the primary vertex. It builds a variable giving a probability that all tracks in the jet originate from the primary vertex. The negative side of the distribution of the displacement (impact parameter significance IP/σ_{IP}, signed with respect to the jet axis) of tracks in a jet is symmetrized to get a calibration function that is used

to calibrate the mentioned probability. On the other hand, in the SV0 tagger the secondary inclusive vertex formed by the decay products of the b-hadron, including products of the eventual subsequent c-hadron decay, is reconstructed. The signed decay length significance is used to discriminate b-jets against non-b-jets.

In order for b-tagging to be used in physics analyses, the efficiency with which a jet originating from a b-quark is tagged by a b-tagging algorithm needs to be measured, as well as the probability to tag a jet originating from a light-flavor quark, referred to as the mistag rate.

One way to measure the b-tagging efficiency is by using muon-jets. Though muons originate also from other processes, a major source is the semi-leptonic decay of the b- or c-quarks resulting from the b-quark decays. In the p_T^{rel} [66] measurement the momentum of a muon orthogonal to the flight axis of the jet it is associated to is used to measure the b-jet content of a given sample. Templates of p_T^{rel} for b- , c- and light-flavor jets are fit to the data before and after b-tagging and the efficiency is calculated as $\epsilon = N_{b,tag}/N_b$.

A similar measurement uses uncorrelated taggers to numerically calculate the b-tagging efficiency from a set of 8 equations (System8 [70]). System8 is designed to minimize the dependence on simulation and it is a very promising method that will be used in future b-tagging calibration results.

Another possibility to calibrate the b-tagging efficiency is to select a physics process providing a sample of b-jet with high purity. Two channels are used in ATLAS:

- semi-leptonic decay chain $b \rightarrow D^* \mu X \rightarrow D^0(\rightarrow K\pi)\pi\mu X$ [66]. The mass reconstruction combined with the muon requirement yields a high b-jet purity and therefore gives direct access to the b-tagging efficiency.

- events with a top quark and an antitop quark [66]. The top quark almost exclusively decays into a W-boson and a b-quark. Different methods to measure the b-tagging efficiency in a $t\bar{t}$-enriched sample have been developed and they all yield promising results that are becoming especially important as the integrated luminosity increases.

All of the described techniques have been used to measure the b-tagging efficiency in data. The results are all in good agreement with each other and the

efficiency in data is very close to that obtained in simulated events as shown in figure 1.27.

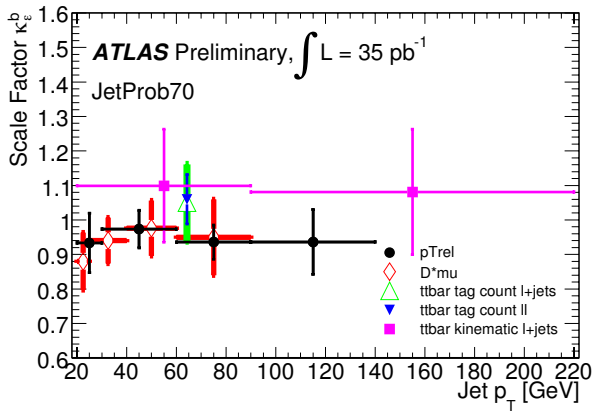

Figure 1.27: The measured b-tagging efficiency scale factors $k_{\epsilon b}^{data/sim}$ for the p_T^{rel}, $D^*\mu$ and $t\bar{t}$ methods for the JetProb70 algorithm [66]

Advanced taggers use more information to tag b-jets than the early data taggers [67]. The IP3D high-performance tagging algorithm uses a likelihood ratio technique in which input variables are compared to pre-defined smoothed and normalized distributions for both the b- and light-jet hypotheses, obtained from Monte Carlo simulation. The distributions in this case are two-dimensional density functions of the signed transverse impact parameter significance and longitudinal impact parameter significance of tracks in jets, taking advantage of the correlations between the two variables.

To further increase the discrimination between b-jets and light jets, the inclusive vertex formed by the decay products of the b-hadron, including the products of the eventual subsequent charm hadron decay, can be sought (SV1 tagger). The decay length significance measured in three dimensions and signed with respect to the jet direction is used as a discriminating variable between b-jets and light jets, as well as three of the vertex properties: the invariant mass of all tracks associated to the vertex, the ratio of the sum of the energies of the tracks in the vertex to the sum of the energies of all tracks in the jet, and the number of two-track vertices. These

variables are combined using a likelihood ratio technique.

Further discrimination can be achieved with another algorithm, called JetFitter, which exploits the topological structure of weak b- and c-hadron decays inside the jet. A Kalman filter is used to find a common line on which the primary vertex and the b- and c-vertices lie, as well as their position on this line, giving an approximated flight path for the b-hadron. With this approach, the b- and c-hadron vertices are not necessarily merged, even when only a single track is attached to each of them. The discrimination between b-, c- and light jets is based on a neutral network using similar variables as in the SV1 tagging algorithm above, and additional variables such as the flight length significances of the vertices.

Thanks to the likelihood ratio method used for IP3D and SV1, the algorithms can be easily combined by adding their respective weights. The combination JetFitter+IP3D is based on artificial neural network techniques with Monte Carlo simulated training samples and additional variables describing the topology of the decay chain.

The advanced taggers greatly improve light-jet rejection at a fixed b-tagging efficiency as is clearly visible in figure 1.28. At same b-jet efficiency, the light jet rejection can be increased by a factor of 2 to 5 with new taggers allowing better background rejection. On the other hand for same light-jet rejection, the working point can be chosen at higher efficiency. This is very promising for searches with low production cross section.

1.10.4 Missing Transverse Energy

In proton-proton collision the interacting parton momentum is unknown, and so is impossible to use the momentum conservation along the z axis. Instead the momentum conservation law can be used in the transverse plane where the total momentum is zero summing over all particles involved in the event, including non interacting particles like neutrinos.

The missing transverse energy (E_T^{miss}) is defined as:

$$E_T^{\text{miss}} = \sqrt{\left(E_x^{\text{miss}}\right)^2 + \left(E_y^{\text{miss}}\right)^2} \tag{1.10}$$

where $E_x^{\text{miss}} = -\sum E_x$ and $E_y^{\text{miss}} = -\sum E_y$ and $E_{x,y}$ are the energies measured in the detector.

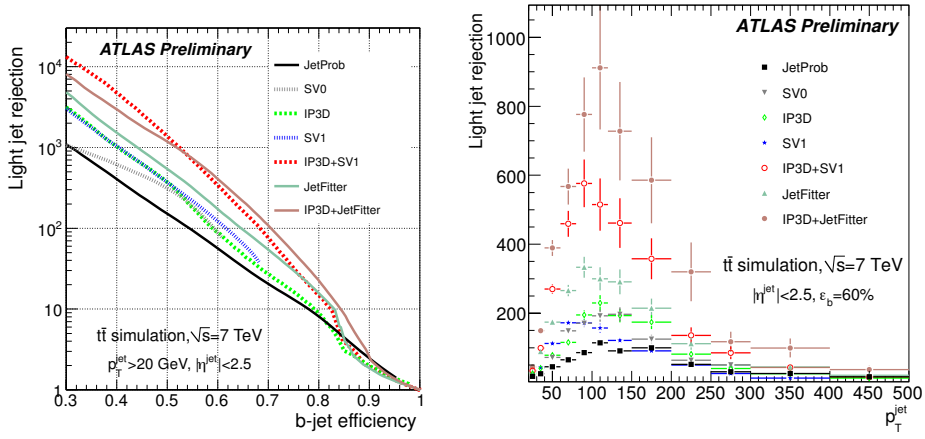

(a) (b)

Figure 1.28: Light-jet rejection as a function of the b-jet tagging efficiency for the early tagging algorithms (JetProb and SV0) and for the high performance algorithms, based on simulated $t\bar{t}$ events (left), and light-jet rejection as a function of the jet transverse momentum p_T, for operating points of the various tagging algorithms leading to the same b-jet tagging efficiency of 60%, based on simulated $t\bar{t}$ events (right) [67]

It is also necessary a correction to take into account dead or inactive detector components.

Having an extremely precise measure of E_T^{miss} in ATLAS is fundamental for the study of many physics channels, e.g. the W decay, the top quark semi-leptonic decay and event discovery channels like Higgs and SUSY.

The E_T^{miss} reconstruction includes contributions from energy deposits in the calorimeters and muons reconstructed in the muon spectrometer. Muons reconstructed from the inner detector are used to recover muons in regions not covered by the muon spectrometer. The E_T^{miss} reconstruction uses calorimeter cells calibrated according to the reconstructed physics object to which they are associated. Calorimeter cells are associated with a reconstructed and identified high-p_T parent object in a chosen order: electrons, photons, hadronically decaying τ-leptons, jets and muons. Cells not associated with any such objects are also taken into account in the E_T^{miss} calculation.

Once the cells in calorimeters are associated with objects as described above, the E_T^{miss} is calculated as follows:

$$\begin{aligned} E_{x(y)}^{\text{miss}} = E_{x(y)}^{\text{miss},e} + E_{x(y)}^{\text{miss},\gamma} + E_{x(y)}^{\text{miss},\tau} + E_{x(y)}^{\text{miss,jets}} \\ + E_{x(y)}^{\text{miss,softjets}} + (E_{x(y)}^{\text{miss,calo},\mu}) + E_{x(y)}^{\text{miss,CellOut}} + E_{x(y)}^{\text{miss},\mu} \end{aligned} \tag{1.11}$$

where each term is calculated from the negative sum of calibrated cell energies inside the corresponding objects (within $|\eta| < 4.9$), and the $E_{x(y)}^{\text{miss},\mu}$ is calculated from the negative sum of the momenta of muon tracks reconstructed with $|\eta| < 2.7$. Because of the high granularity of the calorimeter, it is crucial to suppress noise contributions and to limit the cells used in the E_T^{miss} sum to those containing a significant signal. This is achieved by using only cells belonging to three-dimensional topological clusters, previously described in section 1.10.3, with the exception of electrons and photons for which a different clustering algorithm is used.

The calibration scheme used is the one yielding the best performance in 2010 data. Electrons are calibrated with the default electron calibration (see section 1.10.1), photons are used at the EM scale, that provides the correct scale for energy deposited by electromagnetic showers, and the τ-jets are calibrated with the local hadronic calibration (LCW) [71]. The jets are reconstructed with the anti-k_t algorithm, with distance parameter $R = 0.4$. They are calibrated with the LCW scheme if their p_T is smaller than 20 GeV (soft jets) and with the LCW+EMJES

scheme if their p_T is greater than 20 GeV. The contribution from topoclusters not associated to high-p_T objects is calculated with LCW calibration combined with tracking information.

The values of E_T^{miss} and its azimuthal coordinate (ϕ^{miss}) are then calculated as:

$$\begin{aligned} E_{\text{T}}^{\text{miss}} &= \sqrt{\left(E_x^{\text{miss}}\right)^2 + \left(E_y^{\text{miss}}\right)^2} \\ \phi^{\text{miss}} &= \arctan(E_y^{\text{miss}}, E_x^{\text{miss}}) \end{aligned} \tag{1.12}$$

The total transverse energy in the calorimeters, $\sum E_T$, which is an important quantity to parameterize and understand the E_T^{miss} performance, is defined as:

$$\sum E_{\text{T}} = \sum_{i=1}^{N_{\text{cell}}} E_i \sin\theta_i \tag{1.13}$$

where E_i and θ_i are the energy and the polar angle, respectively, of calorimeter cells associated to topoclusters within $|\eta| < 4.9$. Cell energies are calibrated according to the scheme described above for E_T^{miss}.

Chapter 2

Impact parameter resolution studies

The ATLAS Inner Detector tracking system is devoted to the identification of the tracks associated to particles emerging from the interaction point during collisions. The hardware devices that constitute the Inner Detector (i.e. Pixel Detector, SCT and TRT) and their general performances have been described in chapter 1. This chapter, instead, discusses the measurement of the impact parameter resolution of the tracks generated by the charged particles that pass through the detector. The goal of this study is to provide the computed impact parameter performance to a general user that needs these informations for a specific physics analysis.

When a particle traverses a tracking device, the detector identifies the position where it is crossed. In the ATLAS environment, at the nominal luminosity of $10^{34}\text{cm}^{-2}\text{s}^{-1}$, approximately 1000 particles will emerge from the collision point during each event. Each of them will generate a path of measurements through the sub-detectors. The tracking system must be able to resolve the tracks associated to each particle and to describe it with a well defined set of parameters. Since the input of the software devoted to this task is a simple collection containing all the measurements, two conceptually separated steps are accomplished in sequence:

- the *pattern recognition* identifies the groups of measurements relative to the same particle, giving an initial estimate of its trajectory

- the *track fitting* describes the trajectories with the best possible precision, taking into account details as e.g. the different resolution of the sub-detectors, the interaction with different material layers, and the variations of the magnetic field

Many different approaches exists to each of the two problems and the ATLAS collaboration explored many of them. At present time basically one routine is used to analyze collision data: the *New Tracking* [72, 73] (see section 2.2.2). This approach uses common definitions, described in the ATLAS Event Data Model (see section 2.2.1), to represent the input and the output data.

Precise tracking is an indispensable tool for any collider experiment. Efficient identification of electrons and muons, based on tracking, is necessary to separate new phenomena from the overwhelming QCD background. Lepton signatures require muon tracking-based triggers and precise measurement of the momentum of muons and electrons. E.g. at the Large Hadron Collider (LHC) Z and W bosons are identified through their leptonic decays and used both to discover new physics phenomena and to calibrate the detectors.

Furthermore the capability to reconstruct detached vertices to identify long-lived particles is an essential tool for the precise study of the top quark, the heaviest and least studied of the six known quarks. Tagging b-jets is also an essential tool in discovery physics in all case when the new particles have a preferential decay to heavy quarks, like the Higgs bosons of supersymmetry.

2.1 Charged particle tracking in a magnetic field

During tracking procedures, many local coordinate systems are considered, as well as the global one presented in section 1.4.1. A typical issue is to identify a set of parameters that can describe a track in all the different systems. Furthermore, tracking devices are immersed in magnetic fields, in order to be able to measure the momentum of particles. A track can be parametrized with respect to a surface in many different ways, but it is convenient to choose some general set of parameters which have a physical interpretation when considering motion in a magnetic field and which can be consistently used when extrapolating particles to measurement surfaces and to the interaction region.

A charged particle that moves in a magnetic field is always subjected to a *Lorentz force*:

$$\frac{\mathrm{d}\vec{p}}{\mathrm{d}t} = q\vec{v} \times \vec{B} \tag{2.1}$$

that is perpendicular to the velocity $\vec{v}$ of the particle and to the magnetic field $\vec{B}$ itself. The force acts as a bending on the trajectory $\vec{r}$ of the particle:

$$\frac{\mathrm{d}^2\vec{r}}{\mathrm{d}s^2} = \frac{q}{p}\frac{\mathrm{d}\vec{r}}{\mathrm{d}s} \times \vec{B} \tag{2.2}$$

where the trajectory length s has been used in place of time to describe the evolution of the system. The bending is clearly perpendicular to the magnetic field.

The ATLAS Inner Detector is immersed in a solenoidal magnetic field (see section 1.4.3). In a first approximation, this field can be described as a uniform field directed along the z-axis. In this case, the Lorentz force acts only in the transverse plane. Since it does not produce any work, the transverse component of the momentum p_T is a constant of motion. If the curvature radius is called ρ, it can be concluded that:

$$p_T = cB\rho \rightarrow p_T[\mathrm{GeV}] = 0.3B[\mathrm{T}]\rho[\mathrm{m}] \tag{2.3}$$

introducing an error of less than 0.1% on the light speed.

The motion of the particle can thus be described by an helix. Figure 2.1 shows the trajectory, with the variables used to describe it.

At large momentum the trajectory can be approximated with a straight line

$$\xi = a + bz \tag{2.4}$$

in the plane containing the magnetic field and with a parabola

$$y = a + b\xi + \frac{c}{2}\xi^2 \tag{2.5}$$

in the bending plane perpendicular to the magnetic field. The parameter of the quadratic term is related to the momentum of the particle in the bending plane through the radius of the circumference $c = -\rho^{-1}$.

2.1.1 ATLAS convention

In the case of uniform magnetic field, directed along the z-axis, the motion of a particle can be described using five variables. When a reference system is chosen

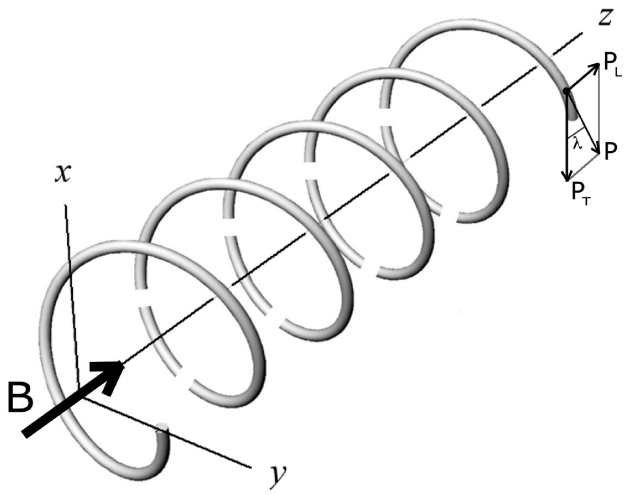

Figure 2.1: Trajectory of a charged particle in a uniform magnetic field

for ATLAS, a key point is that ATLAS features two different tracking devices: the Inner Detector and the Muon Spectrometer. Since their magnetic field setups are somewhat perpendicular (see section 1.4.3), a helical parameterization bound to the Inner Detector solenoidal field would leave the Muon Spectrometer with an almost meaningless choice of parameters. For this reason, the parameterization chosen is closely bound to the constants of motion of both devices. The ATLAS parameter choice is thus:

$$\mathbf{T} = (l_1, l_2, \phi, \theta, q/p)^{\mathrm{T}} \tag{2.6}$$

where l_1 and l_2 denote the local coordinate on a given surface, ϕ and θ are the azimuthal and polar angle of the track direction, respectively, and q/p is the inverse momentum multiplied by the charge of the particle q.

The most significant case is defined by the state of the track in the interaction region. In this case the closest approach to the beam axis (the *perigee*) is taken as a reference. If the starting point (x_0, y_0) is choosen to be the perigee, the parametrization in equation 2.6 becomes:

$$\mathbf{T} = (d_0, z_0, \phi_0, \theta, q/p)^{\mathrm{T}} \tag{2.7}$$

Thus the d_0, defined as $\pm\sqrt{x_0^2 + y_0^2}$, and z_0 parameters are calculated as the local coordinate of the perigee in the $\xi - z$ plane defined by the perigee itself and by the beam axis. The d_0 parameter results to be a signed quantity, defined to be positive when the direction of the track is clockwise in the $x - y$ plane. Figure 2.2 shows a sketch illustrating the perigee representation using ATLAS conventions. The perigee representation will be used through this chapter. Other common parameters that will be used are the pseudorapidity η, defined in equation 1.3, and $z_0 \sin\theta$. Using the latter, the pair d_0 and $z_0 \sin\theta$ corresponds to the distances of the track from the origin, projected respectively in the $x-y$ plane and in the plane defined by the z-axis and by the momentum of the particle ($\xi - z$ plane in figure 2.2). They will be referred to as *transverse* and *longitudinal impact parameter* in the following.

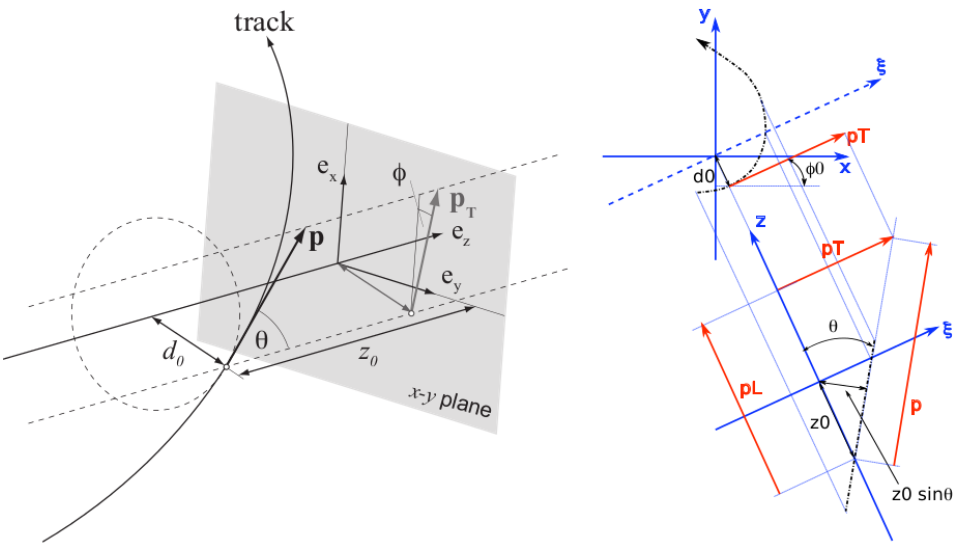

Figure 2.2: Representation of the track parameters at the perigee, according to ATLAS conventions

2.1.2 Resolution in impact parameter and momentum

The variables that have the most important role in physics analysis are the momentum of particles, and their impact parameter. The momentum of particle is

necessary in order to reconstruct invariant masses of resonances and may allow to improve the calorimeter estimation of jet energy. The measurement of the impact parameter allows to discriminate particles that have an appreciable lifetime, such as hadrons containing b-quarks, from particles that are instantly produced decaying in the primary interaction point. In fact, as described in section 1.10.3.1, many b-tagging algorithms are based on the impact parameter measurement.

While track fitting is performed with sophisticated procedures[1] in order to take into account the inhomogeneity of the magnetic field and the contribution of detector material, most features can be qualitatively understood with simplified models. In this section, it will be assumed that the magnetic field is constant and uniformly parallel to the beam axis (z-axis). This allows to study the trajectory of particles in the transverse plane ($x-y$ plane) and in the longitudinal one ($z-R$ plane) independently.

In the following I discuss the error on the impact parameter and on the particle momentum and how they are related to the design of a spectrometer.

2.1.2.1 Straight line fit in the $z-R$ plane

Let us consider $N+1$ position sensitive detectors having a measurement error σ, equally spaced and placed at positions $z_0, ..., z_N$; the spectrometer length is $L = z_N - z_0$ and the distance of its center from the interaction point is $z_c = (z_0 + z_N)/2$.

Choosing a reference frame with the origin at the center of the track (see figure 2.3), the errors on the track parameters a and b (see equation 2.4) are uncorrelated ($\sigma_{ab} = 0$), and the error on the extrapolation at the interaction point is given by

$$\sigma_{ip}^2 = \sigma_a^2 + \sigma_b^2 z_c^2 = \frac{\sigma^2}{N+1} + \frac{\sigma^2}{N+1}\frac{12N}{N+2}\frac{z_c^2}{L^2} \tag{2.8}$$

The above formula shows how the error of the impact parameter depends on the error of the slope of the track (σ_b) and on the distance of the center of the spec-

[1] The most popular approach to track finding and fitting is the combinatorial *Kalman filter* [74] where the full knowledge of the track parameters at each detector layer is used to find compatible measurements in the next detector layer, forming combinatorial trees of track candidates. Generalizations of the Kalman filter are the *Gaussian sum filter* [75], which is used to account for the bremsstrahlung energy loss of electrons, and the *adaptative methods* [76], which are used for vertex reconstruction. In this thesis, I will not address the problem of the optimal track fit, for which many excellent articles exist (see for example [77]).

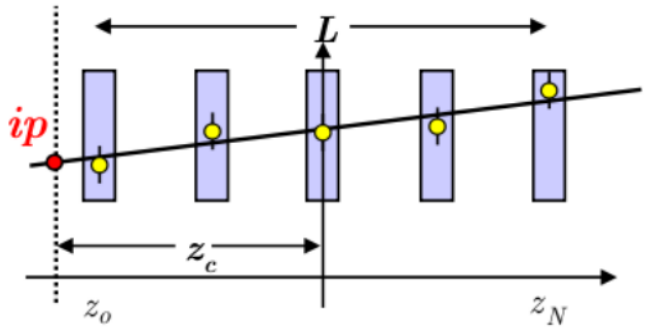

Figure 2.3: Sketch of the linear fit in $z - R$ plane

trometer from the interaction point (z_c). To minimize the error on the impact parameter we have to:

- use detectors with excellent spatial resolution σ
- make the spectrometer as long as possible to reduce the error on the slope
- place the spectrometer as close as possible to the interaction point

Excellent spatial resolution is obtained with silicon detectors designed to have $\sigma \sim 10$ μm or better. As such detectors are very expensive, the maximum spectrometer length L is limited. To overcome this limitation, the spectrometers are usually split into an inner vertex detector and a central tracking detector. The latter can be made long (large L) making the error on the slope small. Compact pixel vertex detectors provide excellent spatial resolution very near to the interaction point.

2.1.2.2 Quadratic fit in the $x - y$ plane

Let us consider $N + 1$ measuring detectors equally spaced and placed at positions $x_0, ..., x_N$. The spectrometer length is $L = x_N - x_0$. The error on the coefficients

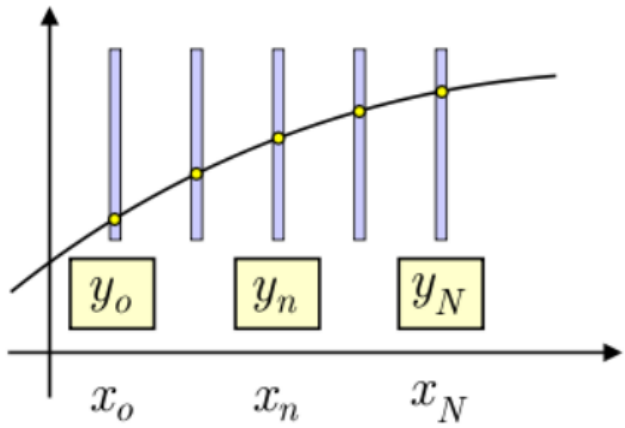

Figure 2.4: Sketch of the quadratic fit in $x - y$ plane

of the parabola in equation 2.5 are:

$$\sigma_a^2 = \sigma^2 A_N, \qquad A_N = \frac{3(3N^2 + 6N - 4)}{(N-1)(N+1)(N+3)} \tag{2.9}$$

$$\sigma_b^2 = \frac{\sigma^2}{L^2} B_N, \qquad B_N = \frac{12N}{(N+1)(N+2)} \tag{2.10}$$

$$\sigma_c^2 = \frac{\sigma^2}{L^4} C_N, \qquad C_N = \frac{720N^3}{(N-1)(N+1)(N+2)(N+3)} \tag{2.11}$$

The a parameter can be identified as the impact parameter: in this approximation, its precision depends only on the resolution of the vertex detector. The c parameter is instead related to the curvature radius ($c = -1/\rho$) of the trajectory and its uncertainty is equal to the one associated to the transverse momentum of the particle (see equation 2.3). The relative uncertainty on the transverse momentum can thus be expressed as:

$$\frac{\delta p_T}{p_T} = \frac{\sigma p_T}{0.3BL^2} \sqrt{C_N} \tag{2.12}$$

where the common units GeV, Tesla and metres are used. The formula illustrates the basic features of the momentum measurement with a magnetic spectrometer:

- the relative transverse momentum resolution is proportional to the transverse momentum

- the strong dependence on the spectrometer length L calls for large detectors to achieve good momentum resolution
- the transverse momentum resolution is inversely proportional to the magnetic field
- the dependence on the number of measured coordinates is weak; however the number of coordinates is important for the robustness of the pattern recognition

One last aspect that arise from the computation of the uncertainty of the parabolic fit parameters is the correlation between the a parameter and the c parameter (i.e. the correlation between momentum and impact parameter resolution). In fact their covariance can be expressed as:

$$\sigma_{ac} = -\frac{15N^2}{(N-1)(N+1)(N+3)}\frac{\sigma}{L^2} \tag{2.13}$$

This means that the extrapolation in the magnetic field affects also the uncertainty of the impact parameter. Compared to the simple case discussed in equation 2.8 the general formula contains additional terms that may further degrade the precision and that account for the error in the extrapolation back to the origin caused by the uncertainty on the curvature of the track.

2.1.3 Multiple scattering effect on resolution

The resolution that can be obtained on track parameters is greatly influenced by the quantity of material crossed by the particles. The main effects of material on particle motion are energy loss and directional scattering. The effect of the energy loss on the particle momentum can be neglected if considering thin detector layers, because they absorb only a small fraction of the total energy of through going particles. However, the performance requirements of the ATLAS Inner Detector are more stringent than any tracking detector built so far for operation at a hadron collider. The harsh environment and the pile-up from multiple interactions per bunch crossing make a high detector granularity mandatory, with electronics, readout services and cooling within a detector volume that must have good mechanical stability. The overall weight ($\sim$ 4.5 tons) and material budget of the ID (in terms of radiation length X_0 and interaction length λ) are therefore much

larger than those of previous tracking detectors. The consequences of this are quite serious:

- many electrons lose most of their energy through bremsstrahlung before reaching the electromagnetic calorimeter
- approximately 40% of photons convert into an electron-positron pair before reaching the LAr cryostat and the electromagnetic calorimeter
- even in the case of low-energy charged pions, a significant fraction will undergo an inelastic hadronic interaction inside the inner detector volume

Figure 2.5 show the integrated radiation length, X_0, and interaction length, λ, traversed by a straight track as a function of $|\eta|$ at the exit of the ID envelope. The most striking feature is the onset of non-active service and structural material at the interface of the barrel and end-cap regions. This includes cooling connections at the end of the SCT and TRT barrels, TRT electrical connections, and SCT and TRT barrel services extending radially to the cryostat, to the PPB1 patch-panel, and then along the cryostat wall. Another service contribution is from the pixel services at $|\eta| > 2.7$, which leave the detector along the beam-pipe; their extended range in $|\eta|$ can clearly be seen. A large fraction of the service and structural material is external to the active ID envelope, therefore deteriorating the calorimeter resolution but not the tracking performance. Table 2.1 lists the contribution to X_0 as a function of radius for different elements of the ID and for straight tracks at $|\eta| = 0$ and $|\eta| = 1.8$.

The multiple scattering effect arises because a particle that traverses detector material undergoes successive small angle deflections, caused by (mainly Coulomb) scattering on nuclei. An introduction to the multiple scattering effect can be found in [78] and in articles referenced there, while figure 2.6 shows the main variables that should be considered to describe multiple scattering in a plane. The integration of all the interactions inside the material results in a final deflection θ_{plane} and in a displacement y_{plane} with $\left\langle y^2_{\text{plane}} \right\rangle \approx 1/3x^2 \left\langle \theta^2_{\text{plane}} \right\rangle$. The displacement can thus be neglected if the material layer is thin, as in the Inner Detector devices. The deflection θ_{plane}, instead, is important because it gets multiplied by the extrapolation length. It is Gaussian distributed and symmetrically centered around zero. However, large angle single scattering processes disturb the purely Gaussian probability density function and add some non-Gaussian tails (i.e. $\propto \sin^{-4}(\theta_{\text{plane}}/2)$).

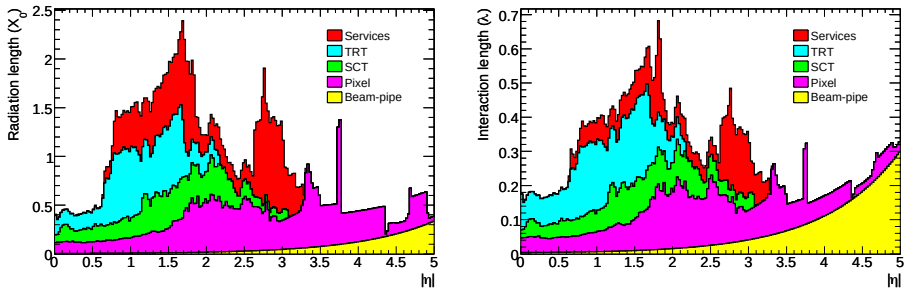

(a) (b)

Figure 2.5: Material distribution (X_0, λ) at the exit of the ID envelope, including the services and thermal enclosures. The distribution is shown as a function of $|\eta|$ and averaged over ϕ. The breakdown indicates the contributions of external services and of individual sub-detectors, including services in their active volume

	$\|\eta\| = 0$		$\|\eta\| = 1.8$	
	Radius (mm)	**X_0**	**Radius (mm)**	**X_0**
Exit beam-pipe	36	0.0045	36	0.014
Exit pixel layer-0	57	0.037	57	0.105
Exit pixel layer-2	172	0.108	172	0.442
Entry SCT	253	0.119	253	0.561
Entry TRT	552	0.205	621	0.907
Exit TRT	1081	0.469	907	1.126

Table 2.1: Integrated radiation length (X_0) from interaction point, estimated as a function of radius R for $|\eta| = 0$ and for $|\eta| = 1.8$, using the detailed description of the inner-detector material implemented in the simulation. The quoted radii are the maximum radii over which the integration is made. The data are averaged over ϕ

The variance of the deflection θ_{plane} is given by:

$$\left\langle \theta^2_{\text{plane}} \right\rangle = \left(\frac{0.0136 \text{ GeV}}{\beta c} \frac{q}{p} \right)^2 \frac{x}{X_0} \left[1 + 0.038 \log \left(\frac{x}{X_0} \right) \right]^2 \tag{2.14}$$

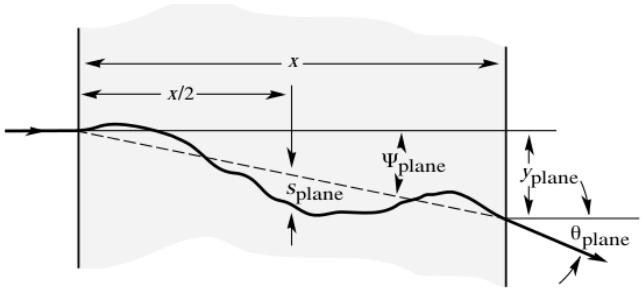

Figure 2.6: Quantities used to describe the multiple scattering effect

In this expression, the path x of the particle in the material enters in terms of radiation lengths ${X_0}^2$, while q/p represent the charge over momentum tracking variable. The logarithmic correction term is adopted for the slightly underestimated screening of the nucleus Coulomb potential in materials with lower Z.

The expression reported in equation 2.14 is used during reconstruction to evaluate multiple scattering contribution to the particle trajectory. In the ATLAS track parameterisation, the path length inside material can be expressed by using the thickness of each detector layer d_i:

$$x = \frac{d_i}{\sin\theta_{\text{loc}}} \approx \frac{d_i}{\sin\theta} \tag{2.15}$$

where the azimuthal angle at the given detector surface θ_{loc} has been approximated by the global azimuthal angle θ.

The final effect of multiple scattering on the polar angle θ can thus be described by adding to its uncertainty a term computed from equation 2.14:

$$\delta\theta = \sqrt{\left\langle \theta^2_{\text{plane}} \right\rangle} = \frac{q}{p\sqrt{\sin\theta}} \frac{0.0136 \text{ GeV}}{\beta c} \sum_{i=1}^{n_{\text{layers}}} \sqrt{\frac{d_i}{X_{0_i}}} = \frac{\sigma_{\theta\text{MS}}}{p\sqrt{\sin\theta}} \tag{2.16}$$

where the logarithmic term has been neglected. Similarly, the contribution to ϕ uncertainty can be computed. Since the azimuthal angle is projected in the transverse plane, one more correction term of $1/\sin\theta$ has to be applied in order to account for the out of plane projection:

$$\delta\phi = \frac{1}{\sin\theta}\sqrt{\left\langle \theta^2_{\text{plane}} \right\rangle} = \frac{\sigma_{\theta\text{MS}}}{p_T\sqrt{\sin\theta}} \tag{2.17}$$

[2]The radiation length of a material is the mean length (in cm) to reduce the energy of an electron by the factor $1/e$.

These multiple scattering contribution are managed by the fitting algorithms and their impact on remaining track parameters can be explicitly calculated. The contribution to momentum resolution, for example, is

$$\frac{\delta p}{p} = \frac{1}{0.3B}\frac{0.0136}{\beta}\sqrt{xC_N}X_0 L \tag{2.18}$$

If this equation is compared with equation 2.12, it can be noticed that, when multiple scattering dominates propagation, the relative resolution is independent on momentum and on detector resolution. Also the lever arm effect is reduced to a $1/\sqrt{L}$ dependence. As in the previous cases, the $\sin\theta$ dependence can be shown explicitly:

$$\frac{\delta p}{p} = \frac{\sigma_{p\mathrm{MS}}}{\sqrt{\sin\theta}} \tag{2.19}$$

The impact parameter is affected by a contribution that can be written as:

$$(\delta d_0)^2 = \sum_{i=1}^{n_{\mathrm{layers}}} R_i^2 \left\langle (\theta_i^{\mathrm{scat}})^2 \right\rangle \tag{2.20}$$

where R_i is the distance of each layer from the perigee in the transverse plane and $\theta_i^{\mathrm{scat}} = \theta_{\mathrm{plane}}/\sin\theta$. Using equation 2.14, the uncertainty on the impact parameter becomes:

$$\delta d_0 = \frac{\sigma_{ip\mathrm{MS}}}{p_T\sqrt{\sin\theta}} \tag{2.21}$$

Finally, when considering z_0, equation 2.20 can be used as a starting point. One obtains $\theta_i^{\mathrm{scat}} = \theta_{\mathrm{plane}}$, while the distance to be considered is $R_i/\sin\theta$. In addition, another $1/\sin^2_\theta$ term must be added to equation 2.20, due to the fact that the longitudinal impact parameter is actually the *projection* of z_0, perpendicular to the momentum. The complete expression becomes:

$$\delta z_0 = \frac{\sigma_{ip\mathrm{MS}}}{p_T\sqrt{\sin^3\theta}} \tag{2.22}$$

As a general conclusion, the multiple scattering phenomena introduce a dependence of the resolution of each track parameter on the momentum and on the polar angle of the track.

2.1.4 Alignment

The intrinsic resolution of the tracking detectors is usually better than the precision of the detector assembly. Moreover, the position of the detectors may change with

time due to magnetic field and environmental effects like change of temperature. To fully profit from a tracking device performance, the best possible knowledge of its component positions is essential.

Alignment procedures are used to measure and monitor the position of the detectors over time to recover the intrinsic resolution of the measurements of the particle trajectories. These procedures combine the use of dedicated optical alignment systems based on beams of laser or LED light and the fit of the corrections from the nominal to the real positions using a (large) set of reconstructed trajectories of particles.

The alignment with optical systems is based on a network of online measurements of the relative positions between light sensitive detectors which are precisely mounted on the particle detectors. The number of measurements largely exceeds the degrees of freedom of the overall system and the position of the particle detectors are computed as free parameters in a fit to the whole set of measurements. The accuracy of the single measurement is typically a few microns and systematic effects dominate the alignment precision: the final precision was different for each part, down to $\mathcal{O}(10\ \mu\text{m})$ for the positioning of pixel staves and $\mathcal{O}(1\ \text{mrad})$ for their rotation. Moreover a Frequency Scanner Interferometer optical system has been integrated in the SCT package, to monitor the position of its structures with a micron-scale precision.

Besides survey constraints, software based alignment procedures are applied during track reconstruction. All these techniques are track based, i.e. track fitted to particle trajectories are used to determine the position and the orientation of the modules. The base assumption is that the distribution of the residual between the predicted and measured positions of hits[3] for a perfectly aligned detector are centered around zero and their width is determined only by intrinsic detector resolution and by multiple scattering. When modules are shifted, instead, the mean of residual distributions shifts as well. Figure 2.7 shows how a misaligned module influences residual distributions.

The track-based alignment is faster when the extrapolation of the measured trajectory on the detector layer has an intrinsically small statistical error. This is the case for the ATLAS Inner Detector where there are many measurement layers separated by small extrapolation distance and with limited material in between

[3] A hit is a measurement point assigned to a track.

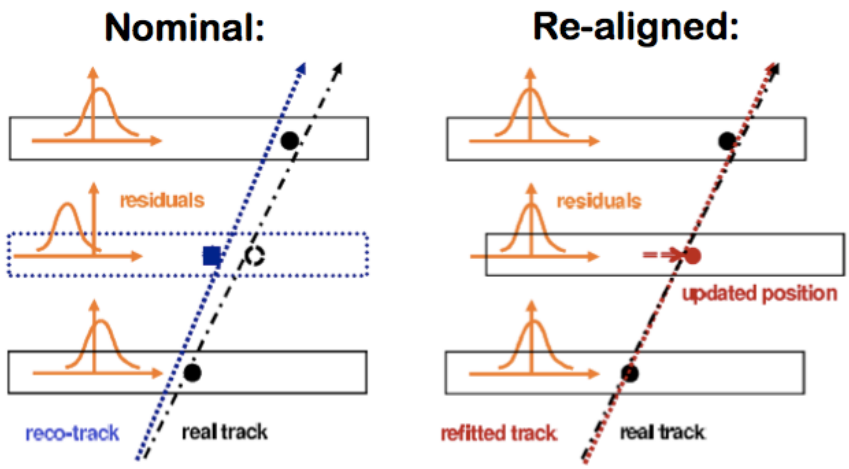

Figure 2.7: Connection between alignment of modules and residual distributions

layers, resulting in small multiple scattering errors. The muon systems instead have less measurement points with large extrapolation distance and in some cases large multiple scattering in between layers. Precise knowledge of the magnetic field map is needed for the track extrapolation. This induces systematic errors in the track-based alignment which are usually smaller for the inner detectors where the magnetic field is constant and larger for the muon systems where the magnetic field varies along the trajectory of the particle.

Optical alignment methods require free line of sight between optical detectors, which is a limitation especially important for the inner trackers, where the particle detectors are densely packed in nearby layers and many services have to be routed. Therefore, the Inner Detector is aligned using track-based procedures while optical systems are used to monitor a limited number of degrees of freedom, providing valuable information on the stability of the detectors.

The track-based alignment uses mainly tracks originating from the interaction point which are not able to constrain all parameters. A number of correlated

displacements of the detector layers do not produce at first-order a variation of the chi-square of the fit like, for example, a correlated shift along z as function of r. These correlated movements are constrained using different data samples like cosmic rays and also applying constraints like common vertex in multi-track events and mass constraints on the decay products of known resonances.

The large muon systems are prone to temperature effects and to movements induced by ramping the magnets up and down. In ATLAS the muon chambers move by several millimeters when the magnets are being turned on, with a reproducibility of about 1 mm, larger than the intrinsic resolution of the detectors.

The ATLAS muon system is aligned mainly with optical systems. The specifications requires better than 50 μm alignment accuracy. ATLAS uses a sophisticated optical system [79, 80, 81] to monitor the relative position of the components of the chambers to a precision of ~ 10 μm and the relative position of the chambers to a precision of ~ 30 μm.

The alignment performance of the Inner Detector has been discussed in section 1.5.4.4.

Depending on the number of independent detectors to be aligned, the simultaneous fit of a large number of parameters can be computationally challenging. In some cases the alignment problem can be factorized into a number of smaller and weakly correlated problems. This is the case in the ATLAS end-cap alignment which comprises about 10^4 fitted parameters in total and can be factorized in 864 partial fits of 9 or 12 parameters each, and two global fits of 384 parameters each, reducing the computational time by several orders of magnitude. This factorization cannot be applied to the Inner Detector where the number of strongly correlated detectors is large.

2.2 Tracking in ATLAS

2.2.1 The tracking Event Data Model

ATLAS has developed a common *Event Data Model* (EDM) for the reconstruction of tracks at the same time in the innermost tracking sub-detectors and in the muon detectors in offline as well as online reconstruction [82]. The tracking EDM follows the clear distinction between event data classes and algorithmic classes as laid out

by the Athena framework. At the level of the tracking EDM, this implies that the track class does not contain code to perform track fits for example, but that a fitting tool uses tracking EDM objects as input and the track class as output. Common interfaces to objects representing detector data at different stages of the reconstruction help to structure the reconstruction process as a highly modular data flow, which is presented in figure 2.8. In the first step, the detector information is prepared for the track reconstruction by applying measurement and geometric calibrations which depend on the part of the detector the data is coming from. All different types of input data are combined under one common base class. The actual track finding and subsequent processing of tracks is done using common services and tools. The base class structure and its equivalents at later stages during the track reconstruction allows the definition of a common container class, the track, which is the output of the high-level pattern recognition algorithms. The tracks are then passed through various processing stages until track particles are created, which are used in physics analyses.

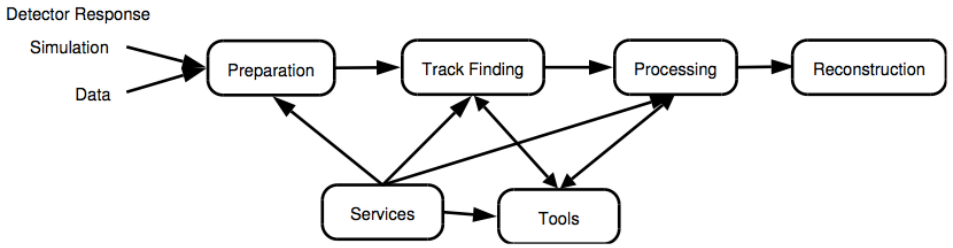

Figure 2.8: Simplified steps for the reconstruction of tracks. The detector information is prepared for the reconstruction using common classes. The track finding and subsequent processing of tracks use common services and tools due to common interfaces

2.2.2 Inner Detector track reconstruction with New Tracking

The ATLAS *New Tracking* (NEWT) [72, 73] reconstruction software consists of a sequence of algorithms. The single components are defined through interfaces and use, where possible, common tools and services to perform certain tasks. The tracking EDM as introduced in the section before acts hereby as the language between

the different components. This allows single parts of the entire reconstruction process to be modified or exchanged without disrupting the untouched parts of the software chain.

The main sequences of the NEWT software chain are the *inside-out* and the consecutive *outside-in* track reconstruction, which will be outlined in the following.

Preprocessing of silicon detector measurements The creation of three-dimensional representations of the silicon detector measurements, which are called SpacePoint objects, takes place before the actual track reconstruction. In case of the pixel detector, a SpacePoint corresponds to the two-dimensional local measurement of the pixel chip and its constraint on the surface that represents the detector element. A single SCT cluster consists of a one-dimensional precision measurement only, which cannot be directly transformed into a three-dimensional point. However, due to the SCT module geometry, which comprises a sandwich module structure with a stereo-angle between two modules, the relation of the two modules together can be used to construct the three-dimensional SpacePoint.

2.2.2.1 Inside-out track reconstruction

The primary pattern recognition in the inner detectors follows an inside-out strategy for the track finding and is realized as a sequence of modules. Many of the modules can be divided into two pattern recognition steps, where the second step only works on the reduced output sample of the first. The inside-out sequence can be repeated several times with different parameters to extend the track reconstruction efficiency, e.g. for dedicated low-p_T tracking.

Primary particles are defined as particles with a mean lifetime of greater than 3×10^{-11} s directly produced in a proton-proton interaction or from the subsequent decays or interactions of particles with a lifetime shorter than 3×10^{-11} s. The tracks reconstructed by the inside-out algorithm are required to have transverse momentum $p_T > 400$ MeV.

SpacePoint seeded track finding The SpacePoint objects from both silicon sub-detectors are used for seeding the track candidate search. This search can be divided into two different tasks, the track seed finding and the track candidate creation. The latter is based on the seeds found in the first step. The track seed

finding can be done with or without a constraint on the longitudinal position z of the estimated track origin. Once the SpacePoint seeds are found, the track candidate creation is started with a road building process. The seeds provide enough directional information to build roads of detector elements. The association of hits from these detector elements uses a Kalman filter technique to form a track candidate. Only about 10% of the seeds are successfully extended to track candidates, which is confirmed in the data [43].

Ambiguity solving The SpacePoint seeded track finding results in a high number of ambiguous track candidates, which have to be resolved before extending them into the outer TRT. Many of these track candidates share hits, are incomplete or describe fake tracks, i.e. tracks where the majority of associated measurements do not originate from the same particle. Therefore the tracks have to be ranked according to their likelihood to describe the real trajectory of particles from the underlying physics event. For the classification of tracks, a track scoring strategy has been developed that involves morphological parameters of the track in addition to the fit quality: different characteristics of a track are hereby represented by a beneficial or penalizing score, which form together an overall track score. In general, each hit associated with the track leads to a better score value to favor fully reconstructed tracks rather than small track segments. Hits which are associated to more than one track are attempted to be resolved. An iterative procedure of ranking, hit re-association and fitting determines the new hit content of the tracks which formerly shared hits: the tracks "compete" for the shared hit. Preference is given to well reconstructed tracks with a high track score. This procedure results in only a small fraction of shared hits on the tracks after the ambiguity solving process. Tracks that fall beyond a certain quality cut are not considered for further processing.

TRT extension The track extension from the silicon detectors into the TRT consists of two steps. The first step steers the extension finding on a single track-by-track basis. The tracks which are resolved by the ambiguity processing are used as inputs to find compatible sets of TRT measurements, the candidate extensions. In a second step, every extended track is evaluated with respect to the pure silicon track. The comparison of the two tracks is based on a combined track fit and

uses the track scoring mechanism to compare the track score of the original track with the one after the fit. The track with the higher score is kept for further processing. The fit in this step can modify the silicon hits by flagging them as "outlier" measurements, which are not used for the final track parameter estimate. In case the track score of the silicon track is higher than the one of the extended version, the silicon track is kept and the TRT hits are added onto the track as outlier measurements.

2.2.2.2 Outside-in track reconstruction

The inside-out sequence of the ID New Tracking relies on a track seed to be found in the silicon detector. Although being very efficient, not all tracks can be found through an inside-out procedure: ambiguous hits can shadow the track seed in the silicon and prevent the score of the silicon seeded track to survive the ambiguity processor on the one hand, and on the other hand, tracks coming from secondary decay vertices further inside the Inner Detector volume (e.g. K_S decays) or from photon conversions may not have any silicon hits (or only an insufficient number) to comply with the inside-out sequence. Clearly, when no candidate track in the silicon detector is found, the extension into the TRT is automatically lost. As a third source for missing the TRT extension, substantial energy loss, mostly of electrons, at outer radii of the silicon seeded track and not known to the road building may guide the extension search into the wrong direction. A second, reverse sequence has therefore been deployed that starts a global pattern recognition in the TRT. Track segments are identified using a standard Hough transform mechanism [83], while a dedicated association tool prevents hits that have already been assigned to tracks in the inside-out procedure to be used again (which saves a significant amount of CPU time).

The TRT segments are then followed back into the silicon detector (*backtracking*), which allows to find small track segments in the silicon part that have been missed in the initial inside-out stage.

2.2.2.3 High-pileup environment

Studies of tracking performance in a low pile-up environment have demonstrated excellent algorithmic performance and good agreement between data and simula-

tion [43, 84] (see section 1.5.4.1).

The increasing detector occupancy with pile-up can result in nearby hits from other particles confusing the pattern recognition algorithm such that the track is not correctly reconstructed. Increased occupancy can lead to an increase in combinatorial fake tracks, i.e. reconstructed tracks which could not be matched to either a primary or secondary particle. Previous studies of the performance of ID reconstruction in high pile-up [85] have indicated that fake tracks can be minimized by tightening the quality requirements on reconstructed tracks. A set of robust requirements is therefore defined by selecting tracks with at least 9 hits in the silicon detectors (Pixel + SCT) and exactly zero holes[4] in the Pixel Detector. If a track passes through an inactive module, this is not counted as a hole, but instead added to the hits used to meet the hit requirement.

The tighter hit requirement may cause a loss of efficiency for some physics channels. Therefore track reconstruction is always performed with the loose requirements, while robust selection is used in some reconstruction algorithms, notably the reconstruction of primary vertices.

2.2.3 Reconstruction of the Primary Event Vertex

The reconstruction of the primary event vertex is done in a very modular way and consists of two main tasks: the vertex finding and the vertex fitting [46, 55]. During the primary vertex finding step, vertex seeds are identified and tracks are associated to these seeds. After this, the vertex fit reconstructs the vertex position and its corresponding error matrix. During the data taking period (2010-2012), ATLAS used a very robust vertex finding and fitting approach: a vertex seed is obtained by finding the global maximum in the distribution of z coordinates of all tracks which are compatible with originating from the interaction region. The z coordinates are expressed with respect to the point of closest approach to the beam spot centre. The beam spot centre is determined periodically during each physics run using an adapted version of the vertex reconstruction. For the vertex fit, a robust χ^2 fitting algorithm is used which takes the vertex seed position and the surrounding tracks as input. The fitter deals with outlying track measurements by iteratively down-weighting their contribution to the overall vertex χ^2. Tracks

[4] A hole is a non-existing but expected measurement point given a track trajectory.

which are incompatible with this vertex are used to seed a new vertex. This iterative procedure is repeated until no unassociated tracks remain or no additional vertex seeds can be reconstructed.

By default, both the finding and the fitting procedure use the knowledge of the beam spot parameters. This has a very large impact on vertices reconstructed in events with low track multiplicities. The primary vertex reconstruction performances have been already discussed in section 1.5.4.2.

2.2.3.1 Scale factors for vertex errors

The description of the vertex errors in data is not necessarily the same as in the Monte Carlo simulation. The estimation of the vertex uncertainty provided by the vertex fit is primarily based on the transverse and longitudinal impact parameter errors provided by the track reconstruction algorithm. The latter errors can also be significantly different in simulation and in data, since these depend on various factors, for instance the correct description of sub-detector hit cluster errors, multiple scattering, ionization energy losses due to material in the detector and the residual misalignment.

A correction to the vertex error provided by the vertex fit can be obtained by defining a scale factor K_x for the errors on the vertex x coordinate, x_{PV}:

$$\sigma_{x_{PV},\text{true}} = K_x \sigma_{x_{PV},\text{fit}} \tag{2.23}$$

where $\sigma_{x_{PV},\text{true}}$ is the correct vertex uncertainty and $\sigma_{x_{PV},\text{fit}}$ is the uncertainty estimated by the vertex fit. Similar scale factors can be defined analogously for the y and z coordinates. The scale factor can then be derived from data by considering a large set of reconstructed primary vertices and making the hypothesis that the tracks used in the vertex fit really do originate from the reconstructed interaction point. By randomly splitting the reconstructed vertices in two, each conserving approximately half the original number of tracks, it is possible to use their separation to get an estimate of their combined intrinsic resolution. Further details can be found in reference [46].

The red curves in figures 2.9 (a) and (b) represent the estimated K_x and K_z scale factors as a function of the number of tracks N_{trk} for $\sqrt{s} = 7$ TeV data. The turn-on behavior of the scale factors in low vertex track multiplicity events may be due to the present dependence of the impact parameter error estimates of

the tracks on their transverse momenta. The asymptotic K_{PV} scale factors are measured to be ≈ 0.95 in the x direction and ≈ 0.92 in the z direction. In figures 2.9 (c) and (d) are reported the estimated K_x and K_z scale factors as a function of the number of tracks N_{trk} for $\sqrt{s} = 8$ TeV data. In this case both the scale factors are compatible with one.

For this study the primary vertex scale factor is put equal to 1. The main reason for this choice is that, at the time of writing, there isn't a precise receipt to apply the primary vertex scale factor, and in addition to that the different scale factors depend very strongly on the sample used to calculate them. In particular depend very much on the number of tracks that are used to reconstruct the vertex and from the p_T of these tracks. Furthermore the situation is even more complex, because the scale factor refers to the track contribution to the vertex error, and the fact they are near to one is already encouraging. But the vertex used in this study includes the beam spot constraint, which is independent on track resolution and is actually dominant for low p_T and low multiplicity vertices. That should naturally bring the scale factor near to one. It's also true that the main historical reason to have a "significant" scale factor was during the ATLAS commissioning phase, where tracking was run with artificially increased errors, to compensate for potential misalignment, and at the time of writing we are not in this situation anymore.

2.3 Measurement of the impact parameter resolution of charged particle

2.3.1 Unbiased impact parameters

The transverse and longitudinal impact parameter (IP) of a track, d_0 and $z_0 \sin\theta$, i.e. its distance of closest approach respectively on the transverse and longitudinal plane to the primary vertex, is a key-ingredient for discriminating tracks originating from displaced vertices from tracks originating from the primary vertex. The distances d_0 and $z_0 \sin\theta$ are measured with respect both to the primary vertex in an unbiased way (d_{PV} and $z_{PV} \sin\theta$): if the track under consideration was used for the primary vertex determination, it is first removed from the primary vertex which is subsequently refitted, and the impact parameters are computed with respect to

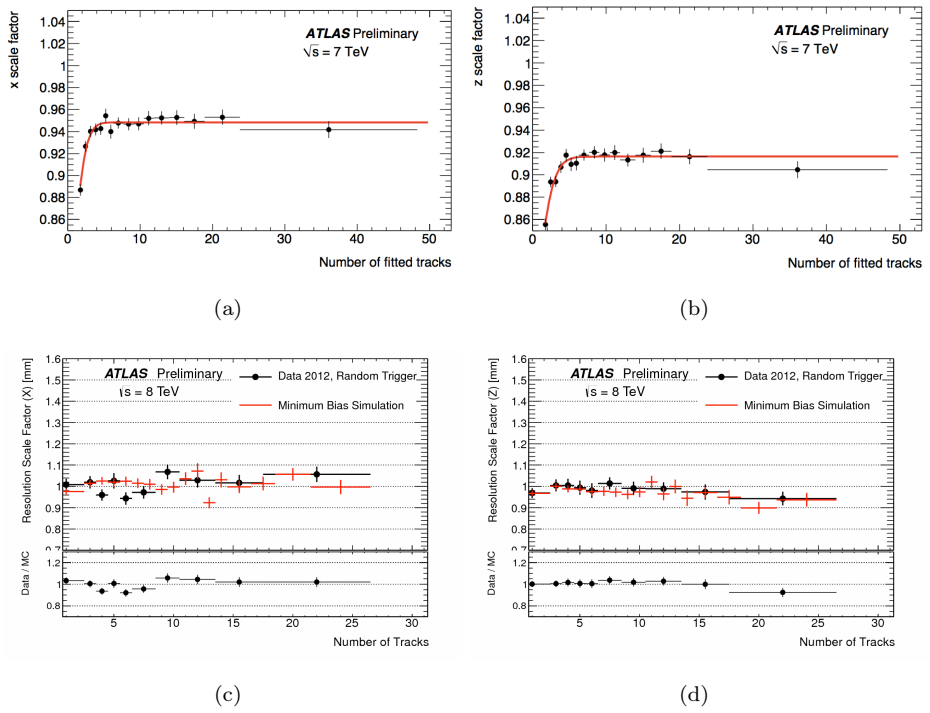

Figure 2.9: estimated K_x (left column) and K_z (right column) scale factors as a function of the number of tracks N_{trk} using the split-vertex technique. The upper line plots correspond to $\sqrt{s} = 7$ TeV data, while the lower line plots to $\sqrt{s} = 8$ TeV data

this new vertex.

2.3.2 Primary Vertex contribution to impact parameter resolution

Due to the fact that both experimental and simulated data have a displaced beam spot position from the centre of the detector and the primary interaction point has a spread itself, it is not possible to measure the impact parameter resolution $\sigma_{IP^{\text{track}}}$ directly, so relating the impact parameter distributions to the purely track-based IP^{track} resolution is not straightforward since it is convolved with the resolution on the primary vertex position: $\sigma^2_{IP} = \sigma^2_{IP^{\text{track}}} + \sigma^2_{PV}$, where σ^2_{PV} is the projection

	run	duration [s]	integrated luminosity [nb^{-1}]	μ range	events
$\sqrt{s} = 7$ TeV data	182456	35	22765	4.2-5.9	15.3×10^6
$\sqrt{s} = 8$ TeV data	207620	65	182653	8.5-29	46.7×10^6

Table 2.2: Details of $\sqrt{s} = 7$ TeV and $\sqrt{s} = 8$ TeV data samples considered

of the primary vertex error along the axis of closest approach of the track to the primary vertex on the transverse or longitudinal plane.

The method applied in this study to unfold the effect of the primary vertex resolution from the measurement of the impact parameter resolution itself is described in section 2.3.6.

2.3.3 Data samples and event selection

2.3.3.1 Data

This study is based on a limited fraction of proton-proton collisions at $\sqrt{s} = 7$ TeV and $\sqrt{s} = 8$ TeV data collected respectively in 2011 and 2012 with nominal magnetic field conditions. These samples contain a sufficient number of tracks for this study and they were selected from data-periods in which the detector and the LHC conditions were stable. For each run only those luminosity blocks (periods corresponding to about two minutes of data-taking) satisfying standard Inner Detector data quality requirements (i.e. all components of the Inner Detector were fully operational [86]) were analysed. In particular the events considered are selected by all the triggers that require jets, missing transverse energy or tau leptons. Further details about the data samples considered are reported in table 2.2.

2.3.3.2 Monte Carlo

The simulated QCD samples from proton-proton collisions at $\sqrt{s} = 7$ TeV and $\sqrt{s} = 8$ TeV used in this study are generated respectively with PYTHIA6.4 and PYTHIA8 [87]. In particular the JX QCD for 2011 simulation at $\sqrt{s} = 7$ TeV and the JZXW QCD for 2012 simulation at $\sqrt{s} = 8$ TeV samples, also referred to as "di-jet" samples, are used. They are divided into sub-samples containing reconstructed jets above various E_T thresholds, as reported in table 2.3.

sample	E_T range [GeV]
J0	8-17
J1	17-35
J2	35-70
J3	35-70
J4	70-140
J5	280-560
J6	560-1120
J7	1120-2240
J8	2240-4480

Table 2.3: List of E_T ranges of PYTHIA di-jet sub-samples

For data-Monte Carlo comparisons the simulated samples J4 QCD and JZ4W QCD, respectively for $\sqrt{s} = 7$ TeV and $\sqrt{s} = 8$ TeV proton-proton collisions, has been used because is the sample that matches reasonable better data. This will be shown later in section 2.3.9.3.

2.3.3.3 Event selection

The track selection for this study is designed to select well-measured tracks and reject fake tracks and tracks from long-lived particles (K^0_S, Λ or other hyperon decays) and material interactions (photon conversions or hadronic interactions). First of all the selected tracks must be included in the primary vertex reconstruction. Moreover at least seven precision hits (pixel or micro-strip hits) are required in the silicon detectors. In addition, at least two hits in the pixel detector are required. A successful extension of the track into the TRT detector is not explicitly required, but is fulfilled by most tracks within its acceptance. Only tracks with $p_T > 500$ MeV and $|\eta| \leqslant 2.5$ are considered. In order to suppress cosmic-ray and beam-related backgrounds, events were required to contain at least one primary collision vertex with at least ten tracks.

The total number of tracks after these cuts is about 162 millions for 2011 $\sqrt{s} = 7$ TeV data and about 350 million for 2012 $\sqrt{s} = 8$ TeV data. The simulated tracks are about 90 millions and 150 millions respectively for 2011 and 2012 Monte Carlo.

2.3.4 Primary vertex properties and track parameters distributions

The position of the primary vertex along the beam axis for 2012 data and simulation is shown in figure 2.10 (a). It shows significant discrepancies between the beam spot dimension in data and simulation. Moreover a significant discrepancy between data and Monte Carlo is clear visible in the distribution in figure 2.10 (b) of the number of pile-up interaction vertices in each event. This discrepancy is due to the fact that the considered simulation has been optimized for more recent data collected with higher pile-up conditions.

Both the longitudinal position of the interaction point and the pile-up vertices can influence some properties of the tracks, for example the number of hits on the tracks in the pixel or SCT detectors. A weighting technique is deployed, based on the ration between data and Monte Carlo distributions, which reweighs both the distributions in the Monte Carlo simulation to the corresponding distribution measured in the data.

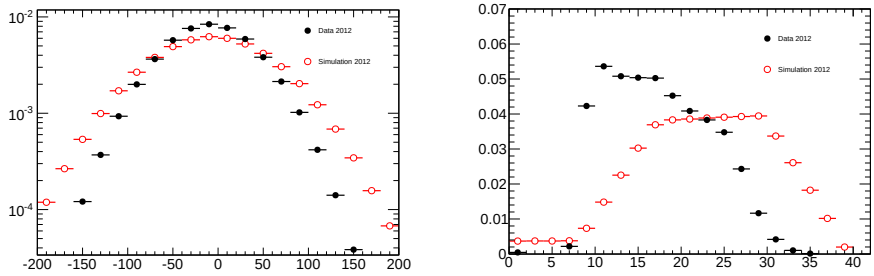

(a) z-position of primary vertex (mm)

(b) number of pile-up vertices

Figure 2.10: z-position of primary vertex (a) and number of pile-up vertices (b) in collisions at $\sqrt{s} = 8$ TeV. The data (solid black dots) are compared to the Monte Carlo simulation (empty red dots)

Figure 2.11 shows the distributions of the basic track parameters ϕ (a), η (b) and the transverse momentum p_T (c) in proton-proton collisions at $\sqrt{s} = 8$ TeV for tracks passing the selection cuts listed in section 2.3.3.3. The overall agreement between the data and the Monte Carlo simulation is very good for the ϕ distribu-

tion. The two dips are due to disabled modules in the pixel b-layer. Both η and p_T distribution show a discrepancy between data and Monte Carlo. The same weighting technique adopted previously has been applied for the p_T of the tracks. This technique has not been applied for the η distribution and has been used only for 2012 $\sqrt{s} = 8$ TeV Monte Carlo because at the time of writing it is still preliminary.

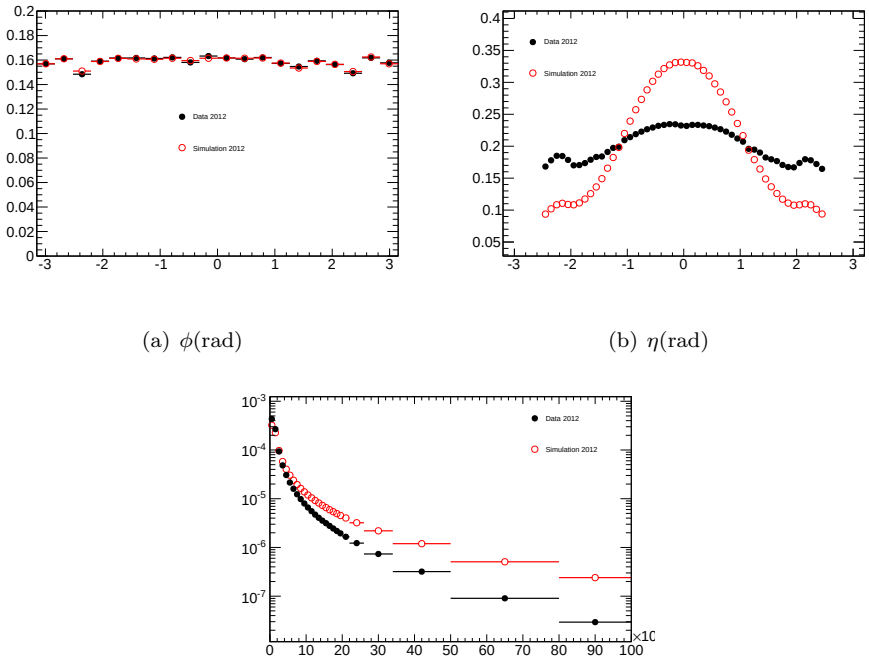

(a) ϕ(rad)

(b) η(rad)

(c) p_T(GeV)

Figure 2.11: Track parameters in collisions at $\sqrt{s} = 8$ TeV: ϕ (a),η (b) and the transverse momentum p_T (c). The data (solid black dots) are compared to the Monte Carlo simulation (empty red dots)

In figure 2.12 are shown the distributions of the transverse and longitudinal impact parameters, d_0 and $z_0 \sin\theta$, of tracks fulfilling the selection cuts. The impact parameters are measured with respect to the primary event vertex in an unbiased way as explained in section 2.3.1. The simulated distributions of d_0 and $z_0 \sin\theta$ are slightly narrower compared to the data. It should be noted that both the distributions shown consists of the purely track-based d_0 resolution convoluted with

the resolution of the primary vertex position (see equation 2.3.2) that is different between data and simulation, as shown in figure 2.10. In addition, a small fraction of tracks may not originate from the primary interaction vertex.

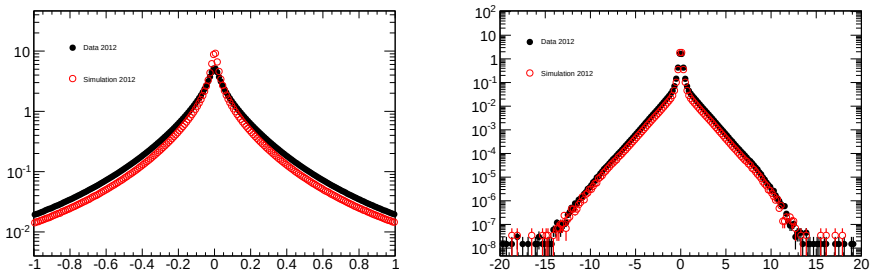

(a) d_0 (mm) (b) $z_0 \sin\theta$ (mm)

Figure 2.12: Distributions of the transverse and longitudinal impact parameters, d_0 (a) and $z_0 \sin\theta$ (b), in proton-proton collisions at $\sqrt{s} = 8$ TeV for tracks passing the selection cuts. The data (solid black dots) are compared to the Monte Carlo simulation (empty red dots)

2.3.5 Tracks classification

The tracks are divided into different categories of transverse momentum, pseudorapidity and hit content to ensure a quasi constant resolution within a single subset. Moreover the inclusive impact parameter distributions shown in figure 2.12 are clearly non Gaussian. A classification of the tracks leads to more reasonably Gaussian distributions, even if not definitively.

Both the transverse and the longitudinal impact parameter (respectively d_0 and $z_0 \sin\theta$) resolution has been measured for each track category. The different tracks categories are obtained with a binning of these variables:

- η
- $1/p_T\sqrt{\sin\theta}$
- number of b-layer hits and shared hits

The variables choice is directly connected to what was previously explained about charged particle tracking in a magnetic field in section 2.1. In fact the pseudorapidity η has been chosen because the intrinsic detector resolution and hit pattern depends on it, and $1/p_T\sqrt{\sin\theta}$ has been chosen instead of bare p_T because it is directly linked to the multiple scattering contribution to the impact parameter resolution which is modeled by (see section 2.1.3):

$$\sigma_{IP} = \sqrt{a^2 + \frac{b^2}{p^2(\sin\theta)^3}} \tag{2.24}$$

Finally, the third category select tracks with zero, exactly one, and more than one b-layer hits. Moreover the high p_T jets form a very dense environment. There is a non-negligible probability that several hits merge into a single indistinguishable cluster (*shared hits*). The effect of a merged hit is an increased hit position error. If the shared hit is in the b-layer this leads to a deterioration of the impact parameter resolution. For this reason, each of these sub-categories is itself divided in sub-categories selecting tracks that have zero, one shared hit in the b-layer with another track, and one or more shared hits in the other silicon layers.

The most relevant category is the one with tracks that have one b-layer hit and zero shared hits. In the following I will discuss the results mainly for this category.

At the beginning of this study, the third category wasn't divided in sub-categories reflecting the presence of shared hits in the silicon detectors. Only a classification in the number of b-layer hits was made. The reason why the sub-categories has been added will be clear in section 2.3.9.3, where the study of the jet-p_T systematic effect on the performed impact parameter resolution measurement will be detailed.

Note that each track belongs exclusively to one category.

2.3.6 Unfolding of primary vertex errors

As already described, the impact parameter is expressed with respect to the primary vertex. This has the disadvantage of adding the primary vertex resolution to the intrinsic resolution of the track. Moreover, even the unbiased primary vertex resolution depends on the p_T and η of the single track, due to possible correlations of this track with the remaining tracks present in the same event: this potentially distorts the distribution of impact parameter resolution as a function of p_T and η.

The main aim of this section is to unfold the effect of the primary vertex resolution from the measurement of the impact parameter resolution itself.

2.3.6.1 Unfolding method

The method relies on an iterative unfolding procedure. The core of the impact parameter resolution can be described, e.g. for the transverse impact parameter, by the function:

$$R(d_0) = \int \exp\left[-\frac{1}{2}\frac{d_0^2}{\sigma_{d_0}^2 + \sigma_{PV}^2}\right] P\left(\sigma_{PV}\right) d\sigma_{PV} \tag{2.25}$$

where the integrand is a Gaussian with a width corresponding to the square root of the squared sum of the intrinsic track resolution σ_{d_0} and of the resolution of the primary vertex σ_{PV}. This distribution is integrated over the distribution of values of resolutions of the primary vertex $P\left(\sigma_{PV}\right)$ corresponding to all the tracks considered. Since the primary vertex fit uses the beam spot constraint, the beam spot width is already included in the estimated uncertainty of the primary vertex. Starting from the distribution of equation 2.25, it is possible to obtain the unfolded distribution by multiplying the measured impact parameter of each track by a correction factor. E.g. for the transverse impact parameter w.r.t. PV:

$$d_{PV} \to d_{PV}\sqrt{\frac{(K\sigma_{d_0})^2}{(K\sigma_{d_0})^2 + \sigma_{PV}^2}} \tag{2.26}$$

where K is a corrective factor that depends on the iteration index. For the first iteration K is equal to one. For each iteration, $\sigma_{d_{PV}}$ can be evaluated fitting each d_{PV} distribution and for the i-th iteration it should be:

$$(\sigma_{d_{PV}})_i = K_i\sigma_{d_0}\sqrt{\frac{1 + \frac{(K_{i+1}\sigma_{d_0})^2}{\sigma_{PV}^2}}{1 + \frac{(K_i\sigma_{d_0})^2}{\sigma_{PV}^2}}} \tag{2.27}$$

and then calculate the new K for the next iteration.

The iterative procedure ends when the fitted $\sigma_{d_{PV}}$ is stable within approximatively 0.01%. About 5 iterations are needed to make the K factor converge to stable values. These stable values goes from ~ 0.8 to ~ 1.2.

This procedure is a generalization of the one described in reference [88].

2.3.6.2 Validation of the method

The method has been validated using Monte Carlo simulations (*closure test*) by comparing the unfolded resolution to the true track resolution. The figure 2.13 shows e.g. the transverse impact parameter d_{PV} resolution as a function of track η grouped in bins of increasing $1/p_T\sqrt{\sin\theta}$ (a) and the zoom of the first two $1/p_T\sqrt{\sin\theta}$ bins (b), i.e. $1/p_T\sqrt{\sin\theta} > 10$ GeV and > 20 GeV. At high p_T the effect is larger because the primary vertex resolution contributes by a large fraction to the overall error, while the multiple scattering dominates the low p_T region and the primary vertex uncertainty is negligible. The Monte Carlo "pure" (before unfolding) distribution of the reconstructed d_{PV} is different from the MC true prediction, but after 5 iterations, the unfolded resolution agrees with the Monte Carlo truth. The same level of agreement has been observed for the longitudinal impact parameter resolution.

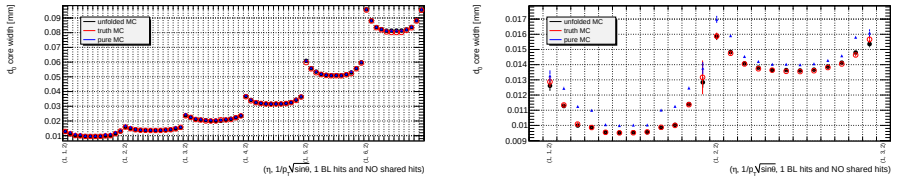

(a) (b)

Figure 2.13: Validation of the unfolding method for e.g. the transverse impact parameter measured core width for tracks with one b-layer hit in the Pixel Detector and 0 shared hits in the silicon detectors as a function of track η grouped in bins of increasing $1/p_T\sqrt{\sin\theta}$ (a). The (b) plot is a zoom of the first 2 bins at hight tracks p_T, i.e. $1/p_T\sqrt{\sin\theta} > 10$ GeV. The unfolded Monte Carlo (black dots), after 5 iterations, are compared to the Monte Carlo truth (red empty dots) and to the "pure" Monte Carlo, after 0 iterations (blue triangles). These plots are made with simulated tracks at $\sqrt{s} = 8$ TeV proton-proton collisions

2.3.7 Impact parameter distribution fit procedure

To evaluate the width of the core of the impact parameters distributions, and hence estimate the impact parameter resolution, a Gaussian fit on the whole distribution

is first applied and the temporary mean_{tmp} and σ_{tmp} are obtained. The second step consists in defining a new fit range within $\text{mean}_{\text{tmp}} \pm 2 \cdot \sigma_{\text{tmp}}$ and finally refit the distribution within the new range. The width of 2σ was chosen to avoid the contribution from secondary particles which populate the tails.

In figure 2.14 is shown the Gaussian fit applied on the core of the transverse impact parameter distributions for tracks in a central η bin ($0 < \eta < 0.25$) with one b-layer hit in the Pixel Detector and 0 shared hits in the silicon detectors, and for two different $p_T\sqrt{\sin\theta}$ bins: $p_T\sqrt{\sin\theta} > 20$ GeV (left column) and 0.4 GeV$< p_T\sqrt{\sin\theta} < 0.5$ GeV (right column). The unfolded Monte Carlo (top row), after 5 iterations, and the "pure" Monte Carlo (middle row), i.e. after 0 iterations, are compared to the Monte Carlo truth (bottom row). It's immediately visible that the Gaussian fits follow quite well the shape of the core of the distributions, while the tails are responsible for making the overall distribution not a pure Gaussian. In principle, in order to try to represent also the tails, it is possible to fit the distributions with a double Gaussian function, but this is not the case of the study I'm describing. In fact, the goal of this study is to provide the computed impact parameter performance to a general user that needs these informations for a specific physics analysis, e.g. the smearing of the simulated impact parameter resolutions b-tagging (see section 2.3.10). So in the case of a double Gaussian fit it becomes difficult to manage with two different values for the measured impact parameter resolution of each track.

In addition, the plots in figure 2.14 show once again that the method applied to unfold the primary vertex, is much more effective at high p_T. This fact can be verified comparing the fit output sigmas: at high p_T the sigma converges to the MC truth value, while at low p_T it remains practically unchanged.

2.3.8 Unfolded impact parameter resolution

The unfolding procedure described in section 2.3.6 has been applied to data, in order to derive the unfolded track transverse and longitudinal impact parameter resolutions for each track category (see section 2.3.5) and to compare it to the expectations provided by Monte Carlo simulations.

In figure 2.15 is shown the comparison between data and simulation for proton-proton collisions at $\sqrt{s} = 7$ TeV for both transverse and longitudinal impact pa-

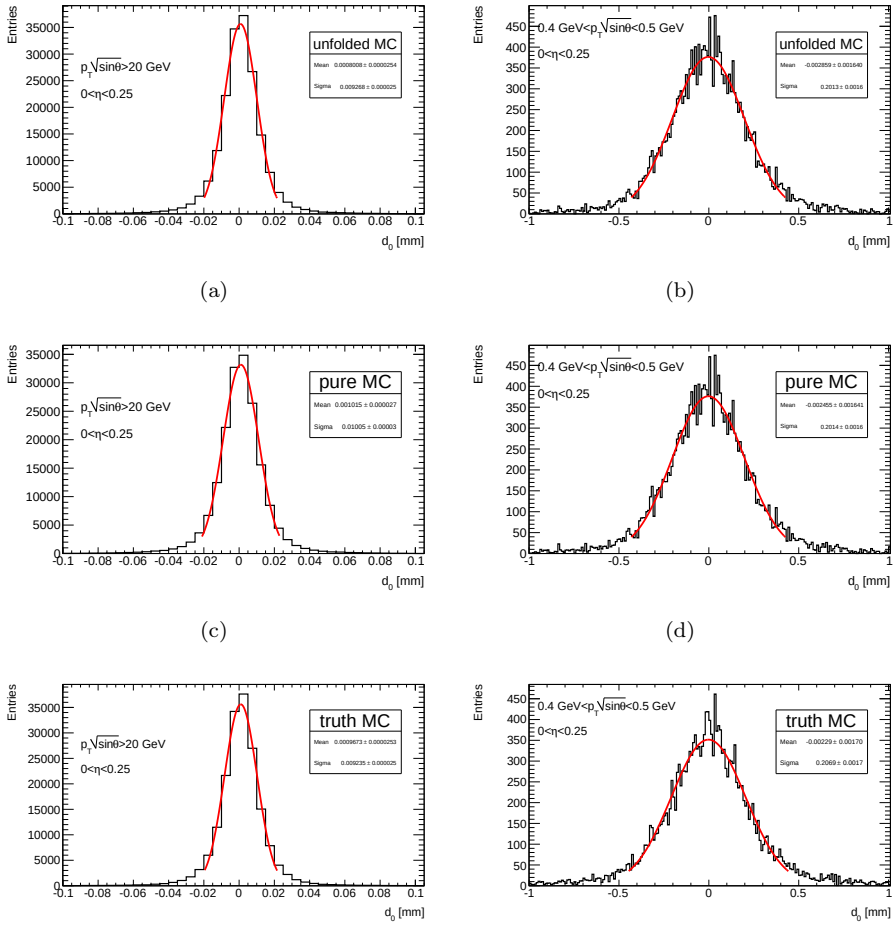

Figure 2.14: Gaussian fit applied on the core of the transverse impact parameter distributions for tracks in a central η bin ($0 < \eta < 0.25$) with one b-layer hit in the Pixel Detector and 0 shared hits in the silicon detectors, and for two different $p_T\sqrt{\sin\theta}$ bins: $p_T\sqrt{\sin\theta} > 20$ GeV (left column) and 0.4 GeV$< p_T\sqrt{\sin\theta} < 0.5$ GeV (right column). The unfolded Monte Carlo (top row), after 5 iterations, and the "pure" Monte Carlo (middle row), i.e. after 0 iterations, are compared to the Monte Carlo truth (bottom row)

rameter measured core width for tracks with one b-layer hit in the Pixel Detector and 0 shared hits in the silicon detectors as a function of the pseudorapidity η for two different $p_T\sqrt{\sin\theta}$ regions. The two regions are: $p_T\sqrt{\sin\theta} > 20$ GeV and 0.4 GeV$< p_T\sqrt{\sin\theta} < 0.5$ GeV. For high p_T data tracks the transverse impact parameter resolution increases from $\sim$ 11 μm in the barrel region to $\sim$ 13 μm in the end-caps, while for low p_T data tracks it increases from $\sim$ 200 μm in the barrel region to $\sim$ 250 μm in the end-caps. On the other hand for high p_T data tracks the longitudinal impact parameter resolution decreases from $\sim$ 110 μm in the barrel region to $\sim$ 30 μm in the end-caps, while for low p_T data tracks it decreases from $\sim$ 320 μm in the barrel region to $\sim$ 240 μm in the end-caps. The main reason for this behavior is that in the barrel region the longitudinal impact parameter resolution is dominated by the intrinsic z dimension of the pixels. In the end-cap regions instead, a charged particle crosses with high probability more than one pixel, leading to a more precise reconstruction of the hit. In addition, the track parameter z_0 is more diluted in the forward region by the $\sin\theta$ coefficient, which is approximatively one in the central region.

The Monte Carlo describes quite well the data especially for low p_T tracks, where the multiple scattering and ionization loss are dominant, meaning that the material amount in the Inner Detector is well described, but the discrepancy between data and MC is bigger for high p_T tracks, where the intrinsic Inner Detector resolution is dominant. In this case for the transverse impact parameter the additional contribution with respect to what is predicted from the Monte Carlo is about 1 μm in the barrel region and about 2 μm in the end-caps, while for the longitudinal impact parameter the data are well described by the Monte Carlo in the barrel region, but the additional contribution with respect to what is predicted from the Monte Carlo is about 10 μm in the end-caps.

The discrepancies shown between data and simulation for high p_T tracks points to either or both the presence of residual misalignments in the detector and the simulation accuracy of the intrinsic detector resolution. In the first case, even if the accuracy of the alignment has been significantly improved (see section 1.5.4.4), the discrepancies might be explained by residual misalignment of the inner tracking detector, while an ideally aligned detector is assumed in the simulation. On the other hand, in the second case, the simulation of the intrinsic detector resolution is extremely sensitive to how is modeled the detector. This is especially relevant

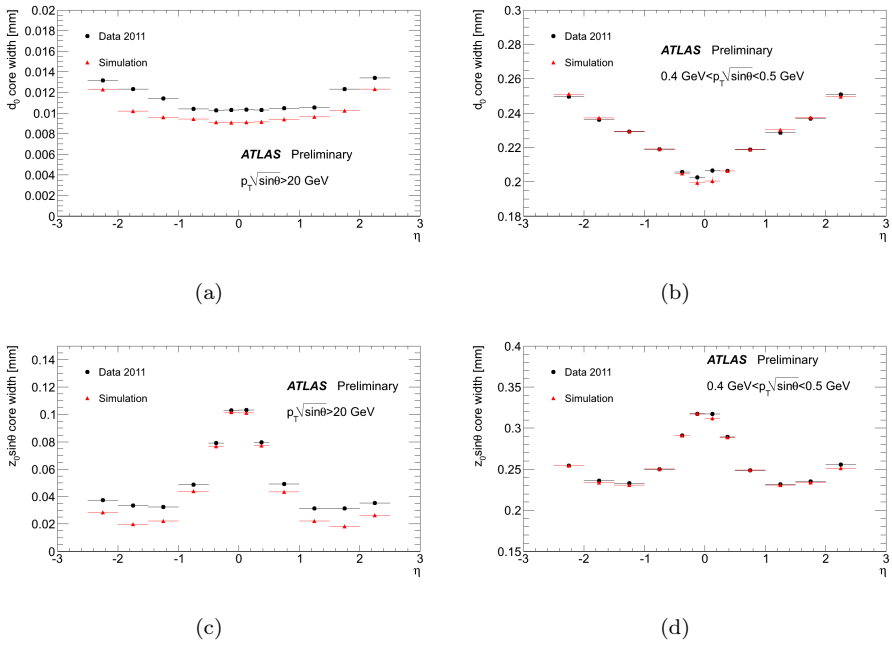

Figure 2.15: 2011 $\sqrt{s} = 7$ TeV proton-proton collisions: transverse and longitudinal impact parameter measured core width for tracks with one b-layer hit in the Pixel Detector and 0 shared hits in the silicon detectors as a function of the pseudorapidity η for two different $p_T\sqrt{\sin\theta}$ regions: $p_T\sqrt{\sin\theta} > 20$ GeV (a,c) and 0.4 GeV$< p_T\sqrt{\sin\theta} < 0.5$ GeV (b,d). The data (black dots) are compared to the Monte Carlo simulation (red triangles)

because the position reconstruction is performed by a neural network algorithm, which is expected to provide an excellent resolution, but need to be trained on simulated samples. This dependence on simulation may results in an optimistic estimation of achievable resolution. E.g. figure 2.16 shows that the simulation predicts a slightly different cluster size (of few %) with respect to the one measured from data. The small difference is due to the fact that the Lorentz angle in the simulation is slightly larger than in the data. This can induce to a little disagreement of the intrinsic detector resolution simulation.

At the moment is not possible to understand which is the most relevant of these two effects, so further deeper analysis is required.

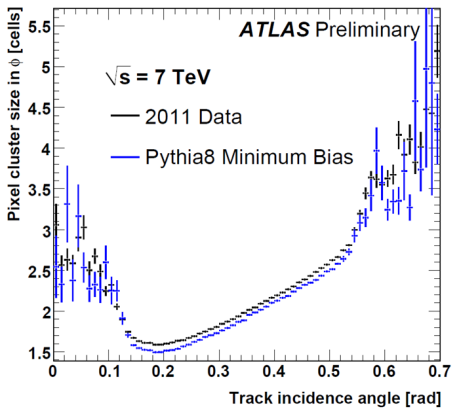

Figure 2.16: Data-MC comparison of pixel cluster size as a function of the track incident angle in $R\phi$ direction for 2011 data and Pythia8 simulation. The agreement in cluster size vs angle is good, the small difference is due to the fact that the Lorentz angle in the simulation is slightly larger than in the data

In figure 2.17 is shown the comparison between data and simulation for proton-proton collisions at $\sqrt{s} = 7$ TeV for both transverse and longitudinal impact parameter measured core width for tracks with one b-layer hit in the Pixel Detector and 0 shared hits in the silicon detectors as a function of $1/p_T\sqrt{\sin\theta}$ for two different η regions. The two regions are: $0 < \eta < 0.25$ and $1 < \eta < 1.5$. These plots shows a general good agreement between data and Monte Carlo simulation. In particular, looking at the slope of the curves, is clear once again that a good description of the amount of the material in the Inner Detector has been achieved. Furthermore,

note that the asymptotic values (high p_T tracks) of both the transverse and the longitudinal impact parameter core widths are compatible with the ones reported in figure 2.15.

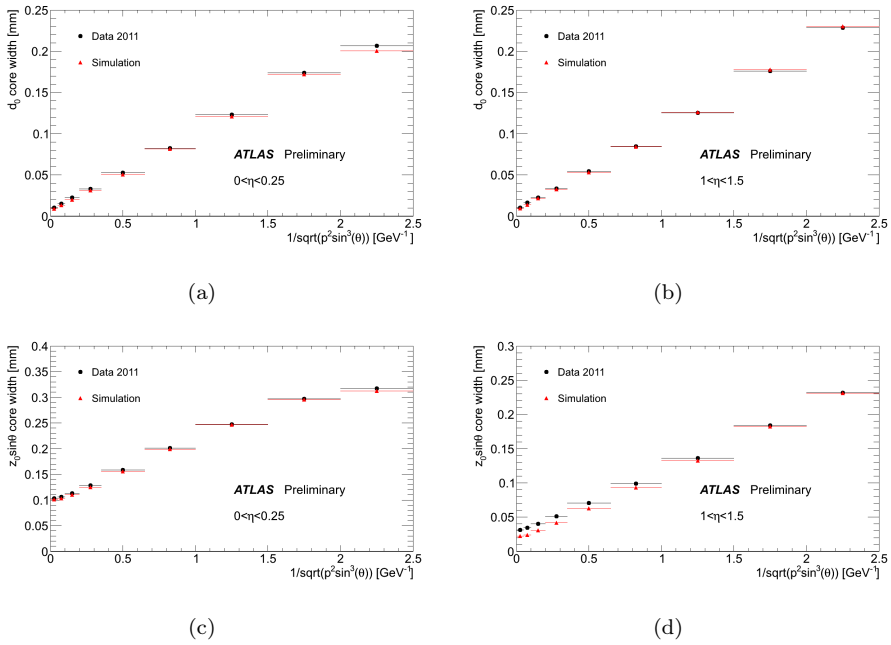

Figure 2.17: 2011 $\sqrt{s} = 7$ TeV proton-proton collisions: transverse and longitudinal impact parameter measured core width for tracks with one b-layer hit in the Pixel Detector and 0 shared hits in the silicon detectors as a function of $1/p_T\sqrt{\sin\theta}$ for two different η regions: $0 < \eta < 0.25$ (a,c) and $1 < \eta < 1.5$ (b,d). The data (black dots) are compared to the Monte Carlo simulation (red triangles)

The transverse and longitudinal impact parameter resolution has been measured also for 2012 data at $\sqrt{s} = 8$ TeV proton-proton collisions.

In figure 2.18 is shown the comparison between data and simulation for both transverse and longitudinal impact parameter measured core width for tracks with one b-layer hit in the Pixel Detector and 0 shared hits in the silicon detectors as a function of the pseudorapidity η for the same two different $p_T\sqrt{\sin\theta}$ regions shown for 2011 results.

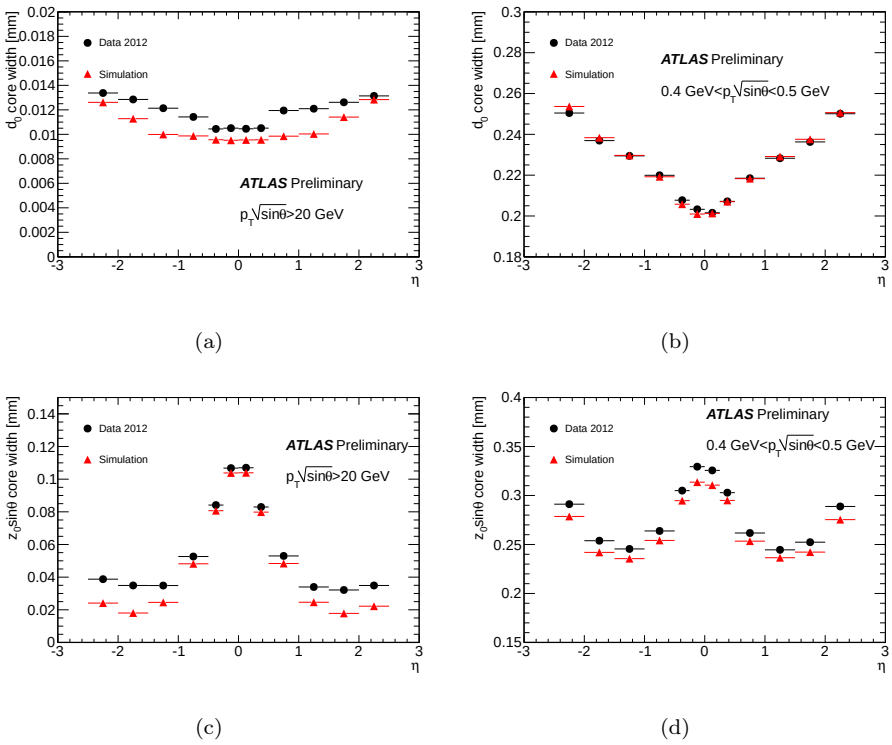

Figure 2.18: 2012 $\sqrt{s} = 8$ TeV proton-proton collisions: transverse and longitudinal impact parameter measured core width for tracks with one b-layer hit in the Pixel Detector and 0 shared hits in the silicon detectors as a function of the pseudorapidity η for two different $p_T\sqrt{\sin\theta}$ regions: $p_T\sqrt{\sin\theta} > 20$ GeV (a,c) and 0.4 GeV$< p_T\sqrt{\sin\theta} < 0.5$ GeV (b,d). The data (black dots) are compared to the Monte Carlo simulation (red triangles)

In figure 2.19 is shown the comparison between data and simulation for both transverse and longitudinal impact parameter measured core width for tracks with one b-layer hit in the Pixel Detector and 0 shared hits in the silicon detectors as a function of $1/p_T\sqrt{\sin\theta}$ for $0 < \eta < 0.25$ and $1 < \eta < 1.5$ as for 2011 data.

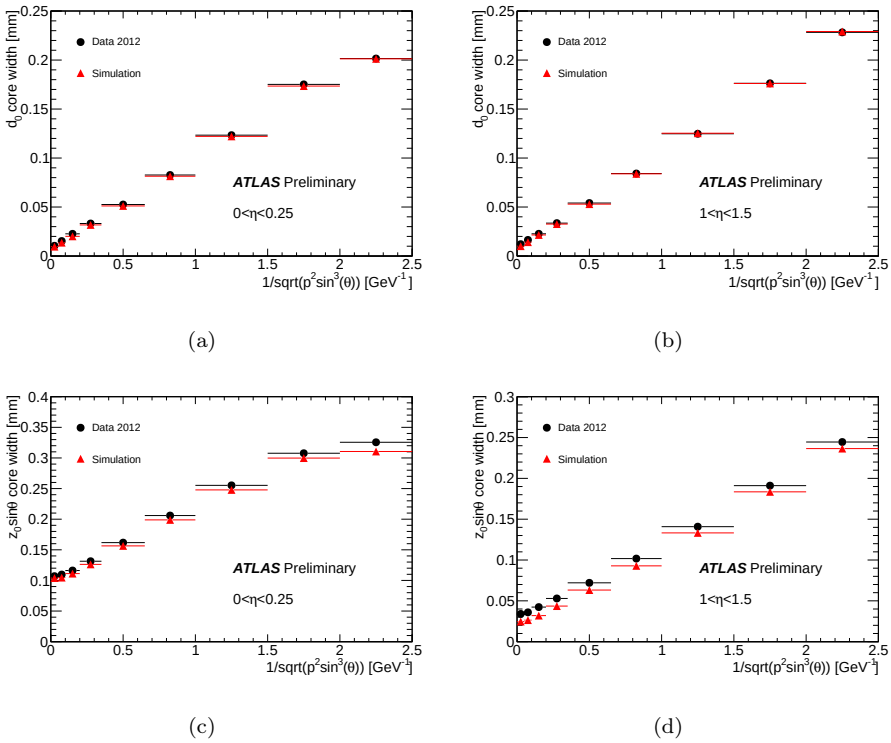

Figure 2.19: 2012 $\sqrt{s} = 8$ TeV proton-proton collisions: transverse and longitudinal impact parameter measured core width for tracks with one b-layer hit in the Pixel Detector and 0 shared hits in the silicon detectors as a function of $1/p_T\sqrt{\sin\theta}$ for two different η regions: $0 < \eta < 0.25$ (a,c) and $1 < \eta < 1.5$ (b,d). The data (black dots) are compared to the Monte Carlo simulation (red triangles)

The values of both the transverse and longitudinal impact parameter core widths for $\sqrt{s} = 8$ TeV proton-proton collisions are compatible with what has been obtained for 2011 tracks. This fact is surely expected because the classification of the tracks basically makes this measurement independent from the center

of mass energy of the proton-proton collisions. Furthermore, it is clear that the same comments made for 2011 results are applicable also for 2012 data apart from a bigger discrepancy between data and simulation in the longitudinal impact parameter resolution in the low $p_T\sqrt{\sin\theta}$ region. The additional contribution with respect to what is predicted from the Monte Carlo is about 20 μm both in the barrel region and in the end-caps. This discrepancy has not been understood yet, but the problem is under investigation. One of the possible reasons could be an aging effect that slightly alters the uniformity of the electric field applied to the depletion region of the silicon detectors.

In all 2011 and 2012 plots only the statistical error is associated to each point, often smaller than the point itself. In section 2.3.9 studies of the most important systematic effects that has been performed are detailed.

It is very interesting to compare the results just presented with the expected performance of the ATLAS Inner Detector, presented in 2008 [55], for what concern the transverse and longitudinal impact parameter resolution measurement. Figure 2.20 shows the transverse (a) and longitudinal (b) impact parameter resolutions for isolated pions[5], all without a beam constraint and assuming the effects of misalignment, miscalibration and pile-up to be negligible. The resolutions are taken as the RMS evaluated over a range which includes 99.7% of the data (corresponding to $\pm 3\sigma$ for a Gaussian distribution). The TRT measurements are included in the track fits for tracks with $|\eta| < 2$, beyond which there are no further TRT measurements. The expected transverse impact parameter resolution is compatible with the measurement presented in this thesis, while the measured longitudinal impact parameter resolution is much better than the expected values, especially for tracks with high p_T and high η. Table 2.4 shows the values of the impact parameters measured and expected resolution for high p_T tracks in two η regions, corresponding to the barrel and end-caps.

2.3.9 Systematic effects

In addition to the statistical uncertainty, which is quite small because of the high statistics available, there are some systematic effects that can have an impact on the performed measurement. The considered systematic effect arises from the impact

[5] Muons suffer less from interactions and hence provide the best reference

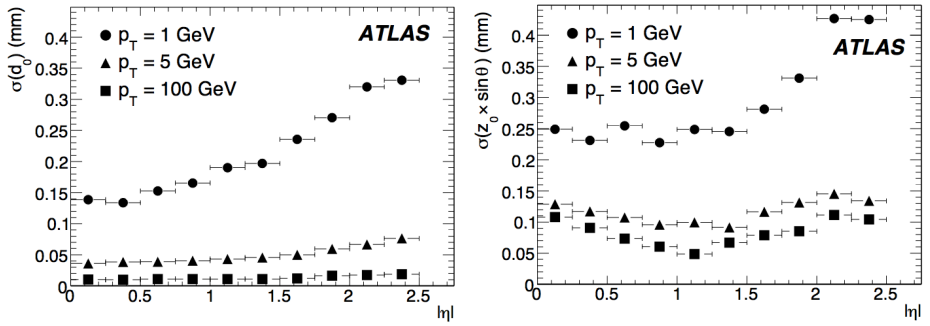

(a) (b)

Figure 2.20: Transverse (a) and longitudinal (b) impact parameter resolution as a function of $|\eta|$ for pions with $p_T = 1$, 5 and 100 GeV

		barrel	end-cap
Measured	d_0 [μm]	11	13
	$z_0 \sin\theta$ [μm]	110	30
Expected	d_0 [μm]	10	12
	$z_0 \sin\theta$ [μm]	110	70

Table 2.4: Measured and expected impact parameter resolutions for tracks with high p_T. The values are shown for two η regions, corresponding to the Inner Detector barrel and end-caps

parameter fit procedure, the pile-up level, and the jet-p_T of the sample.

In this section I'll show only the results for the transverse impact parameter, but the study has been performed also for the longitudinal impact parameter and very similar results has been obtained.

2.3.9.1 Impact parameter fit procedure

As discussed in section 2.3.7, to extract the resolutions, the distributions of the impact parameters have been fitted in each bin with a Gaussian function within 2σ of their mean. In particular the choice of the fit coefficient of 2σ to extract the core resolution of the impact parameters is arbitrary. In principle, the impact parameter distributions width depends on the fit coefficient applied, precisely because of the non gaussian shape of the distributions, mainly due to the presence of large tails populated by tracks from secondary or badly measured particles.

Three different fit coefficients have been applied to the fit procedure: 1.5, 2 and 3. In all these cases the closure test on Monte Carlo[6] of the method applied for the unfolding of the primary vertex contribution to impact parameter resolution has been performed (see figure 2.21). In all the cases 5 iterations are needed to make the impact parameter core width converge to stable values, and after them the unfolded impact parameters reproduce well the Monte Carlo truth prediction for all the three different fit coefficients applied.

Figures 2.22 and 2.23 show the comparison respectively of the simulated and the measured transverse impact parameter core width as a function of the pseudorapidity η for two different $p_T\sqrt{\sin\theta}$ regions ($p_T\sqrt{\sin\theta} > 20$ GeV and 0.4 GeV$< p_T\sqrt{\sin\theta} < 0.5$ GeV), having applied the three different fit coefficients. Simulated tracks from proton-proton collisions at $\sqrt{s} = 7$ TeV with one b-layer hit in the Pixel Detector have been used. It is clear from these plots that the impact parameter core widths depend on the fit coefficient applied. As expected, the core width increases with the increasing fit coefficient due to the fact that the contribution to the fit of the tails becomes larger. Anyhow, in both data and Monte Carlo, for high p_T tracks, only a little discrepancy exist in the barrel region having applied 1.5 and 2 as fit coefficients, while in the end-caps regions, the discrepancies between the three cases are of the order of 1-2 μm. For low p_T tracks the three cases differ in

[6]The 2011 Monte Carlo simulation sample has been used for this study.

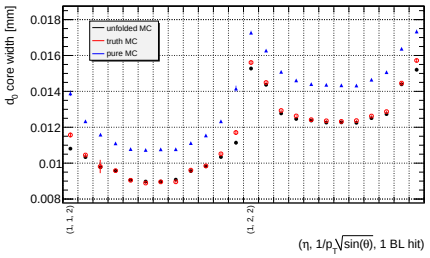

(a) Fit coefficient = 1.5

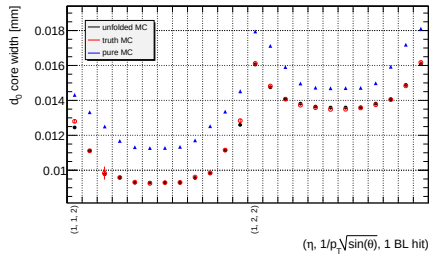

(b) Fit coefficient = 2

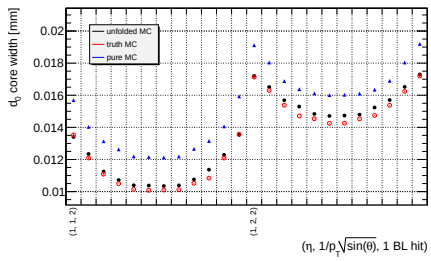

(c) Fit coefficient = 3

Figure 2.21: Closure test on Monte Carlo of the primary vertex unfolding method described in section 2.3.6 having applied three different fit coefficients: 1.5 (a), 2 (b) and 3 (c). The transverse impact parameter measured core width for tracks with one b-layer hit in the Pixel Detector as a function of track η grouped in the two high-p_T bins, i.e. $1/p_T\sqrt{\sin\theta} > 10$ GeV, is shown

the whole η region of about 10-30 μm.

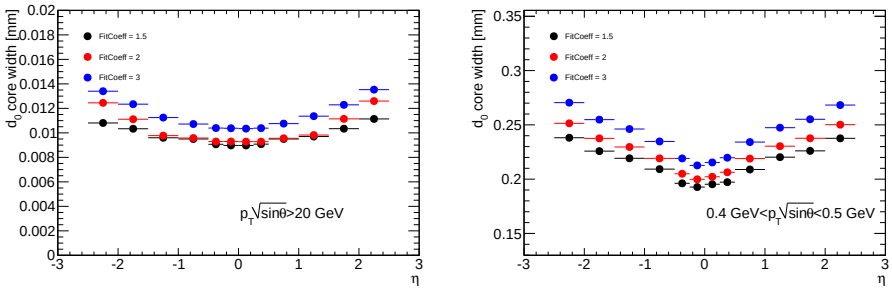

(a) (b)

Figure 2.22: MC 2011 $\sqrt{s} = 7$ TeV proton-proton collisions: transverse impact parameter core width for tracks with one b-layer hit in the Pixel Detector as a function of the pseudorapidity η for two different $p_T\sqrt{\sin\theta}$ regions: $p_T\sqrt{\sin\theta} > 20$ GeV (a) and 0.4 GeV$< p_T\sqrt{\sin\theta} < 0.5$ GeV (b). The core widths has been evaluated using three different fit coefficients applied to the fit procedure: 1.5 (black dots), 2 (red dots) and 3 (blue dots)

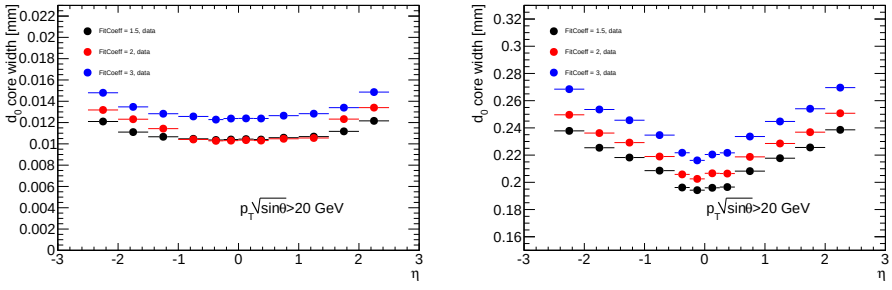

(a) (b)

Figure 2.23: 2011 $\sqrt{s} = 7$ TeV proton-proton collisions data: transverse impact parameter core width for tracks with one b-layer hit in the Pixel Detector as a function of the pseudorapidity η for two different $p_T\sqrt{\sin\theta}$ regions: $p_T\sqrt{\sin\theta} > 20$ GeV (a) and 0.4 GeV$< p_T\sqrt{\sin\theta} < 0.5$ GeV (b). The core widths has been evaluated using three different fit coefficients applied to the fit procedure: 1.5 (black dots), 2 (red dots) and 3 (blue dots)

A better feeling on the goodness of the fits themselves is obtained by looking at the plots in figure 2.24. The Gaussian fits, having applied the three different fit coefficients, on the core of the transverse impact parameter distributions is shown. Simulated tracks from proton-proton collisions at $\sqrt{s} = 7$ TeV in a central η bin ($0 < \eta < 0.25$) with one b-layer hit in the Pixel Detector, and for two different $p_T\sqrt{\sin\theta}$ bins ($p_T\sqrt{\sin\theta} > 20$ GeV and 0.4 GeV$< p_T\sqrt{\sin\theta} < 0.5$ GeV) has been used. Having set the fit coefficient to 1.5, is reasonable to think that the core of the distributions is not described entirely but only partially from the fit. On the other hand the contribution of the tails becomes much larger with the result that the Gaussian fit doesn't represent well anymore the shape of the core of the distributions. Therefore the best choice in order to better describe the core of the distributions is certainly to set the fit coefficient to 2.

2.3.9.2 Pile-up

The track reconstruction of events with high pile-up suffers from the increased combinatorial background at all levels, from seeding to track finding and selection of good tracks, up to the reconstruction in the TRT at high occupancy. This can lead to the presence of more fake tracks candidates. At the same time, the number of shared clusters increases as hits from neighboring tracks merge into single larger clusters.

For these reasons the impact parameter resolution can be affected from different pile-up level. To study this systematic effect a sample of proton-proton collision data at $\sqrt{s} = 7$ TeV with a larger average number of interactions per bunch crossing ($< \mu >= 16.7$) with respect to the reference 2011 sample ($< \mu >= 5.84$).

The events have been classified in three groups with different number of pile-up interactions μ: $10 \leq \mu < 14$, $14 \leq \mu < 18$, and $18 \leq \mu < 22$. For each group the transverse and longitudinal impact parameter resolutions have been measured. Figure 2.25 shows the transverse impact parameter measured core width for tracks with one b-layer hit in the Pixel Detector as a function of the pseudorapidity η for two different $p_T\sqrt{\sin\theta}$ regions ($p_T\sqrt{\sin\theta} > 20$ GeV (a) and 0.4 GeV$< p_T\sqrt{\sin\theta} <$ 0.5 GeV), comparing the three groups of events with different μ. Only a slightly dependence on pile-up of the measured impact parameter resolution is visible: the first two groups of event with less pile-up level show a good agreement between each other, while the group of events with higher pile-up level disagree with the

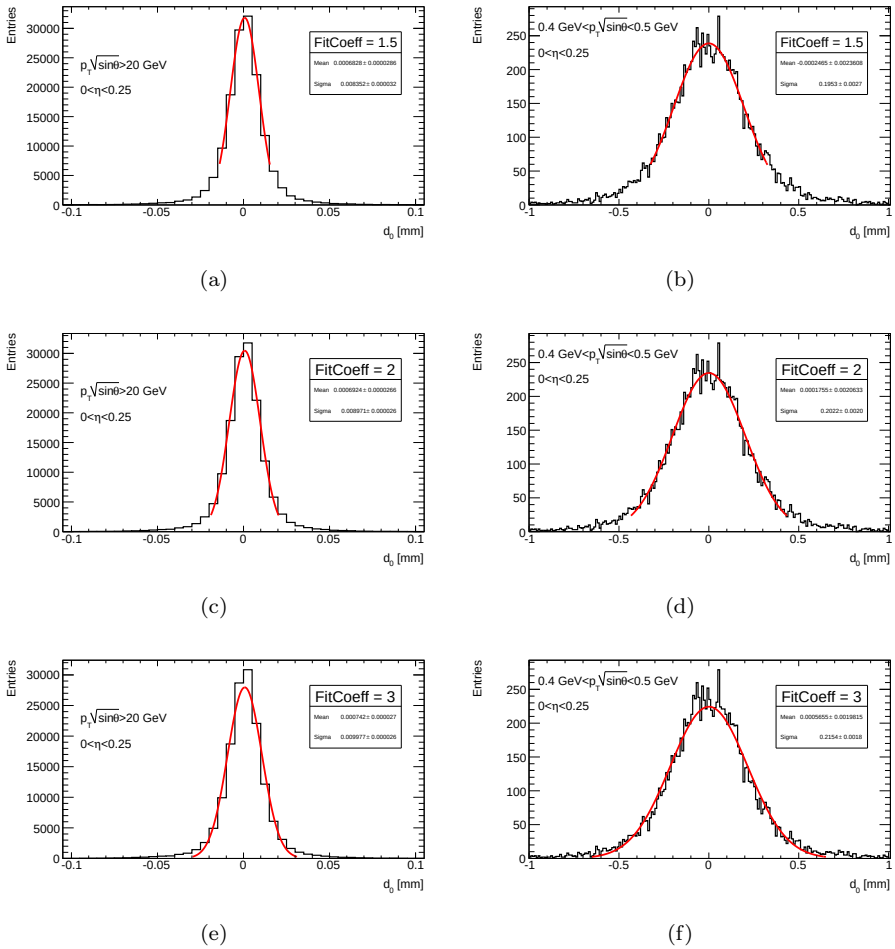

Figure 2.24: Gaussian fits applying three different fit coefficients on the core of the transverse impact parameter distributions for tracks in a central η bin ($0 < \eta < 0.25$) with one b-layer hit in the Pixel Detector, and for two different $p_T\sqrt{\sin\theta}$ bins: $p_T\sqrt{\sin\theta} > 20$ GeV (left column) and 0.4 GeV$< p_T\sqrt{\sin\theta} < 0.5$ GeV (right column). The fit coefficients applied are: 1.5 (top row), 2 (middle row) and 3 (bottom row)

others of about 10-20% at high p_T, and of about 5% at low p_T.

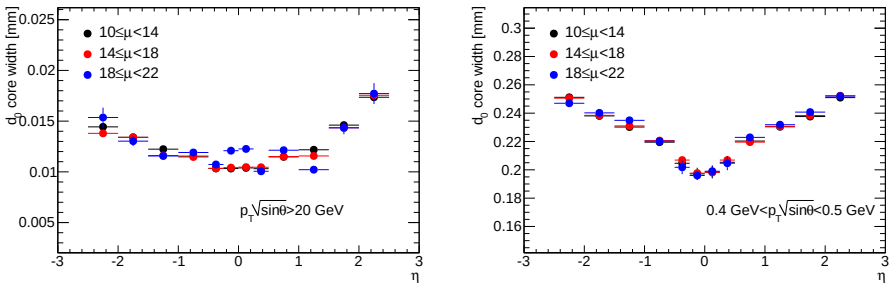

(a) (b)

Figure 2.25: 2011 $\sqrt{s} = 7$ TeV proton-proton collisions with $< \mu >= 16.7$: transverse impact parameter measured core width for tracks with one b-layer hit in the Pixel Detector as a function of the pseudorapidity η for two different $p_T\sqrt{\sin\theta}$ regions: $p_T\sqrt{\sin\theta} > 20$ GeV (a) and 0.4 GeV$< p_T\sqrt{\sin\theta} < 0.5$ GeV (b). The core widths has been evaluated for three different groups of events with different number of pile-up verticesμ: $10 \leq \mu < 14$ (black dots), $14 \leq \mu < 18$ (red dots), and $18 \leq \mu < 22$ (blue dots)

2.3.9.3 Jet-p_T

For this study, as explained in section 2.3.3.2, the di-jet Monte Carlo samples has been used. These samples are constructed such that each of them cover a different jet-p_T range. The tracks composition is therefore different between each sample. In particular moving from low to high jet-p_T, the number of the particles belonging to the jets increase logarithmically. This leads to the fact that, on average, the particles are more energetic and more collimated. In conclusion, since the density of the tracks increases, the probability of getting hit-to-track assignment errors is larger, introducing an effect that can lead to a degradation of the impact parameter resolution.

To study this systematic effect di-jet Monte Carlo samples from J4 to J8 of proton-proton collision data at $\sqrt{s} = 7$ TeV has been considered. In figure 2.26 is shown the truth simulated transverse impact parameter core width for tracks with one b-layer hit in the Pixel Detector as a function of the pseudorapidity η for two

different $p_T\sqrt{\sin\theta}$ regions ($p_T\sqrt{\sin\theta} > 20$ GeV (a) and 0.4 GeV$< p_T\sqrt{\sin\theta} < 0.5$ GeV), comparing data with five di-jet Monte Carlo samples with increasing jet-p_T range, from J4 to J8. In the region where the impact parameter resolution is dominated by the multiple scattering, i.e. low p_T tracks (figure 2.26 (b)), no significant differences are visible between the JX samples. On the other hand, in the region with high p_T tracks (figure 2.26 (a)), a clear dependence on jet energy, and hence on track density, is visible especially in the barrel region. In fact the simulated transverse impact parameter resolution increase from $\sim 9\mu$m to $\sim 13\mu$m.

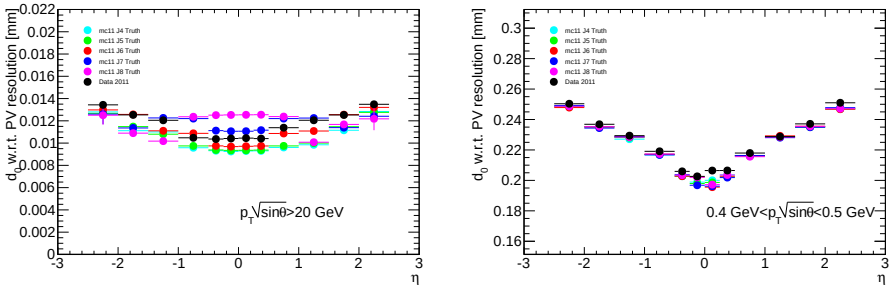

(a) (b)

Figure 2.26: 2011 $\sqrt{s} = 7$ TeV proton-proton collisions: transverse impact parameter core width for tracks with one b-layer hit in the Pixel Detector as a function of the pseudorapidity η for two different $p_T\sqrt{\sin\theta}$ regions: $p_T\sqrt{\sin\theta} > 20$ GeV (a) and 0.4 GeV$< p_T\sqrt{\sin\theta} < 0.5$ GeV (b). The core widths has been evaluated for five di-jet Monte Carlo samples with increasing jet-p_T range, from J4 to J8. The truth simulated values (colored dots) are compared with data (black dots)

In order to try to understand the strong dependence of the impact parameter resolution on the track density, the tracks has been divided in two sub-categories: tracks with and without shared hits with another track in the silicon detectors. Tracks that share at least one hit are only a few per cent ($\sim$ 2-3%) of the whole tracks amount in the di-jet Monte Carlo samples.

Figure 2.27 shows the truth simulated transverse impact parameter core width as a function of the pseudorapidity η, for tracks with $p_T\sqrt{\sin\theta} > 20$ GeV, one b-layer hit in the Pixel Detector, and respectively without (a) and with (b) shared hits

in the silicon detectors. As expected, the transverse impact parameter resolution of tracks that don't share hits with other tracks is reasonably independent from jet-p_T. while a large dependence on it still remains for tracks that share at least one hit. In the third final tracks category, as explained in section 2.3.5, the tracks that have shared hits in the b-layer are considered separately from tracks that share hits in the other silicon layers. In fact, shared hits in the b-layer are expected to have a bigger effects on the track parameters.

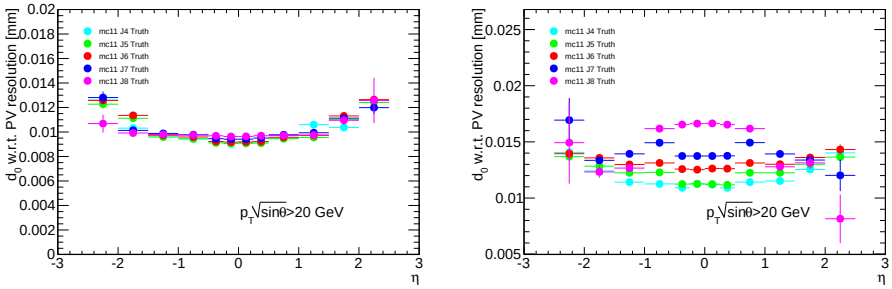

Figure 2.27: MC 2011 $\sqrt{s} = 7$ TeV proton-proton collisions: transverse impact parameter core width for tracks with $p_T\sqrt{\sin\theta} > 20$ GeV, one b-layer hit in the Pixel Detector, and respectively without (a) and with (b) shared hits in the silicon detectors. The core widths has been evaluated for five di-jet Monte Carlo samples with increasing jet-p_T range, from J4 to J8

Instead of merging all the di-jet Monte Carlo samples and apply an event-based reweighting, as already mentioned in section 2.3.3.2, only the J4 sample has been chosen to be compared with data. In order to find out the sample that better matches the data, especially for high p_T tracks, a comparison between the distributions of the simulated from the track fit impact parameter of the JX samples with the ones measured from data has been done. In figure 2.28 are shown data and di-jet Monte Carlo (J4,J6, and J8) intrinsic transverse (a) and longitudinal (b) impact parameter distributions for tracks in a central η bin ($0 < \eta < 0.25$) with $p_T\sqrt{\sin\theta} > 20$ GeV, and one b-layer hit in the Pixel Detector, while in table 2.5 are reported the mean and RMS of each distribution in figure. It is clearly reasonable to conclude that the di-jet J4 Monte Carlo sample is the one that better describe

	σ_{d_0}		$\sigma_{z_0 \sin\theta}$	
	mean [μm]	RMS [μm]	mean [μm]	RMS [μm]
Data 2011	10.61	2.94	103.8	17.91
mc11 J4	10.67	2.90	103.5	17.30
mc11 J6	10.49	3.24	103.3	18.53
mc11 J8	11.97	4.70	104.9	20.54

Table 2.5: Intrinsic transverse and longitudinal impact parameter distributions mean and RMS comparison between data and di-jet Monte Carlo (J4,J6, and J8) for tracks in a central η bin ($0 < \eta < 0.25$) with $p_T\sqrt{\sin\theta} > 20$ GeV, and one b-layer hit in the Pixel Detector

data, both in terms of the distribution shape and of the mean and RMS. All the other track categories have been explored and from all of them the same conclusion has been drawn.

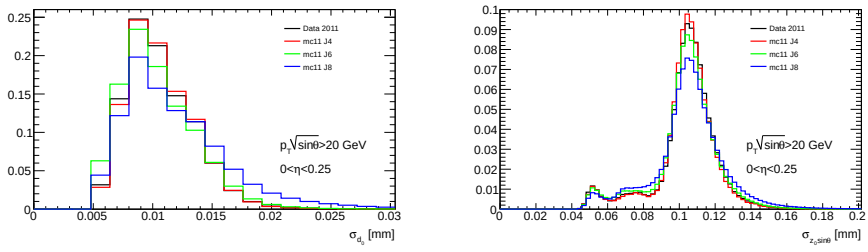

(a) (b)

Figure 2.28: 2011 $\sqrt{s} = 7$ TeV proton-proton collisions: data and di-jet Monte Carlo (J4,J6, and J8) distributions of the intrinsic resolution on the transverse (a) and longitudinal (b) impact parameter for tracks in a central η bin ($0 < \eta < 0.25$) with $p_T\sqrt{\sin\theta} > 20$ GeV, and one b-layer hit in the Pixel Detector

2.3.10 Impact parameter smearing

In many applications the simulation is used to compute quantities, like resolutions and efficiencies, used in measurements. In those applications a good agreement

between data and simulation is required. All observed disagreements which may have an impact on the measurements need to be either corrected or taken into account in the evaluation of systematic uncertainties.

In the case of the impact parameter, the ATLAS simulation does not take into account the effect of residual misalignments. The simulation may also not describe perfectly the amount of material in the detector, or the intrinsic resolution of the tracking detector. Typically that translate into a worse resolution of the real detector compared to the simulation.

The measured impact parameter resolutions are used to evaluate the impact parameter smearing terms, defined as:

$$k_{\text{smear}} = \sqrt{\left(\sigma_{d_{PV}}^{\text{DATA}}\right)^2 - \left(\sigma_{d_{PV}}^{\text{MC}}\right)^2} \tag{2.28}$$

These terms may be used to apply an additional smearing to the MC in order to make it look like data. It is clear that the simulated impact parameter distributions are smeared only if $\sigma_{d_{PV}}^{\text{DATA}} > \sigma_{d_{PV}}^{\text{MC}}$.

In tables 2.6 and 2.7, respectively, the transverse and longitudinal impact parameter core width, measured and simulated, are reported for tracks with $p_T\sqrt{\sin\theta} >$ 20 GeV, one b-layer hit in the Pixel Detector, and without shared hits in the silicon detectors. The rightmost column of each table shows the transverse impact parameter smearing terms. Values are reported for both $\sqrt{s} = 7$ TeV and $\sqrt{s} = 8$ TeV proton-proton collision data and Monte Carlo.

One important application of the smeared impact parameter distributions can be found in the measurement of the mistag rate[7] of b-tagging algorithms [89]. Within this measurement, the impact parameter smearing represent one of the most important systematic effect. In fact, the b-tagging performance is very sensitive to the resolution of the fitted track parameters and the proper estimation of the errors, especially in light-flavor jets where a large fraction of the b-tagged jets originate from prompt tracks which appear to be displaced.

The measured disagreement result in a final systematic uncertainty of about 6% in the barrel region, where it is usually small with respect to other sources (mainly the effect of trigger selection). It amounts up to 22% for high p_T jets in the end-cap region, where it is the major individual contributor [89].

[7] probability to tag a jet originating from a light-flavor quark as b-jet

d_0 core width vs η - $\sqrt{s} = 7$ TeV - $p_T\sqrt{\sin\theta} > 20$ GeV - 1 b-layer hit - no shared hits			
η bin	d_0 core width [μm] DATA	d_0 core width [μm] MC	smearing term [μm]
$[-2.5, -2]$	13.18 ± 0.09	12.30 ± 0.13	4.74
$[-2, -1.5]$	12.31 ± 0.05	10.20 ± 0.08	6.89
$[-1.5, -1]$	11.42 ± 0.04	9.61 ± 0.05	6.17
$[-1, -0.5]$	10.41 ± 0.03	9.43 ± 0.03	4.41
$[-0.5, -0.25]$	10.28 ± 0.04	9.12 ± 0.04	4.74
$[-0.25, 0]$	10.30 ± 0.04	9.09 ± 0.03	4.84
$[0, 0.25]$	10.35 ± 0.04	9.12 ± 0.03	4.89
$[0.25, 0.5]$	10.30 ± 0.04	9.15 ± 0.04	4.73
$[0.5, 1]$	10.47 ± 0.03	9.38 ± 0.03	4.65
$[1, 1.5]$	10.55 ± 0.04	9.63 ± 0.05	4.31
$[1.5, 2]$	12.32 ± 0.05	10.21 ± 0.08	6.89
$[2, 2.5]$	13.40 ± 0.09	12.32 ± 0.13	5.27
d_0 core width vs η - $\sqrt{s} = 8$ TeV - $p_T\sqrt{\sin\theta} > 20$ GeV - 1 b-layer hit - no shared hits			
η bin	d_0 core width [μm] DATA	d_0 core width [μm] MC	smearing term [μm]
$[-2.5, -2]$	13.37 ± 0.06	12.61 ± 0.34	4.44
$[-2, -1.5]$	12.84 ± 0.04	11.27 ± 0.11	6.15
$[-1.5, -1]$	12.13 ± 0.02	9.99 ± 0.04	6.88
$[-1, -0.5]$	11.42 ± 0.02	9.87 ± 0.02	5.74
$[-0.5, -0.25]$	10.44 ± 0.02	9.55 ± 0.03	4.22
$[-0.25, 0]$	10.50 ± 0.02	9.51 ± 0.02	4.45
$[0, 0.25]$	10.45 ± 0.02	9.54 ± 0.03	4.27
$[0.25, 0.5]$	10.50 ± 0.02	9.55 ± 0.03	4.36
$[0.5, 1]$	11.94 ± 0.02	9.85 ± 0.03	6.75
$[1, 1.5]$	12.09 ± 0.02	10.03 ± 0.05	6.75
$[1.5, 2]$	12.61 ± 0.04	11.40 ± 0.12	5.39
$[2, 2.5]$	13.13 ± 0.06	12.83 ± 0.35	2.79

Table 2.6: $\sqrt{s} = 7$ TeV (top) and $\sqrt{s} = 8$ TeV (bottom) proton-proton collisions: measured and simulated values of the transverse impact parameter core width for tracks with $p_T\sqrt{\sin\theta} > 20$ GeV, one b-layer hit in the Pixel Detector, and without shared hits in the silicon detectors. In the rightmost column the transverse impact parameter smearing terms, defined as $\sqrt{\left(\sigma_{d_{PV}}^{\mathrm{DATA}}\right)^2 - \left(\sigma_{d_{PV}}^{\mathrm{MC}}\right)^2}$, are reported

$z_0 \sin\theta$ core width vs η - $\sqrt{s} = 7$ TeV - $p_T\sqrt{\sin\theta} > 20$ GeV - 1 b-layer hit - no shared hits			
η bin	$z_0 \sin\theta$ core width [μm] DATA	$z_0 \sin\theta$ core width [μm] MC	smearing term [μm]
$[-2.5. - 2]$	37.38 ± 0.27	28.49 ± 0.34	24.20
$[-2. - 1.5]$	33.50 ± 0.17	19.77 ± 0.14	27.04
$[-1.5. - 1]$	32.52 ± 0.11	22.29 ± 0.10	23.68
$[-1. - 0.5]$	48.78 ± 0.13	43.87 ± 0.16	21.33
$[-0.5. - 0.25]$	78.98 ± 0.25	76.86 ± 0.34	18.18
$[-0.25.0]$	103.09 ± 0.31	101.60 ± 0.42	17.46
$[0.0.25]$	103.24 ± 0.32	101.24 ± 0.42	20.22
$[0.25.0.5]$	79.54 ± 0.26	77.37 ± 0.34	18.45
$[0.5.1]$	49.31 ± 0.13	43.49 ± 0.15	23.24
$[1.1.5]$	31.42 ± 0.11	22.21 ± 0.10	22.22
$[1.5.2]$	31.28 ± 0.15	18.29 ± 0.13	25.38
$[2.2.5]$	35.21 ± 0.26	26.34 ± 0.32	23.37
$z_0 \sin\theta$ core width vs η - $\sqrt{s} = 8$ TeV - $p_T\sqrt{\sin\theta} > 20$ GeV - 1 b-layer hit - no shared hits			
η bin	$z_0 \sin\theta$ core width [μm] DATA	$z_0 \sin\theta$ core width [μm] MC	smearing term [μm]
$[-2.5, -2]$	38.75 ± 0.18	24.11 ± 0.70	30.34
$[-2, -1.5]$	34.90 ± 0.10	18.03 ± 0.18	29.88
$[-1.5, -1]$	34.85 ± 0.07	24.54 ± 0.10	24.74
$[-1, -0.5]$	52.62 ± 0.08	48.17 ± 0.12	21.18
$[-0.5, -0.25]$	84.12 ± 0.16	80.68 ± 0.23	23.81
$[-0.25, 0]$	106.76 ± 0.20	103.79 ± 0.28	25.01
$[0, 0.25]$	106.98 ± 0.20	103.91 ± 0.27	25.44
$[0.25, 0.5]$	82.94 ± 0.16	79.82 ± 0.22	22.53
$[0.5, 1]$	52.98 ± 0.08	48.35 ± 0.12	21.66
$[1, 1.5]$	33.97 ± 0.07	24.62 ± 0.11	23.41
$[1.5, 2]$	32.13 ± 0.10	17.80 ± 0.18	26.75
$[2, 2.5]$	34.89 ± 0.18	22.20 ± 0.66	26.92

Table 2.7: $\sqrt{s} = 7$ TeV (top) and $\sqrt{s} = 8$ TeV (bottom) proton-proton collisions: measured and simulated values of the longitudinal impact parameter core width for tracks with $p_T\sqrt{\sin\theta} > 20$ GeV, one b-layer hit in the Pixel Detector, and without shared hits in the silicon detectors. In the rightmost column the longitudinal impact parameter smearing terms, defined as $\sqrt{\left(\sigma^{\mathrm{DATA}}_{z_{PV}\sin\theta}\right)^2 - \left(\sigma^{\mathrm{MC}}_{z_{PV}\sin\theta}\right)^2}$, are reported

Chapter 3

Measurement of the charge asymmetry in top quark pair production in proton-proton collision data at $\sqrt{s} = 7$ TeV

Top quark physics is presently and will be widely explored at the LHC: after QCD jets, W and Z bosons, the production of top quarks is the dominant high-p_T process in proton-proton collisions at multi-TeV energies. The LHC can be considered a top quark factory: the top quark pair production cross section is indeed enhanced by a factor 20 with respect to the Tevatron even at 7 TeV centre-of-mass energy. Top quark physics is a rich subject. Top quark events are very useful for detector commissioning and, moreover, they can provide a consistency test of the actual particle physics theory, the Standard Model (SM). Furthermore, the precise measurement of some quantities, such as top quark charge asymmetry, can be a window on new physics. Finally, top quark events are an important background for many processes predicted by new physics models.

The aim of this chapter is to give an introduction to top quark physics and describe the measurement of the top quark charge asymmetry.

3.1 The top quark

After the discovery of the b-quark in 1977 [90], several arguments suggested the existence of an isospin partner, the top quark. First of all, the renormalizability of the SM requires the sum of the charges within a family to be 0 [91]. Given the b-quark and the τ lepton, another component with charge $q_t = 2/3$ was needed. Another argument was the fact that interactions changing the flavor through neutral currents (Flavor Changing Neutral Currents, FCNC) are strongly suppressed. The proposed mechanism to explain this observation (GIM mechanism) required that each family had the same isospin structure. Finally, a proof originated from the measurements of $Z \to b\bar{b}$ rate at the Large Electron Positron collider (LEP) at CERN and at the Stanford Linear Accelerator Center (SLAC) [92]: the measured decay rate of the Z boson into a b-quark pair was much higher than the one predicted for the case of an isospin singlet b-quark. These results were, at opposite, in very good agreement with the SM prediction, including an isospin partner.

Since 1977, indirect measurements constrained the mass of the top quark. In addition, direct searches for the top quark were done by many experiments, increasing the lower limit on m_t.

In 1995 the top quark has been finally observed at the CDF [93] and DØ [94] experiments at the Tevatron in proton-antiproton collisions at 1.8 TeV centre-of-mass energy.

3.1.1 Top quark pair production at hadron colliders

At hadron colliders, $t\bar{t}$ pairs are mainly produced through strong interactions described by perturbative QCD. Interactions between the quark and gluon constituents of the colliding hadrons (either protons or antiprotons) participate in a hard scattering process and produce a top quark and an antitop quark in the final state. At Born level approximation, top quark pairs can be produced via gluon-gluon fusion (gg) or via the annihilation of quark-antiquark pairs ($q\bar{q}$). The relevant leading order Feynman diagrams for the contributing processes are shown in figure 3.1.

Due to the fact that hadrons are composite particles, consisting of partons with unknown fractions x of the initial hadron momenta, the initial state of the parton interaction is not precisely known. However, hadron interactions in proton-

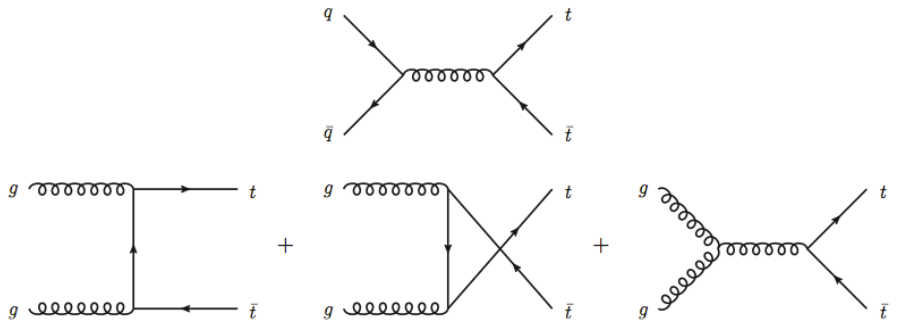

Figure 3.1: Lowest order diagrams contributing to top quark pair production at hadron colliders. Top quarks are produced via strong interaction, either in quark-antiquark annihilation (top) or gluon-gluon fusion (bottom)

proton and proton-antiproton collisions can be described by separating the partonic reactions into a short distance and a long distance contribution.

The long distance part can be factorized into longitudinal parton momentum distribution functions (PDFs) $f_i\left(x_i, \mu_F^2\right)$, where μ_F^2 denotes an (arbitrary) factorization scale describing the separation of the long and short distance contributions. An additional renormalisation scale μ_R^2 is introduced to account for higher order corrections, where ultraviolet divergent terms may emerge and a renormalisation approach can be used to absorb such divergences into corresponding counter terms. Both scales μ_F^2 and μ_R^2 are commonly chosen to correspond to the momentum transfer $\mu_F^2 = \mu_R^2 = Q^2$. Furthermore, for the calculation and simulation of top quark processes, Q^2 is typically chosen such that $\mu_F = \mu_R = Q = m_t$ corresponds to the top pole mass m_t and the associated scale variation dependency is studied.

The PDFs represent the probability distribution of observing a parton of type i at a given scale μ_F^2 with a longitudinal parton momentum fraction x_i. Since these probabilities cannot be universally derived from QCD, they have to be provided from experimental studies of the proton structure, mostly from deep inelastic lepton-proton scattering experiments at the H1 [95, 96, 97, 98] and ZEUS [99, 100, 101] experiments at the HERA electron-proton collider. As an example, the e^+p and e^-p production cross sections measured in deep-inelastic scattering experiments at HERA can be found in figure 3.2 in comparison to the CTEQ10 PDF next-to-leading order (NLO) prediction [102].

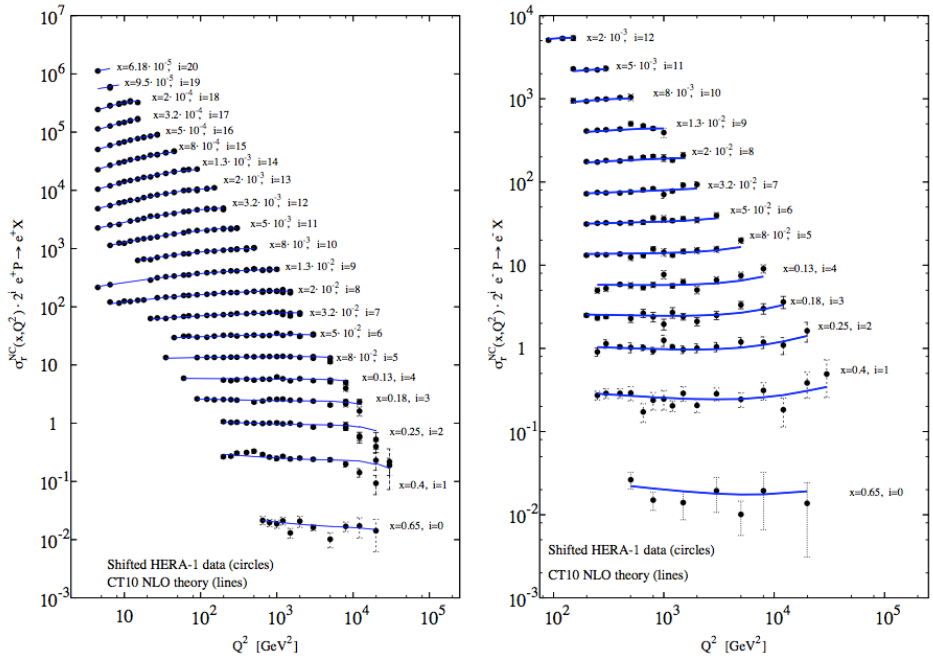

Figure 3.2: Comparison of CTEQ10 NLO predictions for reduced cross sections in e^+p (left) and e^-p (right) neutral-current deep inelastic scattering experiments from combined HERA-1 data, with correlated systematic shifts included [103]

The short distance term arises from the hard scattering process of the respective partons, denoted by the partonic cross section for partons i and j, σ_{ij}. This contribution is characterized by high momentum transfer. Hence, it is not dependent on the incoming hadron type or the respective wave functions and can be described by perturbative QCD, as indicated by the leading order diagrams in figure 3.1.

At a given center of mass energy $\sqrt{s}$ and for a top mass parameter m_t, the total top quark pair production cross section can be calculated from the short distance and long distance terms as

$$\sigma_{t\bar{t}}\left(\sqrt{s}, m_t\right) = \sum_{i,j} \int\int \mathrm{d}x_i \mathrm{d}x_j f_i\left(x_i, Q^2\right) f_j\left(x_j, Q^2\right) \times \sigma_{ij\to t\bar{t}}\left(m_t^2, x_i, x_j, \alpha_s\left(Q^2\right), Q^2\right) \tag{3.1}$$

where the summation is performed over all permutations of $i, j = \{q, \bar{q}, g\}$. The

PDFs of the initial state protons are denoted by $f_i\left(x_i, Q^2\right)$ and $f_j\left(x_j, Q^2\right)$, respectively.

The probability of a parton i to be carrying a momentum fraction of x_i decreases significantly with rising x_i, as can be seen in figure 3.3, where two PDFs from the CTEQ10 PDF set are shown as an example. The PDFs have been evaluated at scales $\mu = 5$ GeV and $\mu = m_t$, respectively, where $\mu = Q$.

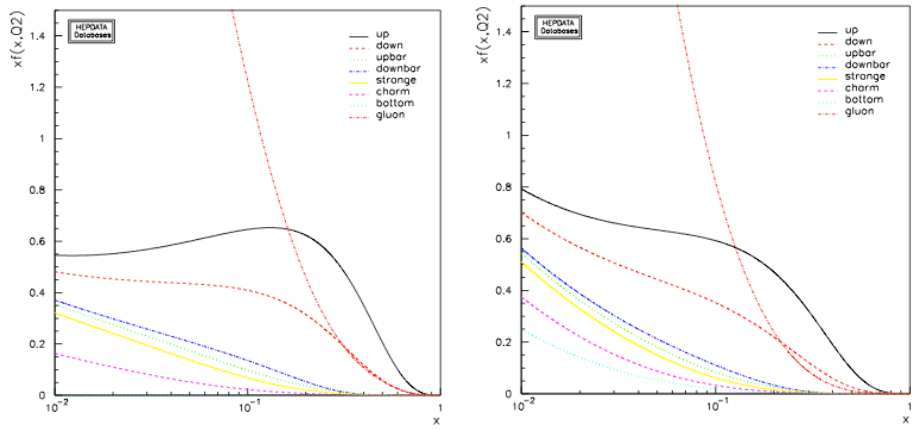

(a) $\mu = 5$ GeV (b) $\mu = m_t$

Figure 3.3: CTEQ10 parton distribution functions at different momentum transfers for gluons and different quark/antiquark flavors. Shown are the PDF sets for $\mu = 5$ GeV (left) and $\mu = m_t$ (right) [102]

The minimal energy carried by the two incoming partons to produce a top quark pair at the threshold (i.e. at rest), is given by

$$\sqrt{x_i x_j s} \geq 2m_t \tag{3.2}$$

and hence, assuming both partons carrying the same momentum fractions as an approximation, $x_i \approx x_j \equiv x$:

$$x \approx \frac{2m_t}{\sqrt{s}} \tag{3.3}$$

This corresponds to a typical value of $x \approx 0.05$ at the LHC for a centre of mass energy of $\sqrt{s} = 7$ TeV. As shown in figure 3.3, the gluon PDFs dominate significantly over any other parton in the corresponding range of x. Consequently,

the production of top quark pairs at the LHC is dominated by gluon-gluon fusion ($\sim 80\%$ at $\sqrt{s} = 7$ TeV). At the Tevatron (where the typical value of x is of the order of 0.2) the production of top quarks is dominated by quark-antiquark annihilation processes ($\sim 85\%$), in particular involving up and down valence quarks. Since the centre of mass energy at the LHC is significantly higher, top quark pairs are typically produced above the threshold, but still within the gluon-gluon fusion dominated range of the PDFs. The total $t\bar{t}$ cross section at the LHC is predicted in an approximate next-to-next-to-leading order (NNLO) calculation to be 165^{+11}_{-16} pb [104, 105, 106] for a centre-of-mass energy of $\sqrt{s} = 7$ TeV and $m_t = 172.5$ GeV. Preliminary measurements have been performed at both ATLAS [107] and CMS [108], yielding:

$$\sigma_{t\bar{t}}\left(\sqrt{s} = 7\text{TeV}\right) = 177 \pm 3(\text{stat})^{+8}_{-7}(\text{syst}) \pm 7(\text{lum.})\ \text{pb} \qquad \text{ATLAS} \tag{3.4}$$

$$\sigma_{t\bar{t}}\left(\sqrt{s} = 7\text{TeV}\right) = 162 \pm 2(\text{stat}) \pm 5(\text{syst}) \pm 4(\text{lum.})\ \text{pb} \qquad \text{CMS} \tag{3.5}$$

respectively. Both measurements are in agreement with the Standard Model prediction as shown in figure 3.4.

This cross section is several orders of magnitude lower than, for example, the SM Z and W boson production cross sections or the inclusive QCD multi-jet production cross section at comparable values of Q^2. This can be seen in figure 1.7, where the total production cross sections for several SM processes are shown as a function of centre of mass energy of the colliding (anti)protons. Consequently, a sophisticated real-time selection to identify the relevant final state particles and obtain a good signal to background separation with respect to other SM processes and, more importantly, the dominant QCD multi-jet background, is crucial for all top quark related measurements at the LHC. Furthermore, an extensive theoretical understanding and modeling of these backgrounds is necessary to facilitate the measurement of top quark properties to highest precision and in order to achieve a sensitivity to potential deviations from the Standard Model expectations.

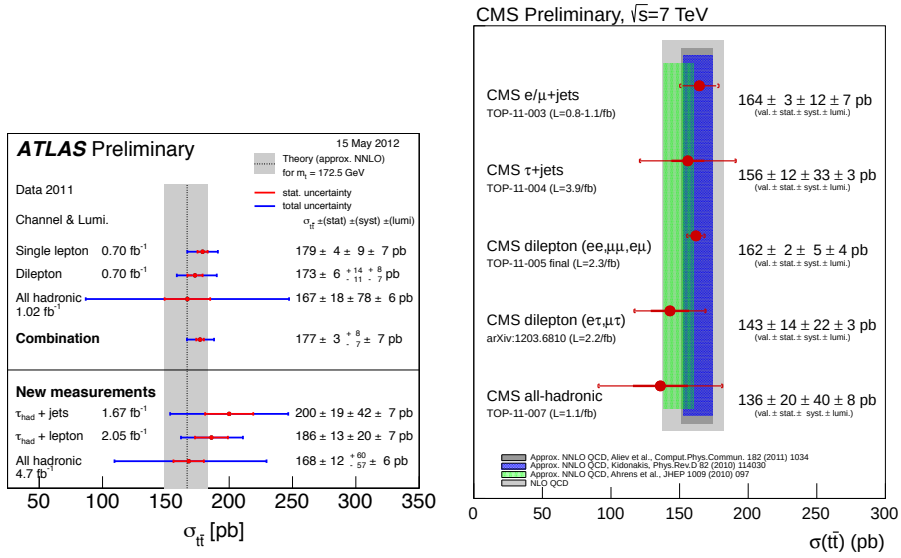

(a) (b)

Figure 3.4: ATLAS (left) and CMS(right) measurements of the total $t\bar{t}$ cross section for proton-proton collisions at a centre-of-mass energy of $\sqrt{s} = 7$ TeV [107, 108]

3.1.2 Top quark decay modes

Due to the magnitude of the CKM matrix element V_{tb}[1] being close to unity [78], the top quark decays in almost 100% of the cases via electroweak charged current interaction into a b-quark and W boson, which then in turn decays either leptonically into a charged lepton and the corresponding (anti)neutrino or hadronically into a quark-antiquark pair. At leading order, the Standard Model prediction for the total decay width of the top quark, Γ_t^0, is given by

$$\Gamma_t^0 = \frac{G_F m_t^3}{8\pi\sqrt{2}} |V_{tb}|^2 \tag{3.6}$$

where G_F denotes the Fermi coupling constant

$$G_F = \frac{\sqrt{2}}{8} \frac{g^2}{M_W^2} \tag{3.7}$$

[1]The Cabibbo-Kobayashi-Maskawa (CKM) matrix is a unitary matrix that contains information on the strength of flavor changing weak decays. The elements of this matrix, V_{ij}, are free parameters of the SM and have to be determined experimentally.

Taking into account higher order corrections at next-to-leading order, the total top quark decay width becomes

$$\Gamma = \Gamma_t^0 \left(1 - \frac{M_W^2}{m_t^2}\right)^2 \left(1 + 2\frac{M_W^2}{m_t^2}\right)^2 \left[1 - \frac{2\alpha_s}{3\pi}\left(\frac{2\pi^2}{3} - \frac{5}{2}\right)\right] \tag{3.8}$$

where terms of order m_b^2/m_t^2 and $(\alpha_s/\pi)M_W^2/m_t^2$ have been neglected. At a top mass of 170 GeV and α_s evaluated at the Z scale, this yields an approximate predicted decay width of $\Gamma_t \approx 1.3$ GeV and a corresponding mean lifetime of $\tau_t \approx 0.5 \cdot 10^{-24}$ s, which is significantly lower than the time scale corresponding to the strong hadronization scale $\Lambda_{\mathrm{QCD}} \approx 250$ MeV. Hence, the top quark decays before being able to form hadronic bound states such as the $t\bar{t}$-quarkonium. Consequently, the top quark spin/polarization properties are preserved in its decay and are transferred to the decay products.

Since the top quark decays almost exclusively into a b-quark and W boson, the resulting final state decay channels are well defined and can be separated into three cases, characterized by the final state particles:

- *Full hadronic final state (alljets)*: both W bosons from the $t\bar{t}$ pair decay into quarks, leading to a total amount of six quarks including the b-quarks from the initial top and antitop decays.

- *Semileptonic final state (lepton+jets)*: one W boson from the $t\bar{t}$ pair decays into quarks, while the second one decays leptonically, leading to a total of four quarks including the b-quarks from the initial top and antitop decays, and one charged lepton and its corresponding (anti)neutrino (see fig 3.5).

- *Dileptonic final state (dilepton)*: both W bosons from the $t\bar{t}$ decay into a charged lepton and the corresponding (anti)neutrino, respectively. In addition, two remaining b-quarks from the top and antitop decays are produced.

If the charged lepton is a tau in the semileptonic or dileptonic channel, either a muon or electron and the corresponding (anti)neutrino, or further quarks from the hadronic decay of the tau lepton are produced.

The respective W branching ratios (BR) at leading order (LO) can be found in table 3.1. Taking these branching fractions into account, possible $t\bar{t}$ final states and their approximate relative probabilities are shown schematically in figure 3.6.

Decay mode	LO BR	Measured BR
$W^{\pm} \to q\bar{q}$	$\frac{6}{9}$	$(67.60 \pm 0.27)\%$
$W^{\pm} \to e^{\pm}\nu_e$	$\frac{1}{9}$	$(10.75 \pm 0.13)\%$
$W^{\pm} \to \mu^{\pm}\nu_{\mu}$	$\frac{1}{9}$	$(10.57 \pm 0.15)\%$
$W^{\pm} \to \tau^{\pm}\nu_{\tau}$	$\frac{1}{9}$	$(10.25 \pm 0.20)\%$

Table 3.1: Theoretical (LO) and measured W branching ratios [78]

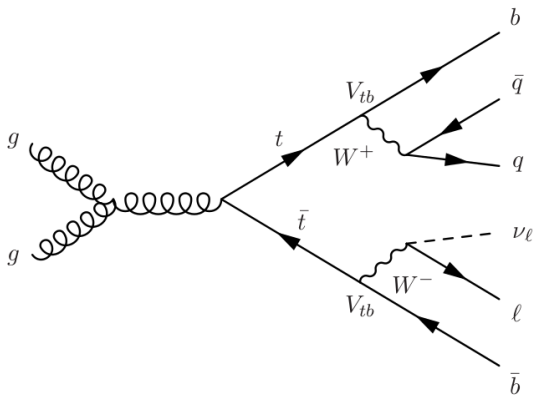

Figure 3.5: The Feynman diagram for the top quark production via gg-fusion and the further decay in the semi-leptonic channel Top quark pair decay channels (left) and branching fractions (right)

3.1.3 Top quark properties

Several properties of the top quark have been studied in collider experiments such as the Tevatron and the LHC. Amongst them, the top quark mass has been determined with a relative uncertainty of only 0.5% by combining the most recent measurements from DØ and CDF [109]. This combination constitutes the most precise (in relative terms) mass measurement of any quark so far. Since the top quark does not form hadronic bound states, the top quark mass m_t is defined as

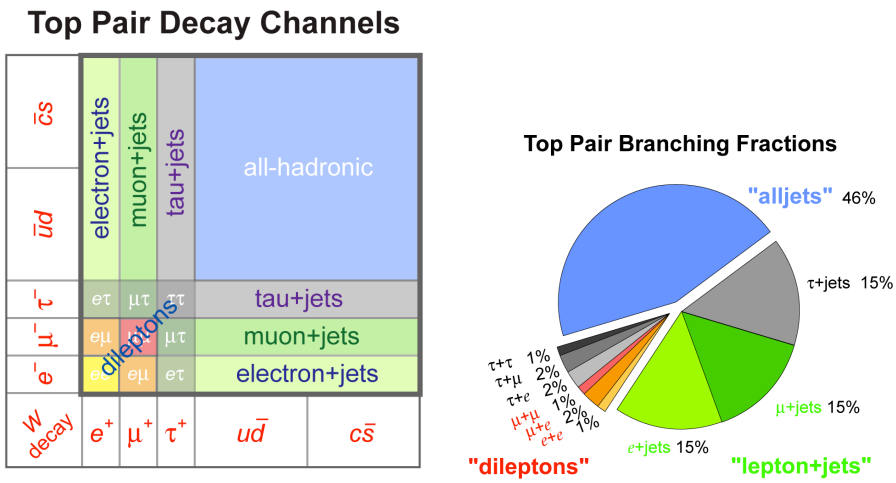

(a) (b)

Figure 3.6: Top quark pair decay channels (left) and branching fractions (right)

the pole mass in this context and is measured to be

$$m_t = 173.18 \pm 0.56\,(\text{stat.}) \pm 0.75\,(\text{syst.}) \qquad \text{Tevatron [109]} \qquad (3.9)$$

$$m_t = 173.36 \pm 0.38\,(\text{stat.}) \pm 0.91\,(\text{syst.}) \qquad \text{CMS [110]} \qquad (3.10)$$

$$m_t = 174.5 \pm 0.6\,(\text{stat.}) \pm 2.3\,(\text{syst.}) \qquad \text{ATLAS [29]} \qquad (3.11)$$

Many other measurements have been performed at the Tevatron or the LHC, including those of the electric charge, the width, the branching ratio in Wb, the correlations between the spin of top and antitop in pair production, the polarization of the W produced in the top quark decay. All of them are in agreement with the Standard Model expectation.

3.2 Charge asymmetry in top quark pair production

This section is dedicated to top quark charge asymmetry measurement, which is one of the main topic of this thesis. The section is organized as follows. After a brief description of SM and BSM predictions, the analysis I have contributed will

be detailed, and then it will be compared with the measurements performed at the Tevatron and at the LHC by the CMS collaboration.

The measurements of this asymmetry acquired great importance and interest after the claim of an evidence for a mass dependent forward-backward asymmetry in top quark pair production from the CDF and DØ experiments at Tevatron (see section 3.2.3). For a top quark pair invariant mass of $m_{t\bar{t}} > 450$ GeV, the asymmetry in the $t\bar{t}$ rest frame was ~ 3 standard deviations above the NLO QCD prediction of $A_{FB}^{SM} = (6 \pm 1)\%$.

3.2.1 Charge asymmetry in the SM

Top quark charge asymmetry is defined for quark-antiquark initial states and consists in the fact that the number of the top quark emitted in the direction of the incoming quark can be different, even slightly, from the number of the ones emitted in the direction of the incoming antiquark, as shown in figure 3.7.

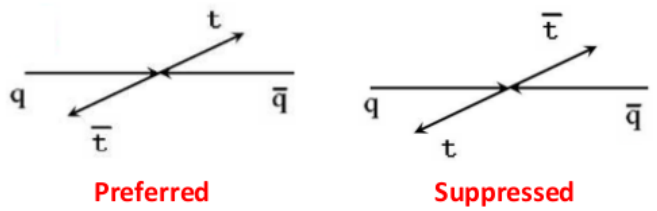

Figure 3.7: Schematic view of top quark pair charge asymmetry

The top quark charge asymmetry can only occur in asymmetric initial states in top quark pair production at LO, so the only contribution comes from $q\bar{q}$ annihilation, while at NLO also qg and $q\bar{g}$ contribute. In order to quantify a potential charge asymmetry created in the Standard Model or BSM models, the natural choice of observable would be the production angle θ of the top-antitop quarks with respect to the incoming partons from the hard scattering process, as depicted in figure 3.8. The corresponding differential charge asymmetry $A(\cos\theta)$ at the partonic level is namely given by [111]

$$A(\cos\theta) = \frac{N_t(\cos\theta) - N_{\bar{t}}(\cos\theta)}{N_t(\cos\theta) + N_{\bar{t}}(\cos\theta)} \tag{3.12}$$

in the $q\bar{q}$ rest frame, where $N_{t(\bar{t})}(\cos\theta)$ is the number of top (antitop) quarks produced at a certain angle θ.

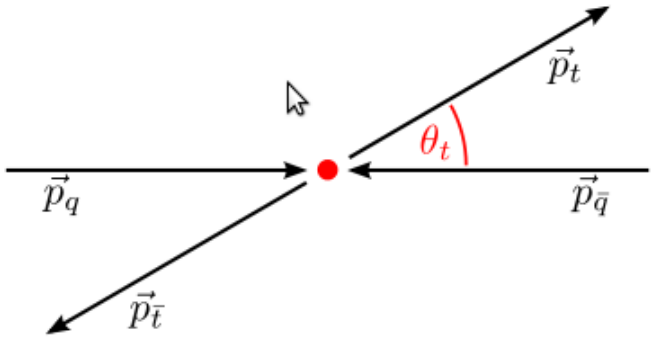

Figure 3.8: Top quark pair production kinematics in quark-antiquark annihilation. The initial state partons and their momenta p_q and $p_{\bar{q}}$ and the produced top quarks and their momenta p_t and $p_{\bar{t}}$, respectively, are shown. In addition, the production angle of the top quark θ is shown

Within the SM the charge asymmetry appears at NLO. QCD at tree level (LO) predicts that $t\bar{t}$ quark pair production at hadron colliders is charge symmetric, namely the differential charge asymmetry $A(\cos\theta)$ vanishes for every value of θ. Nevertheless, an asymmetry is generated at NLO from the interference of the diagrams shown in figure 3.9. The interference between tree level and one loop diagrams (first two diagrams) leads to a positive asymmetry, while the interference between *Initial State Radiation* (ISR) and *Final State Radiation* (FSR) diagrams (last two diagrams) leads to a negative one. The former is larger than the latter, so the resulting asymmetry is expected to be positive.

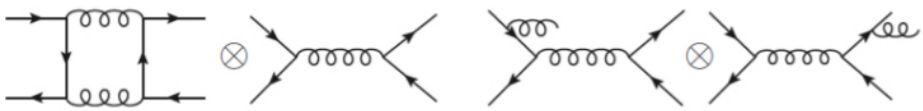

Figure 3.9: Feynman diagrams contributing to the QCD charge asymmetry in quark-antiquark production

For what concerns the two other top quark pair production mechanisms: qg originated processes generate a contribution to the asymmetry much smaller than

$q\bar{q}$, and gg fusion is symmetric.

In the strong production of top quark pairs at hadron colliders, the production angle as such is not accessible experimentally due to the fact that the initial state of the partonic reaction is of probabilistic nature. Since the available information is limited to the hadronic initial state (proton-proton or proton-antiproton) and to the PDFs of the protons and/or antiprotons, respectively, different methods to measure the charge asymmetry, making use only of the final state information of the hadronic collision, must be employed.

At asymmetric hadron colliders such as the Tevatron, where protons are brought to collision with antiprotons, a charge asymmetry in the production of top quark pairs as introduced in equation 3.12, observed in the $t\bar{t}$ rest frame, corresponds directly to an equal-sized geometric forward-backward asymmetry, A_{FB}. In proton-antiproton collisions at the Tevatron energy, the incoming quark will be mainly a valence quark from the proton, while the incoming antiquark will be a valence antiquark of the antiproton. As a consequence the direction of the incoming quark is well represented by the one of the proton beam. Top quark charge asymmetry translates, therefore, in the fact that the top quark is preferentially emitted in the direction of the proton beam. If we consider the proton beam direction as forward and the antiproton one as backward, the most natural variable to study is:

$$A_{FB} = \frac{N(\Delta y > 0) - N(\Delta y < 0)}{N(\Delta y > 0) + N(\Delta y < 0)} \tag{3.13}$$

where A_{FB} is the forward-backward asymmetry, Δy is defined as the difference between top and antitop rapidities calculated with respect to proton beam direction ($\Delta y = y_t - y_{\bar{t}}$).

At proton-proton colliders such as the LHC, no forward-backward asymmetry is visible in the laboratory frame due to the intrinsic symmetry of the initial state collisions. Top quark pair production asymmetry show up in a different way. Quarks in the initial state will mainly be valence quarks, whereas antiquarks will always be sea quarks. As a consequence, the quark momentum fraction will be more frequently higher than the antiquark one and so top quarks, emitted preferentially in the incoming quark direction, will be more boosted than the antitop quarks, so an excess of top quarks in the forward and backward regions is expected in the laboratory frame.

Consequently, different widths of the corresponding rapidity distributions of top quarks and antitop quarks as shown in figure 3.10, and hence, the respective decay products, are predicted. The underlying charge asymmetry in the $t\bar{t}$ rest frame can be extracted either from the final state particles directly or by performing a kinematic reconstruction of the $t\bar{t}$ decay signature.

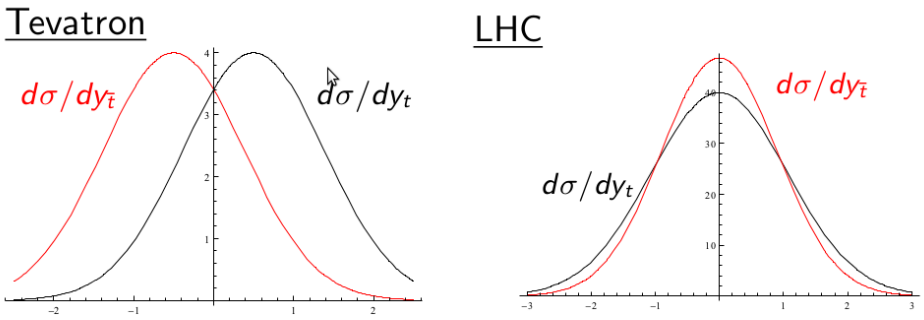

Figure 3.10: Top and antitop quark rapidity distributions: comparison between Tevatron (left) and LHC (right). While at Tevatron the charge asymmetry manifests itself in the fact that top quarks are preferentially emitted in the proton beam direction, at LHC it shows up in the fact that top quark rapidity distribution is broader than antitop quark one

Some variables which are sensitive to the asymmetry are:

$$\Delta|\eta| = |\eta_t| - |\eta_{\bar{t}}| \tag{3.14}$$

$$\Delta|y| = |y_t| - |y_{\bar{t}}| \tag{3.15}$$

$$\Delta y^2 = y_t^2 - y_{\bar{t}}^2 \tag{3.16}$$

where $y_{t(\bar{t})}$ and $\eta_{t(\bar{t})}$ are top (antitop) rapidity and pseudorapidity respectively.

Based on this observation I have studied some observables to measure the top quark charge asymmetry [112]. The first one is defined as:

$$A_C = \frac{N(\Delta|y| > 0) - N(\Delta|y| < 0)}{N(\Delta|y| > 0) + N(\Delta|y| < 0)} = \frac{N(\Delta y^2 > 0) - N(\Delta y^2 < 0)}{N(\Delta y^2 > 0) + N(\Delta y^2 < 0)} \tag{3.17}$$

where $N(\Delta Y > 0)$ is the number of events in which ΔY is positive, while $N(\Delta Y < 0)$ is the number of events in which ΔY is negative. Y is obviously replaceable by $|y|$ or y^2.

Other interesting observables that can be used are the so called forward and central asymmetry:

$$A_{\text{central}} = \frac{N(|y_t| < y_0) - N(|y_{\bar{t}}| < y_0)}{N(|y_t| < y_0) + N(|y_{\bar{t}}| < y_0)} \tag{3.18}$$

$$A_{\text{forward}} = \frac{N(|y_t| > y_0) - N(|y_{\bar{t}}| > y_0)}{N(|y_t| > y_0) + N(|y_{\bar{t}}| > y_0)} \tag{3.19}$$

where y_t and $y_{\bar{t}}$ are top and antitop quark rapidity respectively and y_0 is a free parameter. These two quantities are based on the fact that the number of top quarks is expected to be higher than the number of antitop quarks in the forward region and lower in the central one.

As already mentioned before, since an asymmetry can solely be created from the quark-antiquark annihilation contribution to the top quark pair production cross section, the total charge asymmetry in both proton-proton and proton-antiproton collisions can be significantly diluted due to the (symmetric) gluon-gluon fusion contribution. The dilution of the charge asymmetry is much larger at the LHC due to the increased contribution from this process.

Furthermore the asymmetry in the SM is small, since it appears only at NLO. At the Tevatron a forward-backward asymmetry of $(6 \pm 1)\%$ [113, 114, 115] is expected while at the LHC a charge asymmetry of about 1% is expected [116].

3.2.2 Charge asymmetry in the BSM theories

Some BSM models predict however significant deviations of the asymmetry value from the one predicted by the SM. New physics contributions can enhance or decrease the SM asymmetry. As will be shown in the next section, Tevatron measurements have however excluded the presence of significant negative contributions. Only BSM models giving positive contributions to the asymmetry will be therefore discussed in the following.

Most of the proposed models predict the existence of a new particle that can contribute in $q\bar{q} \to t\bar{t}$ process in s-,u-, or t-channel. All possible vector bosons and scalars contributing have been classified in [117], the most popular ones are described below.

- *Axigluons.* This model predicts the presence of a color octet vector G^{μ} (axigluon) with axial couplings to quarks, which is produced in the s-channel.

Such kind of particle is foreseen by the so-called "chiral models": QCD $SU(3)$ symmetry is considered to come from an higher symmetry group $(SU(3)_L \times SU(3)_R)$; the breaking of this more general symmetry originates 8 massless bosons (gluon) and 8 massive bosons (axigluon). This new particle will show up as a bump in di-jets or $t\bar{t}$ invariant mass spectra. No excesses have been observed at the moment, so it has to have a large mass in order not to be produced on-shell. The contribution to the charge asymmetry can be dominated by the interference with SM diagrams or by the BSM squared amplitude. The interference term is proportional to $(-g_q \cdot g_t)$, where g_q is the coupling of axigluon with light quarks and g_t with top quark. Therefore, in order to have a positive asymmetry either the couplings are so large that the second term dominates or the coupling of the axigluon with the third family has opposite sign with respect to the one with light quarks.

- *Z' and W' bosons.* A neutral vector boson B_μ or a charged boson B^1_μ, like Z' and W' bosons predicted by GUT, can be exchanged in the t-channel as in figure 3.11: $u\bar{u} \to t\bar{t}(Z')$, $d\bar{d} \to t\bar{t}(W')$. As can be seen from the diagrams, $t\bar{t}$

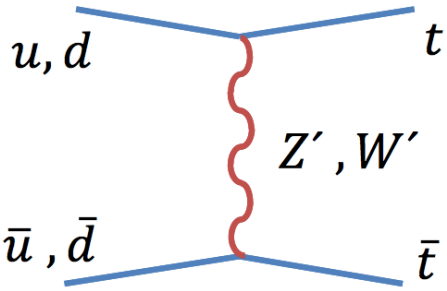

Figure 3.11: Feynman diagram contributing to $t\bar{t}$ charge asymmetry involving Z' or W' bosons

production requires flavor violating couplings, in particular flavor changing neutral currents are foreseen for Z'. In order to have at Tevatron energy an increase of the asymmetry and no excesses in $t\bar{t}$ production cross section, Z' and W' couplings should be large and the contribution to $\sigma_{t\bar{t}}$ coming from SM-BSM interference ($\delta\sigma_{\text{int}}$) should cancel with BSM squared amplitude ($\delta\sigma_{\text{quad}}$): $\delta\sigma_{\text{int}} + \delta\sigma_{\text{quad}} \sim 0$. The cancellation can not occur at the LHC too, so excesses

in $m_{t\bar{t}}$ tails are foreseen. Another constraint to Z' model comes from the fact that it predicts the production of same sign tops (see figure 3.12), which are still unobserved. This can be overcome by choosing particular Z' models.

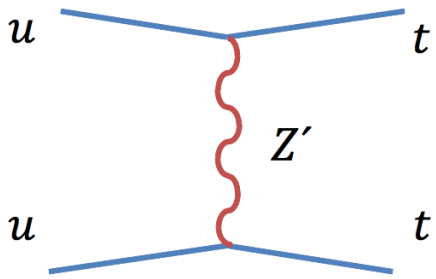

Figure 3.12: Feynman diagram for same sign $t\bar{t}$ pair production

- *Scalar triplet / scalar sextet.* An exotic scalar, color triplet (ω^4) or color sextet (Ω^4), with flavor violating couplings can be exchanged in the u-channel: $u\bar{u} \to t\bar{t}$ (see figure 3.13). These particles are both bosonic colored states differing by their couplings to quarks. For ω^4, the antisymmetry in color indices implies that diagonal couplings to uu, tt identically vanish. For Ω^4, processes like $uu \to uu$ and $uu \to tt$ are at the contrary possible, but the production of same sign tops have not been observed yet. Specific models can however avoid this.

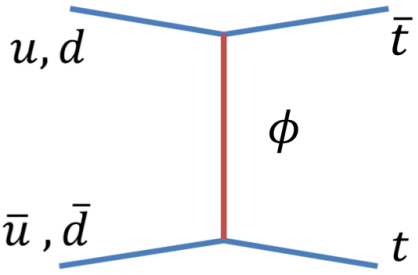

Figure 3.13: Feynman diagram contributing to $t\bar{t}$ charge asymmetry involving ω^4 or Ω^4 scalars

The various models predict different values of the asymmetry at the LHC and

at the Tevatron and different dependencies with respect to $t\bar{t}$ kinematic variables, in particular the top quark pair invariant mass ($m_{t\bar{t}}$).

The measurement of the charge asymmetry at the two colliders will give the possibility to discriminate between these models. The relation between the new physics contribution at the Tevatron (A_{FB}^{new}) for $m_{t\bar{t}} > 450$ GeV with the one to inclusive asymmetry at the LHC (A_C^{new}) is presented in figure 3.14 (a), for the five BSM models studied. This plot has been obtained considering couplings values in agreement with the constraints on the $t\bar{t}$ cross section and tail mentioned above. This plot exhibits a clear difference between models with a W' boson and the rest of models, due to the different $u\bar{u}$ and $d\bar{d}$ parton densities at the two colliders. At the Tevatron both u, d from the proton and $\bar{u}$, $\bar{d}$ from the antiproton are valence quarks, so that $d\bar{d}$ is roughly 1/4 smaller than $u\bar{u}$. At the LHC both $\bar{u}$ and $\bar{d}$ are sea quarks and $d\bar{d}$ is only 1/2 smaller than $u\bar{u}$. If the new physics contribution to the Tevatron asymmetry is sizeable, as suggested by the CDF measurement that will be described in the following, at the LHC models with a W' boson could be distinguished from the rest of models by a measurement of A_C with a relative precision of around 20%. It can be also observed that for the models with a Z' boson there are minimum asymmetries $A_{FB}^{\text{new}} \geq 0.32$ and $A_C^{\text{new}} \geq 0.04$. This effect is due to the constraints coming from top quark pair measured cross section values.

In figure 3.14 (b) new physics contributions to the Tevatron asymmetry for $m_{t\bar{t}} > 450$ GeV are compared to the ones to the LHC asymmetry at high $t\bar{t}$ invariant mass: $m_{t\bar{t}} > 600$ GeV. It can be seen that for models with a Z' boson exchange the asymmetry enhancement is much more pronounced than for the rest of models and a measurement with a relative precision of $\sim 20\%$ would likely distinguish this model from the rest.

Axigluons (G_μ), scalar triplet (ω^4) and scalar sextet (Ω^4) can be distinguished looking at the distribution of the asymmetry as a function of $m_{t\bar{t}}$. While the contribution from axigluon increases significantly at large $m_{t\bar{t}}$, the increment for Ω^4 is less pronounced and for ω^4 a decrease at high $m_{t\bar{t}}$ is foreseen (see figure 3.15).

Various BSM contributions have also a different dependence on $t\bar{t}$ angular distributions [119]. The sensitivity to new physics can be therefore enhanced by comparing the measurements in central and forward regions.

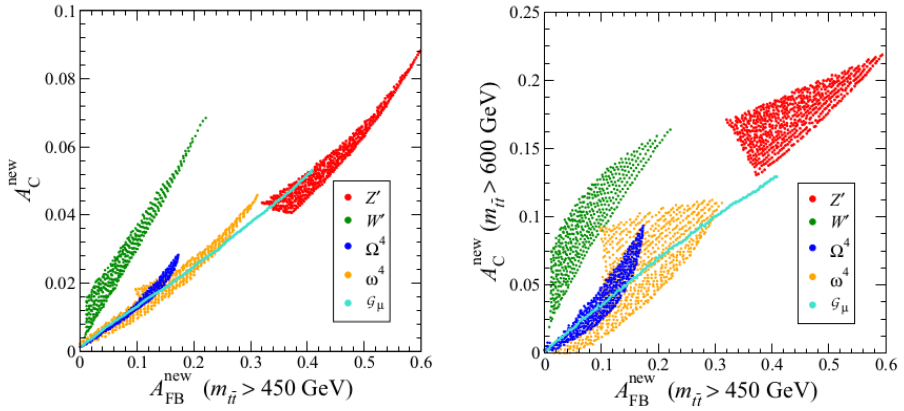

(a) (b)

Figure 3.14: Allowed regions for the new physics contributions to the forward-backward asymmetry at Tevatron and the inclusive charge asymmetry at LHC (a). Allowed regions for the new physics contributions to the forward-backward asymmetry at Tevatron and the charge asymmetry at LHC for $m_{t\bar{t}} > 600$ GeV (b) [118]

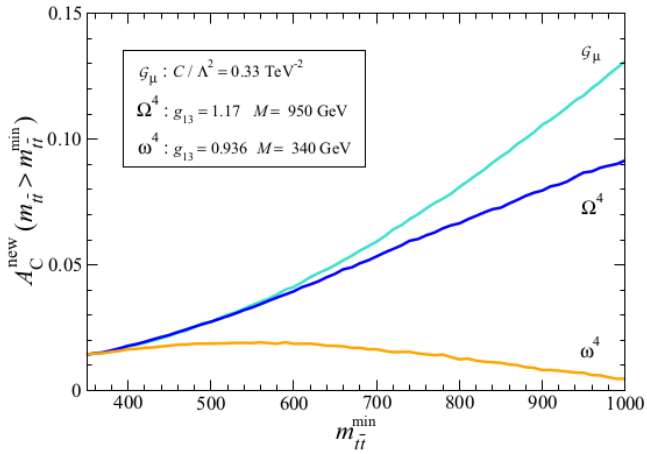

Figure 3.15: Dependence of the charge asymmetry at LHC on the $m_{t\bar{t}}$ cut [118]

3.2.3 Tevatron measurements

Top quark forward-backward asymmetry has been measured both in lepton+jets and di-lepton channel. Two techniques have been explored: the first one performing the reconstruction of top and antitop directions and the other based on leptons angular distributions. Furthermore, differential asymmetry as a function of $m_{t\bar{t}}$ has been measured in lepton+jets channel. The most recent results are discussed in the following.

3.2.3.1 Inclusive asymmetry in lepton+jets channel

The most recent measurements have been performed by CDF [120] and DØ [121] using an integrated luminosity of 5.3 fb^{-1} and 5.4 fb^{-1} respectively. Top and antitop quarks rapidities have been reconstructed from decay products with techniques similar to the one that will be described in section 3.3.4 and an unfolding technique has been used to correct for detector and acceptance effects. The results obtained in the $t\bar{t}$ rest frame are reported below:

$$A_{FB} = (15.8 \pm 7.2(\text{stat.}) \pm 1.7(\text{sys.}))\% \qquad \text{CDF} \tag{3.20}$$

$$A_{FB} = (19.6 \pm 6.5(\text{stat.})^{+1.8}_{-2.6}(\text{sys.}))\% \qquad \text{DØ} \tag{3.21}$$

and are higher than the SM prediction $A_{FB}^{SM} = (6 \pm 1)\%$ by 2σ.

These results are still affected by a significant statistical uncertainty. The most important systematic contributions come from signal modelling, especially ISR and FSR, uncertainty on background contamination and on jet reconstruction.

3.2.3.2 Differential asymmetry in lepton+jets channel

Both the CDF [120] and the DØ [121] collaborations have also measured the charge asymmetry as a function of top quark pair invariant mass ($m_{t\bar{t}}$). While CDF has seen a strong mass dependence, DØ result seems almost independent from $m_{t\bar{t}}$, as can be seen in figure 3.16.

The CDF collaboration, in particular, has measured the asymmetry separately for events with $m_{t\bar{t}} < 450$ GeV and $m_{t\bar{t}} > 450$ GeV and corrected the results for acceptance and detector effects (see figure 3.17). The measured asymmetry for high invariant mass is $A_{FB} = (48 \pm 10(\text{stat.}) \pm 5(\text{sys.}))\%$, 3σ higher than SM prediction

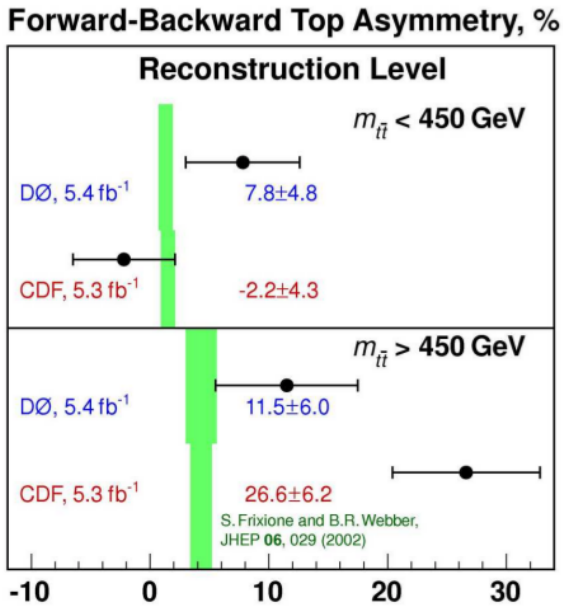

Figure 3.16: Tevatron measurements of top quark charge asymmetry in two bins of top quark pair invariant mass. These results have not been unfolded to correct for detector resolution and acceptance effects [122]

of $A_{FB}^{SM} = (9 \pm 1)\%$. The CDF result has generated a lot of excitement: if this will be confirmed it can be indeed a hint of new physics.

3.2.3.3 Inclusive asymmetry in lepton+jets channel, using lepton variables

In the same channel, DØ collaboration has measured the charge asymmetry using the leptons in each event. Since there is a correlation between the direction of top and antitop quarks and the one of the leptons coming from their decay, top-antitop forward-backward asymmetry translates into the fact that more positive leptons are emitted in the forward direction and more negative leptons in the backward one. Charge asymmetry can be measured therefore as:

$$A_{FB}^{l} = \frac{N_F^l - N_B^l}{N_F^l + N_B^l} \tag{3.22}$$

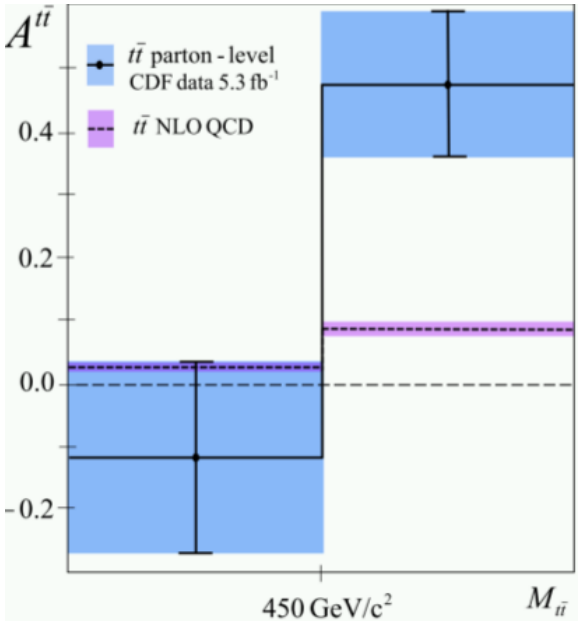

Figure 3.17: CDF measurement of top quark charge asymmetry in two bins of top quark pair invariant mass at production level: the result has been unfolded to correct for detector resolution and acceptance effects [120]

where N_F^l is the number of events that have $q_l y_l > 0$ and N_B^l is the number of events with $q_l y_l < 0$.

The correlation between top quark and lepton directions is not perfect and so the expectation value is $(2.1 \pm 0.1)\%$. After correcting for detector and acceptance effects, the measured value is $A_{FB}^l = (15.2 \pm 3.8(\text{stat.})^{+1.0}_{-1.3}(\text{sys.}))\%$, $\sim 3\sigma$ higher than the prediction.

3.2.3.4 Inclusive asymmetry in di-lepton channel

The CDF collaboration has performed this analysis also in the di-lepton channel [123], using two different techniques. The first one is based on the reconstruction of top and antitop kinematics and the measured value in the $t\bar{t}$ rest frame is:

$$A_{FB} = (42 \pm 15(\text{stat.}) \pm 5(\text{sys.}))\% \tag{3.23}$$

Asymmetry	channel	Measurement(%)	SM prediction(%)
CDF: inclusive	l+jets	$15.8 \pm 7.2(\text{stat.}) \pm 1.7(\text{sys.})$	6 ± 1
DØ inclusive	l+jets	$19.6 \pm 6.5(\text{stat.})^{+1.8}_{-2.6}(\text{sys.})$	6 ± 1
CDF: $m_{t\bar{t}} > 450$ GeV	l+jets	$48 \pm 10(\text{stat.}) \pm 5(\text{sys.})$	9 ± 1
DØ inclusive (lepton)	l+jets	$15.2 \pm 3.8(\text{stat.})^{+1.0}_{-1.3}(\text{sys.})$	2.1 ± 0.1
CDF: inclusive	di-lepton	$42 \pm 15(\text{stat.}) \pm 5(\text{sys.})$	6 ± 1
CDF: inclusive (lepton)	di-lepton	$21 \pm 7(\text{stat.}) \pm 2(\text{sys.})$	not available

Table 3.2: Summary of the measurements and the relative SM predictions

which is 2.3σ higher than the SM prediction. The result is limited by statistical uncertainty; the most important sources of systematic uncertainties comes from background subtraction, signal modelling and jet reconstruction.

The second method takes advantage from the correlation between top and antitop quarks directions and the one of leptons coming from their decay. The difference between top and antitop quarks rapidities is replaced with the one between positive and negative leptons in the event. The lepton based asymmetry is measured to be:

$$A_{FB}^{\Delta\eta} = \frac{N(\Delta\eta_l > 0) - N(\Delta\eta_l < 0)}{N(\Delta\eta_l > 0) + N(\Delta\eta_l < 0)} = 0.21 \pm 0.07(\text{stat.}) \pm 0.02(\text{sys.})\% \qquad (3.24)$$

where $\Delta\eta_l = \eta_{l^+} - \eta_{l^-}$ and the systematic uncertainty is mainly due to background subtraction. This result has not been corrected for detector and acceptance effects yet, so it's not directly comparable with predictions.

The summary of all results and the relative SM predictions are reported in table 3.2.

3.2.4 LHC measurement

The measurement performed by the ATLAS collaboration will be described in detail in the next session. For what concerns the CMS collaboration the analysis has been performed in lepton+jets channel using data corresponding to an integrated luminosity of 5 fb^{-1} [124]. The kinematics of each event is reconstructed using a technique very similar to the one that will be described for the ATLAS analysis

(see section 3.3.4) and then an unfolding technique has been used to correct for acceptance and detector effects. The measured asymmetry has been found to be:

$$A_C^y = 0.004 \pm 0.010(\text{stat.}) \pm 0.011(\text{sys.}) \tag{3.25}$$

where the most important sources of systematic uncertainty comes from signal modelling and JES. The unfolded inclusive $\Delta|y|$ distribution is shown in figure 3.18 (upper left).

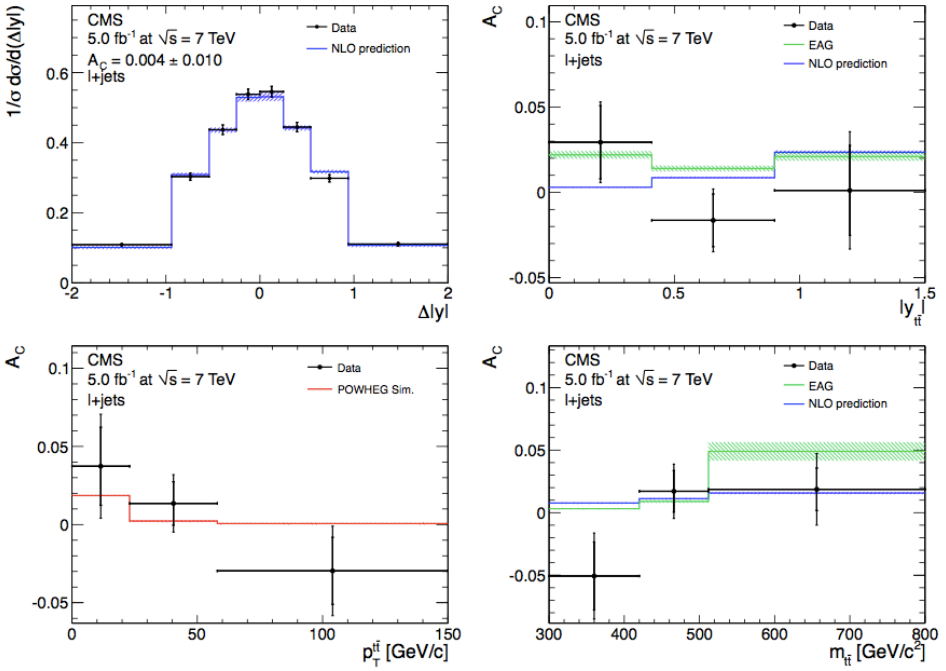

Figure 3.18: Unfolded inclusive $\Delta|y|$ distribution (upper left), corrected asymmetry as a function of $|y|$ (upper right), $p_T^{t\bar{t}}$ (lower left), and $m_{t\bar{t}}$ (lower right). The measured values are compared to NLO calculations for the SM and to the predictions of a model featuring an effective axial-vector coupling of the gluon (EAG). The error bars on the differential asymmetry values indicate the statistical and total uncertainties, determined by adding statistical and systematic uncertainties in quadrature. The shaded areas indicate the theoretical uncertainties on the NLO calculations [124]

The result is in agreement with the SM prediction within the uncertainty. In

addition, the CMS collaboration has measured the asymmetry as a function of rapidity, transverse momentum, and invariant mass of the $t\bar{t}$ system, as can be seen in figure 3.18. Looking at the plots, within the uncertainties the data do not show any significant asymmetry and all measured values are consistent with a null asymmetry as well as with the SM predicted values.

3.3 Measurement of top quark charge asymmetry in ATLAS

This section is dedicated to the description of the measurement of the top quark charge asymmetry. The results presented in the following have been documented in a paper [32], and previously in a conference note of the ATLAS experiment [125], and in an internal report [126].

As already explained in section 3.2.1, the charge asymmetry would show up at the LHC in the fact that the top quark rapidity distribution is broader than the antitop quark one. A sensitive variable is therefore the difference between absolute values of top and antitop quark rapidities and the observable that has been used is defined in equation 3.17.

The analysis has been performed in the semileptonic channel, since it holds a good branching ratio, 34.3%, and a clear signature. These events are characterized by the presence of one isolated lepton (electron or muon[2]), missing transverse energy and jets, some with b-flavour.

The QCD NLO prediction for this asymmetry obtained using the Standard Model $t\bar{t}$ signal sample (generated with MC@NLO [127, 128, 129]) is $A_C^{pp} = (0.60 \pm 0.03)\%$ at the parton level; the uncertainty reported comes from available Monte Carlo (MC) statistics.

Significant enhancements are foreseen by some Beyond the Standard Model (BSM) theories as already explained in section 3.2.2. Deviations from the SM predictions can be therefore a hint of new physics.

[2]Small contributions to $W \to l$ from $W \to \tau \to l$ are included. Events in which one W decays hadronically and the other one in an hadronically decaying $\tau + \nu$ have been not considered, since τ-jets are significantly different from electrons and muons.

3.3.1 Data and Monte Carlo samples

3.3.1.1 Data samples

Data from LHC proton-proton collisions collected by the ATLAS detector between March and June 2011 are used in the analysis, corresponding to an integrated luminosity of (1.04±0.04) fb^{-1}. A peak instantaneous luminosity of about 1.3×10^{33} cm^{-2} s^{-1} was reached and a bunch spacing of 50 ns was used.

As explained in section 1.9.2 only data satisfying specific quality requirements are considered. The ATLAS Top Working Group selects events with stable beams and marked as good quality for the reconstruction of all the objects involved in the top quark pair events selection: trigger, electrons, muons, missing energy, jets and b-tagging.

The triggers used in the analysis are described in section 3.3.2.2 for both electron and muon channel.

3.3.1.2 Monte Carlo samples

Several Monte Carlo samples have been generated to facilitate this analysis, including nominal samples for the signal contribution and various background processes as well as several additional samples used in the evaluation of systematic uncertainties. All samples correspond to the *mc10b* production commonly performed for all ATLAS analyses using a generalised set of parameters to match the data taking conditions during the time period that was considered. In particular, the contribution from in-time and out-of-time pile-up was added to all generated Monte Carlo events. A fixed distribution of average proton-proton interactions per bunch crossing was used, while the actual data taking conditions with respect to pile-up changed over the course of time. In order to correct for the mis-match between individual data taking periods and the simulated pile-up contribution in the MC, an event-based reweighting was performed, taking into account the expected and observed distribution of the average number of interactions per bunch crossing. This pile-up reweighting was performed for all MC samples.

The $t\bar{t}$ signal process has been simulated using the MC@NLO generator (v3.41) [127, 128, 129] which incorporates the CTEQ6.6 [130] parton distribution function set and makes use of a next-to-leading order calculation approach for QCD processes. Both the parton showering and fragmentation processes, and the underlying

event have been modelled using the HERWIG v6.510 [131] and JIMMY [132] generators utilising the CTEQ6.6 and AUET1 [133] tunes to match the ATLAS data, respectively. The inclusive $t\bar{t}$ cross section has been estimated to approximately next-to-next-to-leading order using the HATHOR [134] tool to be 165^{+11}_{-16} pb for $m_t = 172.5$ GeV and the MC has been scaled accordingly. For this analysis, only events with an electron or a muon with p_T larger than 10 GeV in the Monte Carlo truth were considered. The respective cross section was 89.3 pb, including a *k-factor* of 1.117 to rescale the next-to-leading order perturbative QCD cross section in MC@NLO to the approximate next-to-next-to-leading order cross section. The signal sample contained 15×10^6 simulated events, corresponding to an integrated luminosity of about 150 fb^1.

The electroweak single top production was simulated using the MC@NLO and JIMMY generators and the respective cross sections have been calculated at approximately next-to-next-to-leading order to be $64.57^{+2.71}_{-2.01}$ pb in the t-channel, $4.63^{+0.19}_{-0.17}$ pb in the s-channel, and $15.74^{+1.06}_{-1.08}$ pb for Wt production.

The background contribution from the production of heavy gauge bosons with additional jets was modelled using the leading order ALPGEN generator [135], interfaced to HERWIG and JIMMY for the purposes of parton shower and hadronisation simulation. The CTEQ6.1 parton distribution functions and the AUET1 tune were employed for proper ATLAS data matching for both the matrix element evaluations and the parton showering. The production of additional partons was taken into account by generating different sub-samples with different final state parton multiplicities, where additional partons can be either light (u,d,s) partons (simulated in W+jets and Z/γ+jets light flavour samples) or heavy quarks (simulated in $W + c$+jets, $W + c\bar{c}$+jets, $W + b\bar{b}$+jets, and $Z + b\bar{b}$+jets samples, respectively). Since the inclusive W+jets and Z/γ+jets samples included contributions from both light partons and heavy quarks in the matrix element and parton shower simulation, the created overlap in phase space between the inclusive samples and the heavy quark contribution was taken into account by removing double counted events from the respective samples. The production cross sections of the used ALPGEN samples were normalised to the corresponding approximate next-to-next-to-leading order cross sections using *k-factors* of 1.20 (W+jets) and 1.25 (Z+jets), respectively. Furthermore, the relative fractions of the individual W+jets heavy quark contributions to the overall W+jets sample have been determined in data

driven methods, and were accounted for by applying corresponding scale factors to the individual samples. They have been found to be 1.63 ± 0.76 for $W + c\bar{c}$+jets and $W + b\bar{b}$+jets, and 1.11 ± 0.35 for the $W + c$+jets contribution, respectively. The W+jets light quark contributions were scaled accordingly to conserve the overall predicted cross section.

Contributions from diboson (WW, WZ and ZZ) production and decays were simulated using HERWIG at leading order, and the corresponding production cross sections were normalised to the next-to-next-to-leading order predictions, using *k-factors* of 1.48 (WW), 1.60 (WZ) and 1.30 (ZZ), respectively. Each sample was inclusive and has been filtered to include only events containing at least one lepton (electron or muon) with $p_T > 10$ GeV and $|\eta| < 2.8$ at parton level. The *k-factors* have been determined such that the unfiltered HERWIG cross sections agree with the next-to-next-to-leading order calculations.

For the evaluation of the systematic uncertainties of the various generators and the simulation of hadronisation and fragmentation, alternative samples have been used for the signal contribution and the Z+jets background contribution. The $t\bar{t}$ production and decay has been simulated with the POWHEG generator [136], and the corresponding parton showering and fragmentation processes have been modelled using both HERWIG and JIMMY (as used for the nominal MC@NLO sample), and PYTHIA [87] in order to evaluate systematic effects from the parton showering. Furthermore, additional MC@NLO signal samples using different top mass hypotheses of 170 GeV and 180 GeV have been used in order to quantify systematics arising from the uncertainties on the top mass prediction. Finally, several samples using different strengths of initial state radiation (ISR) and final state radiation (FSR) have been generated at leading order using the ACERMC generator [87], corresponding to different contributions of ISR and FSR based on observations in data. An alternative inclusive Z+jets background modelling was performed using the SHERPA generator [137] and the CTEQ6.6 parton distribution functions. Details on the evaluation of systematic uncertainties can be found in section 3.3.6.

All background samples and the samples used for the evaluation of systematic uncertainties corresponded to an integrated luminosity of about $10 - 30$ fb^{-1}.

3.3.2 Event selection

3.3.2.1 Physics object selection

Reconstructing top quark pair events in the detector requires electrons, muons, jets and missing momentum to be simultaneously measured.

- *Electron candidates* are defined as energy deposits in the electromagnetic calorimeter associated with a well-measured track. Identification criteria based on shower shape variables, track quality, and information from the transition radiation tracker are applied to electron candidates. Reconstructed electrons were required to pass the tight electron quality requirements, described in section 1.10.1. In addition, all candidates are required to have $p_T > 25$ GeV and $|\eta_{\text{cluster}}| < 2.47$, where η_{cluster} is the pseudorapidity of the electromagnetic calorimeter cluster associated with the electron. Candidates in the calorimeter transition region $1.37 < |\eta_{\text{cluster}}| < 1.52$ are excluded.

- *Muon candidates* are reconstructed from track segments in different layers of the muon chambers. These segments are combined starting from the outermost layer, with a procedure that takes material effects into account, and matched with tracks found in the Inner Detector. The candidates are then refitted using the complete track information from both detector systems (see *combined* muons in section 1.7), and are required to satisfy $p_T > 20$ GeV and $|\eta| < 2.5$.

- *Jets* are reconstructed with the anti-k_t algorithm [64], described in section 1.10.3, with a distance parameter of $R = 0.4$, starting from clusters of energy in adjacent calorimeter cells at the electromagnetic (EM) scale. The jet energy is corrected to the hadronic scale using p_T- and η-dependent correction factors obtained from simulation and validated with data. Jet quality criteria are applied to identify jets not associated to in-time real energy deposits in the calorimeters caused by various sources (calorimeter noise, non-collision beam-related background, cosmic-ray induced showers).

- *The missing transverse momentum (E_T^{miss})* is reconstructed from clusters of energy calibrated at the EM scale and corrected according to the energy scale of the associated physics object, as described in section 1.10.4. Contributions

from muons are included using their momentum measured from the tracking and muon spectrometer systems. The remaining clusters not associated with the high p_T objects are also included in the missing transverse momentum.

Muons within $\Delta R = 0.4$ of a jet axis[3] and with $p_T > 20$ GeV are removed in order to reduce the contamination caused by muons from hadron decays. Subsequently, jets within $\Delta R = 0.2$ of an electron candidate are removed to avoid double counting electrons as jets.

Isolation criteria are applied to both electron and muon candidates to reduce the backgrounds from hadrons mimicking lepton signatures and backgrounds from heavy flavour decays inside jets. For electrons, the total energy in a cone of $\Delta R = 0.2$ around the electron candidate must not exceed 3.5 GeV, after correcting for energy deposits from pile-up and for the energy associated with the electron. For muons, the sum of track transverse momenta for all tracks with $p_T > 1$ GeV and the total energy deposited in a cone of $\Delta R = 0.3$ around the muon are both required to be less than 4 GeV ignoring the contribution of the muon p_T.

Reconstructing top quark pair events is facilitated by the ability to tag jets from the hadronisation of b-quarks. For this purpose, two b-tagging algorithms are used and their results are combined to extract a tagging decision for each jet: the *JetFitterCombNN* tagging algorithm determines a b-tag probability/weight w for a given jet according to a Neural Network combination of the weights from the IP3D and JetFitter tagging algorithms. As described in section 1.10.3.1) JetFitter b-tagger exploits the topology of b- and c-hadron weak decays inside the jet. A Kalman filter is used to find a common line on which the primary vertex and the b- and c-hadron decay vertices lie, as well as their position on this line, giving an approximate flight path for the b- and c-hadrons. The discrimination between b-, c- and light quark jets is based on a likelihood using the masses, momenta, flight-length significances, and track multiplicities of the reconstructed vertices as inputs. To further increase the flavour discrimination power, the second b-tagger (IP3D) is run which does not attempt to directly reconstruct decay vertices. Instead, this second tagger uses the transverse and the longitudinal impact parameter significances of each track within the jet to determine a likelihood that the jet originates from a b-quark (see section 1.10.3.1).

[3] $\Delta R = \Delta\phi^2 + \Delta\eta^2$, where $\Delta\phi$ and $\Delta\eta$ are the separation in azimuthal angle and pseudorapidity, respectively.

The combined tagger operating point chosen for the analysis corresponds to a 70% tagging efficiency for b-jets in simulated $t\bar{t}$ events while light flavor jets are suppressed by approximately a factor of 100 (see figure 1.28 (a)).

The 30^{th} of April, six of the front end boards (FEBs) of the Liquid Argon (LAr) calorimeter became inoperative due to a problem with a Controller Board. They were then repaired at the beginning of July 2011. A significant fraction of data is affected by this problem (~ 530 pb^{-1}). The most affected physics objects are electrons and jets. If an electron falls in the region of the dead FEBs it will be probably not identified or selected, while jets energy will be mismeasured. To avoid the presence of mismeasured objects in data and to model the problem in Monte Carlo, events with a jet with $p_T > 20$ GeV within $\Delta R = 0.1$ from the LAr hole have been discarded and electrons that fall into the hole have been removed from the event[4]. These cuts have been applied on the data runs affected by the LAr problem and on a fraction of Monte Carlo corresponding to the integrated luminosity of influenced data.

3.3.2.2 Selection of $t\bar{t}$ candidates

The event selection used for the top charge asymmetry measurement was aimed at maximising the signal contribution from the $t\bar{t}$ decay in the semileptonic decay channel. At the same time, the background contribution from different sources was minimised. The two distinct observable final states, muon+jets and electron+jets, were treated independently.

The event selection for the semileptonic decay channel was focused on topologies with at least four reconstructed jets, exactly one isolated lepton (muon or electron) and missing transverse energy.

A preselection of the delivered raw data based on a common *GoodRunsList* has been applied prior to the event selection. This selection included global data quality flags, e.g. requiring stable beams at a centre-of-mass energy of 7 TeV and the LVL1 central trigger and luminosity measurement to be functional, indicating stable running and data taking conditions of the LHC and ATLAS, respectively. Furthermore, the data quality of the individual detector subsystems has been verified. These criteria correspond to a data quality selection efficiency of 84.1% in

[4]For each event with an electron in the hole, E_T^{miss} has been recalculated dropping the electron energy contribution.

the electron+jets channel and 84.3% in the muon+jets channel.

In addition to the baseline selection, which will be described in the following, several corrections have been applied to Monte Carlo samples on an event-by-event basis to account for potential mis-matches in the detector simulation with respect to data.

Muon trigger efficiencies have been taken into account directly by performing a trigger reweighting using trigger efficiencies obtained with a Tag&Probe method, which is shown schematically in figure 3.19, in $Z \to \mu^+\mu^-$ events in data. These events are selected by requiring the presence of a muon satisfying all selection cuts (*tag muon*) and one muon satisfying a subset of cuts (*probe muon*) with an invariant mass in a window around the true Z boson mass. This permits to have a pure Z sample in data. The efficiency of a given selection cut is then obtained as the probability of the probe lepton to pass this cut.

The discrepancies between the simulation and data for electron and muon reconstruction efficiencies and the electron trigger efficiencies as well as the b-tagging efficiencies have been taken into account by applying the corresponding scale factors to the Monte Carlo events. Furthermore, each Monte Carlo event has been assigned a weight according to the average amount of proton-proton interactions per bunch crossing in the respective sample to account for differences in the modelling of pile-up.

The following event selection has been used to enhance the signal to background ratio in the recorded samples. The described selections have been applied to both data and Monte Carlo samples unless stated otherwise:

- Events have been selected online asking an electron or muon trigger to have fired. The muon trigger selects at Level1 regions of interest in the Muon Spectrometer with at least 10 GeV of estimated transverse momentum. The Level2 and event filter then require a muon with $p_T > 18$ GeV, combining both Muon Spectrometer and Inner Detector information. Electron trigger is seeded by a Level1 item, that asks the presence of an electromagnetic cluster of $E_T > 14$ GeV. High level triggers impose some cuts on shower shape of the candidate electron and the presence of an associated track. The E_T threshold is raised to 20 GeV. The efficiency plateau for this trigger is reached at 25 GeV and so the offline p_T cut has been increased from 20 to 25 GeV.

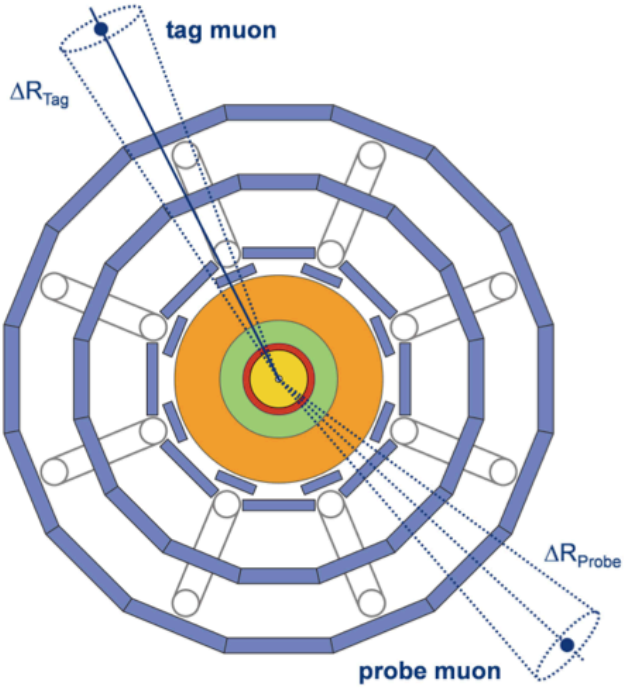

Figure 3.19: The Tag&Probe method. An event selection is performed using the tag object, while the actual trigger efficiency is determined only with the probe object to ensure independence of the two processes

- A primary vertex with at least five tracks associated to it was required to improve rejection of background from the underlying event, pile-up and cosmic radiation.

- Exactly one isolated lepton (one electron and no muon or vice versa) passing the respective object quality criteria with $p_T > 25$ GeV (electron+jets) or $p_T > 20$ GeV (muon+jets), respectively, was required.

- In addition, only for electron+jets channel, the selected electron was required to match the object of the fired trigger.

- Any event where a reconstructed electron and muon share a common track was rejected.

- Any event containing a *bad jet*[5] with $p_T > 20$ GeV at the EMJES scale was rejected
- A missing transverse energy $E_T^{\text{miss}} > 35$ GeV (electron+jets) or $E_T^{\text{miss}} > 20$ GeV (muon+jets) was required.
- A cut of $m_T(W)$[6]> 25 GeV (electron+jets) or a triangular cut of $E_T^{\text{miss}} + m_T(W) > 60$ GeV (muon+jets) was applied in order to suppress the QCD multijet background contribution, since these events typically have low $m_T(W)$ and low E_T^{miss}.
- The presence of at least four identified jets with $p_T > 25$ GeV has been required.
- Cuts to get rid of LAr calorimeter defects (LAr noise bursts and data integrity errors) have been imposed.
- At least one jet which has been b-tagged using the JetFitterCombinedNN algorithm with a weight $w > 0.35$ (corresponding to an overall b-tagging efficiency of about 70% in simulated $t\bar{t}$ events) was required to further improve the signal to background ratio.

As an example the muon selection cutflow is reported in table 3.6 which will be described and commented at the end of section 3.3.7.1.

3.3.3 Background estimates

The main background processes are W+jets, QCD, Z+jets, single top and dibosons events. However it's important not only to predict their normalisation, but also the shapes of kinematic variables.

[5] Jet quality criteria were applied to identify jets which do not correspond to physical in-time energy deposits in the calorimeter. Possible sources for such *bad jets* are for example hardware problems, calorimeter showers induced by cosmic rays and beam remnants.

[6] In this context, $m_T(W)$ denotes the W boson transverse mass, defined as

$$m_T(W) = \sqrt{2p_T^l p_T^\nu \left(1 - \cos(\phi^l - \phi^\nu)\right)} \tag{3.26}$$

where $p_T^{l/\nu}$ and $\phi^{l/\nu}$ describe the lepton and neutrino transverse momentum and azimuthal angle, respectively. The neutrino information is represented by the measured missing transverse energy, E_T^{miss}.

For what concerns Z+jets, single top and dibosons backgrounds that have a minor impact, both normalisations and shapes have been evaluated from Monte Carlo, while the dominant W+jets and QCD backgrounds have been estimated using data driven techniques as will be described in the following.

3.3.3.1 Data driven estimation of the QCD multijet contribution

The identification of top quark pairs decaying semileptonically relies on the identification of one lepton in the final state, carrying a large transverse momentum. Hence, mis-identified leptons (*fake leptons*), which can originate from various sources, pose a non-negligible background to the identification of $t\bar{t}$ signal events. Potential sources for mis-identified leptons include

- semileptonic decays of b-quarks into b-jets containing leptons which pass the isolation criteria,
- muons from decay in-flight of long lived particles such as $\pi^{\pm}$ or K mesons,
- π^0 mesons which are mis-identified as electrons,
- direct photon conversion and reconstruction of electrons produced in the process.

These processes are most dominant in regions where the contribution from prompt leptons are small, most prominently for the background contribution from QCD multijets.

Despite the fact that object and event selection are designed to ensure the suppression of these backgrounds by requiring stringent criteria, the QCD multijet production cross section is orders of magnitudes higher than the top quark pair production cross section. Since the simulation of these backgrounds in Monte Carlo is highly difficult and several of the described contributions are detector dependent, data driven methods are necessary to obtain reliable estimates for the fake lepton background contribution from QCD multijet events.

In both electron and muon channel QCD background has been estimated using a data driven method, the *Matrix Method*. This technique exploits differences in lepton identification-related properties between real and fake leptons. For this purpose, two samples are defined after requiring the final kinematic selection criteria,

differing only in the lepton identification cuts: a *tight* sample and a *loose* sample, the former being a subset of the latter. The tight selection typically employs the final lepton identification criteria used in the analysis.

The method assumes that the number of selected events in each sample (N_{loose} and N_{tight}) can be expressed as a linear combination of the numbers of events with real and fake leptons, in such a way that the following system of equations can be defined:

$$N_{\text{loose}} = N^{\text{sig}} + N^{\text{fake}} \tag{3.27}$$

$$N_{\text{tight}} = \epsilon^{\text{sig}} N^{\text{sig}} + \epsilon^{\text{fake}} N^{\text{fake}} \tag{3.28}$$

where $\epsilon^{\text{sig}}(\epsilon^{\text{fake}})$ represents the probability for a real(fake) lepton that satisfies the loose criteria, to also satisfy the tight ones.

The number of selected events with a loose or a tight lepton, as well as ϵ^{sig} and ϵ^{fake} have been measured in data, as explained in the following.

Muon channel Tight muons have been selected applying all cuts described in section 3.3.2.1. The loose selection is identical to the default one, except for the fact that muon isolation requirement has been dropped.

The signal efficiency ϵ^{sig} has been determined using Tag & Probe method in $Z \to \mu^+\mu^-$ events. The fake efficiencies have been determined using a low-$m_T(W)$ control region with an additional inverted triangular cut:

$$m_T(W) < 20 \text{ GeV} \qquad \text{and} \qquad E_T^{\text{miss}} + m_T(W) < 60 \text{ GeV} \tag{3.29}$$

The real muon contribution from W+jets and Z+jets in the control region has been obtained from Monte Carlo and subtracted to obtain a pure QCD estimation. The efficiencies have been obtained separately for the pretag and tagged selection. They have been also parametrized in muon pseudorapidity η, to reflect the dependency on muon detector acceptance, and in the leading jet transverse momentum p_T^{j1}, since hadronic activity can have an impact on the muon isolation. The dependence of efficiencies on instantaneous luminosity and different pile-up conditions has been checked as well. No significance dependence has been found.

The shape is obtained by applying the matrix method in different bins of the kinematic distributions.

The following sources of uncertainty have been taken into account in the estimate and combined into a joint normalization and shape uncertainty:

- the statistical uncertainty from control samples used to measure real and fake lepton efficiencies have been calculated;
- the effect of using an alternative control region for fake leptons efficiency evaluation asking a high impact parameter significance has been explored;
- the effect of the choice of the control region cuts has been studied by varying up and down the low transverse W mass control region cut by 5 GeV;
- the impact of the uncertainties on W/Z+jets Monte Carlo normalization in the low-$m_T(W)$ control region has been explored for the 1 jet inclusive bin, by shifting W/Z+jets contributions by their normalization uncertainty ($\sim 25\%$).

For each of these variations, the estimate has been redone and the difference within the default one has been taken as uncertainty.

The QCD multijet contribution estimate in the muon channel is reported in table 3.3. Since both shape and normalization have been verified only to a limited extent, a more conservative uncertainty has been used for the final result: the QCD background normalization has been shifted up and down by 50% for the pretag sample and 100% for the tagged one. Work is ongoing in order to further validate this technique and to avoid the use of overestimated uncertainties.

Electron channel As for muons, tight electron selection matches exactly the default electron selection, described in section 3.3.2.1. For what concerns loose selection, some identification cuts have been removed and the isolation request has been relaxed: the electron has been required to satisfy *medium* selection identification cuts with the additional request of one hit in the b-layer and isolation energy has been asked to be less than 6 instead of 3.5 GeV.

The signal efficiency ϵ^{sig} has been determined using Tag&Probe method in $Z \to e^+e^-$ events. The fake efficiency ϵ^{fake} is measured from data in a control region at low missing energy: 5 GeV $< E_T^{\text{miss}} <$ 20 GeV. Electroweak processes contributions have been subtracted using the Monte Carlo predictions in analogy to the muon+jets channel treatment. Both efficiencies have been parametrized as

a function of the electron η and have been evaluated independently for the pretag and the b-tag selection.

To evaluate the systematic uncertainty of the method, different variations have been implemented:

- an alternative control region for ϵ^{fake} has been used: $m_T(W) < 20$ GeV and $E_T^{\text{miss}} > 5$ GeV;
- the upper cut on E_T^{miss} for control region definition has been shifted by ± 5 GeV;
- the impact of real lepton contribution subtraction has been checked by scaling the Monte Carlo contribution by $\pm 25\%$ (equivalent to the W/Z+jets cross section uncertainty for the ≥ 1 jet selection);
- ϵ^{fake} has been parametrized as a function of different variables;
- ϵ^{sig} has been taken from Monte Carlo instead of from data.

For each of these variations, the estimate has been redone, and the difference with the default estimate has been taken as uncertainty. The statistical uncertainty on the determination of both ϵ^{fake} and ϵ^{sig} has been found to be negligible: smaller than 1%.

The QCD multijet contribution estimate in the electron channel is reported in table 3.3. As for muon channel, more conservative uncertainties on the QCD background estimate have been used: 50% and 100% for pretag and tagged samples respectively.

3.3.3.2 Data driven estimation of the W+jets contribution

The expected rate of the W+jets background has been evaluated before the request of b-tagging, mainly because of the lack of statistics in the tagged sample, using the charge asymmetry technique. This result has been then multiplied by the tagging probability to obtain the final estimate.

Due to the fact that the parton density of u quarks in the protons brought to collision in the LHC is on average higher than the parton density of d quarks (which can be observed already at lower momentum transfers, as depicted in figure 3.3), a higher rate of W^+ than of W^- is expected at the LHC.

The W^+ to W^- cross sections ratio

$$r = \frac{\sigma_{pp} \to W^+}{\sigma_{pp} \to W^-} \tag{3.30}$$

is, theoretically, relatively well understood [138]: at LHC energies it is predicted with an uncertainty of few percent. One can therefore use the theoretical prediction for r to measure the W+jets background.

The W+jets background (before the b-tagging requirement) in the signal region (≥ 4 jets) has been extracted from the following formula:

$$N_W = N_{W^+} + N_{W^-} = \left(\frac{r_{MC}+1}{r_{MC}-1}\right)(N_{W^+} - N_{W^-}) \tag{3.31}$$

where r_{MC} has been evaluated from Monte Carlo simulation applying signal selection cuts, and has been determined to be 1.56 ± 0.06 in the electron+jets channel and 1.65 ± 0.08 in the muon+jets channel, respectively. The dominant contributions to the overall uncertainty were due to PDF and jet energy scale uncertainties, and by the uncertainties on the heavy quark contribution fractions (i.e. the relative contributions from $W + b\bar{b}$+jets, $W + c\bar{c}$+jets and $W + c$+jets).

The difference between N_{W^+} and N_{W^-} can be substituted with the difference between the total number of events selected in data with a positively charged lepton (D^+) and the number of selected events with a negatively charged lepton (D^-). To a very good approximation, $N_{W^+} - N_{W^-} \approx D^+ - D^-$, since the other processes are charge symmetric, apart from a small bias expected from single top quark and $t\bar{t}$ productions.

An asymmetry occurs in single top production in s- and t-channels: due to PDF effects, the number of events with top quark (and as a consequence with a positive lepton) is higher than the one with antitop quark (and as a consequence with a negative lepton)[7]. These contributions have been estimated from Monte Carlo simulation and subtracted appropriately from equation 3.31. Also $t\bar{t}$ events can have an impact on this assumption. Because of the charge asymmetry, antitop quarks will be more central than top quarks. Due to limited η coverage of the detector, the number of the selected $t\bar{t}$ events with a negative lepton will be higher than the one with a positive lepton. The impact of $t\bar{t}$ asymmetry has been

[7] colliding particles are two protons, valence quarks are mostly positively charged (uud for the proton) and so top quark to antitop quark production ratio is 1.6 for s- and t-channels.

studied using MC@NLO predictions and the effect has been found to be negligible. To check the effect of a possible BSM contribution, MC@NLO signal sample has been reweighted to create an artificial asymmetry compatible with the excess measured at the Tevatron (see section 3.3.5 for the details about the reweighting technique). Even with this higher asymmetry, no impact has been seen on the W+jets evaluation.

As already mentioned at the beginning of the paragraph, the application of this method directly to the tagged samples is affected by a large uncertainty coming from available statistics and the present knowledge of W+jets heavy flavour (HF) content. The obtained overall W+jets rate N_W has been extrapolated to the full event selection by determining the relative fraction of events passing the requirement of at least one b-tagged jet after requiring exactly two reconstructed jets, $f_{2,\geq 1b\text{-tag}}$, on data, and by determining the ratio $k_{2\to\geq 4}$ of the same fraction for the sample where at least four reconstructed jets were required with respect to $f_{2,\geq 1b\text{-tag}}$, using the W+jets Monte Carlo prediction:

$$N_{W,\geq 1b\text{-tag}} = N_W \cdot f_{2,\geq 1b\text{-tag}} \cdot k_{2\to\geq 4} \tag{3.32}$$

The fraction $f_{2,\geq 1b\text{-tag}}$ has been measured to be 0.063 ± 0.005 in the electron+jets channel and 0.068 ± 0.005 in the muon+jets channel, including statistical and systematic uncertainties. The extrapolation factor $k_{2\to\geq 4}$ has been determined to be 2.52 ± 0.36 in the electron+jets channel and 2.35 ± 0.34 in the muon+jets channel, respectively. The uncertainties include contribution from the statistical limitation of the used Monte Carlo samples and systematic uncertainties.

3.3.3.3 Other backgrouds

In order to quantify the uncertainty on the Z+jets contribution normalisation, a Berends-Giele scaling[8] uncertainty was calculated from MC predictions, corresponding to an overall normalisation uncertainty of 34%. In addition, the Z+jets

[8]The Berends-Giele scaling method exploits the fact that the ratio of $Z + n$ jets to $Z + n + 1$ jets is expected to be approximately constant as a function of n [139, 140]. E.g. the number of Z events in the 4-jet sample can be estimated as:

$$Z^{\geq 4\text{jets}} = Z^{2\text{jets}} \cdot \sum_{i=2}^{\infty} \left(Z^{2\text{jets}} / Z^{1\text{jet}} \right)^i \tag{3.33}$$

background was determined independently from both the ALPGEN and SHERPA generator to quantify the shape uncertainty, which was quoted based on the symmetrised discrepancy of the results obtained with SHERPA with respect to the nominal case, in which ALPGEN samples were used.

For the small backgrounds from single top and diboson production, only normalisation uncertainties were considered. A 5% has been taken for dibosons cross section, while a 11% has been used for single top.

In the calculation of the final uncertainty on background normalisation the contributions coming from object systematics, such as JES uncertainty, and luminosity have been taken into account.

3.3.3.4 Event yield

The final numbers of expected and observed data events in both channels after the full event selection are listed in table 3.3. The number of events in the electron channel is significantly lower than in the muon channel due to the higher lepton p_T requirement and the more stringent missing momentum requirement, which are necessary to reduce the contribution from the multijet background. The overall agreement between expectation and data is good.

3.3.4 Kinematic event reconstruction

As described in section 3.3.2, the signature of a $t\bar{t}$ event in the semileptonic decay channel at leading order is the observation of four reconstructed jets, one isolated lepton and missing transverse energy. A reconstruction of the full $t\bar{t}$ final state was performed following a likelihood approach, using the *KLFitter* package [141].

A probability for the observation of a set of measured quantities under the assumption of a specific model and a set of model parameters is assigned. In this particular case, the model described the $t\bar{t}$ decay and the input quantities are the measured energies of the four jets, the measured quadrimomentum of the lepton, and the missing transverse energy. The fit parameters of the likelihood were the parton energies, the lepton transverse momentum and the three neutrino momentum components. The likelihood was used to assign the measured jets to the decay products of the $t\bar{t}$ system. For this study, all permutations with four out of the five leading jets (if exist) were taken into account for the event reconstruction

Channel	muon+jets		electron+jets	
Selection	≥ 0 b-tag	≥ 1 b-tag	≥ 0 b-tag	≥ 1 b-tag
$t\bar{t}$	7200 ± 600	6300 ± 500	4800 ± 400	4260 ± 350
Single top	460 ± 40	366 ± 32	320 ± 28	256 ± 22
W+jets (data)	8600 ± 1200	1390 ± 310	5400 ± 800	880 ± 200
Z+jets	940 ± 330	134 ± 47	760 ± 270	110 ± 40
Diboson	134 ± 7	22 ± 2	80 ± 5	13 ± 1
QCD multijet (data)	1500 ± 800	500 ± 500	900 ± 500	250 ± 250
Total background	11700 ± 1400	2400 ± 600	7500 ± 900	1500 ± 320
Signal+background	18900 ± 1600	8800 ± 800	12000 ± 1000	5800 ± 500
Observed	19639	9124	12096	5829

Table 3.3: Numbers of events observed in data and expected from $t\bar{t}$ signal events and various background processes for the for the event selection, both with and without the requirement of at least one b-tagged jet. The QCD multijet and W+jets contributions were estimated using data driven methods described in section 3.3.3. Uncertainties are statistical and include the respective systematic uncertainties on the normalisation for QCD multijet and W+jets and the cross section uncertainties on all other contributions. For the QCD multijet background, a conservative 50% (100%) overall normalisation uncertainty for the selection without (with) requiring at least one b-tagged jet was assumed.

to increase the probability of identifying the proper combination in the presence of additional jets (e.g. from ISR or pile-up).

Moreover, the (non-Gaussian) partonic energy resolution (the resolution of the particle jets with respect to the partons) of the final state objects were taken into account through the use of object specific transfer functions in order to obtain the final likelihood:

$$\begin{aligned} L = \quad & \mathcal{B}(\tilde{E}_{p,1}, \tilde{E}_{p,2} | m_W, \Gamma_W) \cdot \mathcal{B}(\tilde{E}_1, \tilde{E}_\nu | m_W, \Gamma_W) \cdot \\ & \mathcal{B}(\tilde{E}_{p,1}, \tilde{E}_{p,2}, \tilde{E}_{p,3} | m_t, \Gamma_t) \cdot \mathcal{B}(\tilde{E}_1, \tilde{E}_\nu, \tilde{E}_{p,4} | m_t, \Gamma_t) \cdot \\ & \mathcal{W}(\hat{E}_x^{\text{miss}} | \tilde{p}_{x,\nu}) \cdot \mathcal{W}(\hat{E}_y^{\text{miss}} | \tilde{p}_{y,\nu}) \cdot \mathcal{W}(\hat{E}_\ell | \tilde{E}_\ell) \cdot \\ & \prod_{i=1}^{4} \mathcal{W}(\hat{E}_{\text{jet},i} | \tilde{E}_{p,i}) \cdot \mathcal{P}_i(b\text{-tag}|\text{quark}) \end{aligned} \tag{3.34}$$

where:

- the $\mathcal{B}$s represent the Breit-Wigner parametrisation of the parton (from which the associated jets originated) energies $\tilde{E}_{p,i}$ and lepton energies $\tilde{E}_\ell$ with respect to the fitted ones. The pole masses of the W boson and the top quark are fixed to $m_W = 80.4$ GeV and $m_t = 172.5$ GeV, respectively. Their widths are taken to be $\Gamma_W = 2.1$ GeV and $\Gamma_t = 1.5$ GeV.

- the $\mathcal{W}$s represent the transfer functions associating the reconstructed quantities ($\hat{X}$) to quarks and leptons produced in the hard scattering ($\tilde{X}$). $\tilde{E}_{p,i}$ are the energies of partons associated to jets with measured energies $\hat{E}_{\text{jet},i}$. These transfer functions are derived from Monte Carlo simulation.

- $\mathcal{P}_i(b\text{-tag}|\text{quark})$ is the b-tagging probability or rejection efficiency, depending on the parton flavour, as obtained from Monte Carlo simulation. This probability was used to take into account the tagging efficiency and rejection rate of the used b-tagging algorithms at a specific working point.

The most probable event topology hypothesis was chosen by iterating over all possible permutations of reconstructed jets, the lepton and the missing energy and by maximising the logarithmic likelihood, $\log L$. The permutation with the highest event probability was used for all further studies. The reconstruction efficiency, obtained in simulations, is shown for both the muon+jets and electron+jets channel in figure 3.20.

As can be seen, the overall efficiencies for the reconstruction of the correct event topology (All Correct) in both channels were 62%(74%) with a fixed mass

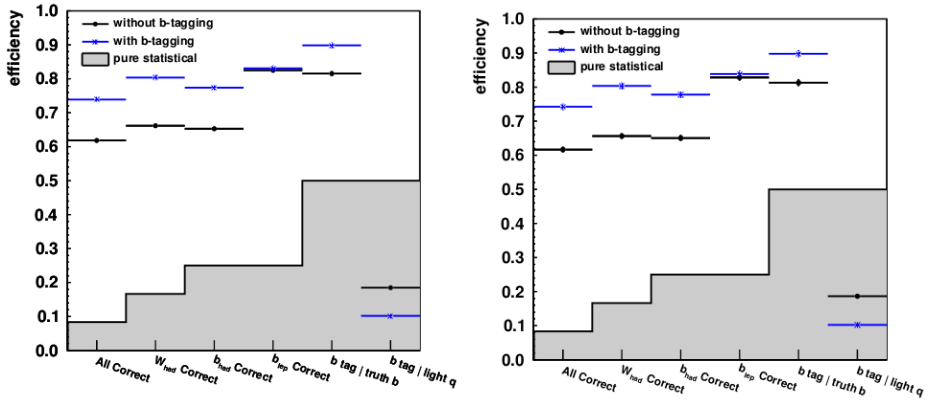

(a) muon+jets channel (b) electron+jets channel

Figure 3.20: *KLFitter* reconstruction efficiencies for the muon+jets (left) and electron+jets (right) channel. The indicated efficiencies denote the probability of reconstructing the correct (or true) combination of objects (only matched events taken into account). The bars marked pure statistical indicate the efficiency which is expected by choosing a combination at random

parameter, without (with) b-tagging information taken into account. In order to associate the reconstructed objects with the corresponding truth quarks and leptons, a simple ΔR matching was applied, using cone sizes of 0.3 for jets and 0.1 for leptons. An event was considered matched if all truth partons originating from the hard scattering process could successfully be identified with reconstructed jets and the truth lepton was matched to a reconstructed one. For the shown performance evaluation, only events where the four reconstructed jets and the lepton were successfully matched to corresponding truth level objects (contributing positively to the reconstruction efficiency) were taken into account. The matching efficiency on simulated $t\bar{t}$ events was about 30% in both channels. Examples for the transfer functions used in the likelihood can be found in figure 3.21, where the fit functions in different energy regions for b-jets in the pseudorapidity range $|\eta| < 0.8$ and for electrons in the pseudorapidity range $0.8 < |\eta| < 1.37$ are shown.

A double Gaussian function was used in the fit of the transfer functions:

$$W(E_{\text{true}}, E_{\text{reco}}) = \frac{1}{\sqrt{2\pi}(p_2 + p_3 p_5)} \left(e^{-\frac{(\Delta E - p_1)^2}{2p_2^2}} + p_3 e^{-\frac{(\Delta E - p_4)^2}{2p_5^2}} \right) \tag{3.35}$$

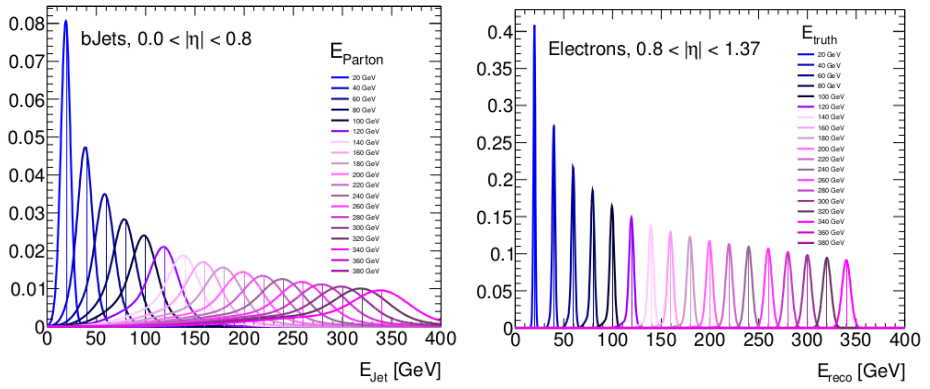

(a) transfer functions for b-jets

(b) transfer functions for electrons

Figure 3.21: Examples for the *KLFitter* transfer functions mapping the measured particle jets to the partons, on the left for b-jets in the range $|\eta| < 0.8$ and on the right for electrons in the range $0.8 < |\eta| < 1.37$. In both cases, the transfer functions for different energies are shown

where the parameters p_1, p_2, p_3, p_4 and p_5 are functions of the true energy of the respective particle and $\Delta E = E_{\text{true}} - E_{\text{reco}}$.

The expected likelihood distributions and the observed ones in data are shown in figure 3.22. The agreement between the data and the predictions is very good.

Distributions of the invariant mass and transverse momentum of the reconstructed top-antitop pair are shown in figure 3.23.

In figure 3.24 the difference between top and antitop rapidities are represented for both channels. Very good agreement between data and signal+background expectation has been observed for all distributions in both electron and muon channel.

3.3.5 Unfolding

3.3.5.1 Motivation

Any measured observable is influenced by imperfections of the used measurement apparatus and procedure itself, such as limited resolution of the detector response, the detector acceptance and object and event selections which are applied to

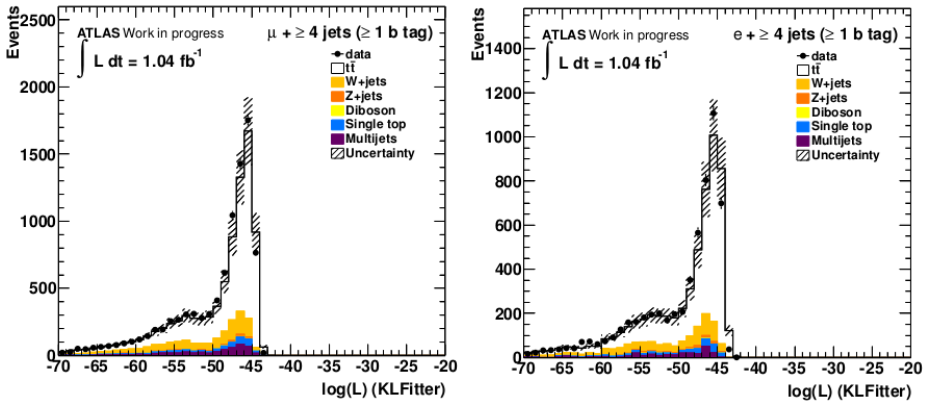

(a) (b)

Figure 3.22: Expected and observed distributions for the likelihood used to reconstruct the $t\bar{t}$ final state for the muon (a) and the electron (b) channel. The data is compared to the sum of the $t\bar{t}$ signal contribution and backgrounds. The background contributions from W+jets and QCD multijet production have been estimated from data, while the other backgrounds are estimated from simulation. Uncertainties include statistical contributions, systematic uncertainties on W+jets and QCD normalisation and also the uncertainties on luminosity, JES, b-tag scale factors and $t\bar{t}$ cross section

the data. In addition, parton level quantities are diluted by the showering and hadronization process. Due to these distortions, any measurement of such observable does not fully represent the original (or true) quantity. Mathematically, the actual measurement can be considered to be a convolution of the true quantity with a function representing the overall detector and selection acceptance and the detector response.

The impact on charge asymmetry has been studied on Monte Carlo using MC@NLO signal sample (SM scenario in the following). In order to check the effect on a non-zero asymmetry, $t\bar{t}$ events have been reweighted in order to simulate an asymmetry compatible with the excess seen by CDF experiment at high $t\bar{t}$ invariant mass (BSM scenario in the following). For this scope, a parametrization proposed by B. Webber [142] has been considered, which consists in assigning a weight, w, to each event coming from $q\bar{q}$ initial state depending on top quark pair

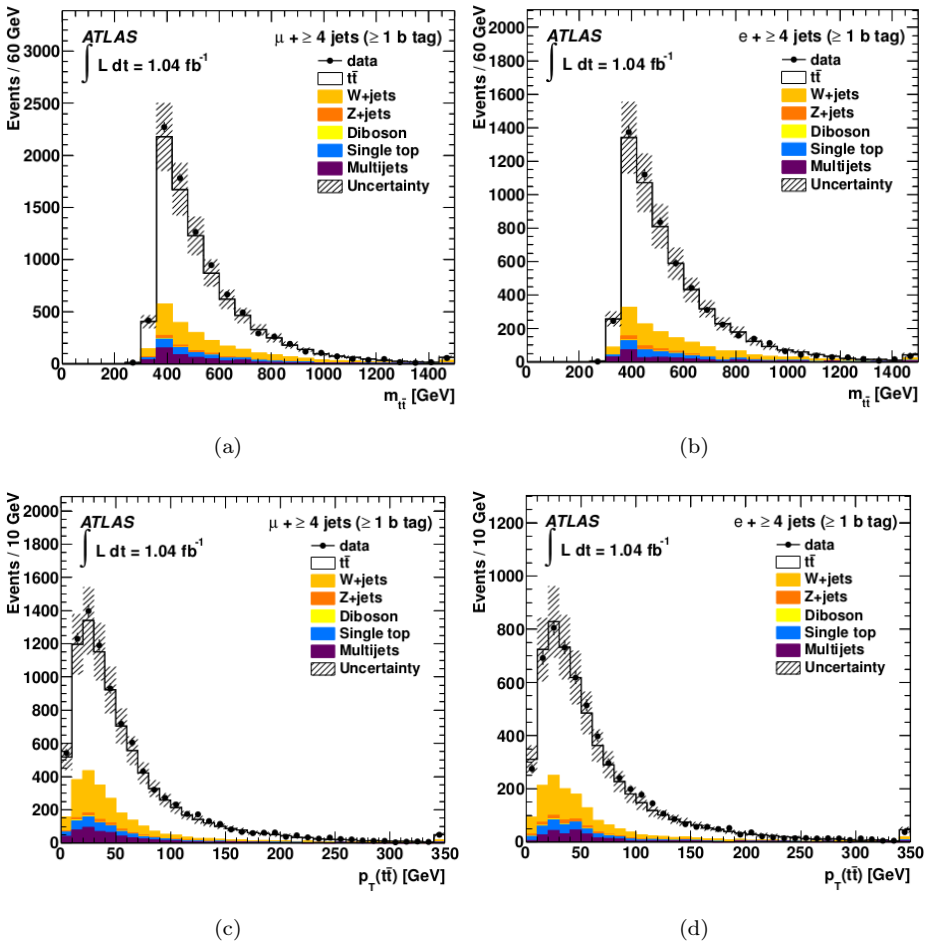

Figure 3.23: Control plots for the $t\bar{t}$ event reconstruction, on the left for the muon+jets, on the right for the electron+jets channel. The top row shows invariant mass $M_{t\bar{t}}$ and the bottom row shows the transverse momentum p_T of the $t\bar{t}$ system. Uncertainties are statistical and for W+jets also include systematic uncertainties on normalisation. For the QCD multijet background, a conservative 100% systematic uncertainty was assumed. In addition, the uncertainties on luminosity, JES, b-tag scale factors and $t\bar{t}$ cross section are shown

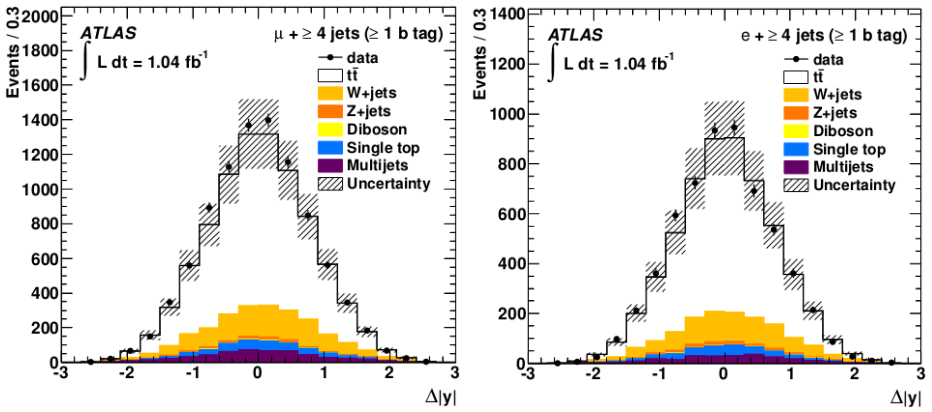

(a) (b)

Figure 3.24: Distributions for the inclusive measurement of $|y_t| - |y_{\bar{t}}|$, on the left for the muon+jets, on the right for the electron+jets channel. Uncertainties are statistical and for W+jets also include systematic uncertainties on normalisation. For the QCD multijet background, a conservative 100% systematic uncertainty was assumed. In addition, the uncertainties on luminosity, JES, b-tag scale factors and $t\bar{t}$ cross section are shown

invariant mass ($m_{t\bar{t}}$) and the difference between top and antitop rapidities (Δy):

$$w = 1 + f(m_{t\bar{t}}) \tanh(\Delta y/2) \tag{3.36}$$

where

$$f(m_{t\bar{t}}) = m_{t\bar{t}}/(200\ \text{GeV}) - 2 \tag{3.37}$$

It is important to remark that this is not a model, but only an empirical parametrization introduced to reproduce the asymmetry measured in the CDF data, by simulating a fictitious asymmetry contribution instead of a specific BSM model.

In order to quantify acceptance and detector resolution effects, the asymmetry at partonic level, before any selection cuts, has been compared to the one measured after selection cuts on Monte Carlo truth decay products and the one after selection cuts on reconstructed decay products.

Figure 3.25 shows the charge asymmetry, defined in equation 3.17, as a function of $m_{t\bar{t}}$ for both the SM (left) and BSM (right) scenario. The three rows represent the set of cuts described above: no selection, selection on Monte Carlo objects

and selection on reconstructed objects. The top and antitop variables used are taken from Monte Carlo truth information: no kinematic reconstruction has been performed at this level. The asymmetry is computed for all the events (black box) and only for on $q\bar{q}$ events (red dots). The uncertainties quoted in the plots are both MC@NLO statistical uncertainty and systematics added in quadrature. Systematic uncertainty has been obtained as the sum in quadrature of different contributions:

- the effect of using different Monte Carlo generators, which has been studied comparing the predictions of MC@NLO and POWHEG samples,
- the effect of using different parton showers: POWHEG+HERWIG prediction has been compared with the one of POWHEG+PYTHIA,
- the impact of changing the tune of ISR and FSR, which has been estimated using ACERMC samples.

The asymmetry is diluted in SM and BSM cases by the application of the selection cuts both on the parton and on the reconstructed objects. In order to be able to compare the measured asymmetry with theoretical predictions, it is therefore important to correct the $\Delta|y|$ distribution for acceptance and detector resolution effects. This is obtained using unfolding techniques as described in the following.

3.3.5.2 Unfolding technique

Let the true quantity be represented by a vector $\vec{t}$ (with entries t_j and $j = 1, 2, ..., n_t$) describing the bin contents of a histogram, and the measured or reconstructed distribution by a corresponding vector $\vec{k}$ (with entries k_i and $i = 1, 2, ..., n_k$), respectively. The underlying detector resolution effects can be described by a transition or *response matrix* R^{res}, which contains the individual transition probabilities and hence the migrations between the observed elements of the distribution and the corresponding true values.

Furthermore, the detector acceptance and applied selection can be quantified by an additional weight factor for each element of R^{res}, taking into account the probability of events from a particular entry of $\vec{t}$ being observed at all in the measurement process. This additional correction, which can be described by a second matrix R^{acc}, together with the response matrix describing the resolution

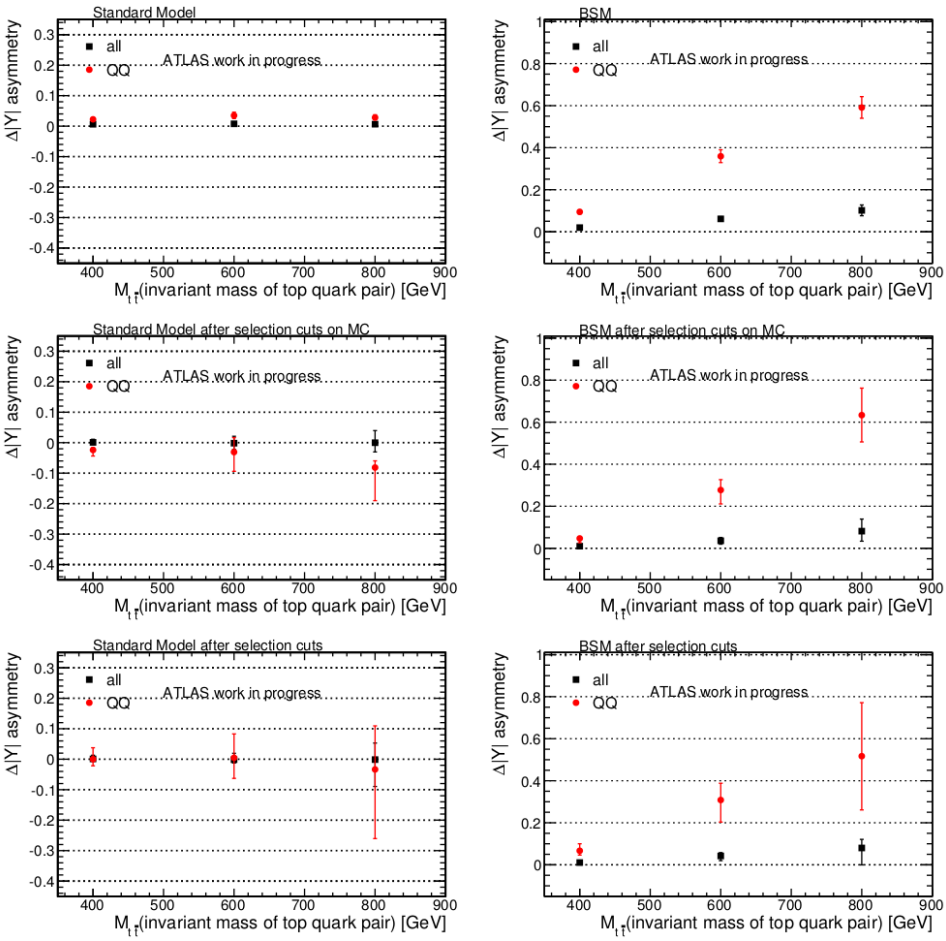

Figure 3.25: $\Delta|y|$ asymmetry as a function of $m_{t\bar{t}}$. The three rows correspond respectively to: no selection cuts applied; selection cuts applied on Monte Carlo objects; selection cuts applied on reconstructed objects. The left plots correspond to the SM scenario, while the right plots correspond to the BSM scenario with the parametrization in equation 3.36. The black boxes represent the value of the asymmetry for all the events passing the various cuts, while the red dots the asymmetry computed only for $q\bar{q}$ events. Statistical and systematics uncertainties as explained in the text are both included and summed up in quadrature

effects, yields the overall response matrix R:

$$R = R^{\text{acc}} R^{\text{res}}, \tag{3.38}$$

denoting the transition probabilities between the observed distribution and the true distribution:

$$\vec{k} = R\vec{t} \tag{3.39}$$

where

$$R_{ij} = P(\text{observed in bin } i | \text{expected in bin } j) = P(k_i|t_j) \tag{3.40}$$

The concept of unfolding is illustrated in figure 3.26, where an example distribution for an arbitrary variable x is shown at the different stages in the measurement process.

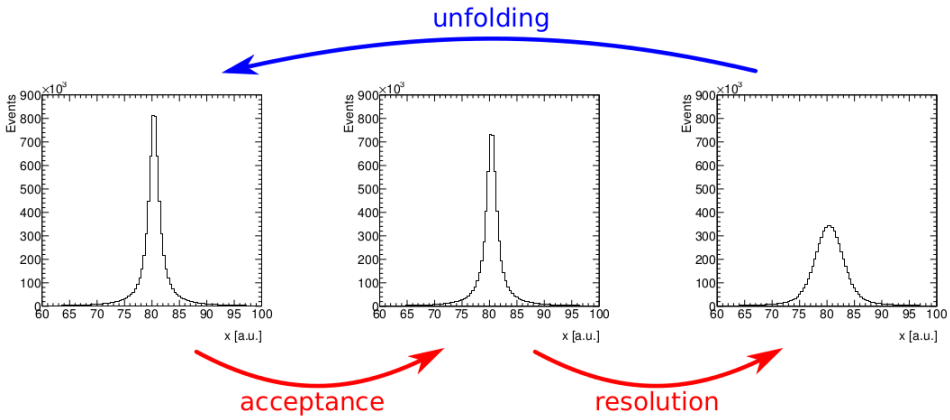

Figure 3.26: Schematic overview of the measurement and unfolding process. The true distribution of an arbitrary variable x (left) is affected by acceptance effects (centre) and resolution effects (right) in the measurement process. The unfolding procedure attempts to reverse these effects to obtain the most probable true distribution corresponding to the given measured distribution

In order to find an estimator for the true distribution given the measured distribution, an unfolding method can be applied to correct for the respective acceptance and resolution effects. In this process, the response matrix is derived from an arbitrary reference sample, typically using Monte Carlo simulations. This procedure is called the *training* step of the unfolding. The obtained response matrix has to be

inverted in order to allow the unfolding of any measured distribution to its corresponding true distribution. Since the response matrix represents the full resolution and acceptance information of the underlying measurement, the unfolding procedure can be performed model-independently, assuming that the detector simulation used in the training sample is sufficiently accurate.

However, in most situations where unfolding is applied, an exact and unique inverse response matrix R^{-1} does not necessarily have to exist, such that

$$RR^{-1} = I \tag{3.41}$$

where I is the unity matrix. Hence, approximations are needed to perform the above matrix inversion to acceptable accuracy.

Limited statistics in the reference sample and the resulting statistical fluctuations can lead to additional and inadvertent bin migration effects in the response matrix, which do not represent the underlying resolution and acceptance effects. Consequently, these contributions have to be suppressed in the matrix inversion process, achieved by applying a regularisation procedure in order to limit the propagation of statistical fluctuations into the unfolded distribution or quantity. This regularisation typically involves a cut-off or weight parameter representing the sensitivity of the unfolding approach with respect to short-ranged bin-by-bin changes. Hence, the regularisation can be regarded as a constraint on the smoothness of the response matrix and hence the unfolded distribution.

The obtained approximate inverse matrix R^{-1} is applied to the distribution measured from data, $\vec{m}$, and the respective unfolded distribution, $\vec{u}$, is obtained as estimator for the true distribution based on the given measurement:

$$\vec{u} = R^{-1}\vec{m} \tag{3.42}$$

Several procedures have been developed to perform the inversion and the necessary regularisation. For this analysis, a procedure based on an iterative approach to perform the inversion of the response matrix following Bayes' theorem is applied[9]. This approach allows incorporating new knowledge to update a prior probability of observation of a given event in an iterative procedure.

[9]The technique utilised were available in the *RooUnfold* package [143], which provided simple interfaces and efficient implementations for the bayesian unfolding method [144].

In order to obtain the inverted response matrix, the posterior probability of obtaining the true distribution $\vec{t}$ given the measured distribution $\vec{k}$ is calculated accordingly, assuming prior knowledge $P_0(t_j)$ for the individual components of $\vec{t}$ based on the true distribution obtained in the Monte Carlo training step of the unfolding:

$$P(t_j|k_i) = \frac{P(k_i|t_j)P_0(t_j)}{\sum_{l=1}^{n_t} P(k_i|t_l)P_0(t_l)} \tag{3.43}$$

Note that in this context, the probability $P(k_i|t_j)$ is identical to the transition probability R_{ij} contained in the response matrix.

The obtained posterior probability distribution function is used as a prior in the next iteration, consecutively updating the existing knowledge about the respective probabilities with increasing number of iterations:

$$\begin{array}{lcllcl} P_1(t_j) & \alpha & \sum_i P(t_j|k_i) \cdot k_i & \alpha & \sum_i P(k_i|t_j) \cdot P_0(t_j) \cdot k_i \\ P_2(t_j) & \alpha & \sum_i P(t_j|k_i) \cdot k_i & \alpha & \sum_i P(k_i|t_j) \cdot P_1(t_j) \cdot k_i \\ & \vdots & & & \end{array} \tag{3.44}$$

Regularisation of the Bayes iterative unfolding procedure can be achieved naturally by restricting the number of iterations N_{It} such that the underlying true distribution is recovered within the statistical uncertainties, and bin-to-bin fluctuations which are of purely statistical nature are suppressed. For a large number of iterations, a convergent state is reached, yielding the true, but strongly fluctuating inverse of the response matrix (thus minimising any remaining systematic bias of the unfolded distribution at the cost of larger statistical uncertainties). The number of iterations necessary to reach convergence depends on different conditions, including the choice of binning, the strength of bin migrations in the response matrix (i.e. the magnitude of its off-diagonal elements), and the initial choice of prior. The optimal choice of N_{It} is case dependent and must be determined following a well-defined procedure, balancing remaining bias and statistical uncertainty of the obtained result.

This approach allowed for a simultaneous unfolding in multiple observables due to the fact that Bayesian unfolding is independent of the ordering of the classes/bins. Since many of the BSM models summarised in section 3.2.2 predict different magnitudes of the charge asymmetry for low and high $m_{t\bar{t}}$ regions, a simultaneous unfolding of $|y_t| - |y_{\bar{t}}|$ and the invariant $t\bar{t}$ mass, $m_{t\bar{t}}$, has been

performed, taking into account bin migrations in both dimensions. Semileptonic $t\bar{t}$ events generated with the MC@NLO generator have been used as reference sample to obtain the response matrix based on the detector simulation. Furthermore, a simple extraction of the covariance matrix of the unfolded distributions was possible.

Two bins are used for $m_{t\bar{t}}$ in the two-dimensional unfolding of $\Delta|y|$ versus $m_{t\bar{t}}$, separated at $m_{t\bar{t}} = 450$ GeV. The choice of this $m_{t\bar{t}}$ value is motivated by the observed CDF forward-backward asymmetry, described in section 3.2.3, and by separating the data sample into two bins with roughly equal number of events.

The response matrix (including both detector and acceptance effects) for the inclusive A_C measurement is shown in figure 3.27.

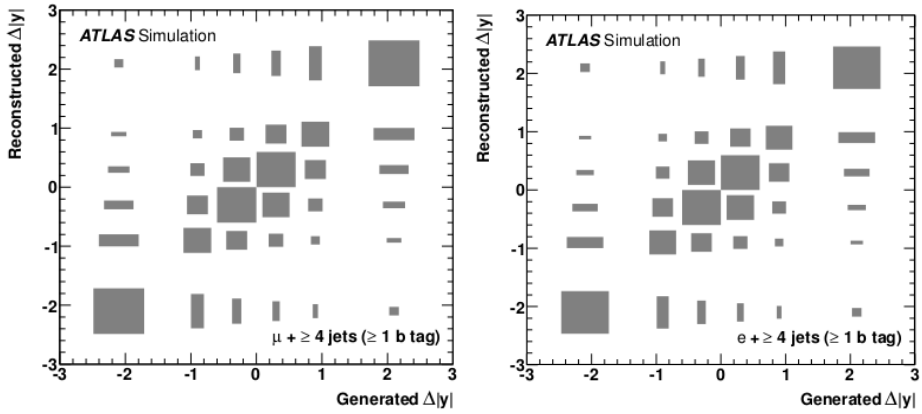

(a) Response Matrix (μ+jets) (b) Response Matrix (e+jets)

Figure 3.27: Correlations between the true and reconstructed values of $\Delta|y|$ encoded in the unfolding response matrix for the muon (left) and electron (right) channels. The value of an entry in the matrix is proportional to the area of the corresponding box

Six bins in $\Delta|y|$, in the range $-3 < \Delta|y| < 3$, are used in the response matrix, with the outermost bins broader than the inner bins in order to avoid the occurrence of bins with no entries in the measured distributions. Only a very small fraction of simulated $t\bar{t}$ events are found to have $|\Delta|y|| > 3$, and hence such events have a negligible influence on the results.

Closure tests are performed in order to check the validity of the unfolding proce-

dure. Reweighted $t\bar{t}$ samples with different amounts of asymmetry are considered. Pseudoexperiments are performed, varying the entries in histograms of the reconstructed distribution, to confirm that the response of the unfolding is linear in the true value of A_C and that the true value of A_C is recovered on average. A total of 40 iterations are used in both channels for the inclusive A_C measurement. For the measurement of A_C as a function of $m_{t\bar{t}}$, 80 iterations are used. The number of iterations is chosen by ensuring that the unfolding procedure has converged in the sense that the absolute change in the unfolded value of A_C after performing an extra iteration is less than 0.001.

The unfolding procedure is applied to the observed $\Delta|y|$ distribution in data, after subtracting background contributions. The value of A_C after unfolding is obtained by counting the numbers of events with $\Delta|y| > 0$ and $\Delta|y| < 0$ in the unfolded $\Delta|y|$ distribution.

3.3.6 Systematic uncertainties

In addition to the statistical uncertainty originating from limited data statistics, there are a number of systematic effects that can have an impact on the performed measurement. These effects were studied individually and a corresponding systematic uncertainty on the measurement result was assigned for each contribution.

In order to evaluate the individual effects, the analysis was performed for each systematic under consideration with a modified response matrix and/or background contribution depending on the modelled effect. The changes typically corresponded to an uncertainty of one or more parameters (e.g. a shift of the muon trigger efficiencies according to the respective uncertainties) or an alternate model (e.g. a different MC generator used for the simulation of $t\bar{t}$ events). The uncertainty was extracted in each case based on the shift in the measurement central value when changing the parameters accordingly, and was symmetrised.

In order to suppress the statistical component of the obtained uncertainty inherent in the re-evaluation of the central value by changing different parameters of the performed measurement, the requirement of at least one b-tagged jet in the event selection was replaced by a reweighting method. The $|y_t| - |y_{\bar{t}}|$ distribution for the Monte Carlo based background contributions (Z+jets, single top and diboson background) was obtained by direct application of the b-tag weights to the

events passing the nominal event selection without the requirement of at least one b-tagged jet.

The following systematics were considered and evaluated for this analysis. All contributions were assigned to the Monte Carlo prediction (signal and/or background, where applicable).

- **Jet energy scale**: the jet energy scale (JES) uncertainty was derived using information from test beam data, LHC collision data and simulation, and was taken into account by scaling up and down the energy of all considered jets by 1σ of the associated transverse momentum uncertainty based on the jet p_T and η. The full event selection and kinematic reconstruction has been re-run with the scaled jets. In addition, the missing transverse energy has been re-evaluated, taking into account the scaled contributions of the jets in p_x and p_y. For jets within the acceptance range, the JES uncertainty varied from about 2.5% for high p_T jets in the central detector region to about 14% for low p_T jets in the forward region.

- **Pile-up (JES)**: the energy of the calorimeter cells associated to a jet receives a contribution due to pile-up. This contribution is subtracted during calibration, but this process has an uncertainty which results into an uncertainty of the jet energy. An additional systematic uncertainty of 5%(7%) for low p_T jets or 2%(3%) for high p_T jets in the $|\eta| < 2.1 (2.1 < |\eta| < 4.5)$ region was added to the JES uncertainty in quadrature.

- **b-jet energy scale**: in order to account for the difference of the energy scale for b-jets with respect to light quark jets, all b-jets (i.e. jets which have a matched truth b-quark in simulations) were scaled by an additional fraction ranging from 2.5% in the low p_T jet region to 0.76% in the high p_T jet region and added to the JES uncertainty in quadrature.

- **Jet reconstruction efficiency**: the jet reconstruction efficiency (JRE) was evaluated by randomly dropping jets from events with a probability of about 2%. The resulting difference with respect to the nominal case was symmetrised and quoted as JRE systematic uncertainty.

- **Jet energy resolution**: a smearing of the jet transverse momentum corresponding to a resolution of about 10% was applied to Monte Carlo events as

systematic to reflect the difference between the jet energy resolution (JER) observed on data and Monte Carlo. The resulting discrepancies were symmetrised and quoted as JER systematic uncertainty.

- **Muon efficiencies**: in order to account for the trigger and reconstruction efficiencies for muons, global and object based scale factors and efficiencies were taken into account and a systematic uncertainty was assigned on an event-by-event basis (for global scale factors) or on an object basis. These were combined into an overall muon efficiency uncertainty of the order of 1%. In addition, a one-sided uncertainty of 1.5% (events with 0 or 1 b-tagged jet) or 2.2% (events with more than 1 b-tagged jet) was assigned to the muon trigger efficiency to account for any mis-modelling in the Monte Carlo simulation.

- **Muon scales and resolution**: since the Monte Carlo muon momentum scales and resolution differed from the ones observed in data, the muon momentum was smeared and a scaling of up to 1.5% was applied on object level to account for this discrepancy. A systematic uncertainty at the sub-percent level was assigned by scaling up and down both the momentum scaling and smearing by 1σ according to the respective uncertainty. In addition, the missing energy was re-evaluated with the modified four-vector information. The full event selection and kinematic reconstruction was performed for the different scales, resulting in a symmetrised systematic uncertainty based on the comparison of the different results of the measurement.

- **Electron efficiencies**: in order to account for the trigger and reconstruction efficiencies for electrons, global and object based scale factors were taken into account. A systematic uncertainty was assigned on an event basis (for global scale factors) or on an object basis, which were combined into an overall electron efficiency uncertainty of the order of 1%.

- **Electron scales and resolution**: in order to take into account discrepancies between the electron energy resolution on Monte Carlo and data, a Gaussian smearing procedure was applied to the electron energy for Monte Carlo events to reflect the resolution in data. In addition, the electron energy in data was corrected to account for a scaling mis-match between data and Monte Carlo.

Both systematic uncertainties were of the order of 1% to 2% and were assigned to the Monte Carlo prediction for consistency.

- **b-tag scale factors**: due to discrepancies in the b-tagging efficiencies and fake rates between data and simulation, all Monte Carlo jets were assigned a specific weight to account for this effect. The obtained b-tag weights for each jet were combined into an event weight by multiplication (corresponding to a logical AND of all jets taken into account). The provided scale factors contained uncertainties which result in small shape variations. In order to determine the deviation in the shapes from the nominal case due to the b-tag scaling and to quantify the corresponding systematic uncertainty on the measurement, the resulting samples were shifted up and down by the provided uncertainties. These were of the order of 8%, depending on the jet p_T and η.

- **PDF uncertainty**: for the MC@NLO signal Monte Carlo, CTEQ6.6 PDFs were utilised to model the incoming partons to the hard scattering process, as described in section 3.3.1.2. The impact of the choice of PDFs was evaluated by varying the eigenvalues of the CTEQ parametrisation or by comparison with the respective MRST2001 parametrisation [145], using the LHAPDF tool [146]. Event weights were determined and the variations in the resulting pseudosamples were taken into account as PDF systematic uncertainty.

- **LAr defects**: parts of the LAr calorimeter readout electronics were inoperative during a significant time period of data taking due to a technical problem. Having occurred after the production of the used Monte Carlo samples, it was necessary to correct for the resulting mismatch between data and simulated events at the analysis level. Monte Carlo events were dropped with a probability corresponding to the relative amount of data affected (84.0%) if an electron or a jet entered the region of degraded acceptance (taking into account the isolation requirements). A systematic uncertainty was assigned based on different transverse momentum requirements for the jets taken into account for this procedure after symmetrisation.

- **ISR and FSR**: in order to take into account initial and final state radiation, which can introduce additional jets in the observed events, different Monte Carlo samples with varying ISR and FSR contributions (ISR and FSR

contributions scaled up and down independently and in combination) were evaluated by replacing the nominal signal sample in the measurement. The systematic uncertainty was quoted as the maximum relative deviation from the nominal leading order sample observed in these variations and applied to the MC@NLO prediction.

- $t\bar{t}$ **modelling**: the impact of using different MC generators for the signal process modelling was studied. In addition to the MC@NLO generator, the POWHEG generator was used for comparison and a symmetrised systematic uncertainty was assigned based on the variations in the measurement results for the alternate modelling.

- **Parton shower/fragmentation**: in addition to the matrix element level MC generator, the effect of different showering models was taken into account by comparing the results for the POWHEG generator with showering performed by PYTHIA and by HERWIG, and a symmetrised systematic uncertainty was assigned based on the variations in the measurement results for the alternate shower modelling.

- **Top mass**: since the top mass parameter was considered fixed, the uncertainty on the measurement of the mass was taken into account separately. Two different Monte Carlo samples generated with different mass parameters (scaled up and down to 180 GeV and 170 GeV, respectively) were used and the observed deviations were linearly interpolated according to the actual uncertainty of 0.5% of the top mass measurement and a symmetrised systematic uncertainty was quoted.

- **Backgrounds**: the uncertainties on the background normalisations and shapes have been already discussed in section 3.3.3. Each background has been varied within the uncertainty and the full analysis chain has been redone. The difference with respect to the default asymmetry values has been taken as systematic. As already mentioned, a conservative uncertainty of 100% has been used for the QCD background.

- **Charge mis-identification**: since the detector momentum resolution is finite, and the lepton charge was identified by taking into account the bending radius of the particle track, a certain probability for mis-identifying the lepton

charge exists, especially for high transverse momentum leptons due to their almost straight trajectories. This probability was evaluated on Monte Carlo and on data to be of the order of 0.2% to 0.5% in the central detector region, and up to 2.5% in the forward region, respectively, in the electron+jets channel. In the muon+jets channel, the probability was found to be below 0.003% in all cases. A corresponding symmetrised systematic uncertainty on the measurement of the charge asymmetry was determined.

- **b-tag charge**: a dependency of the b-tag efficiencies on the b-quark charge can lead to a bias in the measurement due to the requirement of at least one b-tagged jet. Hence, a simple Monte Carlo study on parton level was performed by simulating a difference in the b-tag efficiency of 5% between b and $\bar{b}$ quarks. The resulting impact on the charge asymmetry on parton level was studied and the difference with respect to the nominal case (assuming identical tagging efficiencies for b and $\bar{b}$ quarks) was quoted as systematic uncertainty.

- **MC generator statistics**: since the signal Monte Carlo sample entered directly into the unfolding response matrix and statistical fluctuations in the bins of this matrix can have an impact on the unfolding process, an additional ensemble test was performed by fluctuating the obtained nominal response matrix on a bin-by-bin basis following a Gaussian probability distribution (since the statistics from the MC@NLO sample were very high a Gaussian model could safely be assumed). Uncertainties of the order of 0.3% to 3% have been obtained, depending on the statistics in each bin of the response matrix.

- **Unfolding convergence**: based on the convergence evaluation which was used to determine the optimal amount of regularisation in the unfolding process, a remaining absolute uncertainty of 0.1%, corresponding directly to the choice of convergence criterion, was assigned, representing the potential remaining change with respect to further increase in regularisation.

- **Unfolding bias**: closure tests have been performed using ensembles of pseudodata to quantify any remaining bias from the unfolding at the chosen regularisation strengths by obtaining pull distributions for the measured asym-

metry, normalised with respect to the respective unfolding statistical uncertainty. The remaining bias was extracted from the residuals in the pull distributions in the closure tests and was taken into account as an additional systematic uncertainty. The residual bias after unfolding was extracted from the respective pull distributions corresponding to the regularisation used in the individual cases and taken into account as an additional relative uncertainty on the unfolded results, which was of the order of 1% to 11%.

- **Luminosity**: the relative uncertainty on the measurement of the integrated luminosity of the used data sample was estimated to be 3.7% and was taken into account for the measurement.

A summarized list of all systematics and their contribution to the overall uncertainties can be found in table 3.4.

The systematic uncertainties were dominated by the contributions from ISR/FSR, top mass, jet energy resolution, $t\bar{t}$ modelling and parton shower/fragmentation in both muon+jets and electron+jets channels, and in addition the electron+jets channel is also affected by large uncertainties originating from QCD multijet background.

As described in section 3.3.3, the QCD multijet background contribution has been estimated very conservatively, assuming a 100% normalisation uncertainty. Most of the other large contributions can be traced to the available Monte Carlo statistics in the used samples. Since only $3{\cdot}10^6$ ($t\bar{t}$ modelling, parton shower/fragmentation), or 10^6 (top mass, ISR/FSR) Monte Carlo events were available for the respective samples used in the evaluation of the systematic uncertainties (as opposed to $15{\cdot}10^6$ for the nominal signal sample), the statistical component in the evaluation of the response matrix uncertainty and the unfolding procedure was larger by factors of two to four with respect to the nominal case.

3.3.7 Summary of results

The measured distributions of the top-antitop rapidity difference $\Delta|y| = |y_t| - |y_{\bar{t}}|$ before unfolding are shown in figure 3.24 for the muon and electron channel. Figure 3.28 shows the corresponding $\Delta|y|$ distributions after unfolding. After unfolding, the bins of the measured distribution have statistical and systematic correlations. Adjacent bins of the $\Delta|y|$ distributions are found to be statistically anti-correlated

Source of systematic uncertainty on A_C	Muon channel	Electron channel
QCD multijet	0.001	0.011
Jet energy scale	0.006	0.012
b-tag jet energy scale	0.001	0.001
Pile-up jet energy scale	0.001	0.002
Jet reco efficiency	0.003	0.001
Jet energy resolution	0.006	0.001
Muon efficiencies	0.001	(n.a.)
Muon scales/resolution	<0.001	<0.001
Electron efficiencies	(n.a.)	0.001
Electron scales/resolution	0.001	0.002
b-tag scale factors	0.002	0.004
PDF uncertainty	<0.001	<0.001
LAr hole uncertainty	0.004	0.001
ISR and FSR	0.010	0.010
$t\bar{t}$ modelling	0.011	0.011
Parton shower/fragmentation	0.010	0.010
Top mass	0.007	0.007
W+jets normalisation and shape	0.005	0.008
Z+jets normalisation and shape	0.001	0.005
Single top	<0.001	<0.001
Diboson	<0.001	<0.001
Charge mis-identification	<0.001	<0.001
b-tag charge	0.001	0.001
MC statistics	0.005	0.006
Unfolding convergence	0.001	0.001
Unfolding bias	<0.001	0.004
Luminosity	0.001	0.001
Combined	0.024	0.028

Table 3.4: List of sources of systematic uncertainties and their impact on the measured asymmetry in the electron and muon channel. In cases where asymmetric uncertainties were obtained, a symmetrisation of the uncertainties was performed by taking the average of the absolute deviations under systematic shifts from the nominal value

with negative correlation coefficients of up to -0.6, whereas other correlations are small.

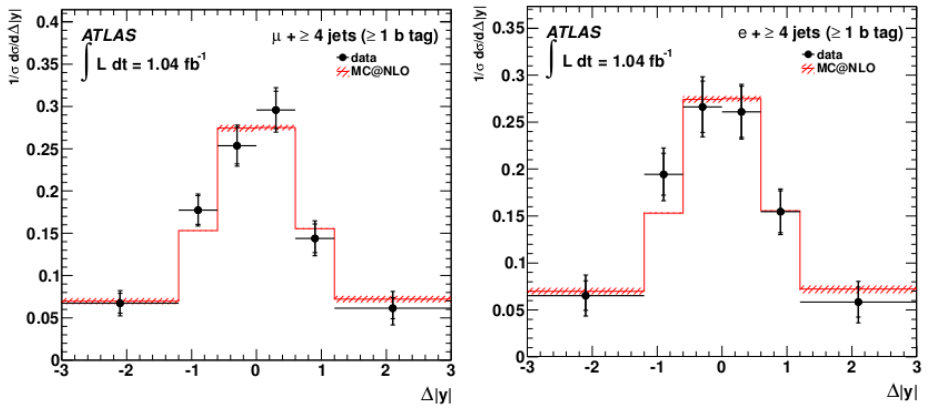

(a) (b)

Figure 3.28: The unfolded $\Delta|y|$ distribution for the muon channel (left) and the electron channel (right) after b-tagging, compared to the prediction from MC@NLO. The uncertainties on the measurement include both statistical and systematic contributions, which are shown separately. The inner part of the error bars corresponds to the statistical component of the uncertainty, while the outer part corresponds to the systematic component. The error bands on the MC@NLO prediction include uncertainties from parton distribution functions and renormalisation and factorisation scales

The measured values of the top charge asymmetry before and after unfolding are summarised in table 3.5.

The analytic best linear unbiased estimator (BLUE) method [147, 148] is used to combine the measurement in the electron and muon channels after correction for detector resolution and acceptance. The measured asymmetries are:

$$A_C = -0.019 \pm 0.028(\text{stat.}) \pm 0.024(\text{syst.}) \tag{3.45}$$

for the integrated sample, and

$$A_C = -0.052 \pm 0.070(\text{stat.}) \pm 0.054(\text{syst.}) \tag{3.46}$$

Asymmetry	reconstructed	detector and acceptance unfolded
A_C (electron)	$-0.034 \pm 0.019(\text{stat.}) \pm 0.010(\text{syst.})$	$-0.047 \pm 0.045(\text{stat.}) \pm 0.028(\text{syst.})$
A_C (muon)	$-0.010 \pm 0.015(\text{stat.}) \pm 0.008(\text{syst.})$	$-0.002 \pm 0.036(\text{stat.}) \pm 0.024(\text{syst.})$

Table 3.5: The measured inclusive charge asymmetry values for the electron and muon channels after background substraction, before and after unfolding

for $m_{t\bar{t}} < 450$ GeV,

$$A_C = -0.008 \pm 0.035(\text{stat.}) \pm 0.032(\text{syst.}) \tag{3.47}$$

for $m_{t\bar{t}} > 450$ GeV.

The measurement for the integrated sample can be compared with the result of the CMS Collaboration in equation 3.25. Figure 3.29 summarizes the measurements for the two $m_{t\bar{t}}$ regions.

These results are compatible with the prediction from the MC@NLO Monte Carlo generator of $A_C = 0.006 \pm 0.0025$, showing no evidence for an enhancement from physics beyond the Standard Model. Even if this is the first measurement performed by the ATLAS collaboration, it gives already the possibility to discriminate between new physics models. As can be seen from figure 3.30, these measurement disfavor models with a new flavor-changing Z' or W' vector boson that have been suggested to explain the measured Tevatron asymmetry.

3.3.7.1 Outlooks

In the future some work will be done in order to lower systematics uncertainties as much as possible. Ongoing improvements in the understanding of the detector will enable to reduce the contributions coming from object reconstruction. Comparison between data and Monte Carlo predictions will also give the possibility to tune different generators and therefore to reduce the uncertainty coming from signal modelling.

Furthermore, other kinematic variables will be considered, as for example the longitudinal momentum of the top quark pair system, and the study of different observables, also using directly leptons variables, will be performed.

A limitation to this study at the LHC is the fact that the asymmetry is diluted by the contribution of the symmetric gg fusion process. The present selection is

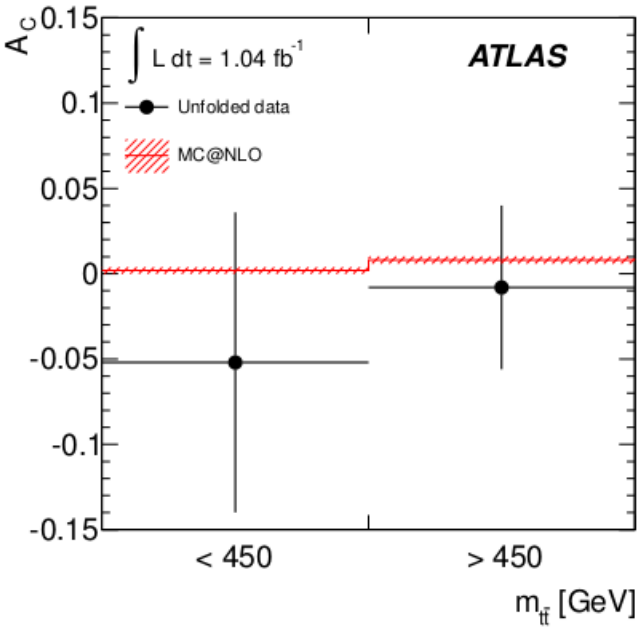

Figure 3.29: Unfolded asymmetries in two regions of $m_{t\bar{t}}$ compared to the prediction from MC@NLO. The error bands on the MC@NLO prediction include uncertainties from parton distribution functions and renormalisation and factorization scales

even reducing the $q\bar{q}$ contribution with respect to the total, as can be seen from table 3.6. This table shows gg fusion and $q\bar{q}$ annihilation contribution to the number of $t\bar{t}$ selected events after each individual selection cut for muon channel. The selection cuts seem to slightly enhance the gg fraction with respect to the $q\bar{q}$ fraction. In fact, the $q\bar{q}/gg$ ratio lowers form 0.24 to 0.18 at the end of the cut-flow.

The dependence of the $q\bar{q}$ fraction on the invariant mass of the top-antitop pair $m_{t\bar{t}}$ has been also studied, as shown in figure 3.31. In order to quantify the effects of the reconstruction algorithms and of detector acceptance, $q\bar{q}$ fraction has been studied at three levels separately: all the events have been considered without applying any selection cuts and calculating $m_{t\bar{t}}$ from true t and $\bar{t}$ kinematic variables (black dots); the events passing all the selection cuts applied at top decay products after reconstruction, but still calculating $m_{t\bar{t}}$ from true t and $\bar{t}$ (red triangles) and the events passing selection cuts as a function of $m_{t\bar{t}}$ calculated from t and

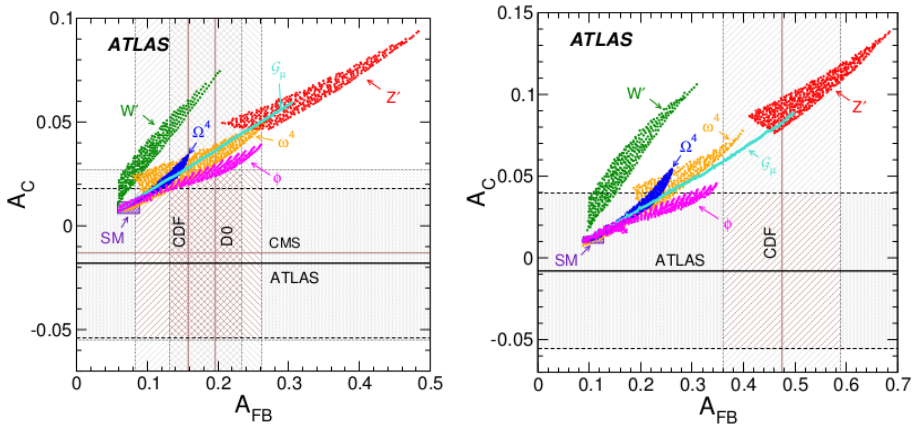

(a) (b)

Figure 3.30: Measured FB asymmetries from the Tevatron and charge asymmetries from the LHC, compared to predictions from the SM as well as predictions incorporating various potential new physics contributions. The horizontal (vertical) bands and lines correspond to the ATLAS and CMS (CDF and DØ) measurements. In (a) the inclusive values are presented and in (b) the ATLAS measurement for $m_{t\bar{t}} > 450$ GeV is compared to the CDF measurement

$\bar{t}$ kinematic variables, obtained with the *KLFitter* algorithm (blue stars). The $q\bar{q}$ fraction is lower in the high mass region, independently on the selection cuts, suggesting a physical effect related to the PDF contributions. Furthermore, in the low $m_{t\bar{t}}$ region, the $q\bar{q}$ fraction lowers after the selection cuts, suggesting an acceptance effect.

Some studies are already ongoing in order to enhance $q\bar{q}$ contribution. A recent proposal [149] consists in putting a cut on $t\bar{t}$ boost along z-axis. Since in $q\bar{q}$ events one of the incoming partons comes from the sea, while other one is a valence quark, the boost along the z-axis will be higher than in events generated by gg fusions, where both partons come from the sea.

Cut-flow efficiency, muon channel				
cut	ε_{tot}	$\varepsilon_{q\bar{q}}$	ε_{gg}	$q\bar{q}/gg$
All events	1.00	0.19	0.79	0.24
Trigger	1.00	0.19	0.79	0.24
Good Vertex	1.00	0.19	0.79	0.24
$\#\mu > 0$	0.23	0.04	0.18	0.24
$\#\mu = 1$	0.22	0.04	0.17	0.24
$\#e = 0$	0.20	0.04	0.16	0.24
Trigger match	0.20	0.04	0.16	0.24
e/μ overlap removal	0.20	0.04	0.16	0.24
Jet cleaning	0.20	0.04	0.16	0.24
$\not{E}_T > 20$ GeV	0.18	0.04	0.15	0.24
$\not{E}_T + M_{T_W} > 65$ GeV	0.17	0.03	0.14	0.24
at least 2 jets $p_T > 25$ GeV, $\|\eta\| < 2.5$	0.17	0.03	0.13	0.24
at least 3 jets $p_T > 25$ GeV, $\|\eta\| < 2.5$	0.14	0.03	0.11	0.22
at least 4 jets $p_T > 25$ GeV, $\|\eta\| < 2.5$	0.09	0.01	0.08	0.18
1 b-tag	0.06	0.01	0.05	0.18

Table 3.6: Muon selection cutflow. The efficiencies ϵ are calculated as the ratio between the number of events passing a specific cut over the total number of events before any cut (the second row). The first column describes efficiency of the various cuts, the second and the third one respectively the $q\bar{q}$ and the gg fraction in the events passing a specific cut while the fourth column shows the relative ratio between $q\bar{q}$ and gg events

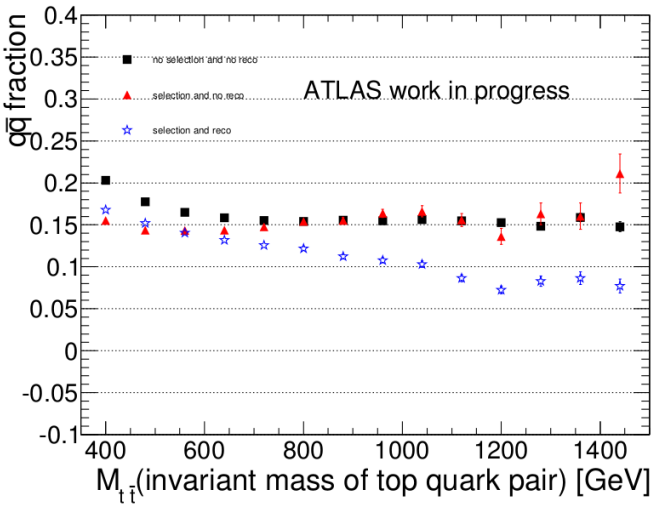

Figure 3.31: $q\bar{q}$ fraction as a function of true $m_{t\bar{t}}$ for all the events (black dots),$q\bar{q}$ fraction as a function of true $m_{t\bar{t}}$ only for the events passing all the selection cuts applied to reconstructed objects (red triangles) and $q\bar{q}$ fraction as a function of reconstructed $m_{t\bar{t}}$ for events passing the same cuts on reconstructed objects (blue stars)

Chapter 4

Search for a scalar top decaying to a chargino and a b-quark in final states with two leptons

The Standard Model (SM) [150, 151] of particle physics describes well the known phenomena below an energy scale of the order of 100 GeV. However, if we consider higher energies up the to Grand Unified Theory (GUT) ($\Lambda_{\mathrm{GUT}} \approx 10^{16}$ GeV) or Planck scale (1.22×10^{19} GeV), we encounter a number of conceptual problems.

One problem is why the electroweak energy scale and the GUT or the Planck scales are so different. It is called hierarchy problem. This affects the Higgs mass: without any cancellation mechanisms, the Higgs mass receive large corrections by the one-loop diagram contributions. It is also a issue that there is no appropriate candidate of dark matter in the SM. Moreover, unification of gravity in the framework of quantum field theory is not achieved in the SM.

Supersymmetry (SUSY) is one of the solutions which aim to solve these problems. In this chapter, motivations to introduce supersymmetry will be explained. If supersymmetry exists, supersymmetric partner particles of the SM particles exist. If supersymmetry is not broken, they have the same masses and the same

quantum numbers as the SM partner particles except for the spin, which differs by 1/2 unit. However, no such particles have been discovered. Therefore supersymmetry must be broken by a certain mechanism. Phenomenological SUSY models differ by the assumed SUSY breaking scenario or by assumptions on the particle spectra and couplings. Among them, the so-called natural supersymmetry models predict light supersymmetric partners of the third generation quarks. In R-parity conserving supersymmetry, the production of supersymmetric partners of the top quark results in a final state with b-jets and missing momentum in an event.

In this chapter I'll give an introduction to the supersymmetry. Then I'll describe the search for the supersymmetric partner of the top decaying to a chargino and a b-quark in final states with two leptons that have been performed using proton-proton collisions at $\sqrt{s} = 7$ TeV and $\sqrt{s} = 8$ TeV recorded by the ATLAS detector.

4.1 Beyond the Standard Model

4.1.1 The limits of the Standard Model

The Standard Model, and in particular the electroweak theory, has been heavily tested in the last $\sim$ 35 years, without finding any significant failure in its predictions. Hence, the motivations to consider the SM as an "effective theory" are essentially related to its mathematical structure, rather than to its capacity to predict the physical processes. Some of these motivations are listed here.

The hierarchical problem The Planck scale is about $M_{\mathrm{Pl}} = G_{\mathrm{N}}^{-1/2} \approx 10^{19}$ GeV where quantum gravity is not negligible anymore (G_{N} is the gravitational constant). On the other hand, the heaviest SM particles have mass of the order of 100 GeV. Why are these two energy scales so different? The problem is strongly related to the structure of the Higgs scalar field. As explained above, the mass of the Higgs boson is $m_{\mathrm{H}}^0 = \sqrt{-2\mu^2}$ at the tree level, but, during the renormalisation process, the value of the mass parameter μ^2 is corrected by a factor $\delta\mu^2$ that comes from the loop-corrections. The physical parameter is then $\mu^2 = \mu_0^2 + \delta\mu^2$, μ_0^2 indicating the tree-level value, and the dependency of $\delta\mu^2$ from the cut-off scale Λ is quadratic. It follows that the correction to the Higgs mass $\delta m_{\mathrm{H}}^2 = c\Lambda^2$ is itself proportional to Λ^2, it is independent to the tree-level value and especially quadratically divergent

with the cut-off scale. If one requires that the physical value of the Higgs mass will be of the order of the electroweak scale keeping the Higgs sector as explained above and if one wants that the SM will be extended until some unification scale (i.e. $\Lambda = 10^{15}$ GeV) one needs to have a fine-tuning for the c constant of 10^{-28}!!

The dark matter problem The recent cosmological observations suggest that about 25% of the mass of the Universe comes from the Dark Matter. Keeping these results as reliable, the SM does not have any candidate to explain which are the constituents of this Dark matter, which should be massive, electrically neutral and weakly interacting particles (WIMP).

The unification problem Starting from the "global SM electroweak fit", the running coupling constants for the three interactions (strong, electromagnetic and weak) do not converge to a single value when one extrapolates them towards the Planck scale, contrasting any theory that foresees the unification of the forces.

There are several other problems not mentioned here (neutrino masses, matter-antimatter asymmetry, fermion masses hierarchy, etc.), but all of them lead to the idea that the SM is an "effective theory" that works fine at the electroweak scale, when it is extended to higher energy.

4.1.2 The Supersymmetry

The Supersymmetry (SUSY) [152, 153, 154, 155] is one of the most favorite candidates to extend the SM, providing natural solutions to many of the problems explained above. Proposed during the 70's, this theory introduces a new symmetry, in addition to those of the SM, that associates a fermionic (bosonic) partner to each SM boson (fermion). The generators of this new symmetry are the Majorana spinors $Q_\alpha(\alpha = 1, ..., 4)$ that act on the physical states changing their spin of a quantity $\pm 1/2$.

This fermionic generators satisfy the following relations:

$$[Q_\alpha, M^{\mu\nu}] = i(\sigma^{\mu\nu})^\beta_\alpha Q_\beta \tag{4.1}$$

$$\{Q_\alpha, \bar{Q}_\beta\} = -2(\gamma_\mu)_{\alpha\beta} P^\mu \tag{4.2}$$

$$[Q_\alpha, P^\mu] = \{Q_\alpha, Q_\beta\} = \{\bar{Q}_\alpha, \bar{Q}_\beta\} = 0 \tag{4.3}$$

with

$$\sigma_{\mu\nu} = \frac{1}{4}[\gamma_\mu, \gamma_\nu] \tag{4.4}$$

$$\bar{Q}_\alpha = Q^T_\alpha \gamma^0 \tag{4.5}$$

where γ_μ are the usual 4×4 Dirac matrices, P^μ is the momentum operator and $M^{\mu\nu}$ is the Lorentz group generator.

In the Minimal Supersymmetric extension of the Standard Model (MSSM), each chiral fermion $f_{\mathrm{L,R}}$ has a scalar sfermion partner $\tilde{f}_{\mathrm{L,R}}$, and each massless gauge boson A_μ, with two helicity states ± 1, has a massless spin $1/2$ gaugino partner with helicities $\pm 1/2$. In order to avoid triangular anomalies, there must also be two complex Higgs doublets and their associated Higgsinos. The interactions of SUSY particles are basically obtained from the Standard Model ones, by replacing any two lines in a vertex by their SUSY partners; for example, the gluon-quark-quark and gluino-quark-squark couplings are the same. See [156, 157, 158, 159] for the construction of the complete Lagrangian. SUSY provides a solution to the hierarchy problem because it implies an equal number of bosons and fermions, which give opposite signs in loops and so cancel the quadratic divergences. This cancellation works to all orders: since the masses of fermions are only logarithmic divergent, this must also be true for boson masses in a supersymmetric theory. When SUSY is broken, the corrections to the Higgs and other scalar masses become proportional to the SUSY mass scale, rather than the Planck scale. If the Higgs is to be light without unnatural fine tuning, then the SUSY particles should have masses below about 1 TeV.

SUSY must of course be broken, since superparticles have not been observed: for example, there are certainly no spin-0 partners of known fermions degenerate in mass with their standard model counterparts. Gauge invariance forbids mass terms in the Lagrangian for all Standard Model particles; masses can be introduced only

by spontaneous symmetry breaking, using the Higgs mechanism. In contrast, mass terms are allowed for all the SUSY particles. Thus, it is possible to parametrize SUSY breaking by introducing by hand SUSY-breaking mass terms for the squarks, sleptons, Higgsinos, the fermionic partner of the scalar Higgs boson, and gauginos. Additional soft terms (bilinear B terms and trilinear A terms with dimension $d < 4$) consistent with gauge invariance can also be added without reintroducing quadratic divergences. Finally, a Higgsino mass term must be included; this must be of the same order as the SUSY breaking terms even though it is SUSY conserving.

The requirements of gauge invariance and renormalizability are sufficient to guarantee that the Standard Model Lagrangian conserves baryon and lepton number. In supersymmetric theories it is possible to violate both, potentially leading to disastrous weak-scale proton decay. The unwanted terms can be eliminated by imposing invariance under R-parity,

$$R = (-1)^{3(B-L)+2S} \tag{4.6}$$

where B, L, and S are respectively the baryon number, the lepton number, and the spin. Hence $R = +1$ for all Standard Model particles and $R = -1$ for all SUSY particles. This has the consequence that SUSY particles must be produced in pairs and that the lightest SUSY particle (LSP) is absolutely stable. R-parity conservation holds automatically in many GUT models under rather general assumptions [160]. Alternatively, weak-scale proton decay can also be avoided by imposing either baryon or lepton number conservation.

4.1.2.1 The MSSM: Minimal Supersimmetric Standard Model

The Minimal Supersymmetric Standard Model (MSSM) is the supersymmetric extension of the SM with the minimal particle content, as listed in table 4.1 and 4.2, with R-parity conservation.

The cancellation of quadratic divergences for scalar masses only requires Supersymmetry for the terms with mass dimension four. In the MSSM, SUSY is broken "by hand" by adding to the Lagrangian all possible soft terms consistent with $SU(3) \otimes SU(2) \otimes U(1)$ gauge invariance. This includes mass terms for all the superpartners and trilinear A terms:

Name	Spin 0	Spin 1/2	$SU(3) \otimes SU(2) \otimes U(1)$
squarks, quarks	$\tilde{Q} = (\tilde{u}_L, \tilde{d}_L)$ $\tilde{u}^*_R$ $\tilde{d}^*_R$	$Q = (u_L, d_L)$ $\bar{u}_R$ $\bar{d}_R$	(3, 2, 1/6) ($\bar{3}$, 1, -2/3) ($\bar{3}$, 1, 1/3)
sleptons, leptons	$\tilde{L} = (\tilde{\nu}, \tilde{e}_L)$ $\tilde{e}^*_R$	$L = (\nu, e_L)$ e_R	(1, 2, -1/2) (1, 1, 1)
Higgs, Higgsinos	$H_u = (H^+_u, H^0_u)$ $H_d = (H^0_d, H^-_d)$	$\tilde{H}_u = (\tilde{H}^+_u, \tilde{H}^0_u)$ $\tilde{H}_d = (\tilde{H}^0_d, \tilde{H}^-_d)$	(1, 2, 1/2) (1, 2, -1/2)

Table 4.1: Chiral supermultiplets in the Minimal Supersymmetric Standard Model. The squarks and sleptons come in three generations. The physical Higgs bosons after symmetry breaking are h, H, A, and $H^{\pm}$

Name	Spin 1/2	Spin 1	$SU(3) \otimes SU(2) \otimes U(1)$
gluino, gluon	$\tilde{g}$	g	(8, 1, 0)
winos, W's	$\tilde{W}^{\pm}$, $\tilde{W}^0$	$W^{\pm}$, W^0	(1, 3, 0)
bino, B	$\tilde{B}$	B	(1, 1, 1)

Table 4.2: Vector supermultiplets in the Minimal Supersymmetric Standard Model. After symmetry breaking, the winos and bino mix with the Higgsinos to give four neutralinos $\tilde{\chi}^0_i$ and two charginos $\tilde{\chi}^{\pm}_i$, and the W^0 and B mix as in the Standard Model

$$
\begin{aligned}
L_{\text{SOFT}} = \quad & -m^2_{H_d}|H_d|^2 - m^2_{H_u}|H_u|^2 + \mu B \epsilon_{ij}(H^i_d H^j_u + h.c.) \\
& -\tfrac{1}{2}M_1\tilde{\bar{B}}\tilde{B} - \tfrac{1}{2}M_2\tilde{\bar{W}}\tilde{W} - \tfrac{1}{2}M_3\tilde{\bar{g}}\tilde{g} \\
& -M^2_{\tilde{Q}}(\tilde{u}^*_L\tilde{u}_L + \tilde{d}^*_L\tilde{d}_L) - M^2_{\tilde{U}}u^*_R u_R - M^2_{\tilde{D}}d^*_R d_R \\
& -M^2_{\tilde{L}}(\tilde{l}^*_L\tilde{l}_L + \tilde{\nu}^*_L\tilde{\nu}_L) - M^2_{\tilde{E}}l^*_R l_R \\
& -\epsilon_{ij}(-\lambda_u A_u H^i_u \tilde{Q}^j \tilde{u}^*_R + \lambda_d A_d H^i_d \tilde{Q}^j \tilde{d}^*_R + \lambda_l A_E H^i_d \tilde{L}^j \tilde{l}^*_R)
\end{aligned}
\tag{4.7}
$$

where Q, L, H_u and H_d denote $SU(2)$ weak doublets as in table 4.1 and a summation over generations is implied. All the parameters are complex numbers in general matrices in flavor space. There are a total of 105 new parameters [161] in addition to the SM ones. One of these is the SUSY-conserving Higgsino mass μ, which must be of the same order as the SUSY breaking masses. Electroweak symmetry cannot be broken by hand in a similar way, since this would destroy gauge invariance. Instead it is broken by the Higgs mechanism as previously explained giving rise to masses for quarks, leptons, W and Z bosons. SUSY requires two Higgs doublets and relates the Higgs self-coupling to gauge couplings:

$$\begin{aligned} V_{\text{Higgs}} = \quad & (m_{H_d}^2 + \mu^2)|H_d|^2 + (m_{H_u}^2 + \mu^2)|H_u|^2 - B_\mu(\epsilon_{ij} H_d^i H_u^j + h.c.) \\ & + \tfrac{1}{8}(g^2 + g'^2)(|H_d|^2 - |H_u|^2)^2 + \tfrac{1}{2} g^2 |H_d^{*i} H_u^i|^2 \end{aligned} \tag{4.8}$$

Once SUSY and the electroweak symmetry are broken, particles with the same quantum numbers will in general mix. The gauginos and Higgsinos mix to form two spin 1/2 charged particles called "charginos" $\tilde{\chi}_i^\pm$ with the matrix in the (W^+,H^+) basis:

$$\begin{pmatrix} M_2 & \sqrt{2} M_{\text{W}} \sin\beta \\ \sqrt{2} M_{\text{W}} \cos\beta & \mu \end{pmatrix} \tag{4.9}$$

and four spin-1/2 neutral particles called "neutralinos" $\tilde{\chi}_i^0$ with the mass matrix in the (B, W^0, H_d, H_u) basis:

$$\begin{pmatrix} M_1 & 0 & -M_Z \cos\beta \sin\theta_{\text{W}} & M_Z \sin\beta \sin\theta_{\text{W}} \\ 0 & M_2 & M_Z \cos\beta \cos\theta_{\text{W}} & M_Z \sin\beta \cos\theta_{\text{W}} \\ -M_Z \cos\beta \sin\theta_{\text{W}} & M_Z \cos\beta \cos\theta_{\text{W}} & 0 & -\mu \\ M_Z \sin\beta \sin\theta_{\text{W}} & -M_Z \sin\beta \cos\theta_{\text{W}} & -\mu & 0 \end{pmatrix} \tag{4.10}$$

where, in both formulae, θ_{W} is the Weinberg angle and $\tan\beta$ is the ratio of the two v.e.v's of the two Higgs doublets.

The phenomenology of the different SUSY models strongly depends on this mixing, but in many of these models one can write the following relation:

$$\frac{M_1}{\alpha_1} = \frac{M_2}{\alpha_2} = \frac{M_3}{\alpha_3} \tag{4.11}$$

with the mass term μ that is of order of $M_{\tilde{g}}$. So that the two lighter neutralinos and the lighter chargino are dominantly gaugino, while the heavier states are dominantly Higgsino and weakly coupled to the first two generations.

Concerning the sfermion sector, while chiral fermions f_{L}, f_{R} must have the same mass by Lorentz invariance, their scalar partners $\tilde{f}_{\mathrm{L}}$, $\tilde{f}_{\mathrm{R}}$ instead may have separate masses. Their squared mass matrix also gets off-diagonal contributions proportional to the fermion mass with the result that this left-right mixing is mainly relevant for the third generation. These eigenstates are called $\tilde{t}_{1,2}$, $\tilde{b}_{1,2}$ and $\tilde{\tau}_{1,2}$ (stop, sbottom and stau), while the mixing for the first two generations is negligible.

4.1.3 Natural models

In section 4.1.1 (hierarchical problem), it was discussed that the quadratic divergence of the Higgs mass can be canceled by introducing supersymmetry. However, one problem arises. Even if the quadratic Λ term is canceled, the next term from loop corrections ($\propto \ln \Lambda$) cannot be eliminated without the physically unjustifiable tuning of a counter-term. This is called "naturalness" problem. For the theory to be natural, certain limits on the masses of scalar particles are required. The tightest limit is the one on the stop mass because of its strong coupling to the Higgs boson. In particular, the minimal requirements for natural SUSY are light stops ($\lesssim 500$ GeV) and light higgsinos. Moreover the lighter stop is expected to have the lightest mass of all squarks. Also the sbottom is expected to be lighter than the other light-flavor squarks. More details can be found on references [159, 162].

4.1.3.1 Stop and sbottom production processes

As described in the previous paragraph, third generation squarks (the stop and the sbottom) are expected to be lighter than the other squarks, and as a result, their production can have a large cross section.

If the stop or the sbottom are relatively light, there are mainly two types of production processes. One is via the decay of gluinos and the other is via direct pair production. If the gluino is not much heavier than the stop, the direct production of gluinos dominates over direct stop (or sbottom) production as shown in figure 4.1. However, if we consider the naturalness of Higgs mass, it is possible that the stop is the only light (i.e. mass on the order of several hundreds GeV) colored

SUSY particle and the other squarks and the gluinos are heavier than a few TeV. In this case, only direct stop pair production would be observed.

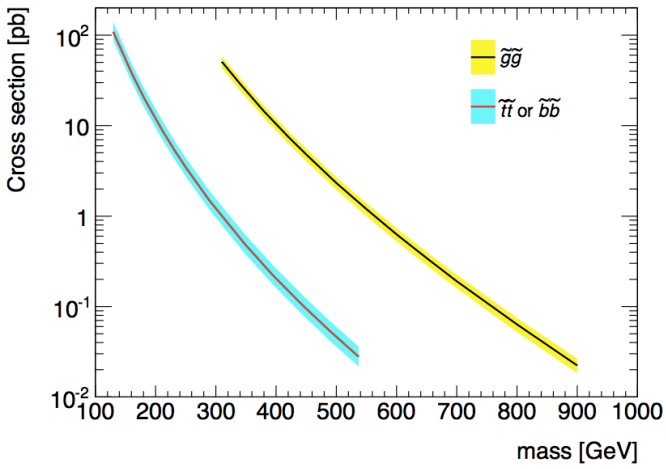

Figure 4.1: Cross-sections for the pair production of gluinos, stops and sbottoms as a function of their masses calculated to NLO using PROSPINO for proton-proton collisions at $\sqrt{s} = 7$ TeV [163, 164]

4.1.3.2 Stop and sbottom decay modes

The decay modes of the stop and the sbottom depend highly on the SUSY particle mass spectrum. For simplicity, only the lightest stop, the lightest chargino and the lightest neutralino are considered as the active SUSY particles; the other SUSY particles are assumed to be heavy enough (masses on the order of TeV) such that they decouple. The decay modes of the sbottom can be inferred by the analogy to the stop.

Two-body decay

A.1 If $m_{\tilde{t}_1} > m_t + m_{\tilde{\chi}_1^0}$, the stop can decay via

$$\tilde{t}_1 \to t + \tilde{\chi}_1^0 \tag{4.12}$$

If the lightest neutralino is the LSP, $\tilde{\chi}_1^0$ cannot decay anymore but the top quark will decay further. The final state therefore consists of multi-jets including b-jets, leptons and E_T^{miss}.

A.2 If $m_{\tilde{t}_1} > m_b + m_{\tilde{\chi}_1^+}$,the stop can decay via

$$\tilde{t}_1 \to b + \tilde{\chi}_1^+ \tag{4.13}$$

Since the lightest chargino is in general heavier than the lightest neutralino, the lightest chargino can decay further via $\tilde{\chi}_1^+ \to \tilde{\chi}_1^0 + f + f'$, where f and f' are any SM fermions. The branching ratios to fermion flavors depend on the corresponding scalar fermion masses.

A.3 If the above two decay modes and the three-body decay modes shown below are all suppressed, the stop can decay via

$$\tilde{t}_1 \to c + \tilde{\chi}_1^0 \tag{4.14}$$

if $m_{\tilde{t}_1} > m_c + m_{\tilde{\chi}_1^0}$ through the one-loop diagram such as shown in figure 4.2. However, this topology is only possible in a limited parameter space.

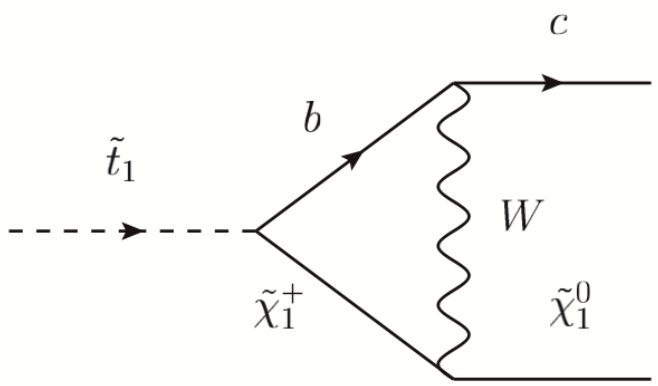

Figure 4.2: One of the $\tilde{t}_1 \to c + \tilde{\chi}_1^0$ decay diagram in one-loop

Three-body decay The branching ratios for three-body decays are much smaller than those of two-body decays. If the two-body decay modes (A1 and A2) are forbidden, however, three-body decays can be dominant.

B.1 If the sleptons are lighter than the stop, the stop can decay via

$$\tilde{t}_1 \to b + \nu + \tilde{l} \tag{4.15}$$

Since a charged LSP is forbidden from the cosmological constraints, none of the sleptons can be the LSP and therefore they will decay further. This results in the final states with b-jets, leptons and E_T^{miss}.

B.2 If the sneutrinos are lighter than the stop, the stop can decay via

$$\tilde{t}_1 \to b + l + \tilde{\nu} \tag{4.16}$$

Regardless of whether one of the sneutrinos is the LSP or not, the sneutrino or other LSP are not detected. This decay mode therefore also results in the final stats with b-jets, leptons and E_T^{miss}.

B.3 If $m_b + m_W < m_{\tilde{t}_1} - m_{\tilde{\chi}_1^0}$, the stop can decay via

$$\tilde{t}_1 \to b + W + \tilde{\chi}_1^0 \tag{4.17}$$

This decay became preferable with respect to the two-body decay A1 only if $m_{\tilde{t}_1} - m_{\tilde{\chi}_1^0} < m_t$. If the lightest neutralino is the LSP, $\tilde{\chi}_1^0$ cannot decay anymore but the W boson will decay further. The final state therefore consists of multi-jets including b-jets, leptons and E_T^{miss}.

These decay processes are different from two-body decays but the final states are the same as one of the decay modes described in the previous paragraph. Therefore by searching for two-body decay modes, these three-body decay modes are also naturally covered.

Four-body decay If all two-body decay modes (A1 and A2) and three-body decay modes (B1 and B2) are forbidden, the branching ratio of the stop decay via four-body decay modes can be dominant.

C.1 In this case, the stop can decay via

$$\tilde{t}_1 \to b + f + f' + \tilde{\chi}_1^0 \tag{4.18}$$

where f and f' are any SM fermions. Figures 4.3 show some examples of tree-level Feynman diagrams of this decay mode. Since this mode has the same order in perturbation theory as the loop-induced A3 decay ($\mathcal{O}(\alpha^3)$), its branching ratio is competitive to that of the A3 mode. For example, it can be enhanced if the charginos have masses not much larger than their present experimental bounds, or if the sfermions are light [165].

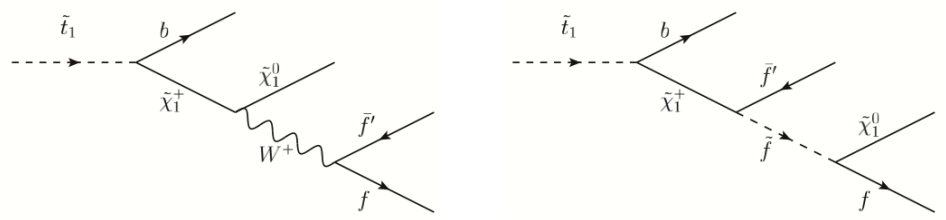

Figure 4.3: The tree-level Feynman diagrams for $\tilde{t}_1 \to b + f + f' + \tilde{\chi}_1^0$

Although this is a different decay process from the two-body decay, the final states are nevertheless b-jets, multi-jets (or leptons) and E_T^{miss}, and also these modes are naturally covered by the two-body decay searches.

4.2 Searches for SUSY with third generation squarks in ATLAS

One of the main goals of the ATLAS experiment at the LHC is the search for new physics beyond the Standard Model (SM), with supersymmetry (SUSY) being one of the best motivated extensions. Despite many theoretical and experimental efforts, squarks and gluinos have not yet been found in any of the inclusive searches [166, 167, 168]. With a total integrated luminosity of 4.7 fb^{-1}, gluino masses below 860 GeV and squark masses below 1320 GeV are excluded at the 95% confidence level in simplified models containing only squarks of the first two generations, a gluino octet and a massless neutralino, for squark or gluino masses below 2 TeV, respectively.

The super-partners of third generation quarks are required by naturalness considerations, to be lighter than approximately 500 GeV (see section 4.1.3), while the Tevatron and previous LHC searches place limits between 100 GeV and 490 GeV, depending on the SUSY scenario. Therefore, it is important to perform dedicated searches for these particles.

Searches for third generation squarks at ATLAS cover a wide range of production and decay mechanisms. Both the direct and gluino mediated production of scalar bottom and scalar top quarks have been studied. In all cases scalar bot-

tom quarks are assumed to decay into bottom and $\tilde{\chi}_1^0$, while for scalar top quarks two scenarios have been studied depending on the mass relation between $m_{\tilde{t}_1}$, m_t and $m_{\tilde{\chi}_1^0}$ as depicted in figure 4.4. Table 4.3 gives an overview of the scenarios investigated by the ATLAS collaboration.

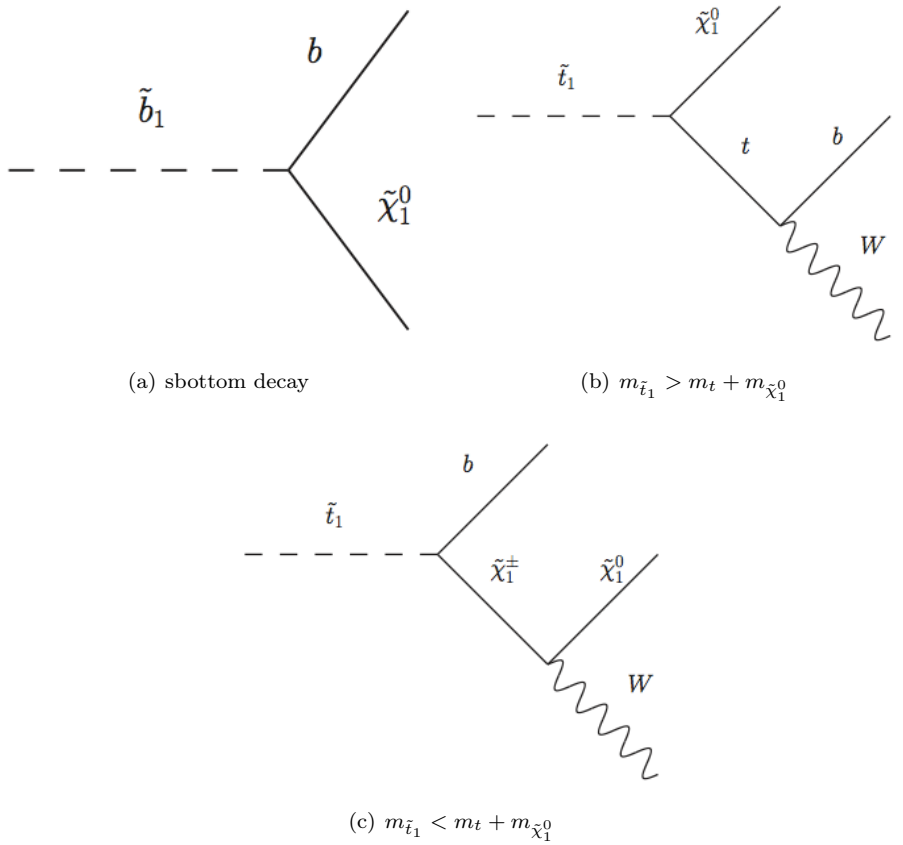

(a) sbottom decay

(b) $m_{\tilde{t}_1} > m_t + m_{\tilde{\chi}_1^0}$

(c) $m_{\tilde{t}_1} < m_t + m_{\tilde{\chi}_1^0}$

Figure 4.4: Investigated decay modes of scalar bottom (left) and scalar top quarks (middle and right)

In all the cases, no significant excess from the SM expectations has been observed and exclusion limits have been set in different areas of parameter space. The obtained limits extend previous ATLAS SUSY searches.

However, since later in this chapter I'll describe the search for the stop decaying to a chargino and a b-quark in final states with two leptons with the ATLAS

Channel	Final state	Scenario	Luminosity	Ref.
gluino-mediation	4-6 jets + 3 b-tags + E_T^{miss}	on- & off-shell $\tilde{g}$ decays	4.7 fb^{-1} (7 TeV) and 12.8 fb^{-1} (8 TeV)	[169, 170]
gluino-mediation	3 leptons + ≥ 4 jets + E_T^{miss}	on- & off-shell $\tilde{g}$ decays	13.0 fb^{-1} (8 TeV)	[171]
$\tilde{t}_1 \to b + \tilde{\chi}_1^{\pm}$	2-lep + E_T^{miss}	very light stops	4.7 fb^{-1} (7 TeV)	[172]
$\tilde{t}_1 \to b + \tilde{\chi}_1^{\pm}$	1/2-lep + b-jet + E_T^{miss}	light stops	4.7 fb^{-1} (7 TeV)	[173]
$\tilde{t}_1 \to t + \tilde{\chi}_1^0$	0-lep + b-jet + E_T^{miss}	heavy stops	4.7 fb^{-1} (7 TeV)	[174]
$\tilde{t}_1 \to t + \tilde{\chi}_1^0$	1-lep + b-jet + E_T^{miss}	heavy stops	4.7 fb^{-1} (7 TeV)	[175]
$\tilde{t}_1 \to t + \tilde{\chi}_1^0$	2-lep + b-jet + E_T^{miss}	heavy stops	4.7 fb^{-1} (7 TeV)	[176]
$\tilde{b}_1 \to b + \tilde{\chi}_1^0$	0-lep + 2 b-jet + E_T^{miss}	direct sbottom	2.05 fb^{-1} (7 TeV) and 12.8 fb^{-1} (8 TeV)	[177, 178]
Natural GMSB	Z + b-jet + E_T^{miss}	direct stop	2.05 fb^{-1} (7 TeV)	[179]

Table 4.3: Overview over searches for third generation squarks at ATLAS performed so far.

detector, I would like to spend few words in the next section about the status of the searches performed so far about the direct production of scalar top quarks.

For the direct pair production of scalar top quarks, five different analyses depending on the scalar top quark decay mode (see figure 4.4) and on the number of isolated leptons from the W boson decays in the decay chain of the top are carried out. Due to the dominant and irreducible $t\bar{t}$ background, all five analyses need to exploit certain kinematic variables that discriminate signal from background. For very light scalar top quarks ($m_{\tilde{t}_1} \ll m_t$), all decay products are soft and b-tagging is not efficient. The corresponding analysis requires two soft leptons and uses the transverse momentum of the leptons as a discriminant variable [172]. Slightly heavier scalar top quarks are searched for using both one- and di-lepton final states [173]. For heavier scalar top quarks directly decaying to t and $\tilde{\chi}_1^0$, three analyses requiring zero [174], one [175] or two [176] isolated leptons are performed. In all of these five analyses, results are consistent with the SM expectation and limits on $m_{\tilde{t}_1}$ and $m_{\tilde{\chi}_1^0}$ are derived as summarized in figure 4.5.

4.3 Search for stop decaying to a chargino and a b-quark in final states with two leptons with the ATLAS detector

This section is dedicated to the description of the search for stop decaying to a chargino and a b-quark in final states with two leptons. The results presented in

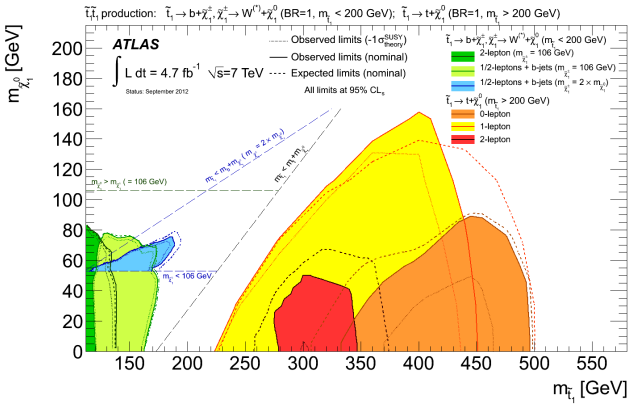

Figure 4.5: Summary of the five dedicated ATLAS searches for scalar top quark pair production based on 4.7 fb^{-1} of proton-proton collision data taken at $\sqrt{s} = 7$ TeV [172, 173, 174, 175, 176]

the following have been documented in a conference note of the ATLAS experiment [180], and in an internal report [181].

Generic searches for supersymmetric particles look for events with large E_T^{miss} and jets plus possibly one or more leptons. Typical selection criteria require hard cut on E_T^{miss} and on the transverse momenta of the jets to reduce Standard Model backgrounds. These criteria are sensitive to the production of gluinos and scalar quarks of the first two generations. However, such criteria have typically rather low efficiencies for sparticles lighter than 400 GeV.

In this section I'll describe the analysis which seeks evidence for pair production of a heavy partner of the top quark, where each of the top partners decays following the pattern:

$$\tilde{t}\tilde{t} \rightarrow \tilde{\chi}^+ b \tilde{\chi}^- \bar{b} \rightarrow \tilde{\chi}_1^0 b l^+ \nu \tilde{\chi}_1^0 \bar{b} l^- \nu \tag{4.19}$$

As already discussed in section 4.1.3.2 (A.2), this decay mode of the stop requires that $m_{\tilde{t}} > m_b + m_{\tilde{\chi}^\pm}$.

Previous ATLAS searches [172, 173] for a scalar top decaying into $\tilde{\chi}^\pm + b$ have focused on scalar top with a mass around or below the top quark mass (see section 4.2). Assuming that the $\tilde{t} \rightarrow \tilde{\chi}^\pm + b$ decay occurs with 100% branching ratio, scalar top with masses between the LEP limit of 103.5 GeV and the top quark mass are only allowed for some values of the lightest neutralino and chargino masses, while

heavier scalar top are allowed for any value of the gaugino masses. The search I'm presenting is sensitive to scalar top with masses between 150 GeV and 420 GeV.

The final states contains two b-jets, two W bosons, real or virtual, and two invisible particles, which is the same final state as for the production and decays of pairs of top quarks, which thus constitute an irreducible background. In the present study the signature with two leptons (e or μ) in the final state, produced in the decay of the two W bosons, is considered. This requests implies a high reduction in statistics, as the BR is 4.9%, but it provides a strong suppression of reducible backgrounds, and, by using the kinematic of the two leptons, a good rejection against top background can be achieved with no direct requirement on the hadronic part of the events, thus yielding a good sensitivity to models where the mass gap between stop and chargino is very small and hence the hadronic activity low.

4.3.1 The stransverse mass

The main discriminant variable used in the analysis is the so called *stransverse mass* m_{T2} calculated on the two leptons and E_T^{miss}. This variable [182, 183] was introduced in the framework of SUSY measurement studies. It addresses the case where two identical particles ("legs") are produced, and both decay into an invisible particle. The vector sum of the transverse momenta of the two invisible particles is measured, and constitutes the E_T^{miss} of the event. The topology is illustrated in figure 4.6, from [182]. The idea is to consider all possible decompositions of the E_T^{miss} into two transverse vectors which are interpreted as the transverse momenta of the invisible particles in the two legs of the event. For each test value of the invisible momenta two transverse masses are built with the visible particles in the events and the maximum of the two values is taken. It is intuitive that the minimum value over all possible decompositions of E_T^{miss} of the variable thus calculated will be lower than the endpoint for the decay on a single leg. As an example, for WW production, m_{T2} will be below the endpoint for the W decay, which corresponds to the W mass.

The m_{T2} variable is defined as a function of the test mass for the invisible particles in the event. If this test mass is put to zero, the definition for m_{T2}

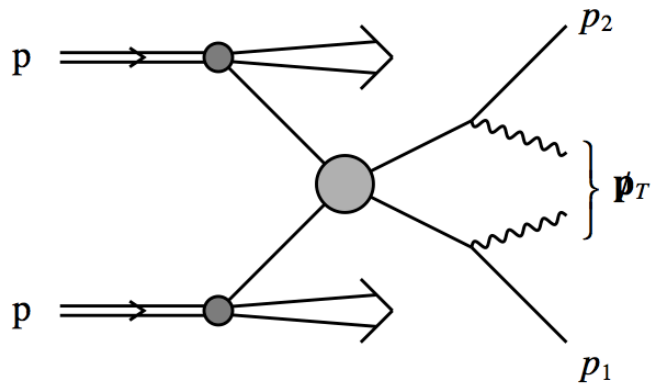

Figure 4.6: Diagram of the generic process under consideration. A hadronic collision that leads to a pair of particles being produced, which each decay into one particle that is observed with momenta p_1 and p_2 respectively; and one particle (shown as a wavy lines) that is not directly detected, and whose presence can only be inferred from the missing transverse momentum, p_T^{miss}

reduces to:

$$m_{T2}^2(\vec{p}_T^{\,\alpha}, \vec{p}_T^{\,\beta}, \vec{p}_T^{\,\text{miss}}) = \min_{\vec{q}_T^{\,1}+\vec{q}_T^{\,2}=\vec{p}_T^{\,\text{miss}}} \left\{ \max \left[m_T^2(\vec{p}_T^{\,\alpha}, \vec{q}_T^{\,1}), m_T^2(\vec{p}_T^{\,\beta}, \vec{q}_T^{\,2}) \right] \right\} \quad (4.20)$$

where m_T indicates the transverse mass, $\vec{p}_T^{\,\alpha}$ and $\vec{p}_T^{\,\beta}$ are the momenta of the two leptons, and $\vec{q}_T^{\,1}$ and $\vec{q}_T^{\,2}$ are vectors which satisfy $\vec{q}_T^{\,1} + \vec{q}_T^{\,2} = \vec{p}_T^{\,\text{miss}}$. The minimum is taken over all the possible choices of $\vec{q}_T^{\,1}$ and $\vec{q}_T^{\,2}$.

For fully leptonic $t\bar{t}$, Wt, and WW events the value of m_{T2} has an upper bound equal to the W-boson mass. For the decay chain shown in equation 4.19 the endpoint will be determined by the mass difference squared $m^2(\tilde{\chi}^{\pm}) - m^2(\tilde{\chi}^0)$, therefore the analysis will only have sensitivity when this quantity is larger than $m^2(W)$.

The bound $m_{T2} < M_W$ for SM events is quite sharp, and by selecting events with $m_{T2} > M_W$ it is thus possible to dramatically enhance the signal over background ratio. The distribution for both the expected backgrounds and two benchmark signal processes can be found in figure 4.18 for events with two leptons, and in figure 4.19 after all selections except that on m_{T2} itself.

4.3.2 Data and Monte Carlo samples

4.3.2.1 Data samples

This analysis uses all the proton-proton collisions data collected in 2011, and those collected in 2012 before the technical stop in September. The standard SUSY group good run list is applied for both years. The total integrated luminosity is 4.7 fb^{-1} at 7 TeV and 13.0 fb^{-1} at 8 TeV.

4.3.2.2 Monte Carlo samples

As stated in the previous paragraph both the 2011 and 2012 data are analyzed. Given the different center of mass energies and pileup conditions of the two years, two different campaigns of Monte Carlo generation both for signal and backgrounds were used, respectively called MC11 and MC12.

Monte Carlo simulated event samples are used to aid in the description of the background and to model the top-quark partner signals.

Background samples Top-quark pair production is simulated with POWHEG [136] interfaced to PYTHIA [87] for the fragmentation and the hadronization processes. The top-quark mass is fixed at 172.5 GeV, and the next-to-leading-order (NLO) parton distribution function (PDF) set CTEQ10 [130] is used. Additional MC samples are used to estimate the event generator systematic uncertainties: a POWHEG sample interfaced with HERWIG [131] and JIMMY [132]; a SHERPA [137] sample; two ACERMC [87] samples produced with variations to the PYTHIA parton shower parameters chosen such that the two samples produce additional radiation consistent with the experimental uncertainty in the data.

Samples of single top (Wt) are simulated with MC@NLO [127, 128, 129], interfaced with HERWIG for the fragmentation and the hadronization processes, including JIMMY for the underlying event.

Samples of Z/γ^* produced in association with jets for MC11 are generated with ALPGEN+HERWIG, while for MC12 are generated with SHERPA for invariant mass of the two leptons above 40 GeV, and with ALPGEN for masses between 10 and 40 GeV.

Samples of $t\bar{t}+Z$ and $t\bar{t}+W$ production are generated with MADGRAPH [184] interfaced to PYTHIA.

Diboson samples (WW, WZ, ZZ) are generated with SHERPA. Additional samples generated with POWHEG and HERWIG are used for the evaluation of the event generator systematic uncertainties.

Standard Model simulated samples are used in the background estimation in various roles. For processes whose small cross sections or similar topology make it difficult to select control samples in the data (single top, $t\bar{t}+Z$ and $t\bar{t}+W$), the background estimate is based on the Monte Carlo simulation. For Z backgrounds (Z+jets, ZZ, WZ) , WW and top pair production, the data are used to normalize the background estimate in an appropriate control region, but the Monte Carlo is used to extrapolate the background rate from the control region to the signal region. The simulation is also used to estimate the number of events in the different control regions which are produced by processes different than the one targeted by each control region. Only processes with two real isolated leptons in the final state have been considered, since processes with at least one fake or not isolated lepton are estimated entirely from data. The background estimate strategy is described in section 4.3.6

Signal samples Scalar top signal samples are generated with HERWIG++ and MADGRAPH respectively in the MC11 and MC12 campaigns. The samples have been generated in a grid of fixed stop, chargino and neutralino masses. The mass ranges are 150-600 GeV for $m_{\tilde{t}}$, 100$-(m_{\tilde{t}}-10$ GeV) for $m_{\tilde{\chi}^{\pm}}$, and 0-($m_{\tilde{\chi}^{\pm}}-10$ GeV). The scalar top is made to decay 100% to $b-\tilde{\chi}^{\pm}$.

Effects of multiple proton-proton interactions in the same bunch crossing (pile-up) are included. Events in MC are reweighted, so that the simulated distribution of the average number μ of proton-proton collisions per bunch crossing matches that in the data. In the MC11 simulation events belong to a few different run numbers, each of them describing the conditions of a subset of the 2011 data. The pileup reweighting tool reweighs each of them to the μ distribution of the corresponding subset. The MC12 events are reweighed to the μ distribution corresponding to the 2012 data sample used in the analysis.

4.3.3 Object definitions

- *Proton-proton interaction vertex* candidates are reconstructed using the Inner Detector tracks. The vertex with the highest squared sum of the p_T of the associated tracks is defined as the primary vertex.

- *Jets* are reconstructed using the anti-k_t jet algorithm [64] with the distance parameter R set to 0.4 and topological clusters as input. In 2011, the jets are calibrated at the EM+JES scale, while in 2012 they are calibrated with the LCW+JES scheme (see section 1.10.3). For both years, they are kept only if they have $p_T > 20$ GeV and lie within $|\eta| < 2.5$. An additional cut on the Jet Vertex Fraction[1] (JVF) is required to suppress pile-up jets, asking for $JVF > 0.75$ in 2011 and $JVF > 0.5$ in 2012.

- *Electron* candidates are required to have $p_T > 20$ GeV, $|\eta| < 2.47$ and to satisfy "medium" electromagnetic shower shape and track selection quality criteria described in section 1.10.1. These preselected electrons are then required to pass "tight" quality criteria which places additional requirements on the ratio of calorimetric energy to track momentum, and on the fraction of hits in the straw tube tracker that pass a higher threshold for transition radiation. The electron candidates are then required to be isolated: the scalar sum of the p_T, $\sum p_T$, of inner detector tracks, not including the electron track, with $p_T > 1$ GeV within a cone in the $\eta - \phi$ plane of radius $\Delta R = \sqrt{\Delta\eta^2 + \Delta\phi^2} = 0.2$ around the electron candidate must be less than 10% of the electron p_T. The numerical values of the cuts used in the "medium" and "tight" criteria are different for the 2011 and 2012 analysis. Obviously, the 2011 criteria are used for 7 TeV data or simulated events and the 2012 criteria are used for 8 TeV data or simulated events. In MC a multiplicative event weight is applied for each selected electron to the overall event weight in order to correct for differences in efficiency between data and MC.

- *Muon* candidates are reconstructed using either a full muon spectrometer track matched to an inner detector track, or a muon spectrometer segment

[1] By combining tracks and their primary vertices with calorimeter jets the Jet Vertex Fraction (or JVF) discriminant is defined, which is a measure of the probability that a jet originated from a particular vertex. Jet selection based on this discriminant is shown to be insensitive to the contributions from uncorrelated soft collisions due to pile-up.

matched to an extrapolated inner detector track. They must be reconstructed with more than one hit in the pixels, more than five hits in both the strips and straw tube detectors. They are required to have $p_T > 10$ GeV, $|\eta| < 2.4$ and must have longitudinal and transverse impact parameters within 1 mm and 0.2 mm of the primary vertex, respectively.

Muon candidates have been also required to be isolated. The $\sum p_T$ of the tracks in a cone of $\Delta R < 0.2$ must be less than 1.8 GeV (excluding the muon track).

- For the 2011 analysis, the *transverse missing energy* calculation adds together jets calibrated at the EM+JES scale with $p_T > 20$ GeV, "medium" electrons with $p_T > 10$ GeV, all the muons from the STACO container (see section 1.10.2), and topological clusters in the calorimeters not belonging to precited objects (*CellOut* term) calibrated at the EM scale.

  In 2012 the transverse missing energy calculation uses calorimeter cells with $|\eta| < 4.9$ and the muons from the STACO container. The cells are calibrated according to the object they belong to. The objects considered are the jets calibrated with the LCW+JES scheme for $p_T > 20$ GeV and with the LCW scheme for 10 GeV $< p_T <$ 20 GeV, and "medium" electrons with $p_T > 10$ GeV. Cells not belonging to any of the object above are again calibrated at the EM scale.

Following the object reconstruction described above, overlaps between jet, electron and muon candidates are resolved. Any jet within $\Delta R = 0.2$ of preselected electrons is discarded. Electrons or muons within $\Delta R = 0.4$ of any remaining jet are then discarded to reject leptons from the decay of a b- or c-hadron.

4.3.4 Event selection

The primary vertex of each event is required to contain at least 5 tracks: this cut reduces the chance of selecting a cosmic-ray event since the d_0 and z_0 of the muons considered in the analysis are calculated with respect to this primary vertex. In case of a cosmic muon, the event is rejected.

Events are accepted if they pass either a single-electron trigger reaching a plateau efficiency of about 97% for isolated electrons, or a single-muon trigger

which reaches a plateau efficiency of about 75% (90%) in the barrel (end-caps). Events are reweighted to match the measured trigger efficiency in data.

Events which contain exactly two opposite-sign (OS) leptons (electrons or muons) are selected if at least one lepton satisfies the leading p_T requirement of $p_T > 25$ GeV for electrons and $p_T > 20(25)$ GeV for muons in the analysis of 2011 (2012) data. The leptons of selected events can either have same flavor (SF) or different flavor (DF). The dilepton invariant mass m_{ll} of SF pairs is required to be either between 20 GeV and 71 GeV or larger than 111 GeV. The rejection of events with very low invariant mass lepton pairs is due to the lack of 7 TeV MC simulated samples for very low-mass ($m < 12$ GeV at truth level) Drell-Yan, while the exclusion of the Z peak region suppresses the Z+jets, WZ, and ZZ backgrounds.

In order to reduce high m_{T2} backgrounds where the value of $E_T^{\rm miss}$, and hence of m_{T2} is increased by a mismeasurement of the hadronic part of the event, two angular cuts are applied: $\Delta\phi_b < 1.5$ and $\Delta\phi_{\rm min} > 1$. The variable $\Delta\phi_b$ is the azimuthal angle between the $E_T^{\rm miss}$ vector and the $\vec{p}_b{}^{ll} = \vec{E}_T{}^{\rm miss} + \vec{p}_T(l_1) + \vec{p}_T(l_2)$ vector, where the $\vec{p}_b{}^{ll}$ variable, introduced in [185], is the opposite of the vector sum of all the hadronic activity in the event. For WW and $t\bar{t}$ backgrounds it measures the transverse boost of the WW system, and for the signal the transverse boost of the chargino-chargino system.

The $\Delta\phi_{\rm min}$ variable is the azimuthal angle difference between the $E_T^{\rm miss}$ vector and the closest jet, where the jets used are those passing the selection described in section 4.3.3.

These cuts suppresses the Z+jets background to negligible levels in the SF channel, and they also select the signal with larger efficiency than the dominant WW and top pair backgrounds.

Finally, signal candidates are required to have m_{T2} values in excess of 90 GeV. Alternative signal regions (SR) with tighter selections ($m_{T2} > 100$ GeV, 110 GeV, or 120 GeV) are also used to increase the sensitivity to signal[2] with larger values of $m^2(\tilde{\chi}^{\pm}) - m^2(\tilde{\chi}^0)$.

[2]The sensitivity is defined as $S/\sqrt{S+B+\Delta B^2}$, where S and B indicates respectively the signal and the background.

4.3.4.1 Cut optimization

As previously explained, the analysis strategy is based on the selection of events with two leptons and a value of m_{T2} larger than the W mass.

In figure 4.7 the distribution of m_{T2} is shown after requiring only the trigger and the presence of two isolated leptons. For the DF channel the dominant backgrounds at high m_{T2} is $t\bar{t}$, followed by WW. These backgrounds present a sharp fall at approximately 90 GeV. The WW presents a longer tail populated by events where one the W is produced off-shell with a mass much higher than the W nominal mass.

For the SF background, even after vetoing invariant masses in the Z region a long tail is observed, requiring additional cuts to separate the signal from the background.

A simple requirement on m_{T2} would already ensure sensitivity over a significant fraction of the parameter space in the DF channel. The main possibilities for extending the region of sensitivity of the analysis are:

- to extend the reach to as high as possible masses by reducing the high tail of the m_{T2} distribution
- to extend the reach to as low as possible chargino-neutralino mass differences. In order to achieve this, the kinematic boundary of the m_{T2} distribution for backgrounds must be sharpened. This approach will be relevant for the lower masses considered, 180 and 240 GeV, which is a crucial region not well covered by previous analyses.

The SF selection suffers from the very long tail from Z production and additional selections are necessary in order to achieve a reasonable level of sensitivity.

The high tail of the m_{T2} distribution from WW production can be suppressed requiring a significant jet activity. This selection however would reduce the sensitivity for the case where the stop and the chargino are degenerate, which is one of the main strength of the present analysis, and this option is not pursued further.

The m_{T2} tail from top events is dominated by events where the E_T^{miss} is increased by experimental effects. This can be observed in figure 4.8 where the true and reconstructed m_{T2} are shown for a sample of top events. Similarly, for Z events, the high m_{T2} tails are from high E_T^{miss} events produced by experimental effects.

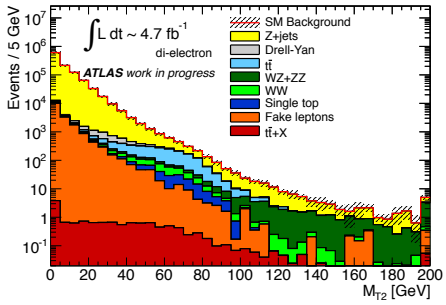

(a) ee

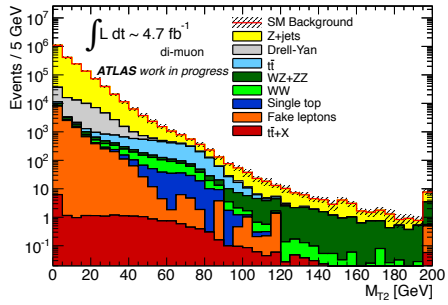

(b) $\mu\mu$

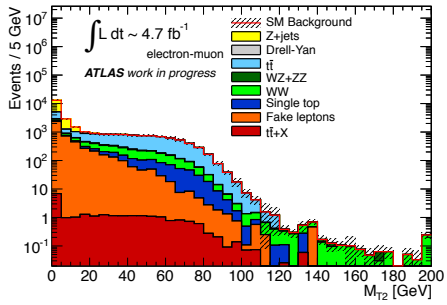

(c) $e\mu$

Figure 4.7: Distribution of the m_{T2} of the two leptons expected for 4.7 fb^{-1}of 7 TeV data, for all events with two selected leptons. All contribution are estimated from MC using the nominal cross section, except the fake background which is derived from data. The top left, top right, and bottom plots report the distributions expected for the ee, $\mu\mu$, and $e\mu$ channels respectively

The additional E_T^{miss} will point towards the hadronic jets which get mismeasured and away from the vector sum of the leptonic activity in the event. Two variables, $\Delta\phi_b$ and $\Delta\phi_{\text{min}}$, were already introduced in section 4.3.4 for this purpose.

The scatter plots of these two variables are shown for $t\bar{t}$ and Z events with $m_{T2} > 90$ GeV in figure 4.9. The E_T^{miss} alignment is very clear for Z, where all of the E_T^{miss} is from instrumental effects, less clear for $t\bar{t}$ into two leptons which has a significant E_T^{miss} for neutrinos. For the signal, as shown in figure 4.10, the upper left corner is populated.

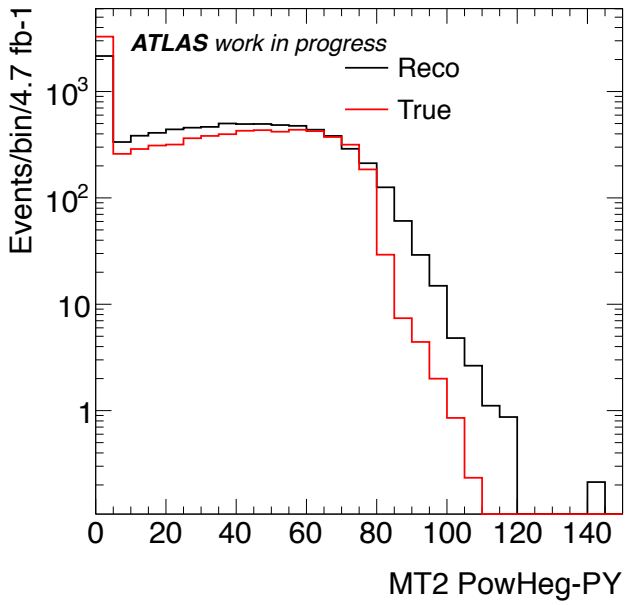

Figure 4.8: Distribution of the m_{T2} in top events. The red line is the distribution at truth level, the black line at reconstruction level

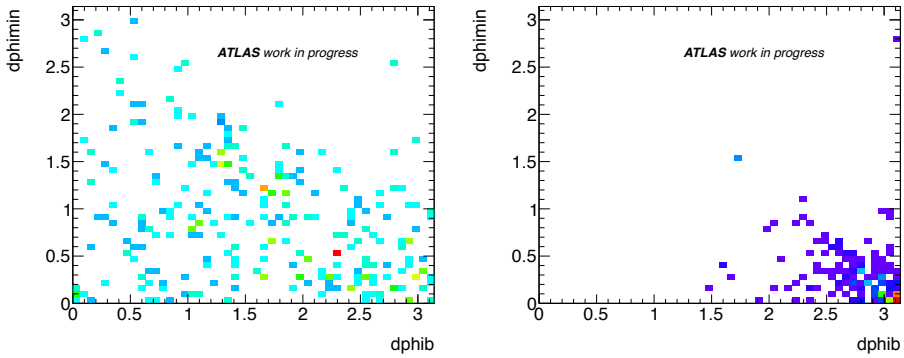

(a) $t\bar{t}$ (b) Z

Figure 4.9: Distribution of the $\Delta\phi_{\min}$ vs $\Delta\phi_b$ variables for $t\bar{t}$ (left) and Z (right) events. Only events with $m_{T2} > 90$ GeV are plotted

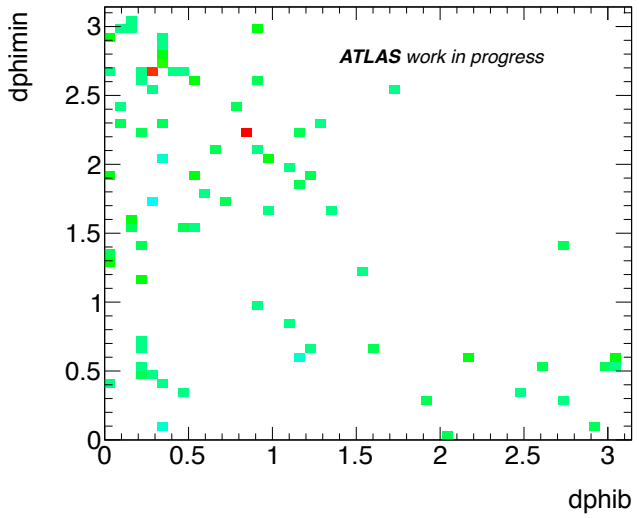

Figure 4.10: Distribution of the $\Delta\phi_{\min}$ vs $\Delta\phi_b$ variable for a signal point with $m(\tilde{t}) = 180$ GeV, $m(\tilde{\chi}^{\pm}) = 160$ GeV, $m(\tilde{\chi}^0) = 60$ GeV. Only events with $m_{T2} > 90$ GeV are plotted

The selections on $\Delta\phi_b$ and $\Delta\phi_{\min}$ were optimized based on the 2011 signal grid, and the values optimising the performance over the full signal grid are: $\Delta\phi_b < 1.5$ and $\Delta\phi_{\min} > 1$.

Signal candidates thus selected are required to have m_{T2} values in excess of 90 GeV (100 GeV, 110 GeV, or 120 GeV). For each mass hypothesis for the scalar top , chargino and neutralino, the best SR was determined as the selection which gives the best expected sensitivity, using the final background estimate and uncertainties and the statistical tools reported and discussed in section 4.3.8.

The distributions of m_{T2} after the cuts on the $\Delta\phi$ variables can be found in figure 4.19. The tail is dominated by $t\bar{t}$ up to 100 GeV, and for higher values by WW.

4.3.4.2 Cut flow

A summary of the SR selection criteria is reported in table 4.4.

The number of events which is expected to survive various stage of the selection is shown in table 4.5 for 2011 and table 4.6 for 2012. The number of expected SM

p_T cut on the trigger lepton	25 for electrons, 20(25) for muons in 2011(2012)
p_T cut on second lepton	20/10 for electrons/muons
p_T cut for third lepton veto	20/10 for electrons/muons
Dilepton invariant mass	$20 < m_{ll} < 71$ or $m_{ll} > 111$ if SF
	$m_{ll} > 20$ if DF
$\Delta\phi_{\min}(E_T^{\text{miss}}$,jets)	> 1
$\Delta\phi(E_T^{\text{miss}}, p_b^{ll})$	< 1.5
$m_{T2}(l,l)$	$> 90, 100, 110, 120$ (defines four SR)

Table 4.4: Selection of signal candidates. All numbers are in GeV

events is computed from MC before the application of the data driven scale factors described in section 4.3.6, except for the fake background which is derived from data (see section 4.3.6.1). The expected rates for one signal benchmark, as well as the number of events observed in data, are also reported.

4.3.5 Kinematic distributions

In this section, a comparison is made between data and MC simulation for the main observables used in the analysis. In all plots, the MC uses the nominal cross sections (i.e., the scale factors from CR measurements are not included). The uncertainty band includes the MC statistics, the main detector response uncertainties (JES, JER, and E_T^{miss} cellout term), the cross section uncertainty, the generator and ISR/FSR uncertainties for $t\bar{t}$. The distributions are also shown separately for each year (2011 and 2012) and for the same and different flavor channels. The overall agreement between data and Monte Carlo is good.

Figures 4.11, 4.12 and 4.13 show the distributions of the p_T of the leading lepton, of the p_T of the sub-leading lepton, and of the transverse missing energy respectively, after the trigger requirements and the selection of 2 isolated leptons.

The invariant mass of the two leptons, the two angular variables $\Delta\phi_{\min}$ and $\Delta\phi_b$, and the p_b^{ll} variable are shown at the same selection level in figures 4.14, 4.15, 4.16, 4.17 respectively. The m_{T2} distribution is shown in figure 4.18.

After the application of the selections on the angular variables and of the veto on same flavor lepton pair in the Z mass window, the distribution of m_{T2} is shown

same flavor Cuts ↓ Process	WW	$WZ + ZZ$	$t\bar{t}$	Z+jets	other SM	fakes	tot SM	signal	data
2 leptons	2024	4923	9650	2957385	123577	27971	3093768	1320	2989970
Z veto	1438	1084	6867	241670	78253	7892	328540	919	308229
$\Delta\phi > 1.0$	1329	951	3792	220420	63206	7242	289019	691	274200
$\Delta\phi_b < 1.5$	935	753	3443	173611	43377	5659	221570	544	212167
$m_{T2} > 90$ GeV	3.33	3.30	7.32	0	1.29	0.43	14.67	58.1	17
different flavor									
2 leptons	1881	254	9164	10241	1029	4498	22491	1282	26658
$\Delta\phi > 1.0$	1739	214	5118	9811	732	3914	17552	987	21305
$\Delta\phi_b < 1.5$	1210	160	4622	8061	610	2870	14663	775	17218
$m_{T2} > 90$ GeV	3.61	0.24	10.59	0	0.73	1.71	15.17	79.1	15

Table 4.5: The expected number of background events is reported at various stages of the event selection, for SF (above) and DF (below) events and 4.7 fb^{-1} at 7 TeV center of mass energy. The numbers are the nominal MC prediction, except for the fake background which is derived from data. The expected rate for a signal with $m(\bar{t}) = 180$ GeV, $m(\tilde{\chi}^{\pm}) = 160$ GeV, $m(\tilde{\chi}^{0}) = 1$ GeV, and the number of events observed in data are also reported

in 4.19.

The usefulness of the selection on the angular variables can be seen from figures 4.20 and 4.21 where their distributions are reported after all the signal region selections except the selection on the variable which is reported in each plot. The signal region is $m_{T2} > 90$ GeV in this plot.

4.3.6 Background estimate

4.3.6.1 General strategy

The dominant SM background contribution to the SR are expected to be the top and the W pair production. The other diboson processes (WZ and ZZ) are also expected to be a significant background. The normalization of these backgrounds are determined using the number of observed events in three control regions (CR), each of which is populated mostly by one of the targeted background sources.

Additional SM processes yielding two isolated leptons and E_T^{miss} (Wt, Z+jets, Drell-Yan, $t\bar{t} + W$ and $t\bar{t} + Z$) and providing a sub-dominant contribution to the SR are determined from MC.

Same Flavor	WW	$ZZ + WZ$	$t\bar{t}$	Z	Other SM	Fake leptons	Total	Data
Signal Leptons	6879	14306	34230	8.873e+06	86630	147725	9.162e+06	9.409e+06
Z veto	4874	2736	24359	586129	85495	18901	722494	741033
$\Delta\phi > 1$	4362	2332	13606	533092	61338	16033	630763	642146
$\Delta\phi_b < 1.5$	3325	1981	12289	473548	48075	13858	553076	558545
$m_{T2} > 90$ GeV	16.1	11.6	58.9	6.3	12.2	2.4	107.5	75
$m_{T2} > 100$ GeV	7.1	8.8	10.1	6.3	2.2	1.6	36.1	27
$m_{T2} > 110$ GeV	4.7	6.7	1.5	3.8	0.6	0.2	17.5	12
$m_{T2} > 120$ GeV	3.5	5.1	0.3	3.8	0.3	0.3	13.3	7
Different Flavor								
Signal Leptons	6936	826	34862	30473	3870	15218	92185	95370
$\Delta\phi > 1$	6227	689	19568	28935	2838	12615	70872	73127
$\Delta\phi_b < 1.5$	4767	547	17736	26401	2413	10723	62587	64357
$m_{T2} > 90$ GeV	25.9	1.1	73.4	0	10.5	5.9	116.8	106
$m_{T2} > 100$ GeV	11.8	0.8	10.7	0	2.0	1.7	27.0	20
$m_{T2} > 110$ GeV	7.3	0.5	2.1	0	0.3	1.0	11.2	12
$m_{T2} > 120$ GeV	5.3	0.4	0.4	0	0.1	0.9	7.1	6

Table 4.6: The expected number of background events is reported at various stages of the event selection, for SF (above) and DF (below) events and for 13.0 fb^{-1} at 8 TeV center of mass energy. The numbers are the nominal MC prediction, except for the fake background which is derived from data. The number of events observed in data is also reported

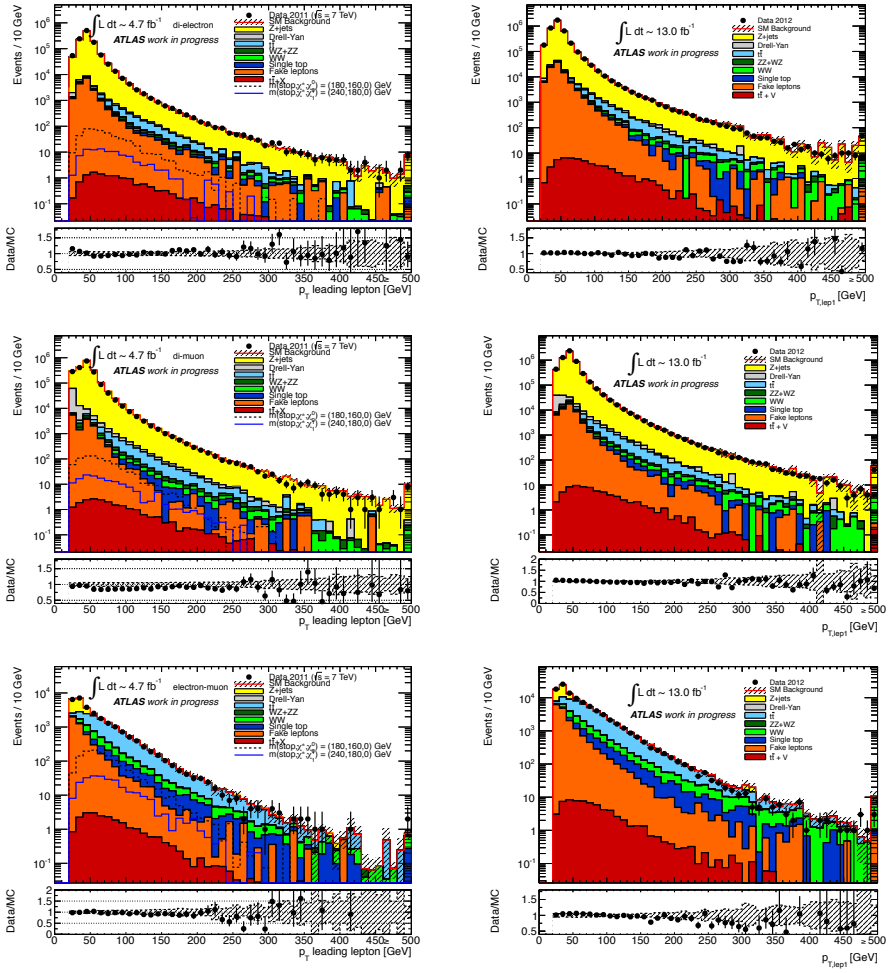

Figure 4.11: Distribution of the transverse momentum of the leading lepton, for events with two isolated leptons for 2011 (left plots) and 2012 (right plots) data. The top, middle and lower plots report the distribution for the ee, $\mu\mu$, and $e\mu$ channel respectively

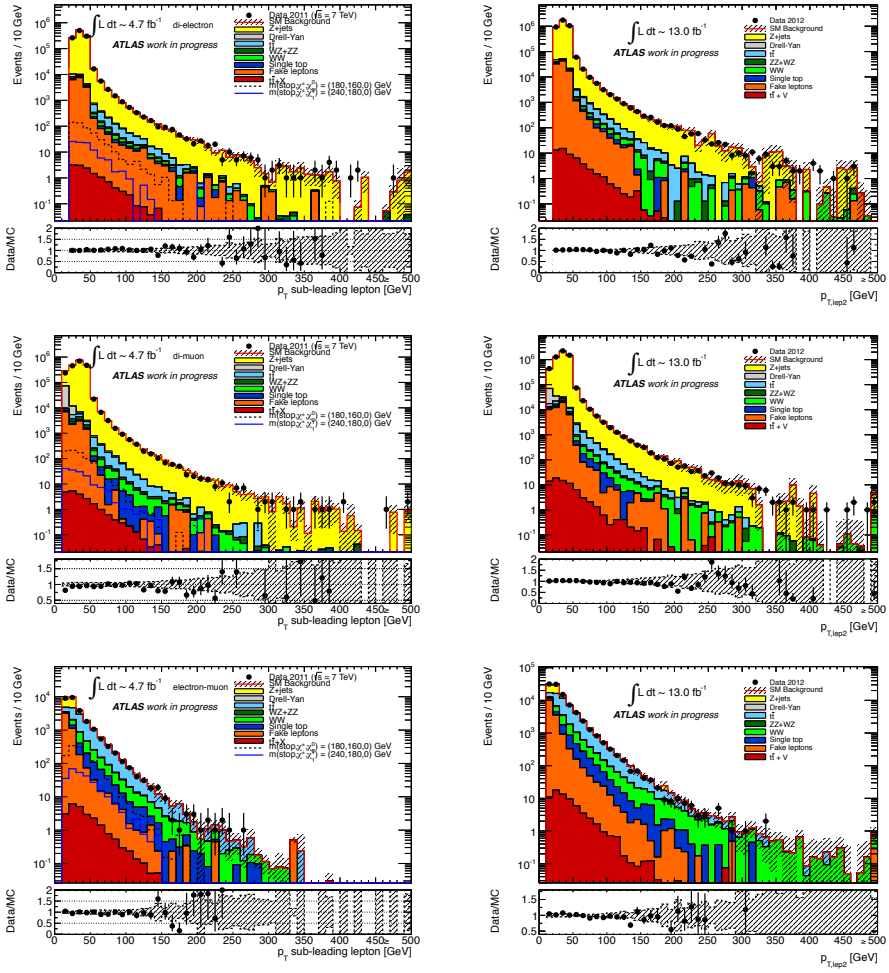

Figure 4.12: Distribution of the transverse momentum of the sub-leading lepton, for events with two isolated leptons for 2011 (left plots) and 2012 (right plots) data. The left, central and right plots report the distribution for the ee, $\mu\mu$, and $e\mu$ channel respectively

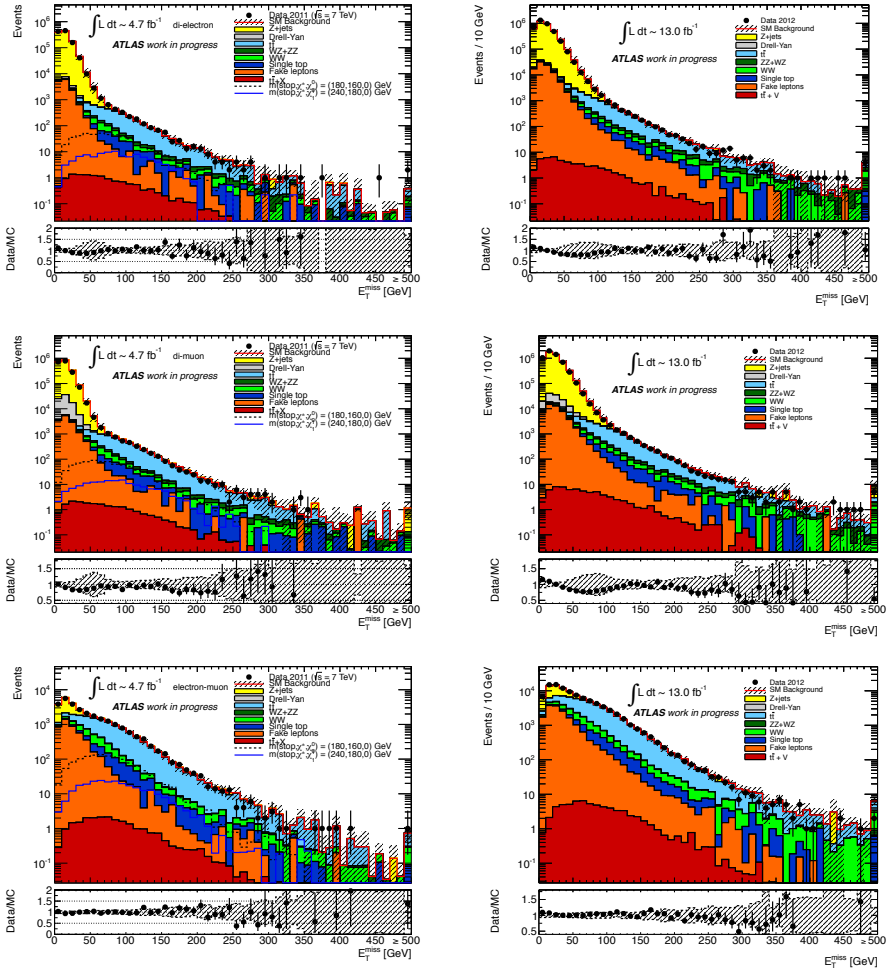

Figure 4.13: Distribution of the transverse missing energy, for events with two isolated leptons for 2011 (left plots) and 2012 (right plots) data. The top, middle and bottom plots report the distribution for the ee, $\mu\mu$, and $e\mu$ channel respectively

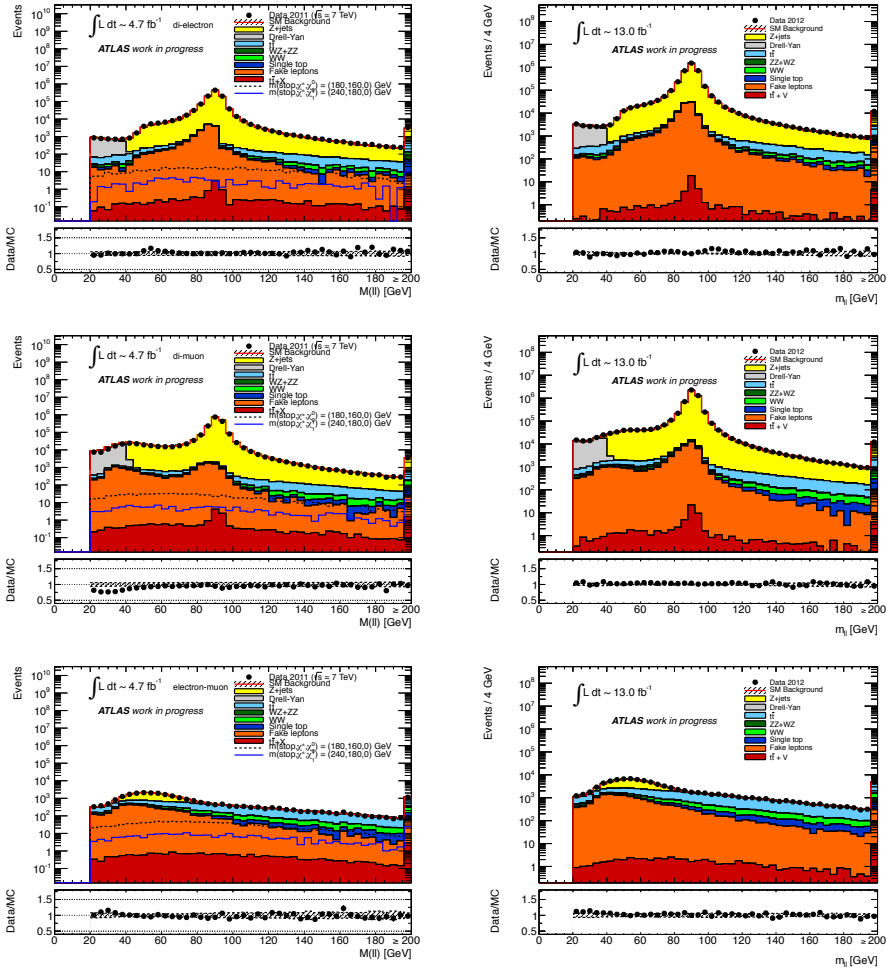

Figure 4.14: Distribution of the invariant mass of the two leptons for events with two isolated leptons for 2011 (left plots) and 2012 (right plots) data. The top, middle and bottom plots report the distribution for the ee, $\mu\mu$, and $e\mu$ channel respectively

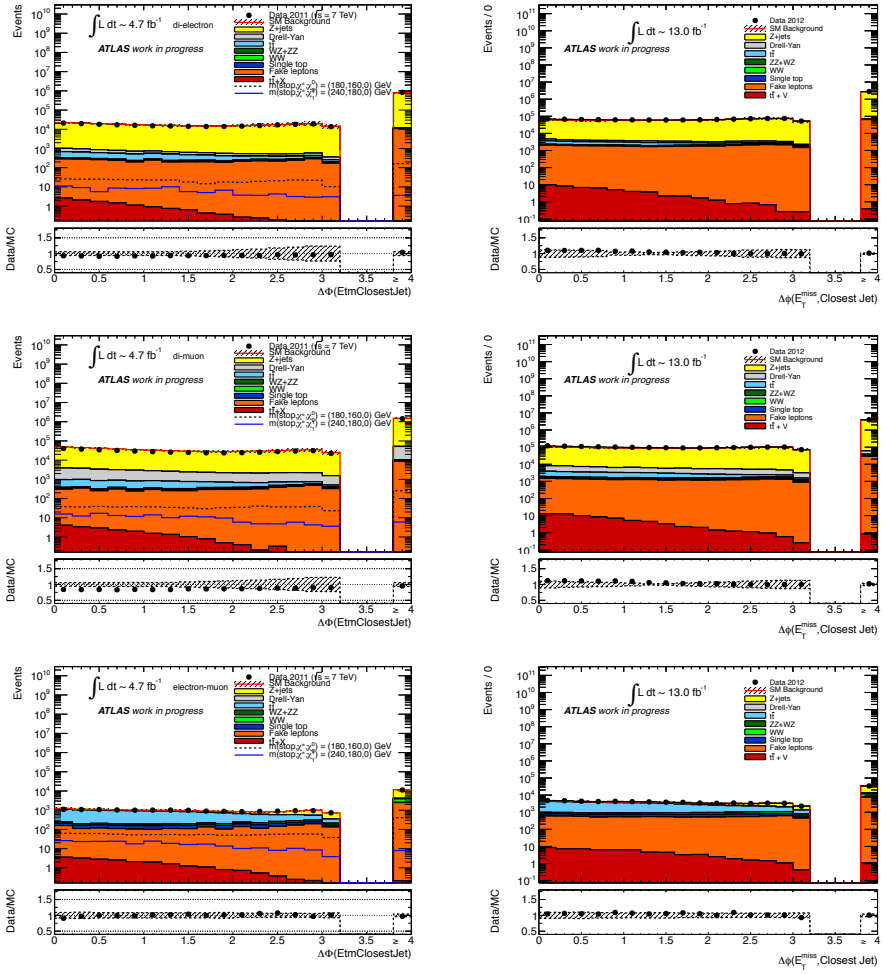

Figure 4.15: Distribution of the angle $\Delta\phi_{\min}$ between transverse missing energy and the closest jet, for events with two isolated leptons for 2011 (left plots) and 2012 (right plots) data. The top, central and bottom plots report the distribution for the ee, $\mu\mu$, and $e\mu$ channel respectively. The entries in the last bin are for those events without jets

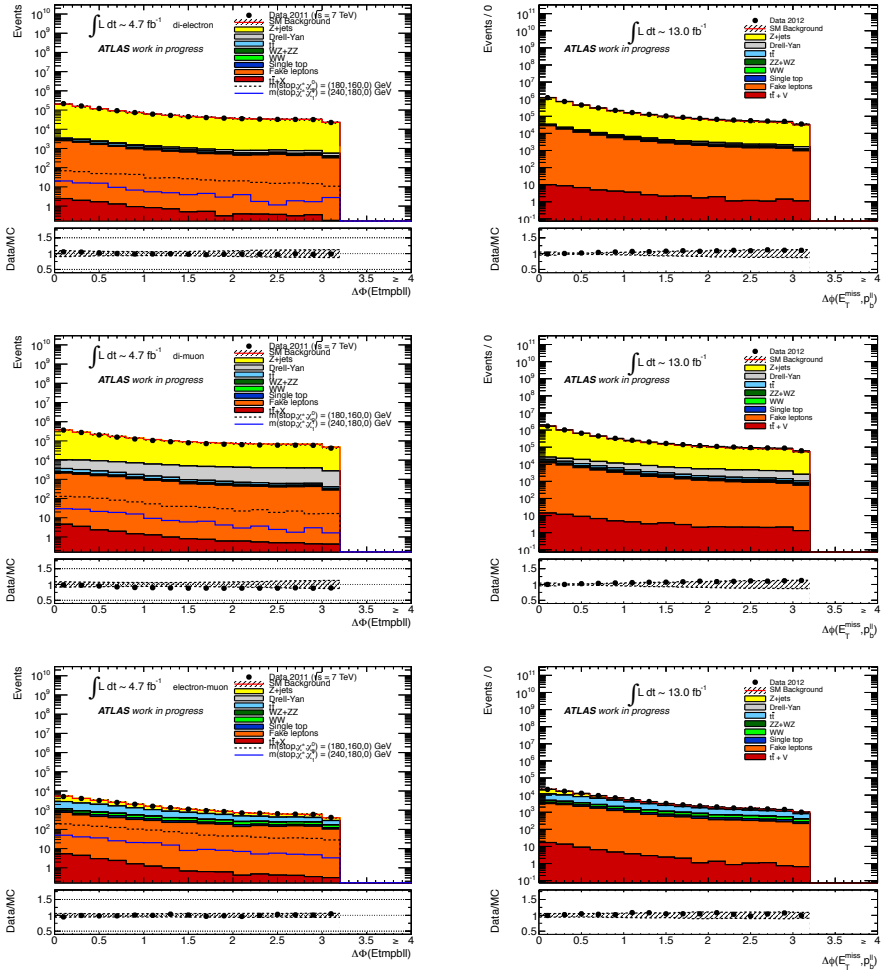

Figure 4.16: Distribution of the angular variable $\Delta\phi_b$ for events with two isolated leptons for 2011 (left plots) and 2012 (right plots) data. The top, central and bottom plots report the distribution for the ee, $\mu\mu$, and $e\mu$ channel respectively

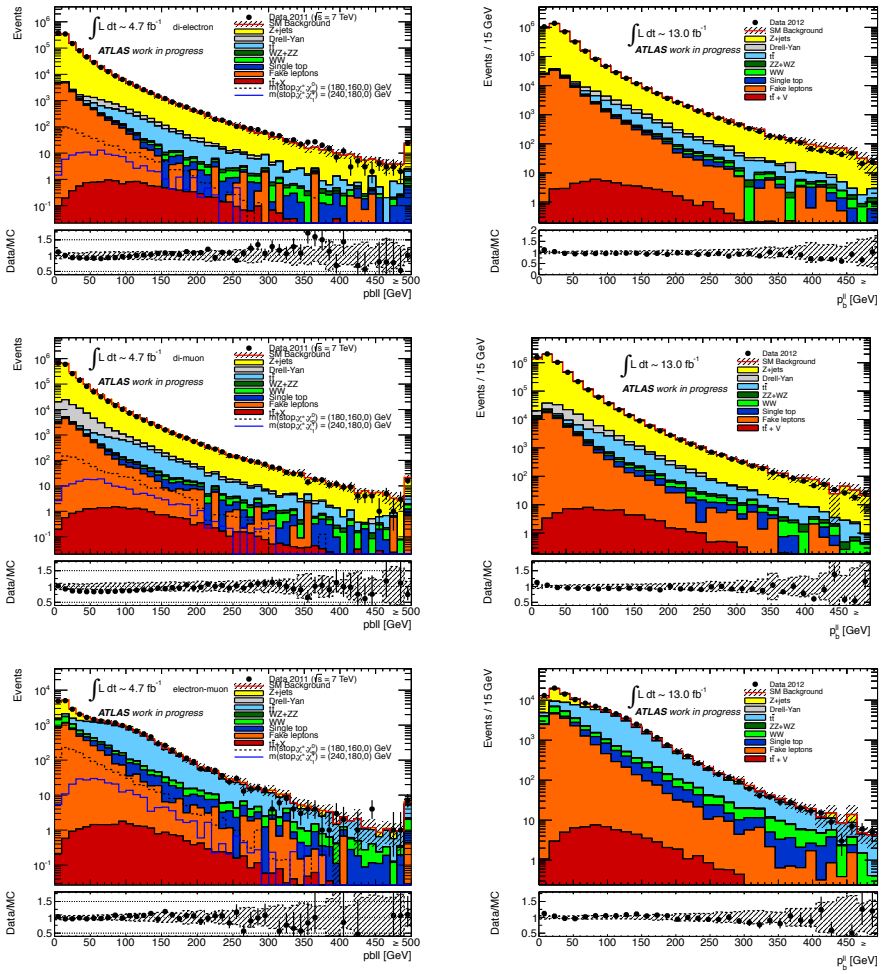

Figure 4.17: Distribution of p_b^{ll} for events with two isolated leptons for 2011(left plots) and 2012 (right plots) data. The top, central and bottom plots report the distribution for the ee, $\mu\mu$, and $e\mu$ channel respectively

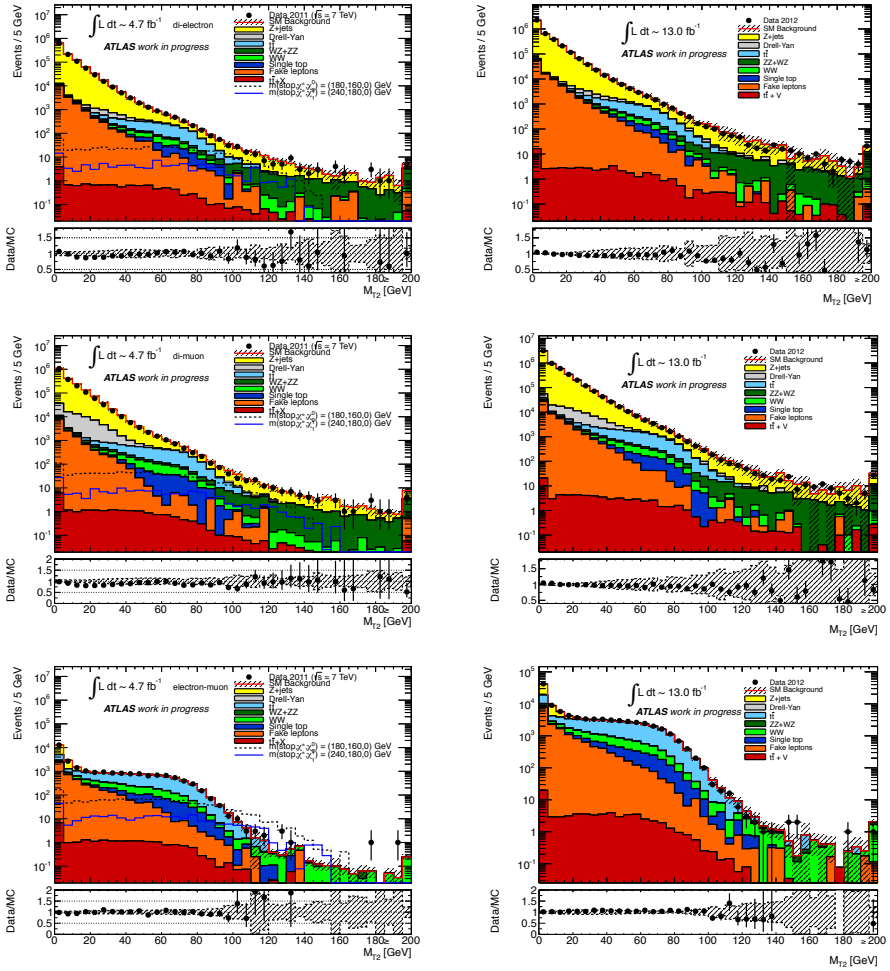

Figure 4.18: Distribution of m_{T2} for events with two isolated leptons for 2011 (left plots) and 2012 (right plots) data. The top, central and bottom plots report the distribution for the ee, $\mu\mu$, and $e\mu$ channel respectively

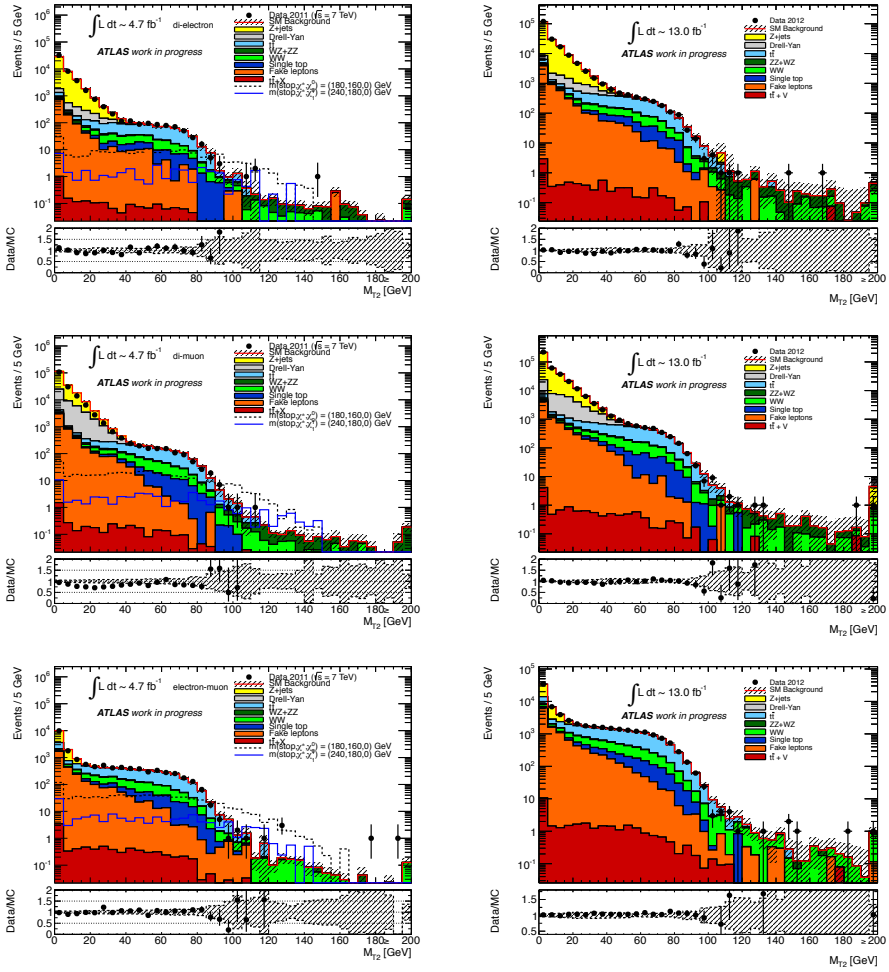

Figure 4.19: Distribution of m_{T2} for events passing all of the signal region selections except that on m_{T2} itself, for 2011 (left plots) and 2012 (right plots) data. The top, central and bottom plots report the distribution for the ee, $\mu\mu$, and $e\mu$ channel respectively

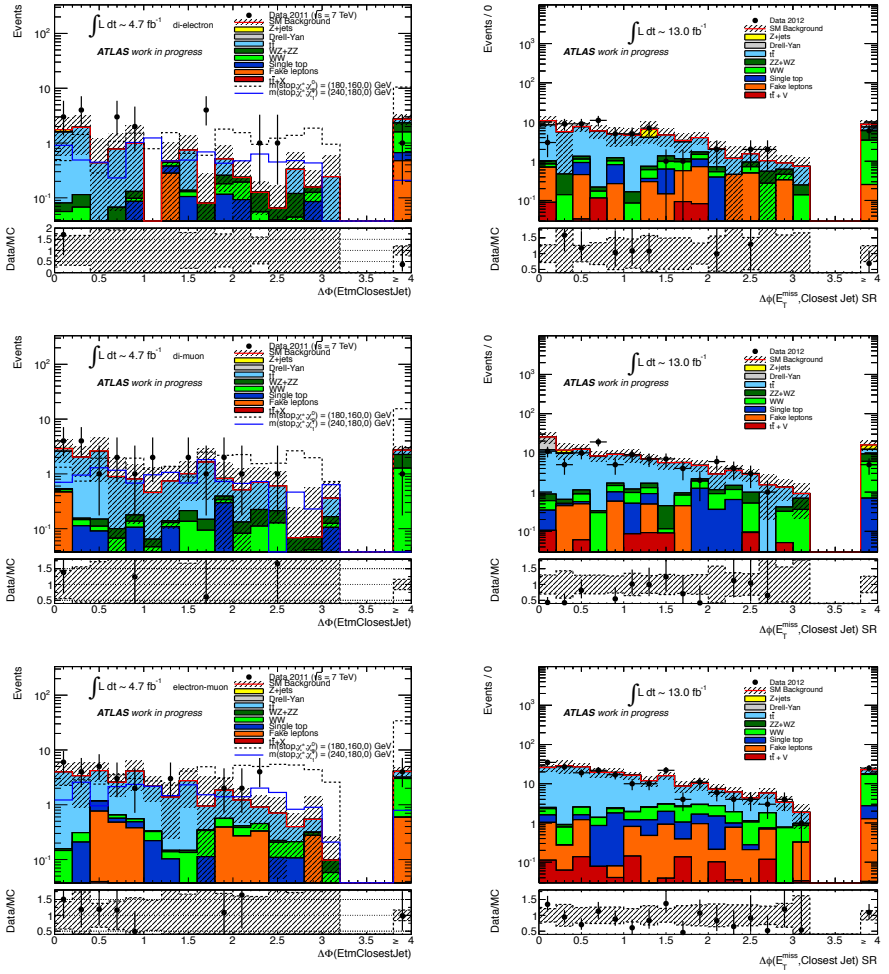

Figure 4.20: Distribution of the angle $\Delta\phi_{\min}$ between transverse missing energy and the closest jet, for 2011 (left plots) and 2012 (right plots) data. The top, central and bottom plots report the distribution for the ee, $\mu\mu$, and $e\mu$ channel respectively. All signal region selection except that on $\Delta\phi_{\min}$ itself are applied

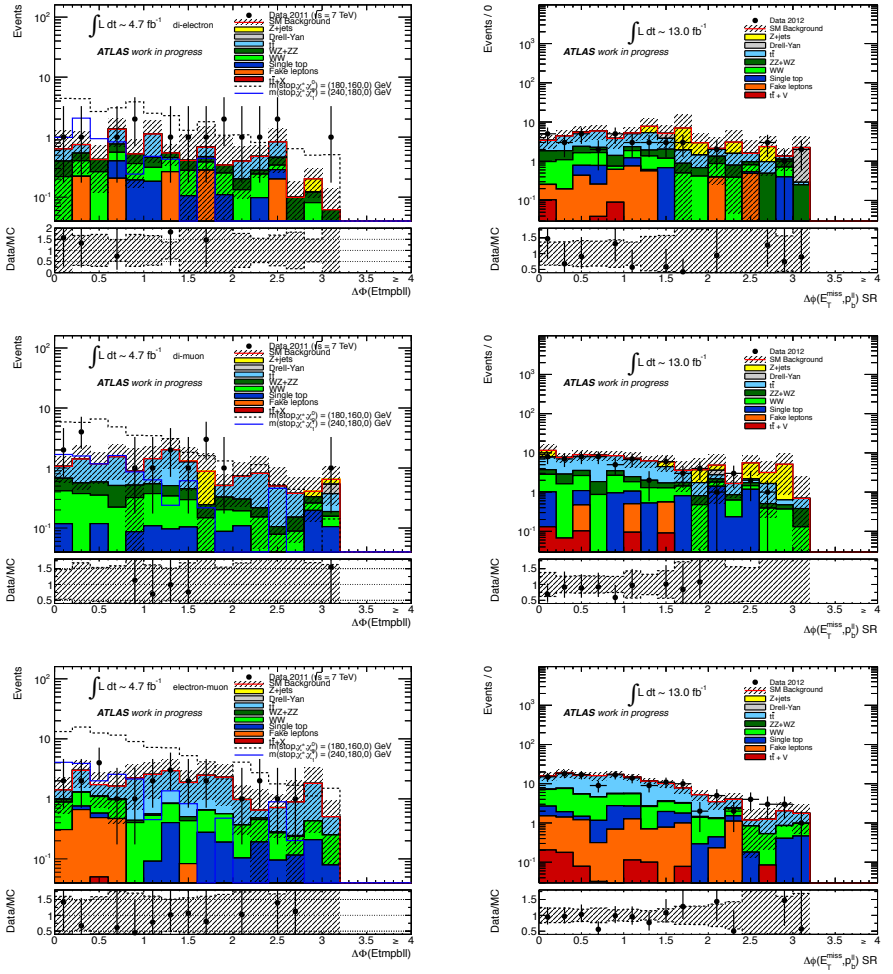

Figure 4.21: Distribution of the angle $\Delta\phi_b$ between transverse missing energy and p_b^{ll}, for events with two isolated leptons for 2011 (left plots) and 2012 (right plots) data. The top, central and bottom plots report the distribution for the ee, $\mu\mu$, and $e\mu$ channel respectively. All SR selections except that on $\Delta\phi_b$ itself are applied

The fake lepton background consists of semi-leptonic $t\bar{t}$, s-channel and t-channel single top, W+jets and light- and heavy-flavour jet production. The contribution from this background is small (less than 10% of the total background). It is estimated from data with a method similar to that described in section 3.3.3.1. Two types of lepton identification criteria are defined for this evaluation: "tight", corresponding to the full set of identification criteria described above, and "loose" corresponding to preselected electrons and muons. The method counts the number of observed events containing loose-loose, loose-tight, tight-loose and tight-tight lepton pairs in the SR. The probability for real leptons passing the loose selection criteria to also pass the tight selection is measured using a $Z \to ll$ sample. The equivalent probability for fake leptons is measured from multijet-enriched control samples. From these probabilities the number of events containing a contribution from one or two fake leptons is calculated. More information about this method can be found in references [65, 176, 181]

The number of events $N^{\text{obs}}(CR)$ observed in each control region is related to the backgrounds yields by the equation

$$N^{\text{obs}}(CR) = \mu_T N_T^{\text{MC}}(CR) + \mu_W N_W^{\text{MC}}(CR) + \mu_Z N_Z^{\text{MC}}(CR) + N_{\text{others}}^{\text{MC}}(CR) + N_{\text{fakes}}^{\text{DD}}(CR) \tag{4.21}$$

where $N_T^{\text{MC}}(CR)$, $N_W^{\text{MC}}(CR)$, $N_Z^{\text{MC}}(CR)$ are the yield predicted by MC in the CR for top-quark pair, WW, and the sum of WZ and ZZ events, respectively. The μ terms are scale factors which are applied to these backgrounds. $N_{\text{others}}^{\text{MC}}(CR)$ is the MC yield for the sum of Wt, Z+jets, Drell-Yan, $t\bar{t}+W$ and $t\bar{t}+Z$ processes, while the number $N_{\text{fakes}}^{\text{DD}}(CR)$ of events with fake leptons is determined from data. The scale factors μ_T, μ_W, and μ_Z are determined by solving the system defined by equation 4.21 for the three CR. The expected background in the SR is then given by the same equation

$$N^{\text{obs}}(SR) = \mu_T N_T^{\text{MC}}(SR) + \mu_W N_W^{\text{MC}}(SR) + \mu_Z N_Z^{\text{MC}}(SR) + N_{\text{others}}^{\text{MC}}(SR) + N_{\text{fakes}}^{\text{DD}}(SR) \tag{4.22}$$

With this approach, the ratio of events from each background source in the different CR and in the SR is used to derive the normalization of the main backgrounds from the data. The systematic uncertainties described in section 4.3.7 affect the ratio of MC expected yields in the various regions and are taken into account to determine the uncertainty on the background prediction.

Technically, the background estimate is performed with a likelihood based method. A likelihood is solved with the three observed rates in the CR as a constraint and the three μ terms as free parameters. The systematics uncertainties are described by nuisance parameters but are not constrained by the fit. Each nuisance parameter is described by a Gaussian centered on zero and of width one. Zero corresponds to the nominal rate in all regions, while ± 1 correspond to the "up" and "down" systematic variations. Systematic uncertainties which are one-sided (like the JER) are symmetrized. Different nuisance parameters are treated as uncorrelated.

4.3.6.2 Definition of control regions

Three control regions are defined:

- **CRT**, defined by DF events with 40 GeV $< m_{T2} <$ 80 GeV, $p_b^{ll} >$ 30 GeV, and passing all the SR selections on other variables. This region is expected to be populated mostly by top-quark pair events, with 77% purity for 2011 data and 73% for 2012 data.

- **CRW**, defined by DF events with 40 GeV $< m_{T2} <$ 80 GeV and $p_b^{ll} <$ 15 GeV, and passing all the SR selections on other variables. This is expected to be populated mostly by WW events, with 69% purity for 2011 data and 60% for 2012 data.

- **CRZ**, defined by same flavor events which pass all the selections of the SR with $m_{T2} >$ 90 GeV, except that the two-lepton invariant mass is required to be between 71 GeV and 111 GeV. This region is expected to be populated mostly by WZ and ZZ events, with a purity of 90% for 2011 data and 74% for 2012 data.

The DF requirement for the top pair and WW CR ensures better purity, since the contamination of Z+jets in the SF channels is significant. The lower signal purity in 2012 is due primarily to the increased pileup level, with a corresponding worsening of the E_T^{miss} resolution. The resolution of p_b^{ll} is also worse, and the separation between WW and the top pair background less effective. The purity in 2012 is nevertheless sufficient to extract the normalization of the single backgrounds with a fit to the data.

In figure 4.22 the distribution of p_b^{ll} is shown for events passing all the cuts of CRT and CRW except p_b^{ll} itself. The two CR thus correspond to the events with $p_b^{ll} > 30$ GeV and $p_b^{ll} < 15$ GeV, respectively, in the figure.

In figure 4.23 the distribution of m_{T2} is shown for same flavor events passing all the cuts of CRZ except that on m_{T2} itself. The CR corresponds to the events with $m_{T2} > 90$ GeV in the figure.

These figures are done with the nominal MC scale factors, and they show that the number of events observed in the CR is in reasonable agreement with the expectations. The expected background composition of the control regions is also reported in table 4.7.

4.3.6.3 Definition of validation regions

Two validation regions are defined, which allows to check that the MC-based extrapolation of the W and top CR to a region with different p_b^{ll} yields an estimate consistent with the data:

- **VRT**, defined by events with 40 GeV $< m_{T2} <$ 80 GeV, at least one jet, 15 GeV $< p_b^{ll} <$ 30 GeV, and passing the SR selections on other variables. This region is expected to be populated mostly (with 61% purity for both 2011 and 2012 data) by top-quark pair events.

- **VRW**, defined by events with 40 GeV$< m_{T2} <$ 80 GeV, no jets, 15 GeV $< p_b^{ll} <$ 30 GeV, and passing the SR selections on other variables. This region is expected to be populated mostly (with 61% purity for 2011 data and 56% for 2012 data) by WW events.

The expected background composition of the VR is reported in table 4.8.

A good VR should be kinematically close to the SR but still expected to contain mostly background events. In figure 4.24 the expected signal yields in VRT and VRW is reported as a function of the chargino and neutralino masses, for a fixed scalar top mass of 180 GeV. This is the lowest simulated scalar top mass and it is a worst-case scenario in this context, since the expected signal contamination decreases with increasing scalar top masses. The yields has to be compared with the expected SM rate reported in table 4.8. The maximum signal contamination is 40%, for a scenario which would give a signal rate much larger than the expected

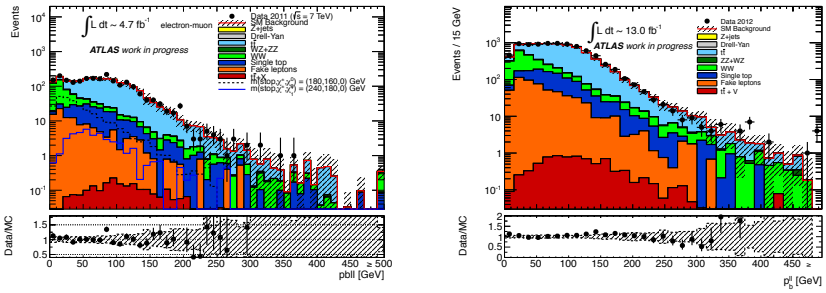

Figure 4.22: Distribution of p_b^{ll} for DF events with two isolated leptons, 40 GeV $< m_{T2} <$ 80 GeV, $\Delta\phi_{\min} > 1$, $\Delta\phi_b < 1.5$ and passing the Z veto, for 2011 (left plots) and 2012 (right plots) data

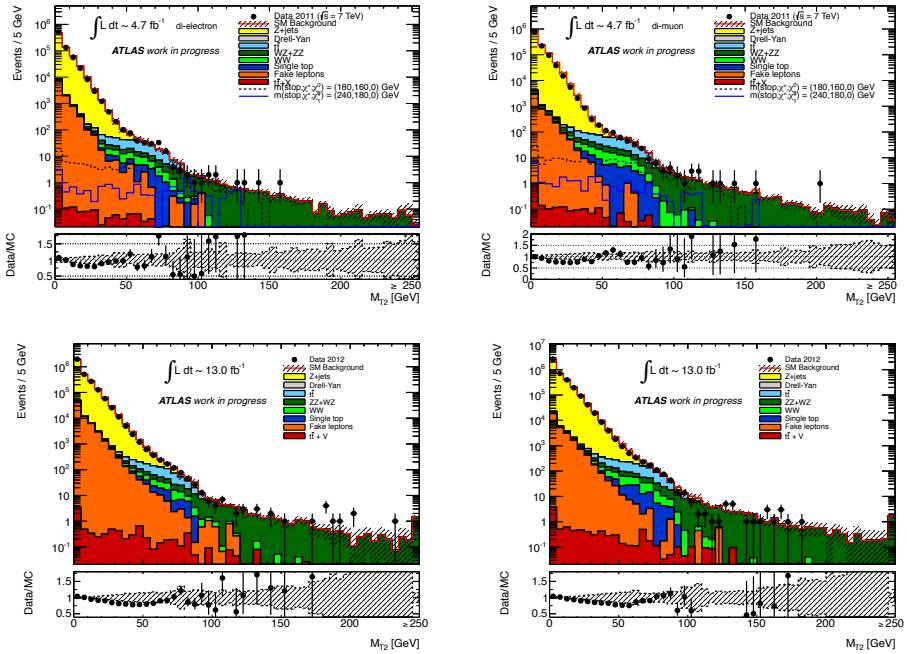

Figure 4.23: Distribution of m_{T2} for events with two same flavor isolated leptons with a invariant mass between 71 GeV and 111 GeV, $\Delta\phi_{\min} > 1$, $\Delta\phi_b < 1.5$ in 2011 (upper plots) and in 2012 (lower plots). The left plots refer to the ee channel and the right plots to the $\mu\mu$ channel

channel,2011	CRW	CRT	CRZ
Observed events	494	3039	34
Fitted bkg events	494 ± 23	3039 ± 56	34 ± 6
Fitted top events	45 ± 12	2307 ± 86	2.2 ± 1.7
Fitted WW events	351 ± 29	222 ± 36	1.0 ± 0.2
Fitted WZ-ZZ events	13 ± 4	23 ± 5	30 ± 6
Fitted other BKG events	39 ± 6	374 ± 21	0.6 ± 0.2
Fitted fakes events	45 ± 6	109 ± 16	0.0
MC exp. SM events	463.6	3119.9	37.2
MC exp. top events	46.8	2396.2	2.3
MC exp. WW events	317.6	200.6	0.9
MC exp. WZ-ZZ events	14.8	25.1	33.5
MC exp. other BKG events	38.6	374.6	0.6
fakes events	44.7	108.8	0.00

channel, 2012	$CRW-SF$	$CRW-DF$	$CRT-SF$	CRT	CRZ
Observed events	443	461	6401	7279	115
Fitted bkg events	459 ± 36	461 ± 22	6638 ± 280	7278 ± 89	115 ± 11
Fitted top events	57 ± 12	82 ± 16	736 ± 203	5233 ± 212	20 ± 9
Fitted WW events	229 ± 28	301 ± 30	672 ± 127	942 ± 180	6.4 ± 1.6
Fitted WZ-ZZ events	8.3 ± 2.3	7.5 ± 2.0	40 ± 8	32 ± 8	74 ± 15
Fitted DY events	41 ± 23	0	557 ± 128	0.1 ± 0.2	0.1 ± 0.2
Fitted Z+jets events	80 ± 20	0	846 ± 165	7 ± 8	11 ± 7
Fitted ttV events	0.0 ± 0.0	0.1 ± 0.1	4.6 ± 0.5	7.7 ± 0.7	1.0 ± 0.3
Fitted Wt events	14 ± 4	19 ± 7	505 ± 37	659 ± 44	0.9 ± 1.3
Fitted fakes events	30.2 ± 5.8	51 ± 9	274 ± 56	396 ± 74	2.1 ± 0.2
MC exp. SM events	419.37	406.84	6449.67	7004.17	150.86
MC exp. top events	55.77	80.06	3656.83	5120.06	19.35
MC exp. WW events	186.09	245.58	545.93	765.40	5.18
MC exp. WZ-ZZ events	12.61	11.30	60.54	48.92	111.13
MC exp. DrellYan events	40.55	0.00	556.62	0.14	0.00
MC exp. Zll events	79.77	0.00	845.95	7.44	11.20
MC exp. ttV events	0.00	0.09	4.59	7.67	1.01
MC exp. Wt events	14.33	18.96	505.02	658.21	0.88
fakes events	30.25	50.85	274.18	396.33	2.13

Table 4.7: Background fit results for the CRW, CRT and CRZ regions, for 2011(above) and 2012 (below) data. Nominal MC expectations (normalized to MC cross-sections) are given for comparison. The errors shown are the statistical plus systematic uncertainties.The "other BKG" lines refer to the Wt, $t\bar{t}+W$, $t\bar{t}+Z$, and Z+jets processes

channel	VRW, 2011	VRT, 2011	VRW, 2012	VRT, 2012
Observed events	245	215	1242	633
Fitted bkg events	307 ± 39	198 ± 28	1292 ± 117	671 ± 65
Fitted top events	21 ± 6	113 ± 21	72 ± 23	379 ± 53
Fitted WW events	197 ± 36	47 ± 18	807 ± 110	124 ± 25
Fitted WZ-ZZ events	7.6 ± 2.3	3.4 ± 1.2	26 ± 6	5.9 ± 1.9
Fitted other BKG events	33 ± 4	28.1 ± 2.1		
Fitted Drell-Yan events			67 ± 26	30 ± 15
Fitted $Z(ll)$ events			125 ± 27	31 ± 21
Fitted $t\bar{t}V$ events			0.0 ± 0.0	0.4 ± 0.2
Fitted Wt events			41 ± 9	60 ± 10
Fitted fakes events	49 ± 9	7 ± 3	152 ± 32	42 ± 10
MC exp. SM events	281.6	196.3	1153	643
MC exp. top events	21.4	117.7	70	371
MC exp. WW events	170.1	40.6	657	101
MC exp. WZ-ZZ events	7.2	3.3	40	9
MC exp. other BKG events	33.4	28.1	233	121
MC exp. DrellYan events			67	30
MC exp. Zll events			125	31
MC exp. $t\bar{t}V$ events			0.0	0.4
MC exp. Wt events			41	60
fakes events	49.1	6.5	1152	42

Table 4.8: Background fit results for the VRW and VRT regions, for 2011 and 2012 data. Nominal MC expectations (normalised to MC cross-sections) are given for comparison. The errors shown are the statistical plus systematic uncertainties

background in the SR. A good agreement is observed between the observed and predicted event yields.

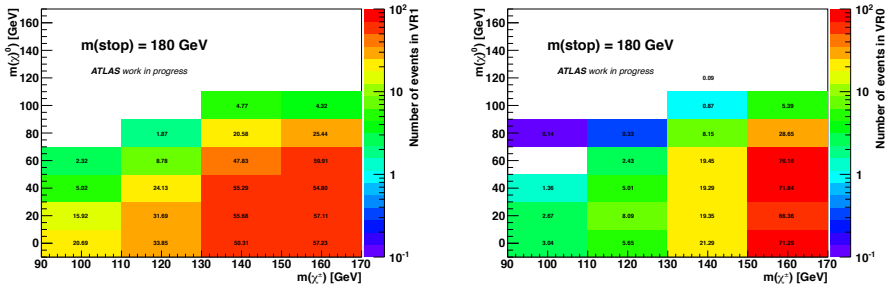

Figure 4.24: Expected signal yield in VRT (left) and VRW (right) as a function of chargino and neutralino masses, for a fixed scalar top mass of 180 GeV, and for 4.7 fb^{-1} of 7 TeV data

4.3.6.4 Validation of the Z+jets background at high m_{T2}

With the strategy described above, the Z+jets background is estimated from Monte Carlo. In order to assess the reliability of the MC simulation of this background at high values of m_{T2}, an additional region dominated by this background is defined.

In figure 4.25 the distribution of the $\Delta\phi_{\rm min}$ and $\Delta\phi_b$ variables is shown for events with same flavor lepton pairs and 71 GeV $< m_{ll} <$ 111 GeV. As it can be seen from the figure, the sample is expected to be dominated by Z+jets events for small (large) values of $\Delta\phi_{\rm min}$ ($\Delta\phi_b$) variable, while at large (small) values WZ and ZZ production is dominant. The CRZ for $WZ + ZZ$ is indeed derived from this sample by applying the additional selections $\Delta\phi_{\rm min} > 1.0$ and $\Delta\phi_b < 1.5$.

The data are in good agreement with the prediction. This proves that the MC simulation describes correctly the rate of Z+jets events for large values of m_{T2}, and the fact that the $\Delta\phi_{\rm min}$ and $\Delta\phi_b$ shapes are well described gives confidence that the Z+jets yield after the cuts on these variables can also be derived from MC.

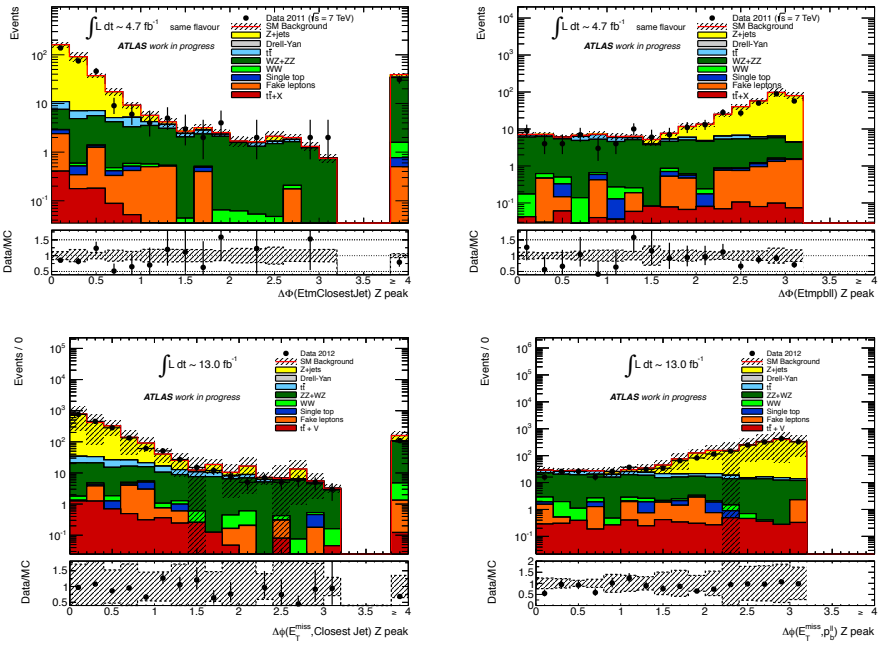

Figure 4.25: Distribution of $\Delta\phi_{\min}$ and $\Delta\phi_b$ for events with same flavor lepton pairs, 71 GeV $< m_{ll} <$ 111 GeV, and $m_{T2} > 90$ GeV, for 4.7 fb^{-1} of 8 TeV data (above) and 13.0 fb^{-1} of 8 TeV data (below)

4.3.6.5 Results of the fit for control and validation regions

The data in the CR have been used to determine the top quark pair, WW, and $WZ+ZZ$ backgrounds scale factors and their yields in the CR, the VR, and the SR. The scale factors for the top, WW, and $WZ + ZZ$ backgrounds which have been derived as a well as the results of the fit for the nuisance parameter are reported in table 4.9.

The scale factor of the $WZ + ZZ$ background in 2012 is lower than unity. This occurs because in 2012 a total of 115 events is observed in CRZ, compared to a MC expected yield of 151 ± 25 events. The main uncertainty on the expected yield is by far the diboson generator uncertainty. The ratio between the total observed and expected rate is thus 0.66 ± 0.14, where the error also included the statistical uncertainty on the observed yield. The observed and expected rate are

thus consistent within 1.7 standard deviations.

The other scale factors are all consistent with unity within their uncertainty.The fit is intended to determine the background normalizations and should not constrain the nuisance parameter. These have indeed all a central value very close to zero (the nominal) and uncertainties close to 1, which indicates no change compared to the original allowed range.

Scale Factor	2011	2012
α(JER)	0.00 ± 1.00	0.00 ± 0.99
α(JES)	-0.01 ± 1.08	0.01 ± 0.96
α(Cellout1)	0.00 ± 0.98	0.00 ± 0.99
α(Cellout2)	0.01 ± 1.01	0.01 ± 0.97
α(pileup)	0.00 ± 0.99	0.00 ± 0.93
α(VVgen)	0.00 ± 1.01	0.00 ± 1.00
α(QCD)	0.00 ± 0.97	0.00 ± 0.92
α(top acer)	0.00 ± 1.00	0.00 ± 0.99
α(top sherpa)	-	0.00 ± 1.00
α(top mc@nlo)	0.00 ± 0.99	-
α(top ISRFSR)	0.00 ± 0.99	0.01 ± 1.03
α(sin. top. ISRFSR)	-	0.01 ± 0.97
α(top PS)	0.00 ± 0.99	0.00 ± 1.00
μ_{Top}	0.95 ± 0.04	1.02 ± 0.04
μ_{WW}	1.08 ± 0.12	1.22 ± 0.20
μ_{WZ+ZZ}	0.90 ± 0.19	0.66 ± 0.14

Table 4.9: Results of the fit: systematic nuisance parameters and scale factors for the $t\bar{t}$, WW, and $WZ + ZZ$ backgrounds. "Cellout1" and "Cellout2" refer to resolution and cluster scale systematics respectively. "VVgen" refers to the diboson generator systematics. "Top PS" refers to the comparison with POWHEG+PYTHIA

4.3.7 Systematic Uncertainties

Various systematic uncertainties affecting the predicted background rates in the signal regions are considered. Such uncertainties are either used directly in the evaluation of the predicted background in the SR when this is derived by MC (Wt, Z+jets, $t\bar{t}+W$ and $t\bar{t}+Z$ production), or to compute the uncertainty on the transfer factor and propagate it to the predicted event yields in the SR when the background is constrained using the fitting method described in section 4.3.6.1 (for $t\bar{t}$ and dibosons).

In addition to these uncertainties also the statistical error coming from the limited MC statistics, which is often denoted as "stat.", has to be considered. Each source of systematics is handled following the latest combined performance group recommendations.

4.3.7.1 Experimental systematics

The following experimental systematic uncertainties were found to be non-negligible:

- **Jet energy scale and resolution**. The uncertainty on the jet energy scale (JES), derived using single particle response and test beam data, varies as a function of the jet p_T and pseudorapidity η [186]. Additional systematic uncertainties arise from the dependence of the jet response on the number of interactions per bunch crossing and on the jet flavor. The components of the jet energy scale uncertainty are varied by $\pm 1\sigma$ in the MC simulation in order to obtain the resulting uncertainty in the event yield.

  Uncertainties related to the jet energy resolution (JER) are obtained with an in-situ measurement of the jet response asymmetry in di-jet events [187]. Their impact on the event yield is estimated by applying an additional smearing to the jet transverse momenta.

  The JES and JER variations applied to the jet momenta are propagated to the E_T^{miss}.

- **Calorimeter cluster energy scale, resolution and pile-up modelling**. The uncertainties related to the contribution to E_T^{miss} from the energy scale and resolution of the calorimeter cells not associated to electrons, muons or

jets, and also from low momentum (7 GeV $< p_T <$ 25 GeV) jets have been evaluated separately and added in quadrature.

In 2011, the uncertainty due to the modelling of pile-up is computed by rescaling the value of the average number μ of proton-proton interactions per bunch crossing used in the pileup reweighting by $\pm 10\%$, and comparing the results with the nominal sample which does not use any rescaling. In 2012, we instead apply the rescaling for the nominal results. The pileup uncertainty is computed by comparing the nominal rates with the results obtained without any rescaling. For both years, the resulting systematic uncertainty is simmetrized.

- **Fake-lepton background uncertainties**. An uncertainty on the fake background is assigned from the comparison of results from different CRs, from the statistics of the control samples used to measure the probabilities to pass the tight selection, and from the statistics of the loose-loose, loose-tight, tight-loose, and tight-tight event samples. The uncertainties on lepton ID measurement and on trigger modelling have a negligible impact on the analysis.

4.3.7.2 Theoretical systematics

The following theoretical systematic uncertainties have been taken into account:

- **Modelling of the diboson background**. The uncertainty associated to the choice of a specific Monte Carlo generator is evaluated comparing the SHERPA and HERWIG samples in the analysis of 2011 data. In the 2012 analysis, SHERPA and POWHEG are compared instead.

- **Modelling of the top pair background**. The predictions of MC@NLO, POWHEG (with two different hadronization simulations), and ACERMC have been compared for the analysis of 2011 data. In the analysis of 2012 data, the predictions of POWHEG (with only one hadronization simulation available), SHERPA and ACERMC are compared instead. We assume that for each selection (CR and SR) used in the analysis, the relative parton shower uncertainty is the same as that calculated for 2011, and we rescale the nominal rates by that amount to evaluate the parton shower and hadronization

systematics.

- **ISR/FSR**. The uncertainty related to ISR and FSR in $t\bar{t}$ events is evaluated considering two different ACERMC samples with varying settings, and taking half of the difference between these samples as systematic uncertainty.

- **Luminosity**. The uncertainty on the luminosity [54] estimated for the whole dataset used in the analysis is taken to be 3.9% for 2011 and 3.6% for 2012, estimated as described in reference [188].

- **Cross section**. The uncertainty related to the cross section value is taken to be 5% for the Z boson production [189]. For $t\bar{t}$, the recommended value of $\sigma_{t\bar{t}} = 167^{+17}_{-18}$ pb at 7 TeV and $\sigma_{t\bar{t}} = 238^{+22}_{-24}$ pb at 8 TeV center of mass energy is used for a top quark mass of 172.5 GeV as obtained from approximate NNLO QCD calculations [134]. The cross section uncertainties for WW, ZZ and WZ are 6%, 5% and 7% respectively [190, 191]. For single top cross sections of 15.7 ± 1.2 pb and 22.4 ± 1.5 are used for the Wt channel at 7 TeV and 8 TeV respectively [192]. For $t\bar{t} + W$ a cross section of $0.168^{+0.023}_{-0.037}$ pb is used for 7 TeV and 0.231 ± 0.046 pb is used for 8 TeV [193]. For $t\bar{t} + Z$ a value of 0.130 ± 0.019 pb is used for 7 TeV and 0.206 ± 0.021 pb is used for 8 TeV [193].

  The uncertainties for $t\bar{t}$ and diboson production cross section do not play any role in the background estimate because these processes are normalized to data in appropriate control regions, but they contribute to the uncertainty on the MC predictions shown in the figures. The uncertainty on Z, single top, and $t\bar{t} + Z$, $t\bar{t} + W$ cross sections contribute to the background uncertainty in the SR but they are negligible compared to other uncertainties, because of the small rates of these backgrounds in the SR.

The breakdown of the background uncertainties in individual sources is reported in tables 4.10 and 4.11. The main uncertainties are MC statistics and the top and diboson theory uncertainty. For the top the largest contribution is the difference between the prediction of POWHEG and ACERMC, and for the dibosons is the difference between SHERPA and POWHEG. The total uncertainty remains between 10% and 30%.

Signal channel,2011	SR90	SR100	SR110
Total statistical ($\sqrt{N_{\text{obs}}}$)	±5.7	±3.9	±3.2
Total background systematic	±4.6 (13.5%)	±3.5 (26.9%)	±1.4 (23.3%)
JES	±1.2 (3.5%)	±0.2 (1.5%)	±0.0 (0.0%)
JER	±0.4 (1.2%)	±0.4 (3.1%)	±0.1 (1.7%)
cellOut1	±0.4 (1.2%)	±0.0 (0.0%)	±0.1 (1.7%)
cellOut2	±0.1 (0.3%)	±0.0 (0.0%)	±0.2 (3.3%)
dibGEN	±1.8 (5.3%)	±1.3 (10.0%)	±0.9 (15.0%)
pileup	±0.2 (0.6%)	±1.2 (9.2%)	±0.8 (13.3%)
qcdSYS	±0.4 (1.2%)	±0.2 (1.5%)	±0.0 (0.0%)
top_ACER	±2.7 (7.9%)	±2.2 (16.9%)	±0.3 (5.0%)
top_GEN	±0.8 (2.4%)	±1.0 (7.7%)	±0.3 (5.0%)
top_ISRFSR	±1.4 (4.1%)	±0.1 (0.8%)	±0.1 (1.7%)
top_PS	±0.2 (0.6%)	±1.1 (8.5%)	±0.2 (3.3%)
MC stat.	±2.4 (7.1%)	±1.2 (9.2%)	±0.6 (10.0%)
mu_Top	±0.7 (2.1%)	±0.2 (1.5%)	±0.0 (0.0%)
mu_WW	±1.1 (3.2%)	±0.6 (4.6%)	±0.4 (6.7%)
mu_WZ_ZZ	±0.8(2.4%)	±0.6 (4.6%)	±0.4 (6.7%)

Table 4.10: Breakdown of the dominant systematic uncertainties on background estimates for the 2011 analysis in the various signal regions. The absolute uncertainty and, in parenthesis, the relative uncertainty are given. Note that the individual uncertainties can be correlated, and do not necessarily add up quadratically to the total background uncertainty. "top ACER" refer to the comparison of the nominal POWHEG+PYTHIA sample with ACERMC. "top GEN" refer to the comparison with MC@NLO sample. "top PS" refer to the comparison of the nominal $t\bar{t}$ sample with POWHEG+JIMMY respectively. "top ISRFSR" refer to the ISR/FSR uncertainty for top samples. The "mu" term refer to the uncertainty on the data-driven normalizations. "dibGEN" is the diboson generator uncertainty

Signal channel, 2012	SR90	SR100	SR110
Total statistical ($\sqrt{N_{\text{obs}}}$)	±13.34	±6.63	±4.69
Total back. syst.	±30.91 (13.8%)	±13.02 (20.3%)	±8.63 (27.8%)
alpha_JER	±3.93 (1.8%)	±1.67 (2.6%)	±0.98 (3.2%)
alpha_JES	±9.96 (4.4%)	±0.60 (0.9%)	±2.74 (8.8%)
alpha_Wt_ISRFSR	±0.21 (0.1%)	±0.03 (0.0%)	±0.00 (0.0%)
alpha_cellOut1	±0.02 (0.0%)	±0.24 (0.4%)	±2.74 (8.8%)
alpha_cellOut2	±4.88 (2.2%)	±1.05 (1.6%)	±2.46 (7.9%)
alpha_dibGEN	±3.90 (1.7%)	±5.70 (8.9%)	±4.70 (15.2%)
alpha_pileup	±15.95 (7.1%)	±3.77 (5.9%)	±0.34 (1.1%)
alpha_qcdSYS	±1.53 (0.7%)	±0.77 (1.2%)	±0.21 (0.7%)
alpha_top_ACER	±17.85 (8.0%)	±2.89 (4.5%)	±0.05 (0.2%)
alpha_top_GEN	±0.22 (0.1%)	±0.40 (0.6%)	±0.91 (2.9%)
alpha_top_ISRFSR	±8.50 (3.8%)	±1.66 (2.5%)	±0.27 (0.9%)
alpha_top_PS	±6.09 (2.7%)	±7.13 (11.1%)	±1.29 (4.2%)
gamma_stat_SR100	±7.93 (3.5%)	±5.46 (8.5%)	±4.17 (13.5%)
mu_Top	±5.68 (2.5%)	±0.89 (1.4%)	±0.16 (0.5%)
mu_WW	±8.45 (3.8%)	±3.83 (6.0%)	±2.41 (7.8%)
mu_WZ_ZZ	±1.78 (0.8%)	±1.34 (2.1%)	±1.00 (3.2%)

Table 4.11: Breakdown of the dominant systematic uncertainties on background estimates for the 2012 analysis in the various signal regions. The absolute uncertainty and, in parenthesis, the relative uncertainty are given. Note that the individual uncertainties can be correlated, and do not necessarily add up quadratically to the total background uncertainty. "top ACER" refer to the comparison of the nominal POWHEG+PYTHIA sample with ACERMC. "top GEN" refer to the comparison with SHERPA sample. "top PS" refer to the comparison of the nominal $t\bar{t}$ sample with POWHEG+JIMMY respectively. "top ISRFSR" refer to the ISR/FSR uncertainty for top samples. The "mu" term refer to the uncertainty on the data-driven normalizations. "dibGEN" is the diboson generator uncertainty

channel 2011	$SR90$	$SR100$	$SR110$
Observed events	32	15	10
Fitted bkg events	34 ± 5	13 ± 4	6.0 ± 1.4
Fitted top events	17 ± 4	4 ± 3	0.6 ± 0.6
Fitted WW events	9.5 ± 2.4	5.2 ± 1.4	3.5 ± 1.0
Fitted WZ-ZZ events	3.3 ± 0.8	2.5 ± 0.6	1.8 ± 0.4
Fitted other BKG events	2.0 ± 0.3	0.5 ± 0.2	0.11 ± 0.04
Fitted fakes events	2.0 ± 1.1	0.8 ± 0.6	$0.00^{+0.29}_{-0.00}$
MC exp. SM events	33.49	11.95	5.57
MC exp. top events	17.91	3.69	0.62
MC exp. WW events	8.25	4.48	3.00
MC exp. WZ-ZZ events	3.40	2.57	1.91
MC exp. other BKG events	2.03	0.47	0.11
fakes events	2.00	0.82	0.00

Table 4.12: Background fit results for the SR90,SR100 and SR110 regions, for an integrated luminosity of 4.7 fb^{-1} at 7 TeV center of mass energy. Nominal MC expectations (normalized to MC cross sections) are given for comparison. The errors shown are the statistical plus systematic uncertainties

4.3.8 Results, it's interpretation and limit setting

In tables 4.12 and 4.13 the number of events observed in the SR is reported and compared to the total expected background. The individual background components, determined as discussed in section 4.3.6, are also reported.

The number of events observed in each SR in 2012 is compared with the SM expectations using frequentist significance tests.

We define a likelihood function $\mathcal{L}(n_s)$ as follows:

$$\mathcal{L}(n_s; \mu, b, \theta) = \text{Poiss}(n_s | s(\mu, b, \theta)) \times N_{\text{syst}}(\theta_0, \theta) \tag{4.23}$$

Poiss(n_s) is a Poisson probability density function (pdf) describing the expected

channel 2012	$SR90$	$SR100$	$SR110$
Observed events	178	44	22
Fitted bkg events	224 ± 31	64 ± 13	31 ± 8
Fitted top events	134 ± 24	21 ± 9	3.8 ± 1.9
Fitted WW events	51 ± 11	23 ± 7	15 ± 5
Fitted WZ-ZZ events	8.4 ± 1.9	6.3 ± 1.8	4.7 ± 1.4
Fitted DY events	2.1 ± 2.9	0.3 ± 0.6	0
Fitted Zll	6 ± 5	6 ± 5	4 ± 6
Fitted ttV events	1.5 ± 0.3	0.9 ± 0.2	0.6 ± 0.2
Fitted Wt events	11 ± 5	1.8 ± 1.9	1.4 ± 0.8
Fitted fakes events	9.6 ± 2.8	3.7 ± 1.4	1.4 ± 0.8
MC exp. SM events	215.4	62.2	30.2
MC exp. top events	131.4	20.7	3.7
MC exp. WW events	41.6	18.9	11.9
MC exp. WZ-ZZ events	12.6	9.5	7.1
MC exp. DrellYan events	2.07	0.28	0.00
MC exp. Zll events	6.24	6.24	3.77
MC exp. ttV events	1.51	0.94	0.60
MC exp. Wt events	10.61	1.78	1.44
fakes events	9.3	4.0	1.6

Table 4.13: Background fit results for the SR90,SR100 and SR110 regions, for an integrated luminosity of 13.0 fb^{-1} at 8 TeV center of mass energy (below). Nominal MC expectations (normalized to MC cross sections) are given for comparison. The errors shown are the statistical plus systematic uncertainties

event counts n_s in each signal region, given the expectation s. μ is the SUSY signal strength to be tested, b is the number of background events, and θ describes the systematic uncertainties as nuisance parameters. N_{syst} models all the different systematic uncertainties described in the previous section. Each parameter θ can be varied around the nominal values θ_0.

The cross section and PDF uncertainty are not included, but limits are quoted for the nominal cross section and for the cross section changed by one standard deviation of the theoretical error. In order to estimate the cross section uncertainty, an envelope of cross section predictions is defined using the 68% C.L. ranges of CTEQ6.6 [130] (including the α_S uncertainty) and MRSTW2008 NNLO [194] PDF sets, together with independent variations of the factorization and renormalization scales by factors of two and one half. The nominal cross section value is taken to be the midpoint of the envelope and the uncertainty assigned is half the full width of the envelope, closely following the PDF4LHC recommendations.

The uncertainties are modeled with a convolution of Gaussian pdfs describing the uncertainties on the signal or on the backgrounds. Uncertainties which affects both the background and the signal are considered as completely correlated. The summary of all uncertainties that affect the background estimates is reported in the tables 4.10 and 4.11.

First, model independent limits at 95% of C.L. are derived on the product $\sigma \times \epsilon \times \mathcal{A}$, where σ is the non-SM cross section, ϵ the selection efficiency, and $\mathcal{A}$ the acceptance of kinematic cuts. These limits are derived for each SR and shown in table 4.14. Only background uncertainties are considered for the model independent limits.

	SR90	SR100	SR110
σ_{vis}^{obs}[fb] (8 TeV)	3.29	1.39	1.18
σ_{vis}^{exp}[fb] (8 TeV)	5.39	2.39	1.58

Table 4.14: Observed and expected upper limits at 95% confidence level on $\sigma \times \epsilon \times \mathcal{A}$

Limits are then placed on the mass of the scalar top, lightest chargino, and $\tilde{\chi}_1^0$ masses, assuming a 100% BR for the decay of the scalar top into $\tilde{\chi}^{\pm} b$. For each signal hypothesis, the SR with the best expected limit is used. In figure 4.26 the

expected (dashed line) and observed (solid line) 95% C.L. limits are reported as a function of the scalar top and chargino masses, for a massless neutralino. The colored band is the $\pm 1\sigma$ band around the expected limit. In the upper plot the limits is reported on the chargino and scalar top mass for a massless neutralino. The sensitivity improves with increasing chargino mass, and it is maximum for a chargino just below the scalar top (minus the b-quark) mass. In the middle plot the limits are shown on the neutralino and scalar top masses for a fixed value of $m(\tilde{t}) - m(\tilde{\chi}_1^{\pm}) = 10$ GeV. In the bottom plot the limit is shown on the neutralino and chargino masses for a fixed 300 GeV scalar top mass.

In conclusion, a supersymmetric scalar top $\tilde{t}$ with a mass between 150 and 450 GeV decaying with 100% BR to a b quark and a chargino is excluded at 95% CL for a chargino approximately degenerate with the scalar top and a massless lightest neutralino. Figure 4.27 shows the summary of the dedicated ATLAS searches for stop decaying to a chargino and a b-quark based on 13 fb^{-1} of proton-proton collision data taken at $\sqrt{s} = 8$ TeV and 4.7 fb^{-1} of proton-proton collision data taken at $\sqrt{s} = 7$ TeV (already shown in figure 4.5), including the analysis described in this chapter (light blue, see also figure 4.26 top-right).

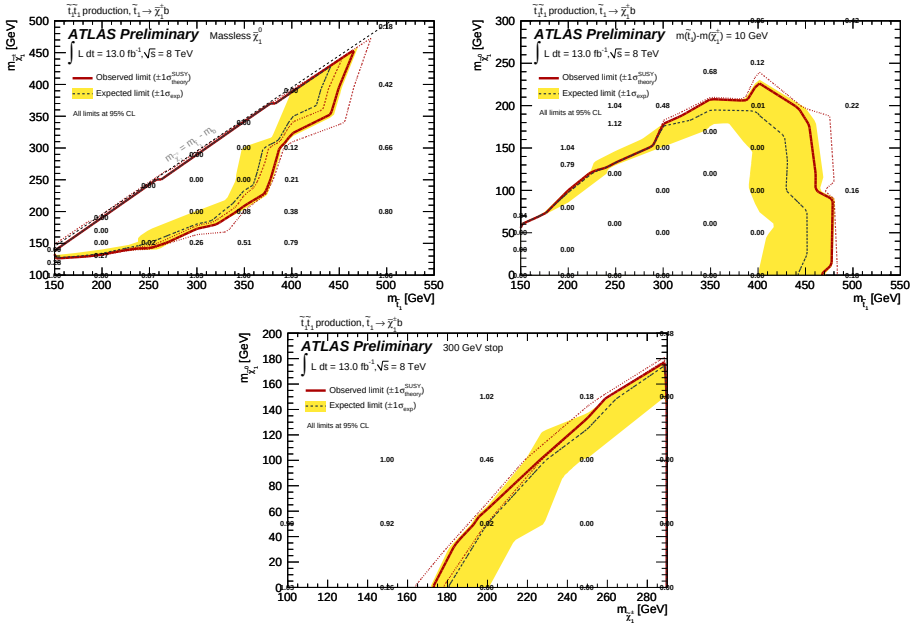

Figure 4.26: Expected 95% CL limits on the masses of the scalar top , $\tilde{\chi}_1^{\pm}$, and $\tilde{\chi}_1^0$, from the analysis of 13.0 fb^{-1} of 8 TeV collisions data. Top: limits on the chargino and scalar top mass for a massless neutralino. Middle: limits on the neutralino and scalar top masses for a fixed value of $m(\tilde{t}) - m(\tilde{\chi}_1^{\pm}) = 10$ GeV. Bottom: limits on neutralino and chargino masses for a fixed 300 GeV stop mass

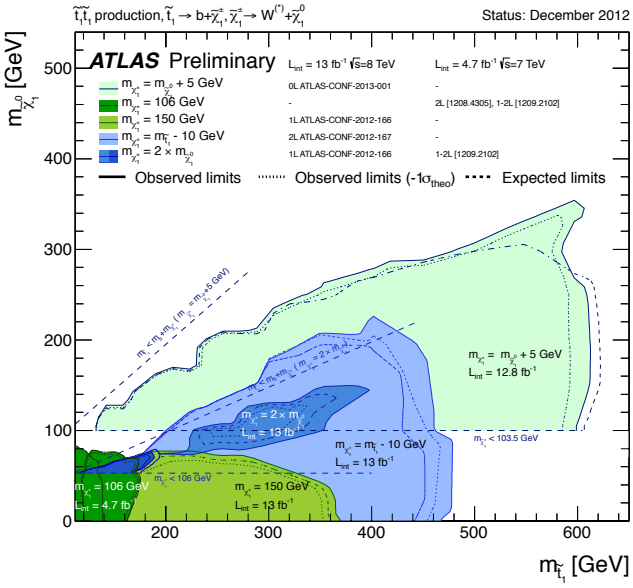

Figure 4.27: Summary of the dedicated ATLAS searches for stop decaying to a chargino and a b-quark based on 13 fb^{-1} of proton-proton collision data taken at $\sqrt{s} = 8$ TeV and 4.7 fb^{-1} of proton-proton collision data taken at $\sqrt{s} = 7$ TeV, including the analysis described in this chapter (light blue)

Bibliography

[1] A. Favareto, *Performance of the track reconstruction in proton-proton collision with the ATLAS detector at the LHC*, in *XCIV Congresso Nazionale della Societá Italiana di Fisica*. 21 - 25 September 2010, Bologna, Italy.

[2] A. Favareto, *Charged track reconstruction and b-tagging performance in ATLAS*, in *LHC on the March*, vol. PoS (IHEP-LHC-2011) 002; ATL-PHYS-PROC-2012-117. 16 - 18 November 2011, Protvino, Russia.

[3] A. Favareto, *Status of the ATLAS Pixel Detector at the LHC and its performance after three years of operation*, in *Frontier Detectors For Frontier Physics*, vol. ATL-INDET-PROC-2012-010. 20 - 26 May 2012, La Biodola, Isola d'Elba, Italy.

[4] L. Evans and P. Bryant, *LHC Machine*, J. Instrum. **3** (2008) S08001.

[5] `https://twiki.cern.ch/twiki/bin/view/AtlasPublic/LuminosityPublicResults`.

[6] ALICE Collaboration, *The ALICE experiment at the CERN LHC*, J. Instrum. **3** (2008) S08002.

[7] ATLAS Collaboration, *The ATLAS Experiment at the CERN Large Hadron Collider*, J. Instrum. **3** (2008) S08003. 437 p.

[8] CMS Collaboration, *The CMS experiment at the CERN LHC*, J. Instrum. **3** (2008) S08004.

[9] LHCb Collaboration, *The LHCb Detector at the LHC*, J. Instrum. **3** (2008) S08005.

[10] ATLAS Collaboration, *Measurement of inclusive jet and dijet production in pp collisions at $\sqrt{s}$ = 7 TeV using the ATLAS detector*, Phys. Rev. D **86** (2011).

[11] ATLAS Collaboration, *Measurement of the inclusive and dijet cross-sections of b-jets in pp collisions at $\sqrt{s}$ = 7 TeV with the ATLAS detector*, Eur. Phys. J. C **71** (2011).

[12] ATLAS Collaboration, *Measurement of the cross-section for b-jets produced in association with a Z boson at $\sqrt{s}$=7 TeV with the ATLAS detector*, Phys. Lett. B **706** (2011).

[13] ATLAS Collaboration, *Measurement of multi-jet cross sections in proton-proton collisions at a 7 TeV center-of-mass energy*, Eur. Phys. J. C **71** (2011).

[14] ATLAS Collaboration, *Measurement of the production cross section for W-bosons in association with jets in pp collisions using 33 pb^{-1} at $\sqrt{s}$ = 7 TeV with the ATLAS detector*, ATLAS-CONF-2011-060 (2011).

[15] ATLAS Collaboration, *Measurement of the production cross section for Z/γ^* in association with jets in pp collisions at $\sqrt{s}$ = 7 TeV with the ATLAS detector*, Phys. Rev. D **85** (2011).

[16] ATLAS Collaboration, *A measurement of the ratio of the W and Z cross sections with exactly one associated jet in pp collisions at $\sqrt{(s)}$ = 7 TeV with ATLAS*, Phys. Lett. B **708** (2011).

[17] ATLAS Collaboration, *Measurement of the cross section for the production of a W boson in association with b-jets in pp collisions at $\sqrt{s}$ = 7 TeV with the ATLAS detector*, Phys. Lett. B **707** (2011).

[18] ATLAS Collaboration, *Measurement of the cross-section for b-jets produced in association with a Z boson at $\sqrt{s}$=7 TeV with the ATLAS detector*, Phys. Lett. B **706** (2011).

[19] ATLAS Collaboration, *Measurement of $W\gamma$ and $Z\gamma$ production in proton-proton collisions at $\sqrt{s}$ = 7 TeV with the ATLAS Detector*, J. High Energy Phys. **09** (2011).

[20] ATLAS Collaboration, *Measurement of the W^+W^- Production Cross Section in Proton-Proton Collisions at $\sqrt{s}$ = 7 TeV with the ATLAS Detector*, ATLAS-CONF-2012-025 (2012).

[21] ATLAS Collaboration, *Measurement of WZ production in proton-proton collisions at $\sqrt{s}$ = 7 TeV with the ATLAS detector*, CERN-PH-EP-2012-179 (2012).

[22] ATLAS Collaboration, *Measurement of the ZZ production cross section and limits on anomalous neutral triple gauge couplings in proton-proton collisions at $\sqrt{s}$ = 7 TeV with the ATLAS detector*, Phys. Rev. Lett. **108** (2011).

[23] ATLAS Collaboration, *Measurement of the transverse momentum distribution of Z/γ^* bosons in proton-proton collisions at $\sqrt{s}$=7 TeV with the ATLAS detector*, Phys. Lett. B **705** (2011).

[24] ATLAS Collaboration, *Measurement of the Transverse Momentum Distribution of W Bosons in pp Collisions at $\sqrt{s}$ = 7 TeV with the ATLAS Detector*, Phys. Rev. D **85** (2011).

[25] ATLAS Collaboration, *Measurement of the W charge asymmetry in the $W \to \mu\nu$ decay mode in pp collisions at $\sqrt{s}$ = 7 TeV with the ATLAS detector*, Phys. Lett. B **701** (2011).

[26] Richard D. Ball, Valerio Bertone, Francesco Cerutti, Luigi Del Debbio, Stefano Forte, Alberto Guffanti, Nathan P. Hartland, Jose I. Latorre, Juan Rojo, Maria Ubiali, *Reweighting and Unweighting of Parton Distributions and the LHC W lepton asymmetry data*, arXiv:1108.1758v1.

[27] ATLAS Collaboration, *Measurement of the t-channel single top-quark production cross section in pp collisions at $\sqrt{s}$ = 7 TeV with the ATLAS detector*, Phys. Lett. B **717** (2012).

[28] ATLAS Collaboration, *Measurement of the top quark pair cross section with ATLAS in pp collisions at $\sqrt{s}$ = 7 TeV using final states with an electron or a muon and a hadronically decaying tau lepton*, Phys. Lett. B (2012).

[29] ATLAS Collaboration Collaboration, ATLAS Collaboration, *Measurement of the top quark mass with the template method in the $t\bar{t} \to$ lepton + jets channel using ATLAS data*, Eur.Phys.J. **C72** (2012) 2046.

[30] ATLAS Collaboration, *Observation of spin correlation in $t\bar{t}$ events from pp collisions at $\sqrt{s}$ = 7 TeV using the ATLAS detector*, Phys. Rev. Lett. **108** (2012).

[31] ATLAS Collaboration, *A search for $t\bar{t}$ resonances with the ATLAS detector in 2.05 fb^{-1} of proton-proton collisions at $\sqrt{(}s)$ = 7 TeV*, Eur. Phys. J. C **72** (2012).

[32] ATLAS Collaboration, *Measurement of the charge asymmetry in top quark pair production in pp collisions at $\sqrt{s}$ = 7 TeV using the ATLAS detector*, Eur. Phys. J. C **72** (2012).

[33] LEP Working Group for Higgs boson searches, ALEPH Collaboration, DELPHI Collaboration, L3 Collaboration, OPAL Collaboration and LEP Working Group for Higgs Boson Searches, *Search for the standard model Higgs boson at LEP*, Phys.Lett. **B565** (2003).

[34] CDF and DØ Collaborations, *Combined CDF and DØ Upper Limits on Standard Model Higgs Boson Production with up to 8.6 fb^{-1} of Data*, `arXiv:1107.5518`.

[35] ATLAS Collaboration, *Observation of a new particle in the search for the Standard Model Higgs boson with the ATLAS detector at the LHC*, Phys. Lett. B **716** (2012).

[36] CMS Collaboration, *Observation of a new boson at a mass of 125 GeV with the CMS experiment at the LHC*, Phys. Lett. B **716** (2012).

[37] ATLAS Collaboration, *Search for squarks and gluinos using final states with jets and missing transverse momentum with the ATLAS detector in $\sqrt{s}$ = 7 TeV proton-proton collisions*, Phys. Lett. B **710** (2011).

[38] ATLAS Collaboration, *Search for supersymmetry in final states with jets, missing transverse momentum and one isolated lepton in $\sqrt{s}$ = 7 TeV pp collisions using 1 fb^{-1} of ATLAS data*, Phys. Rev. D **85** (2011).

[39] ATLAS Collaboration, *Search for supersymmetry in pp collisions at $\sqrt{s}$ = 7 TeV in final states with missing transverse momentum and b-jets with the ATLAS detector*, Phys. Rev. D **85** (2012).

[40] ATLAS Collaboration, *Observation of a Centrality-Dependent Dijet Asymmetry in Lead-Lead Collisions at $\sqrt{s_{NN}}$ = 2.76 TeV with the ATLAS Detector at the LHC*, Phys. Rev. Lett. **105** (2010).

[41] ATLAS Collaboration, *Readiness of the ATLAS Liquid Argon Calorimeter for LHC Collisions*, Eur. Phys. J. C **70** (2010).

[42] ATLAS Collaboration, *Readiness of the ATLAS Tile Calorimeter for LHC collisions*, Eur. Phys. J. C **70** (2010).

[43] ATLAS Collaboration, *Performance of the ATLAS Silicon Pattern Recognition Algorithm in Data and Simulation at $\sqrt{s} = 7$ TeV*, ATLAS-CONF-2010-072 (2010).

[44] ATLAS Collaboration, *Charged-particle multiplicities in pp interactions measured with the ATLAS detector at the LHC*, New J. Phys. **13** (2010).

[45] ATLAS Collaboration, *Measurement of the centrality dependence of J/ψ yields and observation of Z production in lead-lead collisions with the ATLAS detector at the LHC*, Phys.Lett. **B697** (2011) 294–312.

[46] ATLAS Collaboration, *Performance of primary vertex reconstruction in proton-proton collisions at $\sqrt{s}$ =7 TeV in the ATLAS experiment*, ATLAS-CONF-2010-069 (2010).

[47] `https://twiki.cern.ch/twiki/bin/view/AtlasPublic/InDetTrackingPerformanceApprovedPlots`.

[48] ATLAS Collaboration, *Mapping the material in the ATLAS Inner Detector using secondary hadronic interactions in 7 TeV collisions*, ATLAS-CONF-2010-058 (2010).

[49] ATLAS Collaboration, *A study of the material in the ATLAS inner detector using secondary hadronic interactions*, J. Instrum. **7** (2011).

[50] ATLAS Collaboration, *Alignment of the ATLAS Inner Detector Tracking System with 2010 LHC proton-proton collisions at sqrts = 7 TeV*, ATLAS-CONF-2011-012 (2011).

[51] ATLAS Collaboration, *The ATLAS Inner Detector commissioning and calibration*, Eur. Phys. J. C **70** (2010).

[52] A. Andreazza, V. Kostyukhin, and R. J. Madaras, *Survey of the ATLAS Pixel Detector Components*, ATL-INDET-PUB-2008-012; ATL-COM-INDET-2008-006 (2008).

[53] ATLAS Collaboration, *Commissioning of the ATLAS Muon Spectrometer with Cosmic Rays*, Eur. Phys. J. C **70** (2010).

[54] *Improved Luminosity Determination in* **pp** *Collisions at* $\sqrt{s}$ *= 7 TeV using the ATLAS Detector at the LHC*, ATLAS-CONF-2012-080 (2012).

[55] ATLAS Collaboration, *Expected performance of the ATLAS experiment: detector, trigger and physics*, CERN-OPEN-2008-020 (2009).

[56] W. Lampl, S. Laplace, D. Lelas, P. Loch, H. Ma, S. Menke, S. Rajagopalan, D. Rousseau, S. Snyder, and G. Unal, *Calorimeter Clustering Algorithms: Description and Performance*, ATL-LARG-PUB-2008-002; ATL-COM-LARG-2008-003 (2008).

[57] ATLAS Collaboration, *Electron and photon reconstruction and identification in ATLAS: expected performance at high energy and results at 900 GeV*, ATLAS-CONF-2010-005 (2010).

[58] D. Banfi, L. Carminati, and L. Mandelli, *Calibration of the ATLAS electromagnetic calorimeter using calibration hits*, ATL-LARG-PUB-2007-012; ATL-COM-LARG-2007-007 (2007).

[59] `https://twiki.cern.ch/twiki/bin/view/AtlasPublic/ElectronGammaPublicCollisionResults`.

[60] S. Hassani, L. Chevalier, E. Lancon, J. F. Laporte, R. Nicolaidou and A. Ouraou, *A muon identification and combined reconstruction procedure for the ATLAS detector at the LHC using the (MUONBOY, STACO, MuTag) reconstruction packages*, Nucl. Instrum. Meth. **A572** (2007) 77.

[61] T. Lagouri et al., *A muon identification and combined reconstruction procedure for the ATLAS detector at the LHC at CERN*, IEEE Trans. Nucl. Sci. **51** (2004) 3030–3033.

[62] ATLAS Collaboration, *Muon Performance in Minimum Bias pp Collision Data at $\sqrt{s}$ = 7 TeV with ATLAS*, ATLAS-CONF-2010-036 (2010).

[63] `https://twiki.cern.ch/twiki/bin/view/Atlas/MuonPerformancePublicPlots`.

[64] M. Cacciari, G. P. Salam, and G. Soyez, *The Anti-k(t) jet clustering algorithm*, JHEP **0804** (2008) 063.

[65] ATLAS Collaboration, *Measurement of the top quark pair production cross section in pp collisions at $\sqrt{s}$ = 7 TeV in dilepton final states with ATLAS*, Phys. Lett. B **707** (2011) 459–477.

[66] *Calibrating the b-Tag Efficiency and Mistag Rate in 35 pb^{-1} of Data with the ATLAS Detector*, ATLAS-CONF-2011-089 (2011).

[67] ATLAS Collaboration, *Commissioning of the ATLAS high-performance b-tagging algorithms in the 7 TeV collision data*, ATLAS-CONF-2011-102 (2011).

[68] ATLAS Collaboration, *Impact parameter-based b-tagging algorithms in the 7 TeV collision data with the ATLAS detector: the TrackCounting and JetProb algorithms*, ATLAS-CONF-2010-041 (2010).

[69] ATLAS Collaboration, *Performance of the ATLAS Secondary Vertex b-tagging Algorithm in 7 TeV Collision Data*, ATLAS-CONF-2010-042 (2010).

[70] ATLAS Collaboration, *b-Jet Tagging Efficiency Calibration using the System8 Method*, ATLAS-CONF-2011-143 (2011).

[71] ATLAS Collaboration, *Performance of Missing Transverse Momentum Reconstruction in Proton-Proton Collisions at $\sqrt{s}$ = 7 TeV with ATLAS*, Eur. Phys. J. C **72** (2011) 1844.

[72] T. Cornelissen, M. Elsing, S. Fleischmann, W. Liebig, E. Moyse, and A. Salzburger, *Concepts, Design and Implementation of the ATLAS New Tracking (NEWT)*, ATL-SOFT-PUB-2007-007. ATL-COM-SOFT-2007-002 (2007).

[73] F. Akesson, M. J. Costa, D. Dobos, M. Elsing, S. Fleischmann, A. Gaponenko, K. Gnanvo, P. T. Keener, W. Liebig, E. Moyse, A. Salzburger, M. Siebel, and A. Wildauer, *ATLAS Inner Detector Event Data Model*, ATL-SOFT-PUB-2007-006. ATL-COM-SOFT-2007-015 (2007).

[74] R. Fruhwirth, *Application of Kalman filtering to track and vertex fitting*, Nucl.Instrum.Meth. **A262** (1987) 444–450.

[75] R. Fruhwirth, *Track fitting with nonGaussian noise*, Comput.Phys.Commun. **100** (1997) 1–16.

[76] Frühwirth, R. and Strandlie, A., *Track fitting with ambiguities and noise: a study of elastic tracking and nonlinear filters*, Computer Physics Communications **120** (1999) 197–214.

[77] R. Bock, H. Grote, D. Notz, M. Regler, and e. Regler, M., *Data analysis techniques for high-energy physics experiments*, Camb.Monogr.Part.Phys.Nucl.Phys.Cosmol. **11** (2000) 1–434.

[78] J. Beringer et al. (Particle Data Group), *The Review of Particle Physics*, Phys. Rev. D **86** (2012) 010001.

[79] F. P. Machefert, C. Guyot, J. P. Schuller, and P. Schune, *Calibration of a RASNIK system for the ATLAS Muon Spectrometer*, ATL-MUON-2001-010 (2001).

[80] Blum W, Kroha H and Widmann P, *A novel laser-alignment system for tracking detectors using transparent silicon strip sensors*, Nucl. Instrum. Methods **A** no. 367, (1995) 413–7.

[81] Blum W, Kroha H and Widmann P, *Transparent silicon strip sensors for the optical alignment of particle detector systems*, Nucl. Instrum. Methods **A** no. 377, (1996) 404–8.

[82] P. F. Åkesson, T. Atkinson, M. J. Costa, M. Elsing, S. Fleischmann, A. N. Gaponenko, W. Liebig, E. Moyse, A. Salzburger, and M. Siebel, *ATLAS Tracking Event Data Model*, ATL-SOFT-PUB-2006-004. ATL-COM-SOFT-2006-005. CERN-ATL-COM-SOFT-2006-005 (2006).

[83] R. Duda and P. Hart, *Use of the Hough Transformation to Detect Lines and Curves in Pictures*, ACM **15** (1972).

[84] ATLAS Collaboration, *Tracking Results and Comparison to Monte Carlo simulation at* $\sqrt{s} = 900\ GeV$, ATLAS-CONF-2010-011 (2010).

[85] M. Capeans, G. Darbo, K. Einsweiller, M. Elsing, T. Flick, M. Garcia-Sciveres, C. Gemme, H. Pernegger, O. Rohne, and R. Vuillermet, *ATLAS Insertable B-Layer Technical Design Report*, CERN-LHCC-2010-013. ATLAS-TDR-019 (2010).

[86] ATLAS Collaboration, *Data-Quality Requirements and Event Cleaning for Jets and Missing Transverse Energy Reconstruction with the ATLAS Detector in Proton-Proton Collisions at a Center-of-Mass Energy of* $sqrts = 7\ TeV$, ATLAS-CONF-2010-038 (2010).

[87] B.P. Kersevan and E. Richter-Was, *The Monte Carlo event generator AcerMC version 2.0 interfaces to PYTHIA 6.2 and HERWIG 6.5*, TPJU-6/2004 (2004).

[88] ATLAS Collaboration, *Tracking Studies for b-tagging with 7 TeV Collision Data with the ATLAS Detector*, ATLAS-CONF-2010-070 (2010).

[89] ATLAS Collaboration, *Measurement of the Mistag Rate with 5* fb^{-1} *of Data Collected by the ATLAS Detector*, ATLAS-CONF-2012-040 (2012).

[90] S. W. Herb et al., *Observation of a Dimuon Resonance at 9.5 GeV in 400 GeV Proton-Nucleus Collisions*, Phys. Rev. Lett. **39** (1977) 252.

[91] G. 't Hooft and M. Veltman, *Regularization and Renormalization of Gauge Fields*, Nucl. Phys. B **44** (1972) 189.

[92] ALEPH Collaboration, DELPHI Collaboration, L3 Collaboration, OPAL Col- laboration, and SLD Collaboration, LEP Electroweak Working Group and SLD electroweak and Heavy Flavour Group, *Precision Electroweak Measurements on the Z Resonance*, Phys. Rep. **427** (2006) 257.

[93] CDF Collaboration, *Observation of Top Quark Production in $\bar{P} - P$ Collisions*, Phys. Rev. Lett. **74** (1995) 2626.

[94] DØ Collaboration, *Observation of the Top Quark*, Phys. Rev. Lett. **74** (1974) 2632.

[95] H1 Collaboration, *Measurement of the proton structure function $F_2(x, Q^2)$ in the low x region at HERA*, Nucl. Phys. **B407** (1993) 515.

[96] H1 Collaboration, *Inclusive measurement of diffractive deep inelastic ep scattering*, Z. Phys. C **76** (1997) 613.

[97] H1 Collaboration, *A Measurement and QCD Analysis of the Proton Structure Function $F_2(x, Q^2)$ at HERA*, Nucl. Phys. **B470** (1996) 3.

[98] H1 Collaboration, *Deep inelastic inclusive ep scattering at low x and a determination of α_s*, Eur. Phys. J. **C21** (2001) 33.

[99] ZEUS Collaboration, *Measurement of the proton structure function F_2 in e^+p scattering at HERA*, Phys. Lett. B **316** (1993) 412.

[100] ZEUS Collaboration, *Measurement of the F_2 structure function in deep inelastic e^+p scattering using 1994 data from the ZEUS detector at HERA*, Z. Phys. C **72** (1996) 399.

[101] ZEUS Collaboration, *Comparison of ZEUS data with standard model predictions for $e^+p \to e^+X$ scattering at high x and Q^2*, Z. Phys. C **74** (1997) 207.

[102] H.-L. Lai et al., *New parton distributions for collider physics*, Phys. Rev. D **82** (2010).

[103] H1 and ZEUS Collaboration, *Combined Measurement and QCD Analysis of the Inclusive $e^{\pm}p$ Scattering Cross Sections at HERA*, JHEP **1001** (2010) 109.

[104] S. Moch and P. Uwer, *Theoretical status and prospects for top-quark pair production at hadron colliders*, Phys. Rev. D **78** (2008).

[105] U. Langenfeld, S. Moch, and P. Uwer, *New results for $t\bar{t}$ production at hadron colliders*, DESY-09-104; SFB/CPP-09-61; HU-EP-09/31 (2009).

[106] M. Beneke et al., *Threshold expansion of the $gg(q\bar{q}) \to Q\bar{Q} + X$ cross section at $\mathcal{O}(\alpha_s^4)$*, Phys. Lett. B **690(5)** (2010) 483.

[107] `https://twiki.cern.ch/twiki/pub/AtlasPublic/CombinedSummaryPlots/`.

[108] `https://twiki.cern.ch/twiki/pub/CMSPublic/PhysicsResultsTOPSummaryPlots/`.

[109] Tevatron Electroweak Working Group, CDF and DØ Collaborations, *Combination of CDF and DØ results on the mass of the top quark using up to 5.8 $\sim fb^{-}1$ of data*, FERMILAB-TM-2504-E, CDF-NOTE-10549, D0-NOTE-6222 (2011).

[110] CMS Collaboration, *Top mass combination*, CMS-PAS-TOP-11-018 (2012).

[111] Paola Ferrario and German Rodrigo, *Charge asymmetry of top quarks*, PoS (DIS 2010) 191.

[112] Biplob Bhattacherjee and Sudhansu S. Biswal and Diptimoy Ghosh, *Top quark forward-backward asymmetry at Tevatron and its implications at the LHC*, Phys. Rev. D **83** (2011) 091501(R).

[113] L. G. Almeida, G. F. Sterman and W. Vogelsang, *Threshold Resummation for the Top Quark Charge Asymmetry*, Phys. Rev. D **78** (2008) 014008.

[114] O. Antunano, J. H. Kuhn, and G. V. Rodrigo, *Top Quarks, Axigluons and Charge Asymmetries at Hadron Colliders*, Phys. Rev. D **77** (2008) 014003.

[115] M. T. Bowen, S. D. Ellis, and D. Rainwater, *Standard model top quark asymmetry at the Fermilab Tevatron*, Phys. Rev. D **73** (2006) 014008.

[116] Johann H. Kuhn and German Rodrigo, *Charge asymmetries of top quarks at hadron colliders revisited*, LPN11-52; TTP11-26; IFIC/11-45 (2011).

[117] J. A. Aguilar-Saavedra and M. Pérez-Victoria, *Probing the Tevatron $t\bar{t}$ asymmetry at LHC*, JHEP **1105** (2011) 034.

[118] J. A. Aguilar-Saavedra and M. Pérez-Victoria, *Asymmetries in $t\bar{t}$ production: LHC versus Tevatron*, arXiv:1105.4606 [hep-ph] (2011).

[119] J.F. Arguin, M. Freytsis, Z. Ligeti, *Comment on measuring the $t\bar{t}$ forward-backward asymmetry at ATLAS and CMS*, Phys.Rev. D **84** (2011) 071504.

[120] CDF Collaboration, *Evidence for a Mass Dependent Forward-Backward Asymmetry in Top Quark Pair Production*, Phys. Rev. D **83** (2011) 112003.

[121] DØ Collaboration, *Forward-backward asymmetry in top quark-antiquark production*, Phys. Rev. D **84** (2011) 112005.

[122] A. Harel, *A_{FB} at the Tevatron*, slides presented at the 4$^{\text{th}}$ International Workshop on Top Quark Physics, Sant Feliu de Guixols, Spain (September 2011).

[123] CDF Collaboration, *Measurement of the Forward Backward Asymmetry in Top Quark Pair Production in the Dilepton Decay Channel using 5.1 fb^{-1}*, Conf. Note 10436.

[124] CMS Collaboration, *Inclusive and differential measurements of the $t\bar{t}$ charge asymmetry in proton-proton collisions at 7 TeV*, CMS-TOP-11-030; CERN-PH-EP-2012-175 (2012).

[125] ATLAS Collaboration, *Measurement of the charge asymmetry in top quark pair production in pp collisions at $\sqrt{s}$ =7 TeV using the ATLAS detector*, ATLAS-CONF-2011-106 (2011).

[126] Acharya B. et al. (Favareto A.), *Measurement of the top quark charge asymmetry in pp collision data at $\sqrt{s}$ = 7 TeV using the ATLAS detector*, ATL- PHYS-INT-2011-063 (2011).

[127] S. Frixione and B.R. Webber, *Matching NLO QCD computations and parton shower simulations*, JHEP **0206** (2002) 029.

[128] S. Frixione, P. Nason and B.R. Webber, *Webber, Matching NLO QCD and parton showers in heavy flavour production*, JHEP **0308** (2003) 007.

[129] S. Frixione, E. Laenen and P. Motylinski, *Single-top production in MC@NLO*, JHEP **0603** (2006) 092.

[130] P.M. Nadolsky et al., *Implications of CTEQ global analysis for collider observables*, Phys. Rev. D **78** (2008) 013004.

[131] G. Corcella et al., *HERWIG 6.5: an event generator for Hadron Emission Reactions With Interfering Gluons (including supersymmetric processes)*, JHEP **0101** (2001) 010.

[132] J.M. Butterworth et al., *Multiparton interactions in photoproduction at HERA*, Z. Phys. C **72** (1996) 637.

[133] ATLAS Collaboration, *First tuning of HERWIG/JIMMY to ATLAS data*, ATL-PHYS-PUB-2010-014 (2010).

[134] M. Aliev, H. Lacker, U. Langenfeld, S. Moch, P. Uwer, et al., *HATHOR: HAdronic Top and Heavy quarks crOss section calculatoR*, Comput.Phys.Commun. **182** (2011) 1034–1046.

[135] M.L. Mangano et al., *ALPGEN, a generator for hard multiparton processes in hadronic collisions*, JHEP **0307** (2003) 001.

[136] S. Frixione, P. Nason and C. Oleari, *Matching NLO QCD computations with Parton Shower simulations: the POWHEG method*, JHEP **0711** (2007) 070.

[137] T. Gleisberg et al., *Event generation with SHERPA 1.1*, JHEP **0902** (2009) 007.

[138] C. H. Kom and W. J. Stirling, *Charge asymmetry in W+jets production at the LHC*, Eur. Phys. J. **C69** (2010) 67–73.

[139] F. A. Berends, W. T. Giele, H. Kuijf, R. Kleiss, W. J. Stirling Nucl. Phys. B **357** (1991) 1.

[140] S.D. Ellis, R. Kleiss, W. J. Stirling Phys. Lett. B **154** (1985) 435.

[141] J. Erdmann, K. Kroeninger, O. Nackenhorst, and A. Quadt, *Kinematic fitting of ttbar-events using a likelihood approach: The KLFitter package*, ATL-COM-PHYS-2009-551 (2009).

[142] B. Webber. `http://www.hep.phy.cam.ac.uk/theory/webber/MCEGforLHC.pdf`.

[143] T. Adye, *Unfolding algorithms and tests using RooUnfold*, arXiv:1105.1160v1 (2011).

[144] G. D'Agostini, *Improved iterative Bayesian unfolding*, arXiv:1010.0632v1 (2010).

[145] A. D. Martin, R. G. Roberts, W. J. Stirling, and R. S. Thorne, *MRST2001: partons and α_s from precise deep inelastic scattering and Tevatron jet data*, Eur. Phys. J. C **23(1)** (2002) 73.

[146] M. R. Whalley, D. Bourilkov, and R. C. Group, *The Les Houches Accord PDFs (LHAPDF) and Lhaglue*, arXiv:hep-ph/0508110v1 (2005).

[147] L. Lyons, D. Gibaut, and P. Clifford, *How to combine correlated estimates of a single physical quantity*, Nucl. Instrum. Meth. A **270** (1988) 110.

[148] A. Valassi, *Combining correlated measurements of several different physical quantities*, Nucl. Instrum. Meth. A **500** (2003) 391–405.

[149] J. A. Aguilar-Saavedra, A. Juste, F. Rubbo, *Boosting the $t\bar{t}$ charge asymmetry*, arXiv:1109.3710v2 (2011).

[150] M. Kaku, *Quantum Field Theory: A Modern Introduction*. Oxford University Press, 1993.

[151] D. Perkins, *Introduction to High Energy Physics*. Cambridge University Press, 2000.

[152] D. Volkov and V. Akulov, *Is the Neutrino a Goldstone Particle?*, Phys.Lett. **B46** (1973) 109–110.

[153] J. Wess and B. Zumino, *Supergauge Invariant Extension of Quantum Electrodynamics*, Nucl.Phys. **B78** (1974) 1.

[154] J. Wess and B. Zumino, *Supergauge Transformations in Four-Dimensions*, Nucl.Phys. **B70** (1974) 39–50.

[155] Y. Golfand and E. Likhtman, *Extension of the Algebra of Poincare Group Generators and Violation of p Invariance*, JETP Lett. **13** (1971) 323–326.

[156] H. P. Nilles, *Supersymmetry, Supergravity and Particle Physics*, Phys.Rept. **110** (1984) 1–162.

[157] H. E. Haber and G. L. Kane, *The Search for Supersymmetry: Probing Physics Beyond the Standard Model*, Phys.Rept. **117** (1985) 75–263.

[158] J. Wess and J. Bagger, *Supersymmetry and Supergravity: (Revised Edition)*. Princeton Series in Physics. Princeton University Press, 1992.

[159] S. P. Martin, *A Supersymmetry primer*, `arXiv:hep-ph/9709356 [hep-ph]`.

[160] S. P. Martin, *Implications of supersymmetric models with natural R-parity conservation*, Phys.Rev. **D54** (1996) 2340–2348.

[161] S. Dimopoulos and D. W. Sutter, *The Supersymmetric flavor problem*, Nucl.Phys. **B452** (1995) 496–512.

[162] M. Asano, H. D. Kim, R. Kitano, and Y. Shimizu, *Natural Supersymmetry at the LHC*, JHEP **1012** (2010) 019.

[163] W. Beenakker, M. Kramer, T. Plehn, M. Spira, and P. Zerwas, *Stop production at hadron colliders*, Nucl.Phys. **B515** (1998) 3–14.

[164] W. Beenakker, R. Hopker, M. Spira, and P. Zerwas, *Squark and gluino production at hadron colliders*, Nucl.Phys. **B492** (1997) 51–103.

[165] C. Boehm, A. Djouadi, and Y. Mambrini, *Decays of the lightest top squark*, Phys.Rev. **D61** (2000) 095006.

[166] ATLAS Collaboration, *Further search for supersymmetry at* $\sqrt{s} = 7$ *TeV in final states with jets, missing transverse momentum and isolated leptons with the ATLAS detector*, Phys.Rev. **D86** (2012) 092002.

[167] ATLAS Collaboration, *Search for squarks and gluinos with the ATLAS detector in final states with jets and missing transverse momentum using 4.7 fb^{-1} of $\sqrt{s} = 7$ TeV proton-proton collision data*,.

[168] ATLAS Collaboration, *Hunt for new phenomena using large jet multiplicities and missing transverse momentum with ATLAS in 4.7 fb^{-1} of $\sqrt{s} = 7$ TeV proton-proton collisions*, JHEP **1207** (2012) 167.

[169] ATLAS Collaboration, *Search for top and bottom squarks from gluino pair production in final states with missing transverse energy and at least three b-jets with the ATLAS detector*, CERN-PH-EP-2012-194 (2012).

[170] ATLAS Collaboration, *Search for gluino pair production in final states with missing transverse momentum and at least three b-jets using 12.8 fb^{-1} of pp collisions at sqrts = 8 TeV with the ATLAS Detector.*, ATLAS-CONF-2012-145 (2012).

[171] ATLAS Collaboration, *Search for supersymmetry using events with three leptons, multiple jets, and missing transverse momentum in 13.0 fb^{-1} of pp collisions with the ATLAS detector at $\sqrt{s} = 8$ TeV*, ATLAS-CONF-2012-151 (2012).

[172] ATLAS Collaboration, *Search for light scalar top quark pair production in final states with two leptons with the ATLAS detector in $\sqrt{s} = 7$ TeV proton-proton collisions*, CERN-PH-EP-2012-211 (2012).

[173] ATLAS Collaboration, *Search for light top squark pair production in final states with leptons and b-jets with the ATLAS detector in $\sqrt{s} = 7$ TeV proton–proton collisions*, ATLAS-CONF-2012-070 (2012).

[174] ATLAS Collaboration, *Search for a supersymmetric partner to the top quark in final states with jets and missing transverse momentum at $\sqrt{s} = 7$ TeV with the ATLAS detector*, CERN-PH-EP-2012-201 (2012).

[175] ATLAS Collaboration, *Search for direct top squark pair production in final states with one isolated lepton, jets, and missing transverse momentum in $\sqrt{s} = 7$ TeV pp collisions using 4.7 fb^{-1} of ATLAS data*, Phys.Rev.Lett. **109** (2012) 211803.

[176] ATLAS Collaboration, *Search for a heavy top partner in final states with two leptons with the ATLAS detector*, JHEP **11** (2012) 094.

[177] ATLAS Collaboration, *Search for Scalar Bottom Quark Pair Production with the ATLAS Detector in pp Collisions at* $\sqrt{s} = 7$ *TeV*, Phys. Rev. Lett. **108** (2012) 181802.

[178] ATLAS Collaboration, *Search for direct sbottom production in event with two b-jets using 12.8* fb^{-1} *of pp collisions at* $\sqrt{s} = 8$ *TeV with the ATLAS Detector.*, ATLAS-CONF-2012-165 (2012).

[179] ATLAS Collaboration, *Search for scalar top quark pair production in natural gauge mediated supersymmetry models with the ATLAS detector in pp collisions at* $\sqrt{s} = 7$ *TeV*, Phys.Lett. **B715** (2012) 44–60.

[180] ATLAS Collaboration, *Search for a supersymmetric top-quark partner in final states with two leptons in* $\sqrt{s} = 8$ *TeV pp collisions using 13* fb^{-1} *of ATLAS data*, ATLAS-CONF-2012-167 (2012).

[181] Besana M. I. et al. (Favareto A.), *Search for a scalar top decaying to a chargino and a b-quark in final states with two leptons*, ATL-PHYS-INT-2012-102 (2012).

[182] C. Lester and D. Summers, *Measuring masses of semiinvisibly decaying particles pair produced at hadron colliders*, Phys.Lett. **B463** (1999) 99–103.

[183] A. Barr, C. Lester, and P. Stephens, *m(T2): The Truth behind the glamour*, J.Phys. **G29** (2003) 2343–2363.

[184] J. Alwall, M. Herquet, F. Maltoni, O. Mattelaer, and T. Stelzer, *MadGraph 5 : Going Beyond*, JHEP **1106** (2011) 128.

[185] G. Polesello and D. R. Tovey, *Supersymmetric particle mass measurement with the boost-corrected contransverse mass*, JHEP **1003** (2010) 030.

[186] ATLAS Collaboration, *Jet energy measurement with the ATLAS detector in proton-proton collisions at* $\sqrt{s} = 7$ *TeV*, CERN-PH-EP-2011-191 (2011).

[187] ATLAS Collaboration, *Jet energy resolution and selection efficiency relative to track jets from in-situ techniques with the ATLAS Detector Using*

Proton-Proton Collisions at a Center of Mass Energy sqrts = 7 TeV, ATLAS-CONF-2010-054 (2010).

[188] ATLAS Collaboration, *Luminosity Determination in pp Collisions at sqrt(s) = 7 TeV using the ATLAS Detector in 2011*, ATLAS-CONF-2011-116 (2011).

[189] ATLAS Collaboration, *Measurement of the $W \to \ell\nu$ and $Z/\gamma^* \to \ell\ell$ production cross sections in proton-proton collisions at $\sqrt{s} = 7$ TeV with the ATLAS detector*, JHEP **1012** (2010) 060.

[190] S. Frixione and B. R. Webber, *Matching NLO QCD computations and parton shower simulations*, JHEP **0206** (2002) 029.

[191] T. Binoth, M. Ciccolini, N. Kauer, and M. Kramer, *Gluon-induced W-boson pair production at the LHC*, JHEP **0612** (2006) 046.

[192] N. Kidonakis, *Two-loop soft anomalous dimensions for single top quark associated production with a W- or H-*, Phys.Rev. **D82** (2010) 054018.

[193] A. Lazopoulos, T. McElmurry, K. Melnikov, and F. Petriello, *Next-to-leading order QCD corrections to $t\bar{t}Z$ production at the LHC*, Phys.Lett. **B666** (2008) 62–65.

[194] A. Martin, W. Stirling, R. Thorne, and G. Watt, *Parton distributions for the LHC*, Eur.Phys.J. **C63** (2009) 189–285.